Detached-Eddy Simulation of Flow Non-Linearity of Fluid-Structural Interactions Using High Order Schemes

Gecheng Zha (PI), Baoyuan Wang (Ph.D.)

Dept. of Mechanical and Aerospace Engineering
University of Miami
Coral Gables, FL 33124
May 2009

Report Documentation Page		*Form Approved* *OMB No. 0704-0188*

Public reporting burden for the collection of information is estimated to average 1 hour per response, including the time for reviewing instructions, searching existing data sources, gathering and maintaining the data needed, and completing and reviewing the collection of information. Send comments regarding this burden estimate or any other aspect of this collection of information, including suggestions for reducing this burden, to Washington Headquarters Services, Directorate for Information Operations and Reports, 1215 Jefferson Davis Highway, Suite 1204, Arlington VA 22202-4302. Respondents should be aware that notwithstanding any other provision of law, no person shall be subject to a penalty for failing to comply with a collection of information if it does not display a currently valid OMB control number.

1. REPORT DATE **MAY 2009**	2. REPORT TYPE	3. DATES COVERED **00-00-2009 to 00-00-2009**

4. TITLE AND SUBTITLE **Detached-Eddy Simulation of Flow Non-Linearity of Fluid-Structural Interactions Using High Order Schemes**	5a. CONTRACT NUMBER
	5b. GRANT NUMBER
	5c. PROGRAM ELEMENT NUMBER
6. AUTHOR(S)	5d. PROJECT NUMBER
	5e. TASK NUMBER
	5f. WORK UNIT NUMBER

7. PERFORMING ORGANIZATION NAME(S) AND ADDRESS(ES) **University of Miami,Dept. of Mechanical and Aerospace Engineering,Coral Gables,FL,33124**	8. PERFORMING ORGANIZATION REPORT NUMBER

9. SPONSORING/MONITORING AGENCY NAME(S) AND ADDRESS(ES)	10. SPONSOR/MONITOR'S ACRONYM(S)
	11. SPONSOR/MONITOR'S REPORT NUMBER(S)

12. DISTRIBUTION/AVAILABILITY STATEMENT
Approved for public release; distribution unlimited

13. SUPPLEMENTARY NOTES

14. ABSTRACT

15. SUBJECT TERMS

16. SECURITY CLASSIFICATION OF:			17. LIMITATION OF ABSTRACT	18. NUMBER OF PAGES	19a. NAME OF RESPONSIBLE PERSON
a. REPORT **unclassified**	b. ABSTRACT **unclassified**	c. THIS PAGE **unclassified**	**Same as Report (SAR)**	**198**	

Standard Form 298 (Rev. 8-98)
Prescribed by ANSI Std Z39-18

Summary

The objective of this research is to develop an efficient and accurate methodology to resolve flow non-linearity of fluid-structural interaction. To achieve this purpose, a numerical strategy to apply the detached-eddy simulation (DES) with a fully coupled fluid-structural interaction model is established for the first time. The following novel numerical algorithms are also created: a general sub-domain boundary mapping procedure for parallel computation to reduce wall clock simulation time, an efficient and low diffusion E-CUSP (LDE) scheme used as a Riemann solver to resolve discontinuities with minimal numerical dissipation, and an implicit high order accuracy weighted essentially non-oscillatory (WENO) scheme to capture shock waves.

The Detached-Eddy Simulation is based on the model proposed by Spalart in 1997. Near solid walls within wall boundary layers, the Reynolds averaged Navier-Stokes (RANS) equations are solved. Outside of the wall boundary layers, the 3D filtered compressible Navier-Stokes equations are solved based on large eddy simulation(LES). The Spalart-Allmaras one equation turbulence model is solved to provide the Reynolds stresses in the RANS region and the subgrid scale stresses in the LES region.

An improved 5th order finite differencing weighted essentially non-oscillatory (WENO) scheme with an optimized ε value is employed for the inviscid fluxes. The new LDE scheme used with the WENO scheme is able to capture crisp shock profiles and exact contact surfaces. A set of fully conservative 4th order finite central differencing schemes are used for the viscous terms.

The 3D Navier-Stokes equations are discretized based on a conservative finite differencing scheme, which is implemented by shifting the solution points half grid interval in each direction on the computational domain. The solution points are hence located in the center of the grid cells in the computational domain (not physical domain). This makes it possible to use the same code structure as a 2nd order finite volume method. A finite differencing high order WENO scheme is used since a finite differencing WENO scheme is much more efficient than a finite volume WENO scheme.

The unfactored line Gauss-Seidel relaxation iteration is employed for time marching. For the time accurate unsteady simulation, the temporal terms are discretized using the 2nd order accuracy backward differencing. A pseudo temporal term is introduced for the unsteady calculation following Jameson's method. Within each physical time step, the solution is iterated until converged based on pseudo time step.

A general sub-domain boundary mapping procedure is developed for arbitrary topology multi-block structured grids with grid points matched on sub-domain boundaries. The interface of two adjacent blocks is uniquely defined according to each local mesh index system (MIS) which is specified independently. A pack/unpack procedure based on the definition of the interface is developed to exchange the data in a 1D array to minimize data communication. A secure send/receive procedure is employed to remove the possibility of blocked communication and achieve optimum parallel computation efficiency. Two terms, "*Order*" and "*Orientation*", are introduced as the logics defining the relationship of adjacent blocks. The domain partitioning treatment of the implicit matrices is to simply discard the corner matrices so that the implicit Gauss-Seidel iteration can be implemented within each subdomain. This general sub-domain boundary mapping procedure is demonstrated

to have high scalability.

Extensive numerical experiments are conducted to test the performance of the numerical algorithms. The LDE scheme is compared with the Roe scheme for their behavior with RANS simulation. Both the LDE and the Roe scheme can use high CFL numbers and achieve high convergence rates for the algebraic Baldwin-Lomax turbulence model. For the Spalart-Allmaras one equation turbulence model, the extra equation changes the Jacobian of the Roe scheme and weakens the diagonal dominance. It reduces the maximum CFL number permitted by the Roe scheme and hence decreases the convergence rate. The LDE scheme is only slightly affected by the extra equation and maintains high CFL number and convergence rate. The high stability and convergence rate using the Spalart-Allmaras one equation turbulence model is important since the DES uses the same transport equation for the turbulence stresses closure.

The RANS simulation with the Spalart-Allmaras one equation turbulence model is the foundation for DES and is hence validated with other transonic flows including a 2D subsonic flat plate turbulent boundary layer, 2D transonic inlet-diffuser, 2D RAE2822 airfoil, 3D ONERA M6 wing, and a 3D transonic duct with shock boundary layer interaction. The predicted results agree very well with the experiments. The RANS code is then further used to study the slot size effect of a co-flow jet (CFJ) airfoil.

The DES solver with fully coupled fluid-structural interaction methodology is validated with vortex induced vibration of a cylinder and a transonic forced pitching airfoil. For the cylinder, the laminar Navier-Stokes equations are solved due to the low Reynolds number. The 3D effects are observed in both stationary and oscillating cylinder simulation because of the flow separations behind the cylinder. For the transonic forced pitching airfoil DES computation, there is no flow separation in the flow field. The DES results agree well with the RANS results. These two cases indicate that the DES is more effective on predicting flow separation.

The DES code is used to simulate the limited cycle oscillation of NLR7301 airfoil. For the cases computed in this research, the predicted LCO frequency, amplitudes, averaged lift and moment, all agree excellently with the experiment. The solutions appear to have bifurcation and are dependent on the initial perturbation. The developed methodology is able to capture the LCO with very small amplitudes measured in the experiment. This is attributed to the high order low diffusion schemes, fully coupled FSI model, and the turbulence model used. This research appears to be the first time that a numerical simulation of LCO matches the experiment. The DES code is also used to simulate the CFJ airfoil jet mixing at high angle of attack.

In conclusion, the numerical strategy of the high order DES with fully coupled FSI model and parallel computing developed in this research is demonstrated to have high accuracy, robustness, and efficiency. Future work to further maturate the methodology is suggested.

Acknowledgment

Contents

List of Figures

List of Tables

Abbreviation

AoA	Angle of attack
AUSM	Advection upstream splitting method
B − L	Baldwin-Lomax 0-equation turbulence model
CFD	Computational fluid dynamics
CFJ	Co-flow jet
CSD	Computational structured dynamics
CUSP	Convective upwind and split pressure
DDES	Delayed detached-eddy simulation
DES	Detached-eddy simulation
FSI	Fluid-structural interaction
GSLR	Gauss-Seidel line relaxation
LCO	Limit cycle oscillation
LDE	Low diffusion E-CUSP scheme
LDFSS	Low diffusion flux splitting scheme
LES	Large eddy simulation
LU − SGS	Lower-upper symmetric Gauss-Seidel
MIS	Mesh index system
MPI	Message passing interface
MSD	Modeled-stress depletion
MUSCL	Monotone upstream-centered schemes for conservation laws
POD	Proper orthogonal decomposition
RANS	Reynolds averaged Navier-Stokes equations
ROM	Reduced order model
S − A	Spalart-Allmaras 1-equation turbulence model
WENO	Weighted essentially non-oscillatory scheme

Chapter 1

Introduction

1.1 Background

Flow induced structural vibration is one of the most challenging problems affecting the
military and commercial aircraft. Due to the very complicated non-linear flow-structure
interaction phenomena, there is a lack of high fidelity computational tools to study the
basic physics and to accurately predict the structural failure limits. For airframe, there are
problems such as transonic flutter, limit cycle oscillation, buzz, buffet, etc. For propulsion
turbomachinery, there are problems such as high cycle fatigue caused by forced response
or stall flutter, etc. Helicopter rotor blades constantly work under the vibration induced by
blade wake and tip vortexes. The development of advanced methodologies to accurately
simulate fluid-structural interactions will have broad impact on improving the performance
of various aircraft.

The difficult issue that the fluid-structural interaction (FSI) community currently faces
is the non-linearity caused by both fluid and structure [1]. The aerodynamic non-linearity
poses more challenge than the structural one [2, 3]. These problems are often accompanied
or caused by the complicated flow phenomena such as shock wave/turbulent boundary layer
interaction, flow separation, vortex shedding, etc.

The first challenge to resolve aerodynamic non-linearity such as shock wave/turbulent

boundary layer interaction and flow separation is the turbulence simulation. The second issue is the high accuracy requirement of the numerical simulation with low numerical diffusion. A large numerical diffusion can affect the structural response. The third issue is the efficient wall clock time for simulation, which has to mainly rely on parallel computation.

1.2   The Objectives

The objective of this research is to develop a high accuracy and high efficiency tool to simulate the non-linearity of FSI. It is achieved by accomplishing the following tasks:

1) Develop a DES strategy using high order scheme for turbulence.

2) Develop an high order WENO scheme for shock capturing and high order central differencing schemes for viscous terms.

3) Develop a high efficiency low diffusion E-CUSP scheme to be used as the Riemann solver.

4) Develop a high scalability general parallel computation methodology for structured grid.

5) Employ a fully coupled fluid-structural interaction model with implicit time marching.

1.3   Review of the State of the Art

1.3.1   Fluid-Structural Interaction Nonlinearity

Many efforts have been made by using reduced order models(e.g. frequency domain methods), time accurate nonlinear CFD(e.g. time domain Navier-Stokes equations), and CSD (computational structured dynamics) solutions to study the nonlinear fluid-structural interaction problems. The reduced order models (ROM) are mostly based on linearized flow equations and linear or non-linear structural models. The advantage of ROM is their CPU efficiency by significantly reducing the CFD model size. The ROM methods include the

modal analysis of flow field with proper orthogonal decomposition (POD) by Hall and Dowell, et al. [4–7], Lucia, Beran and Silva [8, 9] or the Volterra theory based method used by Silva and Raveh [10].

The reduced order models have made significant progress and are used to study many problems in both external airframe flows and internal turbomachinery flows(Silva et al. 2004,Sarkar et al. 2004, Beran et al. 2004, Tang et al. 2004,Tran et al. 2004, Moffatt et al.2004) [11–16]. A typical conclusion is that the onset of flutter and LCO can be generally predicted quite well with the ROMs, but the vibration amplitude due to primarily the aerodynamic nonlinearity such as LCO is often significantly over-predicted. Resolving the non-linearity of the structural response does not help much as indicated by Tang et al. [2].

Other than the ROMs, the other path that is vigorously under development to pursue calculation of fluid-structural interactions is to solve the time accurate Euler or Navier-Stokes equations in time domain with loosely or fully coupled linear or non-linear structural models. The loosely coupled model means that the structural response lags behind the flow field solution. Within a time step for the loosely coupled method, the structure solver calculates the response after the flow solver is converged. This kind of methods may be limited to first-order temporal accuracy only regardless of the temporal accuracy of the individual solvers [17]. The fully coupled model is that the flow field and structure always respond simultaneously by exchanging the aerodynamic forcing and structural displacement within each inner iteration of a time step. Obviously, only the fully coupled model is rigorous in physical sense.

Bendiksen et al. [18] pioneered the research by using an explicit CFD code coupled with a structural integrator based on the convolution integral to obtain the flutter boundary for a NACA 64A010 airfoil. The loosely coupled model between the fluid and structural solvers include the work of Guruswamy [19], Lee-Rausch et al. [20], Smith [21], Vermeersch et al. [22], Darracq, et. al [23], Prananta, et. al [24], Bohbot et al. [25], and Blom et al. [26]. Alonso and Jameson developed a model which is close to the fully coupled method with the structural displacement updated every several fluid solver iterations [27]. The

implicit Runge-Kutta method with multigrid acceleration is employed for the flow solver in Alonso's work [27] [28]. In 1997-98, Morton and Melville et al. developed an implicit fully coupled fluid structural interaction model, which used the Beam-Warming implicit scheme for the flow solver coupled with a modal structural solver [29] [30] [17]. In 2001, Liu et al. developed a fully coupled method using Jameson's explicit scheme with multigrid method and a finite element structural model [31]. In 2004-2007, Chen and Zha et al. [32–34] developed a fully coupled fluid-structural interaction methodology using implicit Gauss-Seidel iteration, which does not have the factorization error of the Beam-Warming implicit method and hence allows larger time step. A new high efficiency low diffusion upwind scheme, Zha E-CUSP scheme, is employed to reduce CPU time [33, 35–37].

However, the results form the time domain time accurate nonlinear flow solver have not yielded more optimistic results. In general, again, the weak divergence, flutter divergence and onset of LCO can be captured and predicted quite well, but the amplitude of LCO is still significantly over predicted. These can be seen in the work by Bendiksen(1992), Morton and Beran (1999), Weber et al.(2001), and Tang at al. [2, 3, 38, 39]. Even though the inviscid Euler solver can capture the onset of LCO, the viscous Navier-Stokes solvers predict the LCO amplitude closer to experiments than the Euler solver. The LCO amplitude is also dependent on the turbulence model used as pointed out by Tang et al. (2003) [2] when the NLR7301 airfoil is calculated [40, 41]. The non-linear structural model does not really produce better results of LCO as indicated by Gordnier in 2003 [42]. The calculation with wind tunnel wall porosity yields better LCO amplitude, but a significant difference remains if the actual wind tunnel wall porosity is used (Castro et al., 2001) [43].

According to Bendiksen [3], both the LCO and transonic dip may be caused by aerodynamic non-linearity due to shock wave/turbulent boundary layer interaction and the resulted separation. Schewe and Dietz et al. in 2003 and 2004 [40, 41] tend to support this hypothesis even though there was no clear evidence in their experiment that the flow separation occurs with the very small LCO amplitude. Schewe et al. [40] attribute two nonlinearity mechanisms to the amplitude-limiting phenomenon: 1)the oscillating shock strength and

the coupled pulsations of the marginally separated flow beneath the shock; 2) the trailing edge separation they deduced from the significant increase in the r.m.s. value of the pressure fluctuation near trailing edge.

Schewe et al. [40] gave the following important observations and questions: First, the LCOs they captured have very small relative amplitudes of the plunge on the order of 2/1000 to 3/1000 of the chord and the pitching amplitude less than $1°$. They questioned if the LCOs of such small amplitudes are the artifacts of the wind-tunnel experiment or could also occur in the unbounded flow. Second, since all the reported numerical simulations at that time only captured the much greater LCO amplitudes, they questioned if it means the co-existence of multiple LCOs at constant flow conditions. They discovered the multiple coexisting LCOs in their experiments. Third, they found that the wall boundary layer transition from laminar to turbulent does not have much effect on LCO. Fourth, they verified that the wind tunnel wall interference with or without perforated test section does not have much effect on LCOs. Fifth, they observed that the transition from steady to oscillatory state can be either continuous or discontinuous.

The question we want to ask is: where is the difficulty for fluid-structural interaction calculation? The answer appears to be the aerodynamic non-linearity. Bendiksen pointed out in 1992 [3] that both the LCO and transonic dip may be caused by aerodynamic non-linearity due to shock wave/turbulent boundary layer interaction and the resulted separation. The experiments of Schewe and Dietz et al. in 2003 and 2004 [40, 41] for the NLR7301 supercritical airfoil support these findings. Their experimental results indicate that the flow separation at the trailing edge, and the interactions between the shock and the marginal region of separated flow beneath it, may be responsible for limiting the amplitude of the observed LCO.

For large structural deflections and rotations in structure, Bendiksen and Seber recently point out that both structural and aerodynamic non-linearities can have a dramatic qualitative and quantitative effect on the flutter behavior [1]. Neglecting either the structural or the fluid non-linearities can lead to completely erroneous stability predictions.

In this research, only small deflections and rotations in structure are considered. Therefore, the linear structural equations are solved in the fluid-structural interaction calculation. A fully coupled FSI model is used to ensure the simulation accuracy [32–34]. The NLR7301 airfoil with detailed experimental measurement of limited cycle oscillation (LCO) is calculated in 2D using RANS method and in 3D using DES method. This research is the first effort to apply the high order accuracy numerical algorithms and DES to resolve flow non-linearity of flow-structural interactions. The rigorous algorithm of this research appear to be paid off with the numerical simulation matching the experiment excellently for the first time. This simulation also confirms some of the experimental observations and answers some important questions. First, the LCOs with the small relative amplitude is captured with unbounded flows in the numerical simulation. This means they should not be the artifacts of the wind-tunnel experiment and most likely are the factual phenomenon. Second, the co-existence of multiple LCOs at constant flow conditions is confirmed in our simulation. The reason that other numerical simulations only capture the LCOs with large amplitudes may be due to their high numerical dissipation that either smears out the small amplitude LCO or is only able to resolve the large amplitudes LCOs. Third, the numerical simulation of this research confirms that the wall boundary layer transition from laminar to turbulent does not have a large effect on LCOs at high Reynolds number, because our simulation assumes that the boundary layer is fully turbulent from the airfoil leading edge. Fourth, the simulation confirms that the wind tunnel wall interference with or without perforated test section does not have much effect on LCOs because our simulation uses the unbounded flow condition with no wind tunnel wall effect at all. Fifth, the numerically captured LCO is not accompanied with any flow separation due to the very small amplitude. This may rectify the hypothesis that the LCOs are caused by the nonlinearity of flow separation induced by shock/boundary layer interaction. In other words, the nonlinearity of shock/boundary layer interaction with no flow separation is sufficient to trigger a LCO. This may make reduced numerical models feasible to capture LCOs.

1.3.2 Detached-Eddy Simulation

To resolve the aerodynamic non-linearity such as shock wave/turbulent boundary layer interaction and flow separation, the turbulence simulation is critical. The widely used methods for predictions of turbulent flow are based on Reynolds averaged Navier-Stokes equations (RANS). However, RANS models are not able to calculate the flow separation correctly. RANS methods intend to calculate the large scale eddies using a universal model. Large scale turbulence is affected by the flow geometry and boundary conditions and a universal model does not exist.

Large Eddy Simulation (LES) is promising to overcome the disadvantages of the RANS model. In LES, the governing equations are spatially filtered on the scale of the numerical grid. The large energy containing scales are directly simulated, and the small scale eddies, which are generally more homogeneous and universal, are modeled. The large eddies are strongly affected by the flow field geometry boundaries. Therefore the direct computation of the large eddies by LES is more accurate than modeling the large eddies by RANS. The effect of the unresolved small scales of motion is modeled by a subgrid-scale (SGS) model [44] [45] [46] [47] [48] or by the inherent dissipation in the numerical schemes [49] [50]. Because the statistics of the small scale turbulence are more isotropic and universal, a general physical model for small scale eddies is more plausible.

However, for high Reynolds number flows such as those of transonic wings and turbomachinery blades, to resolve the wall boundary layer, LES needs the CPU resource not much less than the Direct Numerical Simulation(DNS). This makes the LES too expensive for high Reynolds number flow calculations. For engineering applications, it is not hopeful for LES to be rigorously used until in another 4 decades [51].

To overcome the intensive CPU requirement for LES, Spalart et al. developed the so called detached-eddy simulation (DES) strategy [51], which is a hybrid RANS and LES method. Near the solid surface within the wall boundary layer, the unsteady RANS model is realized. Away from the wall surface, the model automatically converts to LES. By using the RANS model near the wall, the mesh size as well as the CPU time can be tremendously

reduced. The motivation of DES is that the LES is powerful in regions of massive separation and other free shear flows such as jets, but much too costly in the large area of the wall boundary layers.

Spalart gave a grid guidance for DES in 2001 [52, 53], which divides a flow domain with solid walls to Euler region, RANS region, and LES region. In the RANS region, the domain is further divided to Viscous region and Outer region. The LES region is composed of Viscous, Focus and Departure region. Spalart's DES grid guidance gives sufficient grid resolution for LES region and the transition to Euler region from RANS region. The grid size is dramatically reduced compared to the pure LES.

Even though DES concept is much newer than RANS and LES concept, its application for turbulence simulation has already achieved encouraging success as shown in the work of Tarvin et al. (1999) [54], Spalart (2001) [52, 53], Forsythe et al.(2002) [55], Viswanathan et al. [56], Squires et al. [57, 58], Hsnsen, et al. (2003) [59], Subbareddy et al. (2005) [60], Wang et al. (2008, 2009) [61, 62]. These flows calculated using DES include those for airfoils, cylinders, forbodies, base flows, etc. The results are qualitatively and quantitatively better than the solutions using RANS. DES appears to be a suitable compromise between the physical models of turbulence and CPU efficiency. In those DES applications, almost all the algorithms use 2nd order accuracy except that of Tarvin et al. (1999) [54], which employs fifth order upwind scheme for the inviscid convective terms in space, but 2nd order accuracy for the viscous terms.

However, with the spread of the successful DES application after it was first proposed in 1997, a defect of the first generation DES model(DES97) [51] has been also exposed. It is that the transition from the RANS model to LES in DES97 is not grid spacing independent [63]. DES is originally designed to treat the entire boundary layer using a RANS model and to use LES separated flow regions. A fine mesh with grid spacing much smaller than the boundary layer thickness may exhibit an incorrect behavior in boundary layers and shallow separation regions due to locating the RANS/LES transition within the boundary layer. The grid spacing could be fine enough for the DES length scale to follow the LES

branch, which will lower the eddy viscosity below the RANS level. The resolved Reynolds stresses determined from the velocity fluctuation (LES content) may be lacking because the resolution is not fine enough to fully support it. The DES limiter then reduces the eddy viscosity, and therefore the modeled Reynolds stresses. This phenomenon is referred as modeled-stress depletion (MSD) [63]. This drawback is also considered as one of the possible causes for the inaccurate prediction of flow separation region size with suction flow control when the DES is used as indicated by Rumsey [64].

To overcome the MSD problem and make the DES limiter independent of grid spacing, Spalart suggested a modification to the original DES97 model in 2006 [63], referred to as Delayed DES(DDES). A blending function similar to the one used by Menter and Kuntz [65] for the SST model is introduced to limit the DES length scale to ensure the transition of RANS to LES be independent of grid spacing. The DDES model has demonstrated excellent agreement with experiment and a significant improvement over the DES97 for the tested cases, which include a flat plat boundary layer resolved with mesh spacing significantly smaller than the boundary layer thickness, a circular cylinder, a single airfoil with weak separation near trailing edge, the backward facing step with large separation region, and a multi-element airfoil. The predicted separation onset and separation region length agree well with the experiments.

This research has successfully implemented the Spalart's DES model, which is used for a turbulent cylinder flow [61], prediction of NLR7301 LCO and CFJ airfoil flows at high angle of attack.

Due to the time limitation, this research only adopts the DES97 model [51]. The DDES will be implemented in future.

1.3.3 High Order WENO Scheme

Developing accurate and efficient numerical schemes is one of the most important tasks of the CFD researchers and engineers. It is particularly important when a high fidelity numerical simulation, such as detached-eddy simulation (DES) and large eddy simulation

(LES) is performed for a unsteady flow problem, which is usually very CPU intensive. So far, most of the engineering applications employ the 2nd order numerical accuracy. The high order schemes (higher than 3rd order) are mostly limited to the fundamental research such as high fidelity turbulence simulation (e.g. Large Eddy Simulations and Direct Numerical Simulation) and aeroacoustic calculation. The reason is that the high order schemes are generally not mature enough for robust engineering applications. For example, when a high order scheme is used, the convergence for a steady state solution is usually difficult. How to make a high order scheme converge well is not well studied.

For aerospace engineering applications with shock waves or contact surfaces, the essentially non-oscillatory (ENO) or weighted essentially non-oscillatory (WENO) schemes are attractive for their capability to capture discontinuities and achieve the consistent high order accuracy in smooth regions. By using a convex combination of all candidate stencils to replace the smoothest one in the ENO scheme, a WENO scheme has more advantages over its ENO counterpart. For example, it approaches certain high order accuracy in smooth regions and has better convergence rate due to the smoother numerical flux used. From its appearance [66, 67] to present, the WENO schemes have been extensively applied to different flow problems in many areas.

Titarev and Toro [68] firstly carried out an extension of the finite-volume WENO schemes to three space dimensions with high order accuracy. A finite volume WENO scheme needs higher computational cost than a WENO finite differencing scheme. A WENO finite difference method is more efficient in multi-dimensional calculation due to avoiding the Gaussian integrals. As pointed out in references [68, 69], when the piece-wise parabolic reconstruction is used in two space dimensions, a finite volume WENO scheme require approximately three times more CPU time than the corresponding finite difference WENO schemes. In three space dimensions, the difference is about nine times. Hence, for structured meshes, the finite difference WENO scheme is preferred. In [70–72], the formally high-order accurate WENO shock-capturing method using a third-order total-variation diminishing (TVD) Runge-Kutta time evolution scheme is applied to the re-shocked two-

dimensional single-mode Richtmyer-Meshkov instability [70], the shallow water and the open-channel flow equations [71], and to study adaptive mesh refinement techniques for multi-dimensional hydrodynamic simulation [72]. Sjogreen and Yee [73] used a low dissipation sixth-order spatial and fifth-order WENO scheme with the standard fourth-order Runge-Kutta method to study the supersonic reactive flows.

In a WENO scheme, a Riemann solver is needed to capture the discontinuities. There are two ways to evaluate the Riemann solver fluxes. For WENO finite difference schemes, Shu suggested that the WENO reconstruction be directly applied to the split fluxes from left or right [74]. In this research, we employ a different method, which is to evaluate the conservative variables with WENO scheme and then use the conservative variables to calculate the fluxes based on the Riemann solvers. This is similar to the MUSCL method of Van Leer [75].

Chen et al. [76] presented a class of implicit WENO schemes for the incompressible Navier-Stokes equations, in which the lower-upper symmetric Gauss-Seidel (LU-SGS) relaxation is used for computing steady state solutions. Yang et al. [77] have extended this method to the solutions of steady compressible Navier-Stokes equations. Cadiou and Tenaud [78] proposed an implicit WENO shock capturing scheme for unsteady flows and applied it to one-dimensional Euler equations. The use of WENO spatial operator not only enhances the accuracy of solutions, but also improves the convergence rate of the steady state computation compared with using the ENO counterpart. In references [79, 80], it is found that the factored LU-SGS is significantly less efficient than the unfactored Gauss-Seidel line relaxation method for the steady state flow computation since the former introduces the factorization error limiting the CFL number and convergence rate.

Zhang and Shu [81] found that, when a 5th order WENO scheme combined with a Runge-Kutta time discretization is used to achieve steady state solutions, the residual stops dropping at the truncation error level of the scheme, which is far above the machine zero. They noticed that the original smoothness indicator of Jiang and Shu [67] results in a small oscillation near a steady shock wave. The oscillation propagates to the smooth region and

causes the residual to hang at the truncation error level rather than to approach machine zero. They proposed a modified smoothness indicator near the shock region for the fifth order WENO scheme, which can drive the residual to machine zero for some 1D and 2D problems without the influence from the boundary conditions. But for the other examples, the residuals still fluctuate at the level of ($10^{-2} \sim 10^{-4}$). Zhang and Shu [81] attribute the convergence difficulty to the influence of boundary conditions. At a critical point (the first derivative is zero), the first term in the Taylor series expansion of the IS_k of Zhang and Shu does not satisfy the requirement of $IS_k = D(1 + O(\Delta x^{r-1}))$ to achieve 5th order accuracy. Thus the accuracy of the scheme of Zhang and Shu [81] is only 3rd order at a critical point.

Henrick et al. [82] proposed a mapped WENO scheme to achieve the optimal accuracy order at the critical point of a smooth function and discussed the choice of ε value for the 5th order WENO scheme. When ε is dominant in magnitude, the preconditions of WENO5 scheme approaches those of a central difference scheme. Furthermore, the oscillation on the order of ε^2 may exist near discontinuities. Hence if the ε is too large, it will mitigate the ENO behavior of the method. Henrick et al. suggested that ε can be slightly larger than the square root of the smallest positive number allowed for a particular machine. But they didn't study the convergence behavior for computing steady state solutions.

So far, the 5th order WENO schemes are mostly used for unsteady flow calculation such as LES, DNS, or aeroacoustic calculation [83–85]. For unsteady calculation, if an explicit scheme such as a Runge-Kutta scheme is used, the convergence is generally not an issue. If a dual time stepping procedure [86] is used, the convergence could be an issue within each physical time step. However, for dual time stepping, a fixed number of iterations within each physical time step is often used and the convergence of the solution is sometimes overlooked. The best convergence test is to calculate steady state solutions to see if they can be converged to machine zero. For the transonic flows with shock wave discontinuities, little research has been done to study the convergence behavior for steady state solutions using the high order WENO schemes.

In this research, the 5th order finite differencing WENO scheme [87] is used to evaluate

the inviscid fluxes, and the 4th order central differencing scheme [88] is used to calculate the viscous fluxes. The WENO scheme adopted uses an optimized ε value and is able to remove the weights oscillation, maintain the sensitivity to shock and contact surface discontinuities, achieve optimal weights and thus the minimal dissipation, and obtain solid convergence to machine zero.

1.3.4 Upwind Schemes

An upwind scheme is required as a Riemann solver when a WENO scheme is used. Different from the central differencing schemes [89], upwind schemes are designed to make the flux computation based on the characteristic directions of the governing equations. The upwind schemes have inherent numerical dissipation, which makes the artificial dissipation unnecessary. However, if the numerical dissipations is too large, the physical dissipation can be distorted [90].

The approximate Riemann solver scheme developed by Roe [91] is one of the most famous upwind schemes. By introducing the Jacobian and Roe's average for the variables, the Roe scheme exactly satisfies the Rankine-Hugonoit relations and directly capture the discontinuities. The Roe scheme was considered as the most accurate scheme among the available differencing schemes in 1987 [92]. But the Roe scheme uses matrix dissipation and hence it is time consuming.

To achieve the purpose of efficiency, accuracy and simplicity to use, many efforts have been made to develop upwind schemes only using scalar dissipation instead of matrix dissipation such as that of the Roe's flux difference splitting (FDS) scheme [91]. The examples include AUSM family schemes of Liou [93–97], the Van Leer-Hänel scheme [98], Edwards's LDFSS schemes [99, 100], Jameson's CUSP schemes and limiters [101–103], and the E-CUSP schemes developed by Zha, et al. [36, 37, 104–108], etc.

Pioneered by Liou and Steffen [93,95,96], the researchers seeking the scalar dissipation primarily follow the guideline that the velocity and pressure should be separated to consider their characteristics representing the physics of the convection and waves. Liou and his

colleagues termed their schemes as advection upstream splitting method(AUSM) schemes, and Jameson gave the name of convective upwind and split pressure (CUSP) schemes [101–103].

The CUSP schemes can be basically categorized to two types, the H-CUSP and E-CUSP [101–103]. The H-CUSP schemes have the total enthalpy from the energy equation in their convective vector, while the E-CUSP schemes use the total energy in the convective vector. The Liou's AUSM family schemes, Van Leer-Hänel scheme [98], and Edwards's LDFSS schemes [99, 100] belong to the H-CUSP group. The schemes developed by Zha, et al. [36, 104–106] belong to the E-CUSP group.

Even though the H-CUSP schemes such as AUSM family schemes have achieved great success, from the characteristic theory point of view, the schemes are not fully consistent with the disturbance propagation directions [37, 109], which may affect the stability and robustness of the schemes. By splitting the eigenvalues of the Jacobians to convection (velocity) and waves (speed of sound), one will find that the convection terms only contain the total energy [104], which will lead to the E-CUSP schemes.

Zha and Hu recently suggested an E-CUSP schemes, which has low diffusion and can capture crisp shock wave profiles and exact contact discontinuities [36]. The scheme is consistent with the characteristic directions due to the nature of E-CUSP scheme. The scheme shows the highest stability for two shock tube tests problems compared with several other popularly used upwind schemes for the explicit Euler time marching scheme. The scheme also works well when extended to multi-dimensions [36]. However, the E-CUSP scheme of Zha-Hu may generate temperature oscillation near the computation boundary, in particular when the mesh is skewed. Zha was able to remove the temperature oscillation by introducing the total enthalpy in the smooth factor for the energy equation [37, 109]. However, the scheme loses the capability to capture the exact contact surface due to the modification.

In this research, a LDE scheme is developed by modifying the Zha-Hu E-CUSP scheme using the Mach number splitting of Edwards's LDFSS schemes [99, 100] for the convective

flux. The solutions calculated by the new scheme is smooth and the scheme can capture crisp shock profile and exact contact discontinuity.

1.3.5   Implicit Time Marching Methods

The implicit methods for compressible viscous flow calculation have been widely employed due to their less stiffness and faster convergence rate than the explicit schemes. In general, implicit methods require the inversion of a linearized system of equations. The direct inversion of the linear equations is usually preventively expensive. The implicit linear equations are therefore commonly inverted by iterative methods.

It is known that the approximately factored (AF) implicit schemes such as the Beam-Warming scheme [110] will introduce the factorization errors, which limit the size of the allowable time steps. For 3D linear wave equation, the AF scheme is also not unconditionally stable. The unfactored schemes with no factorization errors such as the line Gauss-Seidel iterations can have larger time steps with faster convergence rate than the AF methods [33, 36, 111–114]. However, the unfactored schemes typically require more CPU time per iteration since the matrices are usually the full Jacobian matrices and can not be diagonalized.

The lower-upper symmetric Gauss-Seidel (LU-SGS) method suggested by Jameson and Yoon [115, 116] has been widely used due to their relatively easier implicit implementation [117–119]. The attractive feature of the LU-SGS is that the evaluation and storage of the Jacobian matrices can be eliminated by making some approximations to the implicit operator. Although the LU-SGS method could be more efficient than explicit schemes and is unconditionally stable for linear wave equation, the factorization is approximated and will necessarily introduce the factorization errors.

For the unfactored implicit Gauss-Seidel relaxation scheme used to solve the 2D incompressible Navier-Stokes equations, Rogers [120] compared the efficiency of point-Jacobi relaxation (PR), Gauss-Seidel line relaxation (GSLR), incomplete lower-upper decomposition, and the generalized minimum residual method preconditioned with each of the three

other schemes. If a forward sweep plus a backward sweep is counted as one sweep, Rogers found that these methods can obtain different efficiency when the different number of the sweeps are used. For three-dimensional incompressible flows, Yuan [79] compared the efficiency of the point-Jacobi relaxation, line Gauss-Seidel relaxation, and diagonalized ADI schemes. Yuan [79] observed that the PR(2) (PR with two sweeps) is optimum in all PR(n), and GSLR(1) is optimum in all GSLR(n). For the line Gauss-Seidel relaxation methods, one can choose one or more of the coordinate directions as the sweep direction [112, 121]. For compressible flows, there is few study on how the sweep directions will affect the convergence rate and CPU time. There is also no study to compare the efficiency of the unfactored GSLR and the factored LU-SGS.

For unsteady flow, Jameson formulated a so called dual time stepping scheme [86]. By introducing a pseudo time term, the unsteady problem at each physical time step is treated as a steady state problem for pseudo time. Without losing time accuracy, the dual time stepping scheme can greatly improve the computation efficiency by enhancing diagonal dominance [28]. It has been widely used by researchers [122–125].

In this research, the unfactored implicit Gauss-Seidel line relaxation scheme is used to solve the 3D compressible Navier-Stokes equations. For unsteady computation, Jameson's dual time stepping scheme [86] is employed to facilitate the implicit iteration. The temporal term is discretized using the 2nd order backward differencing. A comparison indicates that the Gauss-Seidel relaxation has higher convergence rate and CPU efficiency than the LU-SGS and GSLR methods [80].

1.3.6   Parallel Computation

Parallel computing is becoming a powerful tool for computational fluid dynamics (CFD) simulations [126, 127]. By interconnecting PCs or workstations one can develop a distributed parallel computing system to increase the computing power. Hence there are many efforts to develop parallel computation codes or to convert legacy sequential codes for multi-processor parallel computation.

Multi-block structured grids are widely used for CFD parallel computation because of their numerical efficiency and accuracy. The basic idea is to partition a large domain into multiple smaller sub-domains and conduct the computation in the sub-domains simultaneously to save wall clock time. Partitioning to multiple sub-domains also decreases the difficulties of grid generation around complex configurations since structured grids can be generated within each sub-domain independently. The CFD solvers written for parallel computation are usually based on a single program multiple data (SPMD) strategy, which uses the same CFD code for each sub-domain. The sub-domain data exchange at domain partitioning boundaries, or inner boundaries, is usually treated as boundary conditions [128]. The data are exchanged across the boundaries by a mapping procedure after each iteration [129]. The mapping procedure determines the parallel computation efficiency, accuracy and robustness.

Various mapping procedures for multi-block structured grids have been developed since parallel computation was introduced to CFD. However, the procedure and implementation are usually ad-hoc and different code developers may use different methods. The complexity of the procedures depends on the complexity of the geometry to be dealt with. For a simple domain partitioning problem, Evans *et al.* [130] developed a toolkit known as Computer Aided Parallelization Tools(CAPTools) to convert a scalar code to a form suitable for parallel implementation with message passing calls. For complex geometries that have different local mesh index systems, it is difficult and time consuming to treat the inner boundary data exchange. One method to avoid this is to use database systems to manage CFD parallel computation. The NSMB package is a well known CFD solver developed based on a database system called MEM-COM [131, 132]. The portable parallel library APPL and a database manager GPAR are used to implement the parallel computation [133]. However, as database systems are generally dependent on computer platforms, portability of the CFD codes are quite limited. In addition, such database systems are not often available for general CFD code developers. Therefore, it is useful and necessary to develop a general mapping procedure for inner boundary data exchange when a new or legacy structured grid

CFD code is to be implemented for parallel computation.

In this research, a general subdomain boundary mapping procedure is developed to implement parallel computation for structured grid. A high scalability is achieved [134]

1.4   The Strategy of This Research

To achieve the research objectives, a numerical strategy to apply the detached-eddy simulation (DES) with a fully coupled fluid-structural interaction model is established for the first time. The following novel numerical algorithms are also created: a general sub-domain boundary mapping procedure for parallel computation to reduce wall clock simulation time, an efficient and low diffusion E-CUSP (LDE) scheme used as a Riemann solver to resolve discontinuities with minimal numerical dissipation, and an implicit high order accuracy weighted essentially non-oscillatory (WENO) scheme to capture shock waves.

The Detached-Eddy Simulation is based on the model proposed by Spalart in 1997. Near solid walls within wall boundary layers, the Reynolds averaged Navier-Stokes (RANS) equations are solved. Outside of the wall boundary layers, the 3D filtered compressible Navier-Stokes equations are solved based on large eddy simulation(LES). The Spalart-Allmaras one equation turbulence model is solved to provide the Reynolds stresses in the RANS region and provide the subgrid scale stresses in the LES region.

An improved 5th order finite differencing weighted essentially non-oscillatory (WENO) scheme with an optimized ε value is employed for the inviscid fluxes. The new LDE scheme used with the WENO scheme is able to capture crisp shock profiles and exact contact surfaces. A set of fully conservative 4th order finite central differencing schemes are used for the viscous terms.

The 3D Navier-Stokes equations are discretized based on a conservative finite differencing, which is implemented by shifting the solution points half grid interval in each direction on the computational domain. The solution points are hence located in the center of the grid cells in the computational domain (not physical domain). This makes it possible

to use the same code structure as a 2nd order finite volume method. A finite differencing high order WENO scheme is used since a finite differencing WENO scheme is much more efficient than a finite volume WENO scheme.

The unfactored line Gauss-Seidel relaxation iteration is employed for time marching. For the time accurate unsteady simulation, the temporal terms are discretized using the 2nd order accuracy backward differencing. A pseudo temporal term is introduced for the unsteady calculation following Jameson's method. Within each physical time step, the solution is iterated until converged based on pseudo time step.

A general sub-domain boundary mapping procedure is developed for arbitrary topology multi-block structured grids with grid points matched on sub-domain boundaries. The interface of two adjacent blocks is uniquely defined according to each local mesh index system (MIS) which is specified independently. A pack/unpack procedure based on the definition of the interface is developed to exchange the data in a 1D array to minimize data communication. A secure send/receive procedure is employed to remove the possibility of blocked communication and achieve optimum parallel computation efficiency. Two terms, "*Order*" and "*Orientation*", are introduced as the logics defining the relationship of adjacent blocks. The domain partitioning treatment of the implicit matrices is to simply discard the corner matrices so that the implicit Gauss-Seidel iteration can be implemented within each subdomain. This general sub-domain boundary mapping procedure is demonstrated to have high scalability.

The validation computations are conducted for the developed LDE scheme and parallel algorithm. These validation cases include subsonic flat plate turbulent boundary layer flow, RAE2822 transonic airfoil turbulent transonic flow, transonic inlet-diffuser shock wave/turbulent boundary layer interaction, ONERA M6 Wing transonic flow, 3D Transonic Channel Flow, Co-flow jet (CFJ) airfoil internal and external flow and circular cylinder massive turbulent flow.

Finally, the flow non-linearity of the fluid-structural interaction is studied using Reynolds averaged Navier-Stokes (RANS) and Detached Eddy Simulation (DES) method [62]. The

fully coupled fluid-structural interaction procedure [32–34] is employed to simulate the FSI non-linearity of NLR7301 airfoil LCO. When using DES for a 2D geometry, the 2D configuration is extended in spanwise direction to form a 3D geometric model since DES is always used in 3D. The structural equations solved for DES are the same as those of the 2D cases. Two type movements are included in the present fluid-structural interaction: forced pitching movement and flow induced vibration.

Chapter 2

Governing Equations

2.1   3D Navier-Stokes Equations

The governing equations are the spatially filtered compressible Navier-Stokes equations. The spatial filtering removes the small scale high frequency components of the fluid motion, while keeping the unsteadiness associated with the large scale turbulent motion. Following the derivation of Knight et al. [135], the filtered compressible Navier-Stokes equations in Cartesian coordinates can be expressed as:

$$\frac{\partial \mathbf{Q}}{\partial t} + \frac{\partial \mathbf{E}}{\partial x} + \frac{\partial \mathbf{F}}{\partial y} + \frac{\partial \mathbf{G}}{\partial z} = \frac{1}{Re}\left(\frac{\partial \mathbf{E_v}}{\partial x} + \frac{\partial \mathbf{F_v}}{\partial y} + \frac{\partial \mathbf{G_v}}{\partial z}\right) \tag{2.1}$$

where t is time, Re is the Reynolds number. The variable vector $\mathbf{Q}$, inviscid flux vectors $\mathbf{E}$, $\mathbf{F}$, $\mathbf{G}$, and the viscous fluxes $\mathbf{E_v}$, $\mathbf{F_v}$, $\mathbf{G_v}$ are given as the following.

$$\mathbf{Q} = \begin{pmatrix} \bar{\rho} \\ \bar{\rho}\tilde{u} \\ \bar{\rho}\tilde{v} \\ \bar{\rho}\tilde{w} \\ \bar{\rho}\tilde{e} \end{pmatrix}, \mathbf{E} = \begin{pmatrix} \bar{\rho}\tilde{u} \\ \bar{\rho}\tilde{u}^2 + \bar{p} \\ \bar{\rho}\tilde{u}\tilde{v} \\ \bar{\rho}\tilde{u}\tilde{w} \\ (\bar{\rho}\tilde{e} + \bar{p})\tilde{u} \end{pmatrix}, \mathbf{F} = \begin{pmatrix} \bar{\rho}\tilde{v} \\ \bar{\rho}\tilde{v}\tilde{u} \\ \bar{\rho}\tilde{v}^2 + \bar{p} \\ \bar{\rho}\tilde{v}\tilde{w} \\ (\bar{\rho}\tilde{e} + \bar{p})\tilde{v} \end{pmatrix}, \mathbf{G} = \begin{pmatrix} \bar{\rho}\tilde{w} \\ \bar{\rho}\tilde{w}\tilde{u} \\ \bar{\rho}\tilde{w}\tilde{v} \\ \bar{\rho}\tilde{w}^2 + \bar{p} \\ (\bar{\rho}\tilde{e} + \bar{p})\tilde{w} \end{pmatrix}$$

$$
\mathbf{E_v} = \begin{pmatrix} 0 \\ \bar{\tau}_{xx} + \sigma_{xx} \\ \bar{\tau}_{xy} + \sigma_{xy} \\ \bar{\tau}_{xz} + \sigma_{xz} \\ Q_x \end{pmatrix}, \; \mathbf{F_v} = \begin{pmatrix} 0 \\ \bar{\tau}_{yx} + \sigma_{yx} \\ \bar{\tau}_{yy} + \sigma_{yy} \\ \bar{\tau}_{yz} + \sigma_{yz} \\ Q_y \end{pmatrix}, \; \mathbf{G_v} = \begin{pmatrix} 0 \\ \bar{\tau}_{zx} + \sigma_{zx} \\ \bar{\tau}_{zy} + \sigma_{zy} \\ \bar{\tau}_{zz} + \sigma_{zz} \\ Q_z \end{pmatrix}
$$

The overbar denotes a regular filtered variable, and the tilde is used to denote the Favre filtered variable. In above equations, ρ is the density, u, v, w are the Cartesian velocity components in x, y, z directions, p is the static pressure, and e is the total energy per unit mass.

The $\bar{\tau}$ is the molecular viscous stress tensor and is estimated as:

$$
\bar{\tau}_{ij} = -\frac{2}{3}\tilde{\mu}\frac{\partial \tilde{u}_k}{\partial x_k}\delta_{ij} + \tilde{\mu}\left(\frac{\partial \tilde{u}_i}{\partial x_j} + \frac{\partial \tilde{u}_j}{\partial x_i}\right), \qquad i, j = 1, 2, 3 \tag{2.2}
$$

The above equation is in tensor form, where the subscript 1, 2, 3 represent the coordinates, x, y, z, and the Einstein summation convention is used.

The molecular viscosity $\tilde{\mu} = \tilde{\mu}(\tilde{T})$ is determined by Sutherland law.

The σ is the subgrid scale stress tensor due to the filtering process and is expressed as:

$$
\sigma_{ij} = -\bar{\rho}\left(\widetilde{u_i u_j} - \tilde{u}_i \tilde{u}_j\right) \tag{2.3}
$$

The energy flux Q is expressed as:

$$
Q_i = \tilde{u}_j\left(\bar{\tau}_{ij} + \sigma_{ij}\right) - \bar{q}_i + \Phi_i \tag{2.4}
$$

where Φ is the subscale heat flux:

$$
\Phi_i = -C_p\bar{\rho}\left(\widetilde{u_i T} - \tilde{u}_i \tilde{T}\right) \tag{2.5}
$$

The $\bar{q}_i$ is the molecular heat flux:

$$\bar{q}_i = -\frac{C_p \bar{\mu}}{Pr} \frac{\partial \tilde{T}}{\partial x_i} \tag{2.6}$$

$$\bar{\rho}\tilde{e} = \frac{\bar{p}}{(\gamma - 1)} + \frac{1}{2}\bar{\rho}(\tilde{u}^2 + \tilde{v}^2 + \tilde{w}^2) + \rho k \tag{2.7}$$

where γ is the ratio of specific heats, ρk is the subscale kinetic energy per unit volume.

$$\rho k = \frac{1}{2}\bar{\rho}(\widetilde{u_i u_i} - \tilde{u}_i\tilde{u}_i) = -\frac{1}{2}\sigma_{ii} \tag{2.8}$$

In the present calculation, the ρk in Eq.(2.7) is omitted based on the assumption that the effect is small.

In generalized coordinates, Eq.(2.1) can be expressed as the following:

$$\frac{\partial \mathbf{Q}'}{\partial t} + \frac{\partial \mathbf{E}'}{\partial \xi} + \frac{\partial \mathbf{F}'}{\partial \eta} + \frac{\partial \mathbf{G}'}{\partial \zeta} = \frac{1}{Re}\left(\frac{\partial \mathbf{E}'_\mathbf{v}}{\partial \xi} + \frac{\partial \mathbf{F}'_\mathbf{v}}{\partial \eta} + \frac{\partial \mathbf{G}'_\mathbf{v}}{\partial \zeta}\right) \tag{2.9}$$

where

$$\mathbf{Q}' = \frac{\mathbf{Q}}{J} \tag{2.10}$$

$$\mathbf{E}' = \frac{1}{J}(\xi_t\mathbf{Q} + \xi_x\mathbf{E} + \xi_y\mathbf{F} + \xi_z\mathbf{G}) \tag{2.11}$$

$$\mathbf{F}' = \frac{1}{J}(\eta_t\mathbf{Q} + \eta_x\mathbf{E} + \eta_y\mathbf{F} + \eta_z\mathbf{G}) \tag{2.12}$$

$$\mathbf{G}' = \frac{1}{J}(\zeta_t\mathbf{Q} + \zeta_x\mathbf{E} + \zeta_y\mathbf{F} + \zeta_z\mathbf{G}) \tag{2.13}$$

$$\mathbf{E}'_\mathbf{v} = \frac{1}{J}(\xi_x\mathbf{E_v} + \xi_y\mathbf{F_v} + \xi_z\mathbf{G_v}) \tag{2.14}$$

$$\mathbf{F'_v} = \frac{1}{J}(\eta_x \mathbf{E_v} + \eta_y \mathbf{F_v} + \eta_z \mathbf{G_v}) \tag{2.15}$$

$$\mathbf{G'_v} = \frac{1}{J}(\zeta_x \mathbf{E_v} + \zeta_y \mathbf{F_v} + \zeta_z \mathbf{G_v}) \tag{2.16}$$

where J is the transformation Jacobian. The inviscid fluxes in generalized coordinate system are expressed as:

$$\mathbf{E'} = \begin{bmatrix} \bar{\rho}U \\ \bar{\rho}\tilde{u}U + l_x\bar{p} \\ \bar{\rho}\tilde{v}U + l_y\bar{p} \\ \bar{\rho}\tilde{w}U + l_z\bar{p} \\ (\bar{\rho}\tilde{e} + \bar{p})U - l_t\bar{p} \end{bmatrix}, \mathbf{F'} = \begin{bmatrix} \bar{\rho}V \\ \bar{\rho}\tilde{u}V + m_x\bar{p} \\ \bar{\rho}\tilde{v}V + m_y\bar{p} \\ \bar{\rho}\tilde{w}V + m_z\bar{p} \\ (\bar{\rho}\tilde{e} + \bar{p})V - m_t\bar{p} \end{bmatrix}, \mathbf{G'} = \begin{bmatrix} \bar{\rho}W \\ \bar{\rho}\tilde{u}W + n_x\bar{p} \\ \bar{\rho}\tilde{v}W + n_y\bar{p} \\ \bar{\rho}\tilde{w}W + n_z\bar{p} \\ (\bar{\rho}\tilde{e} + \bar{p})W - n_t\bar{p} \end{bmatrix}$$

where U, V and W are the contravariant velocities in ξ, η and ζ directions.

$$\begin{aligned} U &= l_t + \mathbf{l} \bullet \mathbf{V} = l_t + l_x\tilde{u} + l_y\tilde{v} + l_z\tilde{w} \\ V &= m_t + \mathbf{m} \bullet \mathbf{V} = m_t + m_x\tilde{u} + m_y\tilde{v} + m_z\tilde{w} \\ W &= n_t + \mathbf{n} \bullet \mathbf{V} = n_t + n_x\tilde{u} + n_y\tilde{v} + n_z\tilde{w} \end{aligned} \tag{2.17}$$

$\mathbf{l}, \mathbf{m}, \mathbf{n}$ are the normal vectors on ξ, η, ζ surfaces with their magnitudes equal to the elemental surface area and pointing to the directions of increasing ξ, η, ζ.

$$\mathbf{l} = \frac{\nabla \xi}{J}, \ \mathbf{m} = \frac{\nabla \eta}{J}, \ \mathbf{n} = \frac{\nabla \zeta}{J} \tag{2.18}$$

$$l_t = \frac{\xi_t}{J}, \ m_t = \frac{\eta_t}{J}, \ n_t = \frac{\zeta_t}{J} \tag{2.19}$$

For simplicity, all the overbar and tilde in above equations will be dropped in the rest of this report. Please note that the Navier-Stokes equations, Eq.(2.9), are normalized based on a set of reference parameters. The detailed normalization procedure can be found in [136].

2.2 Detached Eddy Simulation of Spalart [52,53]

The closure of the sub-grid scale stresses and heat flux are done by employing the DES of Spalart [52,53]. The sub-grid scale stresses are computed by:

$$\sigma_{ij} = \mu_{DES}(\frac{\partial \tilde{u}_i}{\partial x_j} + \frac{\partial \tilde{u}_j}{\partial x_i} - \frac{2}{3}\frac{\partial \tilde{u}_k}{\partial x\ _k}\,\delta_{ij}) - \frac{2}{3}\rho k \delta_{ij} \qquad i,j = 1,2,3 \qquad (2.20)$$

The turbulent heat flux will be evaluated as:

$$\Phi_i = C_p \frac{\mu_{DES}}{Pr_t}\frac{\partial \tilde{T}}{\partial x_i} \qquad (2.21)$$

where, $\mu_{DES} = \rho v_t$.

The transport equation of the Spalart-Allmaras one equation turbulence model is derived by using empiricism, dimensional analysis, Galilean invariance and selected dependence on the molecular viscosity [137]. The working variable $\tilde{v}$ is related to the eddy viscosity v_t. The transport equation is expressed as

$$\begin{aligned}\frac{D\tilde{v}}{Dt} =&\ c_{b1}\tilde{S}\tilde{v}(1-f_{t2}) - [c_{w1}f_w - \frac{c_{b1}}{k^2}f_{t2}][\frac{\tilde{v}}{d}]^2 \\ &+\frac{1}{\sigma}[\nabla \cdot ((v+\tilde{v})\nabla\tilde{v}) + c_{b2}(\nabla\tilde{v})^2] + f_{t1}\,(\Delta q)^2\end{aligned} \qquad (2.22)$$

In generalized coordinate system, the dimensionlessed conservative form of Eq.(2.22) is given as the following:

$$\begin{aligned}\frac{\partial \frac{1}{J}\rho\tilde{v}}{\partial t} + \frac{\partial \rho\tilde{v}U}{\partial \xi} + \frac{\partial \rho\tilde{v}V}{\partial \eta} + \frac{\partial \rho\tilde{v}W}{\partial \zeta} =&\ \frac{1}{Re}\left(\frac{\partial \frac{\rho}{\sigma}(v+\tilde{v})(\mathbf{l}\bullet\nabla\tilde{v})}{\partial \xi}\right. \\ &\left. +\frac{\partial \frac{\rho}{\sigma}(v+\tilde{v})(\mathbf{m}\bullet\nabla\tilde{v})}{\partial \eta} + \frac{\partial \frac{\rho}{\sigma}(v+\tilde{v})(\mathbf{n}\bullet\nabla\tilde{v})}{\partial \zeta} + \frac{1}{J}S_v\right)\end{aligned} \qquad (2.23)$$

where

$$\begin{aligned}S_v =&\ \rho c_{b1}(1-f_{t2})\tilde{S}\tilde{v} + \frac{1}{Re}\left[-\rho\left(c_{w1}f_w - \frac{c_{b1}}{\kappa^2}f_{t2}\right)\left(\frac{\tilde{v}}{d}\right)^2\right. \\ &\left.+\frac{\rho}{\sigma}c_{b2}(\nabla\tilde{v})^2 - \frac{1}{\sigma}(v+\tilde{v})\nabla\tilde{v}\bullet\nabla\rho\right] + Re\left[\rho f_{t1}(\Delta q)^2\right]\end{aligned} \qquad (2.24)$$

The eddy viscosity v_t is obtained from:

$$v_t = \tilde{v} f_{v1} \qquad f_{v1} = \frac{\chi^3}{\chi^3 + c_{v1}^3} \qquad \chi = \frac{\tilde{v}}{v} \qquad (2.25)$$

where v is the kinematic viscosity. The production term is:

$$\tilde{S} = S + \frac{\tilde{v}}{k^2 d^2} f_{v2}, \qquad f_{v2} = 1 - \frac{\chi}{1 + \chi f_{v1}} \qquad (2.26)$$

where S is the magnitude of the vorticity. The function f_w is given by

$$f_w = g\left(\frac{1 + c_{w3}^6}{g^6 + c_{w3}^6}\right)^{1/6}, \qquad g = r + c_{w2}(r^6 - r), \qquad r = \frac{\tilde{v}}{\tilde{S} k^2 d^2} \qquad (2.27)$$

The function f_{t2} is given by

$$f_{t2} = c_{t3} exp\left(-c_{t4}\chi^2\right) \qquad (2.28)$$

and the trip function f_{t1} is

$$f_{t1} = c_{t1} g_t exp\left[-c_{t2}\frac{\omega_t^2}{\Delta U^2}\left(d^2 + g_t^2 d_t^2\right)\right], \; g_t = min\left(0.1, \frac{\Delta q}{\omega_t \Delta x_t}\right) \qquad (2.29)$$

where, ω_t is the wall vorticity at the wall boundary layer trip location, d is the distance to the closest wall. d_t is the distance of the field point to the trip location, Δq is the difference of the velocities between the field point and the trip location, Δx_t is the grid spacing along the wall at the trip location.

The values of the coefficients are: $c_{b1} = 0.1355, c_{b2} = 0.622, \sigma = \frac{2}{3}, c_{w1} = \frac{c_{b1}}{k^2} + (1 + c_{b2})/\sigma, c_{w2} = 0.3, c_{w3} = 2, k = 0.41, c_{v1} = 7.1, c_{t1} = 1.0, c_{t2} = 2.0, c_{t3} = 1.1, c_{t4} = 2.0$.

In S-A one equation turbulence model, the trip point need to be specified before computation. This is not straightforward to do because the exact position of the trip point is not known in most of the cases. Thus, a full turbulent boundary layer is used by setting $c_{t1} = 0$ and $c_{t3} = 0$. No trip point needs to be specified.

It is observed that the S-A one equation turbulence model is sensitive to initial field.

If the initial field of $\tilde{v}$ is set to a small value, e.g. $\tilde{v} < 1$, the solution may converge with $\tilde{v} = 0$, which is the trivial solution of $\tilde{v}$ when $c_{t1} = c_{t3} = 0$. This will result in a laminar flow solution. If the initial value is too large ($\tilde{v} > 3$), the computation may diverge. In addition, setting up the initial value of $\tilde{v}$ also depends on the schemes to be used. In our computation, it is found that it is generally safe to set the initial value of $\tilde{v}$ to 2.

The boundary conditions of $\tilde{v}$ are given as the following

$$
\begin{aligned}
at\ walls: &\qquad \tilde{v} = 0 \\
far\ field\ inflow: &\qquad \tilde{v} = 0.02 \\
far\ field\ outflow: &\qquad \tilde{v}\ is\ extrapolated
\end{aligned}
$$

In DES, $c_{t1} = 0$, $c_{t3} = 0$. The distance to the nearest wall, d, is replaced by $\tilde{d}$ as

$$\tilde{d} = min(d, C_{DES}\Delta) \tag{2.30}$$

where Δ is the largest spacing of the grid cell in all the directions.

Within the boundary layer close to walls, $\tilde{d} = d$, hence the turbulence is simulated by the RANS mode determined by the Spalart-Allmaras model [137]. Away from the boundary layer, $\tilde{d} = C_{DES}\Delta$ is most of the cases. When the production and destruction terms of the model are balanced, the length scale $\tilde{d}$ will have a Smagorinsky-like eddy viscosity and the turbulence is simulated by the LES model. Analogous to the classical LES theory, the length scale Δ is to cascade the energy to the grid size. The coefficient $C_{DES} = 0.65$ is used as set in the homogeneous turbulence [138]. The Pr_t may take the value of 0.9 within the boundary layer for RANS mode and 0.5 for LES mode away from the wall surface.

Coupled Eqs.(2.9) with the S-A model Eq.(2.23), the conservative form of the governing equations are given as the following:

$$\frac{\partial Q}{\partial t} + \frac{\partial \mathbf{E}}{\partial \xi} + \frac{\partial \mathbf{F}}{\partial \eta} + \frac{\partial \mathbf{G}}{\partial \zeta} = \frac{1}{Re}\left(\frac{\partial \mathbf{R}}{\partial \xi} + \frac{\partial \mathbf{S}}{\partial \eta} + \frac{\partial \mathbf{T}}{\partial \zeta} + D\right) \tag{2.31}$$

where,

$$Q = \frac{1}{J} \begin{bmatrix} \rho \\ \rho u \\ \rho v \\ \rho w \\ \rho e \\ \rho \tilde{v} \end{bmatrix} \tag{2.32}$$

$$\mathbf{E} = \begin{bmatrix} \rho U \\ \rho u U + l_x p \\ \rho v U + l_y p \\ \rho w U + l_z p \\ (\rho e + p) U - l_t p \\ \rho \tilde{v} U \end{bmatrix}, \ \mathbf{F} = \begin{bmatrix} \rho V \\ \rho u V + m_x p \\ \rho v V + m_y p \\ \rho w V + m_z p \\ (\rho e + p) V - m_t p \\ \rho \tilde{v} V \end{bmatrix}, \ \mathbf{G} = \begin{bmatrix} \rho W \\ \rho u W + n_x p \\ \rho v W + n_y p \\ \rho w W + n_z p \\ (\rho e + p) W - n_t p \\ \rho \tilde{v} W \end{bmatrix}$$

$$\tag{2.33}$$

$$\mathbf{R} = \begin{bmatrix} 0 \\ l_k \tau_{xk} \\ l_k \tau_{yk} \\ l_k \tau_{zk} \\ l_k \beta_k \\ \frac{\rho}{\sigma} (v + \tilde{v}) (\mathbf{l} \bullet \nabla \tilde{v}) \end{bmatrix}, \ \mathbf{S} = \begin{bmatrix} 0 \\ m_k \tau_{xk} \\ m_k \tau_{yk} \\ m_k \tau_{zk} \\ m_k \beta_k \\ \frac{\rho}{\sigma} (v + \tilde{v}) (\mathbf{m} \bullet \nabla \tilde{v}) \end{bmatrix}, \ \mathbf{T} = \begin{bmatrix} 0 \\ n_k \tau_{xk} \\ n_k \tau_{yk} \\ n_k \tau_{zk} \\ n_k \beta_k \\ \frac{\rho}{\sigma} (v + \tilde{v}) (\mathbf{n} \bullet \nabla \tilde{v}) \end{bmatrix}$$

$$\tag{2.34}$$

$$D = \frac{1}{J} \begin{bmatrix} 0 \\ 0 \\ 0 \\ 0 \\ 0 \\ S_v \end{bmatrix} \tag{2.35}$$

where, U, V, W are defined as in Eq.(2.17).

$$\beta_k = u_i \tau_{ki} - q_k \tag{2.36}$$

The shear-stress τ_{ik} and total heat flux q_k in Cartesian Coordinate can be expressed as

$$\tau_{ik} = (\mu + \mu_t) \left[\left(\frac{\partial u_i}{\partial x_k} + \frac{\partial u_k}{\partial x_i} \right) - \frac{2}{3} \delta_{ik} \frac{\partial u_j}{\partial x_j} \right] \tag{2.37}$$

$$q_k = -C_p \left(\frac{\mu}{Pr} + \frac{\mu_t}{Pr_t} \right) \frac{\partial T}{\partial x_k} \tag{2.38}$$

2.3   Structural Model

2.3.1   Vortex-induced Oscillating Cylinder

The structural model of the vortex-induced oscillating cylinder is shown in Fig. 2.1. The cylinder is elastically supported and only translational movement is considered in this model.

The structural dynamic equations that govern the motion of the cylinder are:

$$m\ddot{x} + C_x \dot{x} + K_x x = D_f \tag{2.39}$$

$$m\ddot{y} + C_y \dot{y} + K_y y = L_f \tag{2.40}$$
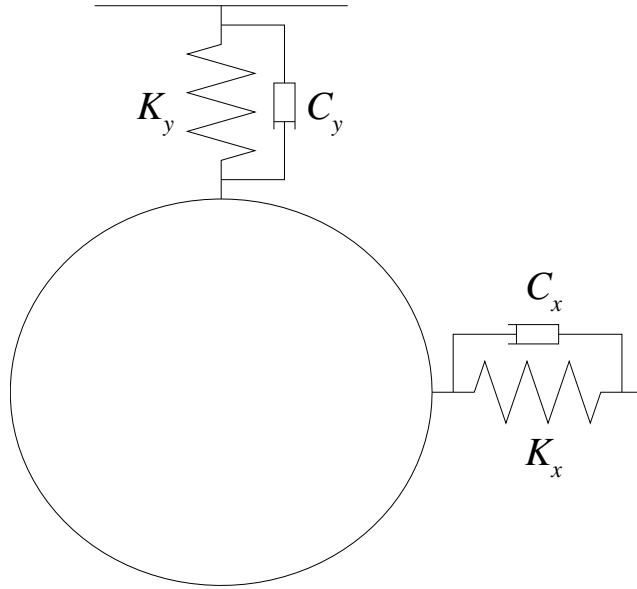
Figure 2.1: Sketch of the elastically mounted cylinder

These equations are solved implicitly together with the equations of flow motion in a fully coupled manner. In Eq. (2.39), $\ddot{x}$, $\dot{x}$, and x represent the dimensionless horizontal acceleration, velocity and displacement of the moving object respectively. Similarly, $\ddot{y}$, $\dot{y}$, and y in Eq. (2.40) represent the acceleration, velocity and displacement in the vertical direction. The terms m, L_f, and D_f are the mass, lift, and drag per unit span respectively, C_x and C_y are the damping coefficients in horizontal and vertical directions, and K_x and K_y are the spring constants in horizontal and vertical directions. In the present study, this 'self-excited oscillators' is assumed to have the same response in both directions, i.e. $C_x = C_y$ and $K_x = K_y$.

If the normalization procedure is applied to Eqs. (2.39) and (2.40) by using the same reference scales of those used for the equations of flow motion, the following nondimensional equations are obtained:

$$\ddot{x} + 2\zeta\left(\frac{2}{\bar{u}}\right)\dot{x} + \left(\frac{2}{\bar{u}}\right)^2 x = \frac{2}{\mu_s\pi}c_d \tag{2.41}$$

$$\ddot{y} + 2\zeta\left(\frac{2}{\bar{u}}\right)\dot{y} + \left(\frac{2}{\bar{u}}\right)^2 y = \frac{2}{\mu_s\pi}c_l \tag{2.42}$$

where ζ is the nondimensional structural damping coefficient calculated by $\zeta = C_{x,y}/[2\sqrt{mK_{x,y}}]$, $\bar{u}$ is the reduced velocity defined by $\bar{u} = U_\infty/(b\omega)$, b is radius of the cylinder, $\omega = \sqrt{K_{x,y}/m}$, the mass ratio defined by $\mu_s = m/\pi\rho_\infty b^2$, and c_d and c_l are the drag and lift coefficients respectively. Then the equations are transformed to a state form and expressed by:

$$M\frac{\partial S}{\partial t} + K \cdot S = Q \tag{2.43}$$

where

$$S = \begin{pmatrix} x \\ \dot{x} \\ y \\ \dot{y} \end{pmatrix}, \; M = [I], \; K = \begin{pmatrix} 0 & -1 & 0 & 0 \\ \left(\frac{2}{\bar{u}}\right)^2 & 2\zeta\left(\frac{2}{\bar{u}}\right) & 0 & 0 \\ 0 & 0 & 0 & -1 \\ 0 & 0 & \left(\frac{2}{\bar{u}}\right)^2 & 2\zeta\left(\frac{2}{\bar{u}}\right) \end{pmatrix}, \; Q = \begin{pmatrix} 0 \\ \frac{2}{\mu_s\pi}c_d \\ 0 \\ \frac{2}{\mu_s\pi}c_l \end{pmatrix}$$

2.3.2 Flow-Induced vibration of NLR7301 Airfoil

A theoretical model of the structural dynamics of the test setup configuration with the two degrees of freedom is sketched in Fig. 2.2.

The non-dimensional form of the equations governing the motion of the two degree of freedom based on the model in Fig. 2.2 can be written as

$$\begin{pmatrix} 1 & -x_\alpha \\ -x_\alpha & r_\alpha^2 \end{pmatrix}\frac{\partial^2 q}{\partial t^2} + 2\begin{pmatrix} \delta_h\omega_h & 0 \\ 0 & r_\alpha^2\delta_\alpha\omega_\alpha \end{pmatrix}\frac{\partial q}{\partial t} + \begin{pmatrix} \omega_h^2 & 0 \\ 0 & r_\alpha^2\omega_\alpha^2 \end{pmatrix}q = \frac{2}{\pi\mu_s}\begin{pmatrix} c_l \\ c_m \end{pmatrix} \tag{2.44}$$
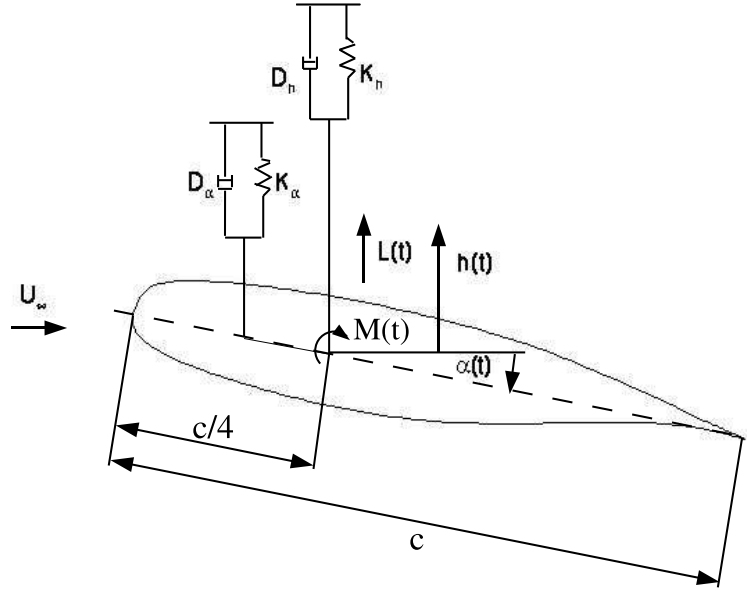
Figure 2.2: Model of the structural dynamics

where, x_α is the static unbalance, r_α is radius of gyration, ω_α is uncoupled circular pitching frequency, ω_h is uncoupled circular heave frequency, δ_α is Lehr pitching damping, δ_h is Lehr heave damping, μ_s is mass ratio, c_l and c_m are lift and moment coefficients respectively. q is defined by:

$$q = \begin{pmatrix} q_1 \\ q_2 \end{pmatrix} = \begin{pmatrix} h \\ \alpha - \alpha_0 \end{pmatrix} \tag{2.45}$$

where h and α are the plunging and pitching displacements respectively, α_0 is the off-wind value of α. The Eqs.(2.44) are transformed to a state matrix form and expressed as

$$M\frac{\partial S}{\partial t} + K \cdot S = Q \tag{2.46}$$

where

$$S = \begin{pmatrix} q_1 \\ \frac{\partial q_1}{\partial t} \\ q_2 \\ \frac{\partial q_2}{\partial t} \end{pmatrix}, \ M = \begin{pmatrix} 1 & 0 & 0 & 0 \\ 0 & 1 & 0 & -x_\alpha \\ 0 & 0 & 1 & 0 \\ 0 & -x_\alpha & 0 & r_\alpha^2 \end{pmatrix}$$

$$K = \begin{pmatrix} 0 & -1 & 0 & 0 \\ \omega_h^2 & 2\delta_h\omega_h & 0 & 0 \\ 0 & 0 & 0 & -1 \\ 0 & 0 & r_\alpha^2\omega_\alpha^2 & 2r_\alpha^2\delta_\alpha\omega_\alpha \end{pmatrix}, \ Q = \begin{pmatrix} 0 \\ \frac{2}{\pi\mu_s}c_l \\ 0 \\ \frac{2}{\pi\mu_s}c_m \end{pmatrix}$$

The detailed derivation of Eq.(2.44) is given in Appendix A.

Chapter 3

The Numerical Method

In this chapter, the numerical methods used to discretize the governing equations are introduced. The flow governing equations are discretized using finite difference method with a fully implicit manner. The inviscid fluxes are discretized using a newly developed low diffusion E-CUSP scheme [107, 108]. The fifth-order WENO scheme [87] is used to reconstruct the conservative variables at volume interfaces. A set of fully conservative fourth-order accurate finite central differencing schemes for the viscous terms is employed in this research [87]. These central differencing schemes are constructed so that the stencil widths are within the one of the WENO scheme. The structure governing equations are discretized and solved implicitly in the same manner to be consistent with the flow governing equations.

3.1   Finite Difference Discretization Using Implicit Method

The 3D Navier-Stokes equations (2.31) are discretized based on a conservative finite differencing, which is implemented by shifting the solution points half grid interval in each direction on the computational domain. The solution points are hence located in the centroids of the grid cells in the computational domain (not physical domain). This makes it possible to use the same code structure of a 2nd order finite volume method.

Using the computational grid shown in Fig. (3.1) as an example, the derivative of a flux is discretized by a finite difference method. Taking inviscid flux $\mathbf{E}$ as an example, the discretized conservative form of its derivative can be written as the following

$$\frac{\partial \mathbf{E}}{\partial \xi}|_i = \frac{\mathbf{E}_{i+1/2} - \mathbf{E}_{i-1/2}}{\Delta \xi} \tag{3.1}$$
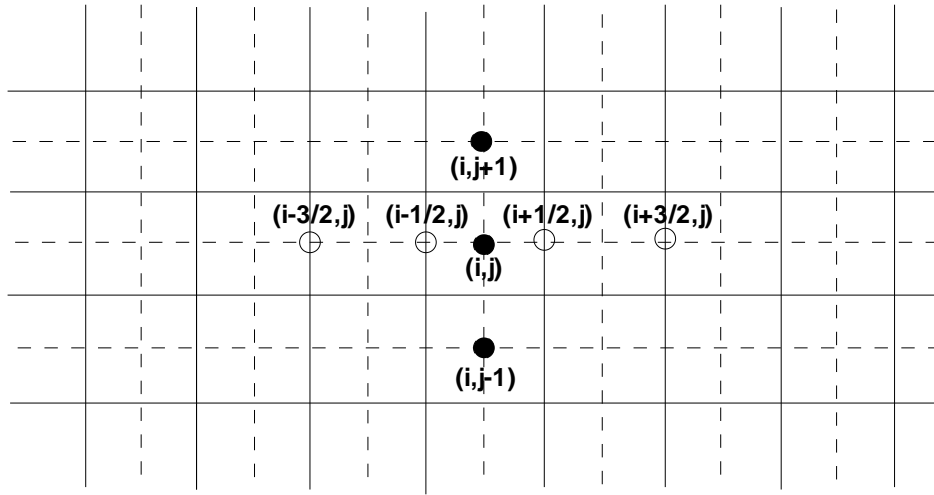
Figure 3.1: Sketch of the computational grid

Since $\Delta\xi = 1$, $\Delta\eta = 1$, $\Delta\zeta = 1$ are used in the generalized coordinate, the governing Eqs.(2.31) can be written as the following implicit form:

$$\frac{1}{\Delta t}\left(Q^{n+1} - Q^n\right) + \left(\mathbf{E}_{i+\frac{1}{2}} - \mathbf{E}_{i-\frac{1}{2}}\right)^{n+1} + \left(\mathbf{F}_{j+\frac{1}{2}} - \mathbf{F}_{j-\frac{1}{2}}\right)^{n+1} + \left(\mathbf{G}_{k+\frac{1}{2}} - \mathbf{G}_{k-\frac{1}{2}}\right)^{n+1}$$
$$= \left(\mathbf{R}_{i+\frac{1}{2}} - \mathbf{R}_{i-\frac{1}{2}}\right)^{n+1} + \left(\mathbf{S}_{j+\frac{1}{2}} - \mathbf{S}_{j-\frac{1}{2}}\right)^{n+1} + \left(\mathbf{T}_{k+\frac{1}{2}} - \mathbf{T}_{k-\frac{1}{2}}\right)^{n+1} + D^n \tag{3.2}$$

where n and $n+1$ are two sequential time levels, which have a time interval of Δt. The 5th order WENO scheme with an upwind scheme Riemann solver is used for reconstructing

inviscid fluxes $\mathbf{E}_{i+\frac{1}{2}}$, $\mathbf{F}_{j+\frac{1}{2}}$ and $\mathbf{G}_{k+\frac{1}{2}}$. A fully conservative 4th order central differencing scheme is used to evaluate the viscous fluxes R, S, T.

3.2   The Low Diffusion E-CUSP (LDE) Scheme

The basic idea of the LDE scheme is to split the inviscid flux into the convective flux E^c and the pressure flux E^p. In generalized coordinate system, the flux $\mathbf{E}$ can be split as the following:

$$\mathbf{E} = E^c + E^p = \begin{pmatrix} \rho U \\ \rho u U \\ \rho v U \\ \rho w U \\ \rho e U \\ \rho \tilde{v} U \end{pmatrix} + \begin{pmatrix} 0 \\ l_x p \\ l_y p \\ l_z p \\ p\overline{U} \\ 0 \end{pmatrix} \tag{3.3}$$

where, U is the contravariant velocity in ξ direction and is defined as the following

$$U = l_t + l_x u + l_y v + l_z w \tag{3.4}$$

$\overline{U}$ is defined as:

$$\overline{U} = l_x u + l_y v + l_z w \tag{3.5}$$

The convective term, E^c is evaluated by

$$E^c = \rho U \begin{pmatrix} 1 \\ u \\ v \\ w \\ e \\ \tilde{v} \end{pmatrix} = \rho U f^c, \quad f^c = \begin{pmatrix} 1 \\ u \\ v \\ w \\ e \\ \tilde{v} \end{pmatrix} \tag{3.6}$$

Let

$$C = c\left(l_x^2 + l_y^2 + l_z^2\right)^{\frac{1}{2}} \tag{3.7}$$

where $c = \sqrt{\gamma R T}$ is the speed of sound. Then the convective flux at interface $i + \frac{1}{2}$ is evaluated as:

$$E^c_{i+\frac{1}{2}} = C_{\frac{1}{2}}\left[\rho_L C^+ f^c_L + \rho_R C^- f^c_R\right] \tag{3.8}$$

where, the subscripts L and R represent the left and right hand sides of the interface.

$$C_{\frac{1}{2}} = \tfrac{1}{2}\left(C_L + C_R\right), \quad C^+ = \alpha_L^+ \left(1 + \beta_L\right) M_L - \beta_L M_L^+ - M_{\frac{1}{2}}^+$$

$$C^- = \alpha_R^- \left(1 + \beta_R\right) M_R - \beta_R M_R^- + M_{\frac{1}{2}}^-$$

$$M_L = \frac{U_L}{C_{\frac{1}{2}}}, \quad M_R = \frac{U_R}{C_{\frac{1}{2}}}$$

$$\alpha_{L,R} = \tfrac{1}{2}\left[1 \pm sign\left(M_{L,R}\right)\right]$$

$$\beta_{L,R} = -max\left[0, 1 - int\left(|M_{L,R}|\right)\right]$$

$$M_{\frac{1}{2}}^+ = M_{\frac{1}{2}}\frac{C_R + C_L\Phi}{C_R + C_L}, \quad M_{\frac{1}{2}}^- = M_{\frac{1}{2}}\frac{C_L + C_R\Phi^{-1}}{C_R + C_L}, \quad \Phi = \frac{(\rho C^2)_R}{(\rho C^2)_L}$$

$$M_{\frac{1}{2}} = \beta_L \delta^+ M_L^- - \beta_R \delta^- M_R^+$$

$$M_{L,R}^\pm = \pm\tfrac{1}{4}\left(M_{L,R} \pm 1\right)^2$$

$$\delta^\pm = \tfrac{1}{2}\left\{1 \pm sign\left[\tfrac{1}{2}\left(M_L + M_R\right)\right]\right\}$$

The pressure flux, E^p is evaluated as the following

$$
E^p_{i+\frac{1}{2}} = \begin{pmatrix} 0 \\ \mathscr{P}^+ p\, l_x \\ \mathscr{P}^+ p\, l_y \\ \mathscr{P}^+ p\, l_z \\ \frac{1}{2} p \left[\overline{U} + \overline{C}_{\frac{1}{2}} \right] \\ 0 \end{pmatrix}_L + \begin{pmatrix} 0 \\ \mathscr{P}^- p\, l_x \\ \mathscr{P}^- p\, l_y \\ \mathscr{P}^- p\, l_z \\ \frac{1}{2} p \left[\overline{U} - \overline{C}_{\frac{1}{2}} \right] \\ 0 \end{pmatrix}_R \tag{3.9}
$$

The contravariant speed of sound $\overline{C}$ in the pressure splitting of energy equation is consistent with $\overline{U}$. It is computed based on C as the following,

$$
\overline{C} = C - l_t \tag{3.10}
$$

The use of $\overline{U}$ and $\overline{C}$ instead of U and C in the pressure splitting of energy to take into account of the grid speed so that the flux will transit from subsonic to supersonic smoothly. When the grid is stationary, $l_t = 0, \overline{C} = C, \overline{U} = U$.

The pressure splitting coefficient is:

$$
\mathscr{P}^\pm_{L,R} = \frac{1}{4} \left(M_{L,R} \pm 1 \right)^2 \left(2 \mp M_L \right) \tag{3.11}
$$

The LDE scheme can capture crisp shock profile and exact contact surface discontinuities. Since the scheme uses scalar dissipation, for DES with one extra equation, the splitting is basically the same as the original scheme. This is an advantage over the Roe scheme, for which the eigenvectors need to be derived when any extra equation is added to the governing equations. It is also more CPU efficient than the Roe scheme due to no matrix operation.

3.3 The Fifth-Order WENO Scheme [87]

The interface flux, $E_{i+\frac{1}{2}} = E(Q_L, Q_R)$, is evaluated by determining the conservative variables Q_L and Q_R using fifth-order WENO scheme [87]. For example,

$$(Q_L)_{i+\frac{1}{2}} = \omega_0 q_0 + \omega_1 q_1 + \omega_2 q_2 \tag{3.12}$$

where

$$q_0 = \frac{1}{3} Q_{i-2} - \frac{7}{6} Q_{i-1} + \frac{11}{6} Q_i$$
$$q_1 = -\frac{1}{6} Q_{i-1} + \frac{5}{6} Q_i + \frac{1}{3} Q_{i+1} \tag{3.13}$$
$$q_2 = \frac{1}{3} Q_i + \frac{5}{6} Q_{i+1} - \frac{1}{6} Q_{i+2}$$

$$\omega_k = \frac{\alpha_k}{\alpha_0 + \ldots + \alpha_{r-1}} \tag{3.14}$$

$$\alpha_k = \frac{C_k}{\varepsilon + IS_k}, \ k = 0, \ldots, r-1$$
$$C_0 = 0.1, \ C_1 = 0.6, \ C_2 = 0.3$$
$$IS_0 = \frac{13}{12} (Q_{i-2} - 2Q_{i-1} + Q_i)^2 + \frac{1}{4} (Q_{i-2} - 4Q_{i-1} + 3Q_i)^2 \tag{3.15}$$
$$IS_1 = \frac{13}{12} (Q_{i-1} - 2Q_i + Q_{i+1})^2 + \frac{1}{4} (Q_{i+1} - Q_{i-1})^2$$
$$IS_2 = \frac{13}{12} (Q_i - 2Q_{i+1} + Q_{i+2})^2 + \frac{1}{4} (3Q_i - 4Q_{i+1} + Q_{i+2})^2$$

where, ε is originally introduced to avoid the denominator becoming zero and is supposed to be a very small number. In [87], it is observed that IS_k will oscillate if ε is small and also shift the weights away from the optimum values in the smooth region. The higher the ε values, the closer the weights approach the optimum weights, C_k, which will give the symmetric evaluation of the interface flux with minimum numerical dissipation. When there are shocks in the flow field, ε can not be too large to maintain the sensitivity to shocks. In [87], the optimized value of $\varepsilon = 10^{-2}$ is recommended for the transonic flow with shock waves.

3.4 Finite Differencing Discretization of Viscous Terms [87]

We take the viscous flux derivative in ξ-direction as the example to explain how the schemes are constructed. To conservatively discretize the viscous derivative term in Navier-Stokes equations Eq.(2.31), we have

$$\frac{\partial R}{\partial \xi}\Big|_i = \frac{\tilde{R}_{i+1/2} - \tilde{R}_{i-1/2}}{\Delta \xi} \tag{3.16}$$

To obtain 4th order accuracy, $\tilde{R}$ needs to be reconstructed as

$$\tilde{R}_{i-1/2} = \sum_{I=i-3/2}^{i+1/2} \alpha_I R_I \tag{3.17}$$

where

$$\alpha_{i-3/2} = -\frac{1}{24}, \ \alpha_{i-1/2} = \frac{26}{24}, \ \alpha_{i+1/2} = -\frac{1}{24}$$

$$R_{i-1/2} = [(\xi_x \tau_{xx}) + (\eta_y \tau_{xy}) + (\zeta_z \tau_{xz})]_{i-1/2}$$

$$\begin{aligned}
(\tau_{xx}) = \ & \mu \{ \tfrac{4}{3} \left[(\xi_x \tfrac{\partial u}{\partial \xi}) + (\eta_x \tfrac{\partial u}{\partial \eta}) + (\zeta_x \tfrac{\partial u}{\partial \zeta}) \right] \\
& - \tfrac{2}{3} [(\xi_y \tfrac{\partial v}{\partial \xi}) + (\eta_y \tfrac{\partial v}{\partial \eta}) + (\zeta_y \tfrac{\partial v}{\partial \zeta}) \\
& (\xi_z \tfrac{\partial w}{\partial \xi}) + (\eta_z \tfrac{\partial w}{\partial \eta}) + (\zeta_z \tfrac{\partial w}{\partial \zeta})] \}
\end{aligned} \tag{3.18}$$

If R in Eq.(3.17) can be approximated with the accuracy order not lower than 4th order, the Taylor series expansion analysis of (3.16) and (3.17) will give

$$\frac{1}{\Delta \xi}(\tilde{R}_{i+1/2} - \tilde{R}_{i-1/2}) = R'(\xi_i) + O(\Delta \xi^4) \tag{3.19}$$

and the 4th order accuracy is achieved (to be proved later). It needs to point out that in Eq.(3.16), $\tilde{R}_{i-1/2}$ can not be replaced by $R_{i-1/2}$. Otherwise, the 4th order accuracy can not be achieved even though the high order approximation of $R_{i-1/2}$ is used. The 4th order accuracy from Eq. (3.16)-(3.19) is also based on the uniform spacing $\Delta \xi = C$.

In order to achieve the highest order accuracy of R_I with $I = i - 3/2, i - 1/2, i + 1/2$, the approximation of each term in Eq. (3.17) using the same points is given below:

$$\mu_I = \sum_{l=m}^{n} C_l^I \mu_{i+l}, \tag{3.20}$$

$$\frac{\partial u}{\partial \xi}\Big|_I = \frac{1}{\Delta \xi} \sum_{l=r}^{s} D_l^I u_{i+l}, \tag{3.21}$$

$$\frac{\partial u}{\partial \eta}\Big|_I = \sum_{l=m}^{n} C_l^I \frac{\partial u}{\partial \eta}\Big|_{i+l,j} \tag{3.22}$$

where

$$\frac{\partial u}{\partial \eta}\Big|_{i,j} = \frac{1}{\Delta \eta} \sum_{l=p}^{q} C_l^c u_{i,j+l}, \tag{3.23}$$

By choosing different ranges for $(m,n), (r,s), (p,q)$ and different coefficients C_l^I, D_l^I, C_l^c, one can obtain different order accuracy approximation to the viscous terms. The principle of choosing $(m,n), (r,s), (p,q)$ is to ensure that the approximation of $\frac{\partial R}{\partial \xi}\Big|_i$ in Eq.(3.16) is a central differencing. For example, let $(m,n) = (-2,1), (r,s) = (-3,2), and\ (p,q) = (-2,2)$, and they give

$$\mu_I = \sum_{l=m}^{n} C_l^I \mu_{i+l} + O(\Delta \xi^4), \tag{3.24}$$

$$\frac{\partial u}{\partial \xi}\Big|_I = \frac{1}{\Delta \xi} \sum_{l=r}^{s} D_l^I u_{i+l} + O(\Delta \xi^5), \tag{3.25}$$

$$\frac{\partial u}{\partial \eta}\Big|_I = \sum_{l=m}^{n} C_l^I \frac{\partial u}{\partial \eta}\Big|_{i+l,j} + O(\Delta \xi^4, \Delta \eta^4), \tag{3.26}$$

where

$$\frac{\partial u}{\partial \eta}\Big|_{i,j} = \frac{1}{\Delta \eta} \sum_{l=p}^{q} C_l^c u_{i,j+l} + O(\Delta \eta^4) \tag{3.27}$$

the coefficients C_l^I, D_l^I, C_l^c can be obtained by Taylor's series expansion and are given in Tables 3.1-3.3. For example,

$$\begin{cases} \mu_{i-3/2} = \frac{1}{16}(5\mu_{i-2} + 15\mu_{i-1} - 5\mu_i + \mu_{i+1}) + O(\Delta \xi^4) \\ \mu_{i-1/2} = \frac{1}{16}(-\mu_{i-2} + 9\mu_{i-1} + 9\mu_i - \mu_{i+1}) + O(\Delta \xi^4) \\ \mu_{i+1/2} = \frac{1}{16}(\mu_{i-2} - 5\mu_{i-1} + 15\mu_i + 5\mu_{i+1}) + O(\Delta \xi^4) \end{cases} \tag{3.28}$$

$$\begin{cases} \frac{\partial u}{\partial \xi}\big|_{i-3/2} = \frac{1}{\Delta \xi}\left(\frac{71}{1920}u_{i-3} - \frac{141}{128}u_{i-2} + \frac{69}{64}u_{i-1} + \frac{1}{192}u_i - \frac{3}{128}u_{i+1} + \frac{3}{640}u_{i+2}\right) + O(\Delta \xi^5) \\ \frac{\partial u}{\partial \xi}\big|_{i-1/2} = \frac{1}{\Delta \xi}\left(-\frac{3}{640}u_{i-3} + \frac{25}{384}u_{i-2} - \frac{75}{64}u_{i-1} + \frac{75}{64}u_i - \frac{25}{384}u_{i+1} + \frac{3}{640}u_{i+2}\right) + O(\Delta \xi^5) \\ \frac{\partial u}{\partial \xi}\big|_{i+1/2} = \frac{1}{\Delta \xi}\left(-\frac{3}{640}u_{i-3} + \frac{3}{128}u_{i-2} - \frac{1}{192}u_{i-1} - \frac{69}{64}u_i + \frac{141}{128}u_{i+1} - \frac{71}{1920}u_{i+2}\right) + O(\Delta \xi^5) \end{cases}$$
(3.29)

The other terms are determined similarly. For comparison, the terms used in Ref. [139, 140] by De Rango and Zingg et al. are given as the following,

$$\begin{cases} \mu_{i-3/2} = \frac{1}{16}(-\mu_{i-3} + 9\mu_{i-2} + 9\mu_{i-1} - \mu_i) + O(\Delta \xi^4) \\ \mu_{i-1/2} = \frac{1}{16}(\mu_{i-2} + 9\mu_{i-1} + 9\mu_i - \mu_{i+1}) + O(\Delta \xi^4) \\ \mu_{i+1/2} = \frac{1}{16}(\mu_{i-1} + 9\mu_i + 9\mu_{i+1} - \mu_{i+2}) + O(\Delta \xi^4) \end{cases}$$
(3.30)

$$\begin{cases} \frac{\partial u}{\partial \xi}\big|_{i-3/2} = \frac{1}{24\Delta \xi}(-u_{i-3} - 27u_{i-2} + 27u_{i-1} - u_i) + O(\Delta \xi^4) \\ \frac{\partial u}{\partial \xi}\big|_{i-1/2} = \frac{1}{24\Delta \xi}(-u_{i-2} - 27u_{i-1} + 27u_i - u_{i+1}) + O(\Delta \xi^4) \\ \frac{\partial u}{\partial \xi}\big|_{i+1/2} = \frac{1}{24\Delta \xi}(-u_{i-1} - 27u_i + 27u_{i+1} - u_{i+2}) + O(\Delta \xi^4) \end{cases}$$
(3.31)

Compare Eqs.(3.28),(3.29) and Eqs.(3.30),(3.31), it can be seen that μ_I in present paper has the same accuracy order, as that of De Rango and Zingg et al., but has small stencil width $(i-2, \cdots, i+1)$, $\frac{\partial u}{\partial \xi}\big|_I$ has the same stencil width, but obtains one accuracy order higher than that in Ref. [139, 140].

Table 3.1: The coefficients of C_l^I

I	C_{-2}^I	C_{-1}^I	C_0^I	C_1^I
$i-3/2$	5/16	15/16	-5/16	1/16
$i-1/2$	-1/16	9/16	9/16	-1/16
$i+1/2$	1/16	-5/16	15/16	5/16

It can be proved that the scheme Eq. (3.16) is symmetric with respect to cell i. For example, the coefficients of $\mu_{i-2}u_{i-3}$, $\mu_{i+2}u_{i+3}$, $\mu_{i-1}u_{i-2}$, and $\mu_{i+1}u_{i+2}$ can be found as (in the following formula, $\tilde{C}_l^I$ and $\tilde{D}_l^I$ are the coefficients of μ_{i+l}, u_{i+l} in R_I for $\tilde{R}_{i+1/2}$, respectively. It's clear that there are $\tilde{C}_l^I = C_{l-1}^{I-1}$ and $\tilde{D}_l^I = D_{l-1}^{I-1}$, $\tilde{\alpha}_I = \alpha_{I-1}$, $I = i-1/2, i+$

Table 3.2: The coefficients of D_l^I

I	D_{-3}^I	D_{-2}^I	D_{-1}^I	D_0^I	D_1^I	D_2^I
$i-3/2$	71/1920	-141/128	69/64	1/192	-3/128	3/640
$i-1/2$	-3/640	25/384	-75/64	75/64	-25/384	3/640
$i+1/2$	-3/640	3/128	-1/192	-69/64	141/128	-71/1920

Table 3.3: The coefficients of C_l^c

C_{-2}^c	C_{-1}^c	C_0^c	C_1^c	C_2^c
1/12	-8/12	0	8/12	-1/12

$1/2, i+3/2)$:

$$
\begin{aligned}
C_{i-2,i-3} &= -\sum_{I=i-3/2}^{i+1/2} \alpha_I C_{-2}^I D_{-3}^I \\
&= -\left[\left(\tfrac{-1}{24}\right) \cdot \tfrac{5}{16} \cdot \tfrac{71}{1920} + \tfrac{26}{24} \cdot \left(\tfrac{-1}{16}\right) \cdot \left(\tfrac{-3}{640}\right) + \left(\tfrac{-1}{24}\right) \cdot \tfrac{1}{16} \cdot \left(\tfrac{-3}{640}\right) \right] \\
&= \tfrac{7}{46080}
\end{aligned}
$$

$$
\begin{aligned}
C_{i+2,i+3} &= \sum_{I=i-1/2}^{i+3/2} \tilde{\alpha}_I \tilde{C}_2^I \tilde{D}_3^I \\
&= \left(\tfrac{-1}{24}\right) \cdot \tfrac{1}{16} \cdot \tfrac{3}{640} + \tfrac{26}{24} \cdot \left(\tfrac{-1}{16}\right) \cdot \tfrac{3}{640} + \left(\tfrac{-1}{24}\right) \cdot \tfrac{5}{16} \cdot \left(\tfrac{-71}{1920}\right) \\
&= \tfrac{7}{46080}
\end{aligned}
$$

$$C_{i-1,i-2} = \sum_{I=i-1/2}^{i+3/2} \tilde{\alpha}_I \tilde{C}_{-1}^I \tilde{D}_{-2}^I - \sum_{I=i-3/2}^{i+1/2} \alpha_I C_{-1}^I D_{-2}^I$$

$$= \left(\tfrac{-1}{24}\right) \cdot \tfrac{5}{16} \cdot \tfrac{71}{1920} + \tfrac{26}{24} \cdot \left(\tfrac{-1}{16}\right) \cdot \left(\tfrac{-3}{640}\right) + \left(\tfrac{-1}{24}\right) \cdot \tfrac{1}{16} \cdot \left(\tfrac{-3}{640}\right)$$

$$- \left[\left(\tfrac{-1}{24}\right) \cdot \tfrac{15}{16} \cdot \left(\tfrac{-141}{128}\right) + \tfrac{26}{24} \cdot \tfrac{9}{16} \cdot \tfrac{25}{384} + \left(\tfrac{-1}{24}\right) \cdot \left(\tfrac{-5}{16}\right) \cdot \tfrac{3}{128}\right]$$

$$= -\tfrac{479}{5760}$$

$$C_{i+1,i+2} = \sum_{I=i-1/2}^{i+3/2} \tilde{\alpha}_I \tilde{C}_1^I \tilde{D}_2^I - \sum_{I=i-3/2}^{i+1/2} \alpha_I C_1^I D_2^I$$

$$= \left(\tfrac{-1}{24}\right) \cdot \left(\tfrac{-5}{16}\right) \cdot \left(\tfrac{-3}{128}\right) + \tfrac{26}{24} \cdot \tfrac{9}{16} \cdot \left(\tfrac{-25}{384}\right) + \left(\tfrac{-1}{24}\right) \cdot \tfrac{15}{16} \cdot \tfrac{141}{128}$$

$$- \left[\left(\tfrac{-1}{24}\right) \cdot \tfrac{1}{16} \cdot \tfrac{3}{640} + \tfrac{26}{24} \cdot \left(\tfrac{-1}{16}\right) \cdot \tfrac{3}{640} + \left(\tfrac{-1}{24}\right) \cdot \tfrac{5}{16} \cdot \left(\tfrac{-71}{1920}\right)\right]$$

$$= -\tfrac{479}{5760}$$

So we have $C_{i-2,i-3} = C_{i+2,i+3}$, $C_{i-1,i-2} = C_{i+1,i+2}$, and so on. Hence the scheme Eq. (3.16) is symmetric with respect to grid node i. The symmetry of central differencing for Eq. (3.16) satisfies the diffusion property of the viscous flux.

Next, we prove that the order of accuracy given by Eq.(3.19) is satisfied. Take the term $T^- = \mu \partial u / \partial \xi$ in Eq.(3.19) as the example,

In $\tilde{R}_{i-1/2}$, at $I = i - 3/2$, based on Taylor's series expansion

$$
\begin{aligned}
T_{i-3/2}^- &= \sum_{l=m}^n C_l^I \mu_{i+l} \left(\tfrac{1}{\Delta \xi} \sum_{l=r}^s D_l^I u_{i+l}\right) \\
&= \left[\mu_{i-3/2} + A_I \mu_{i-3/2}^{(4)} \Delta \xi^4 + O(\Delta \xi^5)\right] \left[\tfrac{\partial u}{\partial \xi}\big|_{i-3/2} + O(\Delta \xi^5)\right] \\
&= \mu_{i-3/2} \tfrac{\partial u}{\partial \xi}\big|_{i-3/2} + A_I \mu_{i-3/2}^{(4)} \tfrac{\partial u}{\partial \xi}\big|_{i-3/2} \Delta \xi^4 + O(\Delta \xi^5)
\end{aligned}
$$

A_I is the coefficient of Taylor's series expansion.

The corresponding term T^+ in $\tilde{R}_{i+1/2}$ is at $I = i - 1/2$, and

$$
\begin{aligned}
T_{i-1/2}^+ &= \sum_{l=m}^n \tilde{C}_l^I \mu_{i+1+l} \left(\tfrac{1}{\Delta \xi} \sum_{l=r}^s \tilde{D}_l^I u_{i+1+l}\right) \\
&= \left[\mu_{i-1/2} + \tilde{A}_I \mu_{i-1/2}^{(4)} \Delta \xi^4 + O(\Delta \xi^5)\right] \left[\tfrac{\partial u}{\partial \xi}\big|_{i-1/2} + O(\Delta \xi^5)\right] \\
&= \mu_{i-1/2} \tfrac{\partial u}{\partial \xi}\big|_{i-1/2} + \tilde{A}_I \mu_{i-1/2}^{(4)} \tfrac{\partial u}{\partial \xi}\big|_{i-1/2} \Delta \xi^4 + O(\Delta \xi^5)
\end{aligned}
$$

Note that $A_I = \tilde{A}_I$, hence

$$T^+_{i-1/2} - T^-_{i-3/2} = \mu_{i-1/2}\frac{\partial u}{\partial \xi}|_{i-1/2} - \mu_{i-3/2}\frac{\partial u}{\partial \xi}|_{i-3/2} + O(\Delta\xi^5)$$

The other two terms can be analyzed similarly as above, then Eq.(3.19)

$$\frac{1}{\Delta\xi}(\tilde{R}_{i+1/2} - \tilde{R}_{i-1/2}) = R^{'}(\xi_i) + O(\Delta\xi^4)$$

is proved, i.e. the constructed schemes are formally 4th order accuracy.

3.5 Implicit Time Integration

3.5.1 Implicit Flow Solver

The time dependent governing equations are solved using dual time stepping method suggested by Jameson [86]. To achieve high convergence rate, the implicit pseudo time marching scheme is used with the unfactored Gauss-Seidel line relaxation. The physical temporal term is discretized implicitly using a three point, backward differencing as the following (The prime is omitted hereafter for simplicity):

$$\frac{\partial Q}{\partial t} = \frac{3Q^{n+1} - 4Q^n + Q^{n-1}}{2\Delta t} \tag{3.32}$$

where $n-1$, n and $n+1$ are three sequential time levels, which have a time interval of Δt. The first-order Euler scheme is used to discretize the pseudo temporal term to enhance diagonal dominance. The semi-discretized equations of the governing equations are finally given as the following:

$$\left[\left(\frac{1}{\Delta\tau} + \frac{1.5}{\Delta t}\right)I - \left(\frac{\partial R}{\partial Q}\right)^{n+1,m}\right]\delta Q^{n+1,m+1} = R^{n+1,m} - \frac{3Q^{n+1,m} - 4Q^n + Q^{n-1}}{2\Delta t} \tag{3.33}$$

where the $\Delta\tau$ is the pseudo time step, R is the net flux evaluated on a grid point using the fifth-order WENO scheme.

3.5.2 Gauss-Seidel Line Relaxation [136]

To enhance diagonal dominance, a first order scheme is used for the implicit pseudo temporal terms. Following the procedure in Hu's Ph.D. report [136], the implicit discretized form of Eq. (3.2) is written as the following

$$
\begin{aligned}
&\bar{B}\Delta Q_{i,j,k}^{n+1} + A^+\Delta Q_{i+1,j,k}^{n+1} + A^-\Delta Q_{i-1,j,k}^{n+1} + B^+\Delta Q_{i,j+1,k}^{n+1} \\
&+B^-\Delta Q_{i,j-1,k}^{n+1} + C^+\Delta Q_{i,j,k+1}^{n+1} + C^-\Delta Q_{i,j,k-1}^{n+1} = \mathbf{RHS}^n
\end{aligned}
\tag{3.34}
$$

$\mathbf{RHS}^n$ is the summation of all the terms on the right hand side (RHS) of the equation.

$$
\begin{aligned}
\mathbf{RHS}^n = \Delta t \Bigg\{ &\left[\left(\mathbf{R}_{i+\frac{1}{2}}^n - \mathbf{R}_{i-\frac{1}{2}}^n \right) + \left(\mathbf{S}_{j+\frac{1}{2}}^n - \mathbf{S}_{j-\frac{1}{2}}^n \right) + \left(\mathbf{T}_{k+\frac{1}{2}}^n - \mathbf{T}_{k-\frac{1}{2}}^n \right) \right] \\
&- \left[\left(\mathbf{E}_{i+\frac{1}{2}}^n - \mathbf{E}_{i-\frac{1}{2}}^n \right) + \left(\mathbf{F}_{j+\frac{1}{2}}^n - \mathbf{F}_{j-\frac{1}{2}}^n \right) + \left(\mathbf{G}_{k+\frac{1}{2}}^n - \mathbf{G}_{k-\frac{1}{2}}^n \right) \right] \Bigg\} + D^n \cdot \Delta t
\end{aligned}
\tag{3.35}
$$

Gauss-Seidel line relaxation is applied in each direction (i, j, k) and is swept one time step forward and backward in each direction. For example, the equation for Gauss-Seidel relaxation following lines along direction i with the index from small to large is written as:

$$
B^-\Delta Q_{i,j-1,k}^{n+1} + \bar{B}\Delta Q_{i,j,k}^{n+1} + B^+\Delta Q_{i,j+1,k}^{n+1} = \mathbf{RHS}'
\tag{3.36}
$$

where

$$
\mathbf{RHS}' = \mathbf{RHS}^n - A^+\Delta Q_{i+1,j,k}^n - A^-\Delta Q_{i-1,j,k}^{n+1} - C^+\Delta Q_{i,j,k+1}^n - C^-\Delta Q_{i,j,k-1}^{n+1}
\tag{3.37}
$$

3.5.3 Implicit Structural Solver

The structural equations (2.43) and (2.46) are discretized and solved implicitly in each physical time step in a manner consistent with flow governing equations (3.33):

$$
\left(\frac{1}{\Delta \tau} I + \frac{1.5}{\Delta t} M + K \right) \delta S^{n+1,m+1} = Q^{n+1,m+1} - M \frac{3 S^{n+1,m} - 4 S^n + S^{n-1}}{2 \Delta t} - K S^{n+1,m} \quad (3.38)
$$

The fluid-structural interaction is implemented in a fully couple manner [33,34]. Within each physical time step, the flow equations and structural equations are solved iteratively until the prescribed convergence criteria is satisfied for both flow and structural solver. After the convergence criteria is reached, the fluid-structural interaction goes to next physical time step.

3.6 Boundary Conditions

To obtain a well posed solution of a given flow problem by solving the Navier-Stokes governing equation, Eq.(2.9), it is necessary to define the boundary conditions for the problem. Since the solution points are located at the centroids of the cells, the ghost cells are used to define the boundaries except for the inviscid flux on wall surface for steady state problems. In other words, most of the boundary conditions are defined by setting up the values of the variables at the ghost cells. Depending on the scheme order of accuracy to be used, the number of ghost cells will vary to match the accuracy of the inner points. Several commonly used boundary conditions are described as the following.

3.6.1 Supersonic Inflow

For supersonic inflow boundary, all the primitive variables are fixed as the initial values of the flow field at the ghost cells.

$$\rho_{gst} = \rho_{int}, u_{gst} = u_{int}, v_{gst} = v_{int}, w_{gst} = w_{int}, e_{gst} = e_{int} \tag{3.39}$$

where, *gst* represents the ghost cell and *int* represents the initial value. In this case, the initial values are set to the values of free stream and used to specify the inflow BCs.

3.6.2   Supersonic Outflow

For supersonic outflow boundary, all the primitive variables are extrapolated with zero gradient from their inner counterparts.

$$\rho_{gst} = \rho_{inn}, u_{gst} = u_{inn}, v_{gst} = v_{inn}, w_{gst} = w_{inn}, e_{gst} = e_{inn} \tag{3.40}$$

where, *inn* represents the inner counterpart.

3.6.3   Subsonic Inflow (For External Flows)

For subsonic inflow boundary, four variables are specified using the free stream values of the flow field. One variable is extrapolated with zero gradient from its inner counterpart. Usually, the static pressure is extrapolated

$$\rho_{gst} = \rho_{int}, u_{gst} = u_{int}, v_{gst} = v_{int}, w_{gst} = w_{int}, p_{gst} = p_{inn} \tag{3.41}$$

3.6.4   Subsonic Outflow (For External Flows)

For subsonic outflow boundary, the static pressure is fixed as the initial values of the flow field. The normalized outflow static pressure is determined by free stream Mach number, $p_{int} = \frac{1}{\gamma M_\infty^2}$. Four variables are extrapolated with zero gradient from their inner counterparts.

$$\rho_{gst} = \rho_{inn}, u_{gst} = u_{inn}, v_{gst} = v_{inn}, w_{gst} = w_{inn}, p_{gst} = p_{int} \tag{3.42}$$

The other variables are calculated based on these 5 variables.

3.6.5 Subsonic Inlet (For Internal Flows)

For subsonic inlet boundary, the prescribed variables are usually total pressure p_t, total temperature T_t and the two flow angles α and β. The total pressure and temperature are used because they are easier to obtain in wind tunnel experiments. A velocity component is extrapolated from its inner counterpart. The other two velocity components are calculated using the flow angles α and β. The extrapolated velocity component is determined by main flow direction which is given by user. For example, if x direction is taken as the main flow direction, the velocity components are calculated as the following:

$$u_{gst} = u_{inn}, \ v_{gst} = u_{gst} \tan \alpha, \ w_{gst} = u_{gst} \tan \beta \tag{3.43}$$

The other variables are calculated using the following normalized relations:

$$T_{gst} = T_t - \frac{1}{2} (\gamma - 1) M_\infty^2 \left(u_{gst}^2 + v_{gst}^2 + w_{gst}^2 \right) \tag{3.44}$$

$$p_{gst} = P_t \left[1 + \frac{\gamma - 1}{2} \frac{M_\infty^2}{T_{gst}} \left(u_{gst}^2 + v_{gst}^2 + w_{gst}^2 \right) \right]^{\frac{\gamma}{\gamma - 1}} \tag{3.45}$$

$$\rho_{gst} = \frac{\gamma M_\infty^2 p_{gst}}{T_{gst}} \tag{3.46}$$

$$e_{gst} = \frac{1}{\gamma(\gamma - 1)} \frac{1}{M_\infty^2} T_{gst} + \frac{1}{2} \left(u_{gst}^2 + v_{gst}^2 + w_{gst}^2 \right) \tag{3.47}$$

3.6.6 Subsonic Outlet (For Internal Flows)

For subsonic outlet boundary, it is the same as the subsonic outflow boundary except that the static pressure is fixed as a given value p_{outlet}.

$$\rho_{gst} = \rho_{inn}, u_{gst} = u_{inn}, v_{gst} = v_{inn}, w_{gst} = w_{inn}, p_{gst} = p_{outlet} \tag{3.48}$$

3.6.7   Wall Boundary

Stationary Walls

For inviscid flux, the wall boundary condition is enforced by setting the normal contravariant velocity on the boundary to zero. For example, if a wall boundary is on a η-surface, the contravariant velocity V is zero on the wall surface, and hence the flux on the wall surface is calculated as,

$$\mathbf{F_w} = \begin{bmatrix} \rho V \\ \rho u V + m_x p \\ \rho v V + m_y p \\ \rho w V + m_z p \\ (\rho e + p) V \end{bmatrix}_w = \begin{bmatrix} 0 \\ m_x p \\ m_y p \\ m_z p \\ 0 \end{bmatrix}_w \tag{3.49}$$

The wall pressure is extrapolated from inner points by the following formulation:

1) 1st order extrapolation

$$p_w = p_1 \tag{3.50}$$

2) 3rd order extrapolation

$$p_w = \frac{1}{6}(11p_1 - 7p_2 - 2p_3) \tag{3.51}$$

For viscous flux, no-slip and adiabatic wall boundary condition is conducted by setting the ghost cell velocity as the negative of the velocity of its inner counterpart based on the reflection condition.

$$\rho_{gst} = \rho_{inn}, u_{gst} = -u_{inn}, v_{gst} = -v_{inn}, w_{gst} = -w_{inn}, e_{gst} = e_{inn} \tag{3.52}$$

Moving Walls

At 2D moving boundary surface, since the wall velocity is not zero, both the inviscid and viscous fluxes on the wall are evaluated using ghost cells. The density and velocity are calculated by extrapolation.

$$\rho_{gst} = \rho_{inn}$$
$$u_{gst} = 2\dot{x}_b - u_{inn} \tag{3.53}$$
$$v_{gst} = 2\dot{y}_b - v_{inn}$$

where, $\dot{x}_b$ and $\dot{y}_b$ are the wall boundary velocity components in x and y direction respectively.

The inviscid normal momentum equation is solved to obtain pressure. The momentum equation can be described as the following:

$$\rho\mathbf{a} = -\nabla\mathbf{p} \tag{3.54}$$

The normal momentum equation is:

$$\nabla p \cdot \mathbf{n} = -\rho\mathbf{a}\cdot\mathbf{n} \tag{3.55}$$

where, $\mathbf{a}$ is the acceleration:

$$\mathbf{a} = \ddot{x}_b\mathbf{i} + \ddot{y}_b\mathbf{j} \tag{3.56}$$

$\mathbf{n}$ is the unit normal vector:

$$\mathbf{n} = \mathbf{n_x}\mathbf{i} + \mathbf{n_y}\mathbf{j} = \frac{1}{\left(\eta_x^2 + \eta_y^2\right)^{1/2}}\left(\eta_x\mathbf{i} + \eta_y\mathbf{j}\right) \tag{3.57}$$

Thus,

$$-\rho \mathbf{a} \cdot \mathbf{n} = -\frac{\rho}{\left(\eta_x^2 + \eta_y^2\right)^{1/2}} \left(\eta_x \ddot{x}_b + \eta_y \ddot{y}_b\right) \tag{3.58}$$

$$
\begin{aligned}
\nabla p \cdot \mathbf{n} &= \left(\frac{\partial p}{\partial x}\mathbf{i} + \frac{\partial \mathbf{p}}{\partial \mathbf{y}}\mathbf{j}\right) \cdot \left(n_x \mathbf{i} + \mathbf{n_y}\mathbf{j}\right) \\
&= \frac{\partial p}{\partial x}n_x + \frac{\partial p}{\partial y}n_y \\
&= \left(\frac{\partial p}{\partial \xi}\xi_x + \frac{\partial p}{\partial \eta}\eta_x\right)n_x + \left(\frac{\partial p}{\partial \xi}\xi_y + \frac{\partial p}{\partial \eta}\eta_y\right)n_y \\
&= \frac{\partial p}{\partial \xi}\left(\xi_x n_x + \xi_y n_y\right) + \frac{\partial p}{\partial \eta}\left(\eta_x n_x + \eta_y n_y\right) \\
&= \frac{1}{\left(\eta_x^2 + \eta_y^2\right)^{1/2}}\left[\frac{\partial p}{\partial \xi}\left(\xi_x \eta_x + \xi_y \eta_y\right) + \frac{\partial p}{\partial \eta}\left(\eta_x^2 + \eta_y^2\right)\right]
\end{aligned}
\tag{3.59}
$$

If the grid on wall surface is orthogonal, $\xi_x \eta_x + \xi_y \eta_y = 0$. Then Eq.(3.59) can be expressed as

$$\nabla p \cdot \mathbf{n} = \frac{1}{\left(\eta_x^2 + \eta_y^2\right)^{1/2}}\left[\frac{\partial \mathbf{p}}{\partial \eta}\left(\eta_x^2 + \eta_y^2\right)\right] \tag{3.60}$$

The normal momentum equation Eq.(3.55) can be written as the following,

$$\frac{\partial p}{\partial \eta} = -\left(\frac{\rho}{\eta_x^2 + \eta_y^2}\right)\left(\eta_x \ddot{x}_b + \eta_y \ddot{y}_b\right) \tag{3.61}$$

3.6.8 Symmetrical Boundary

For a symmetrical boundary, the corresponding velocity component in the ghost cell is mirror reflected about the symmetrical boundary from its inner counterpart. The other variables are extrapolated with zero gradient. For example, if the symmetrical boundary is a x-plane, the boundary condition is defined as the following:

$$\rho_{gst} = \rho_{inn}, u_{gst} = -u_{inn}, v_{gst} = v_{inn}, w_{gst} = w_{inn}, e_{gst} = e_{inn} \tag{3.62}$$

3.6.9 Division Periodic Boundary

For division periodical boundary, the variables and coordinates are periodically defined in the periodical direction (Fig. 3.2). For example, if the periodic boundary is in ξ-direction, the variables are calculated in the same way as inner points.
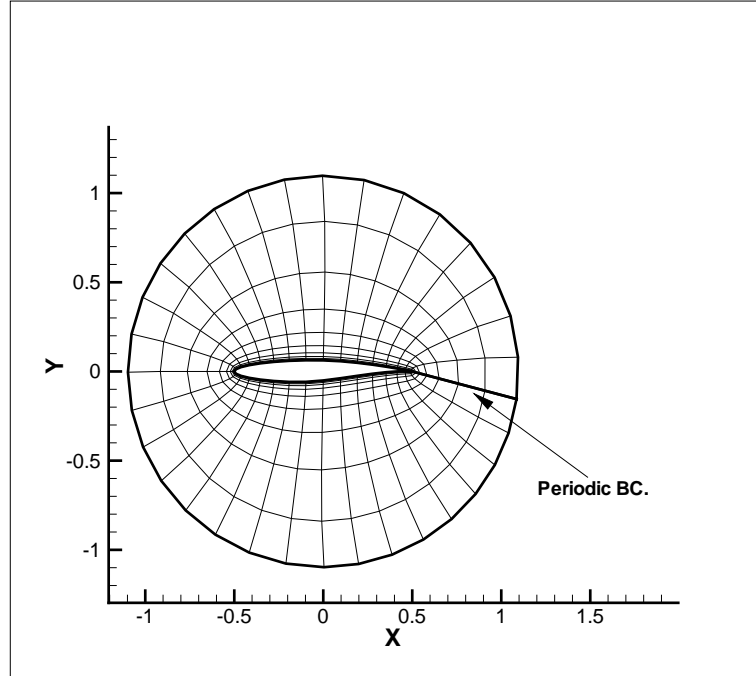

Figure 3.2: periodic boundary

For the ghost cell of the start surface in ξ-direction,

$$\rho_{gst} = \rho_{iend}, u_{gst} = u_{iend}, v_{gst} = v_{iend}, w_{gst} = w_{iend}, e_{gst} = e_{iend} \tag{3.63}$$

For the ghost cell of the ending surface in ξ-direction,

$$\rho_{gst} = \rho_{istart}, u_{gst} = u_{istart}, v_{gst} = v_{istart}, w_{gst} = w_{istart}, e_{gst} = e_{istart} \tag{3.64}$$

where, the *istart* and *iend* represent the first and last cell number in ξ-direction.

3.6.10 Translational Periodic Boundary for Flow Variables only

This boundary condition is used for detached-eddy simulation to simulate a 2D isometric problem (Fig. 3.3) with spanwise periodic BC. Different from the division periodic boundary, the geometric information of the ghost cells in the translational periodic boundary are extrapolated from adjacent inner points. The flow variables still satisfy Eq.(3.63) and (3.64).
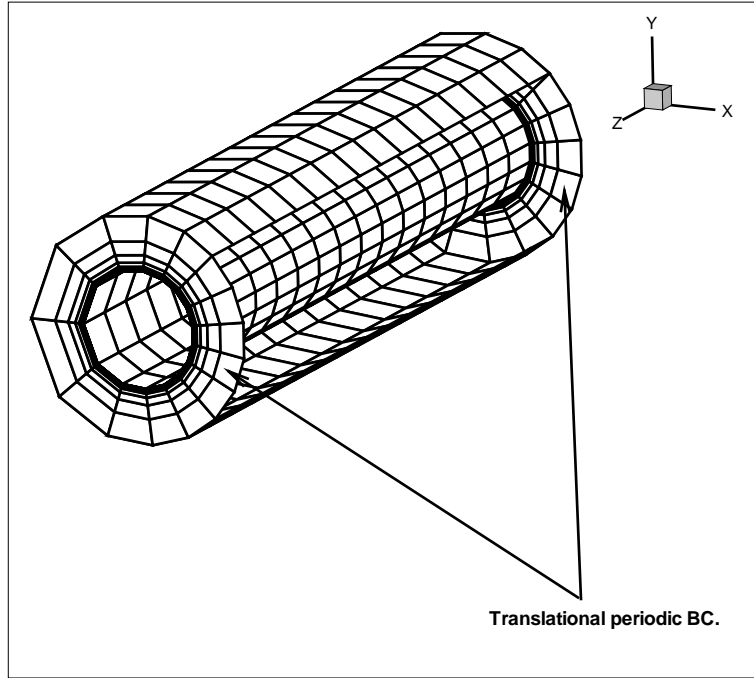

Figure 3.3: translational periodic boundary

3.6.11 Subdomain Boundary (Inner Boundary)

This boundary condition is used to define the interface of two block grids partitioned for parallel computing or multi-block grid computation. The data of the ghost cells or halo cells are given by exchanging the boundary data of the two adjacent blocks. The subdomain boundary mapping procedure and data exchanging process are described in Chapter 5.

Chapter 4

Comparison of the Low Diffusion

E-CUSP Scheme with the Roe Scheme

To demonstrate the accuracy, efficiency, and robustness of the new LDE scheme, several 2D and 3D cases are computed using the LDE scheme and the Roe scheme to compare their performance. Both S-A one equation model and B-L algebraic model are used for comparison. The finite volume solver using 3rd order MUSCL scheme for inviscid fluxes and 2nd order central differencing scheme for viscous terms is employed for this comparison [136].

4.1   Subsonic Flat Plate Turbulent Boundary Layer Flow

The subsonic flat plate is used to examine the performance of the LDE scheme for turbulent boundary layer. The mesh size is 181×81 (see Fig. 4.1). The y^+ of the first cell center to the wall is kept less then 1.0. The Reynolds number is 4×10^6 based on the length of the plate. The inlet Mach number is 0.5.

As shown in Fig. 4.2, both the computational results of the LDE scheme and the Roe scheme agree well with the law of the wall using S-A model. They are slightly better than the results using B-L model in the transition region from the linear viscous sublayer to log layer. With the B-L model, both schemes can use a large CFL number(≥ 100). With the S-
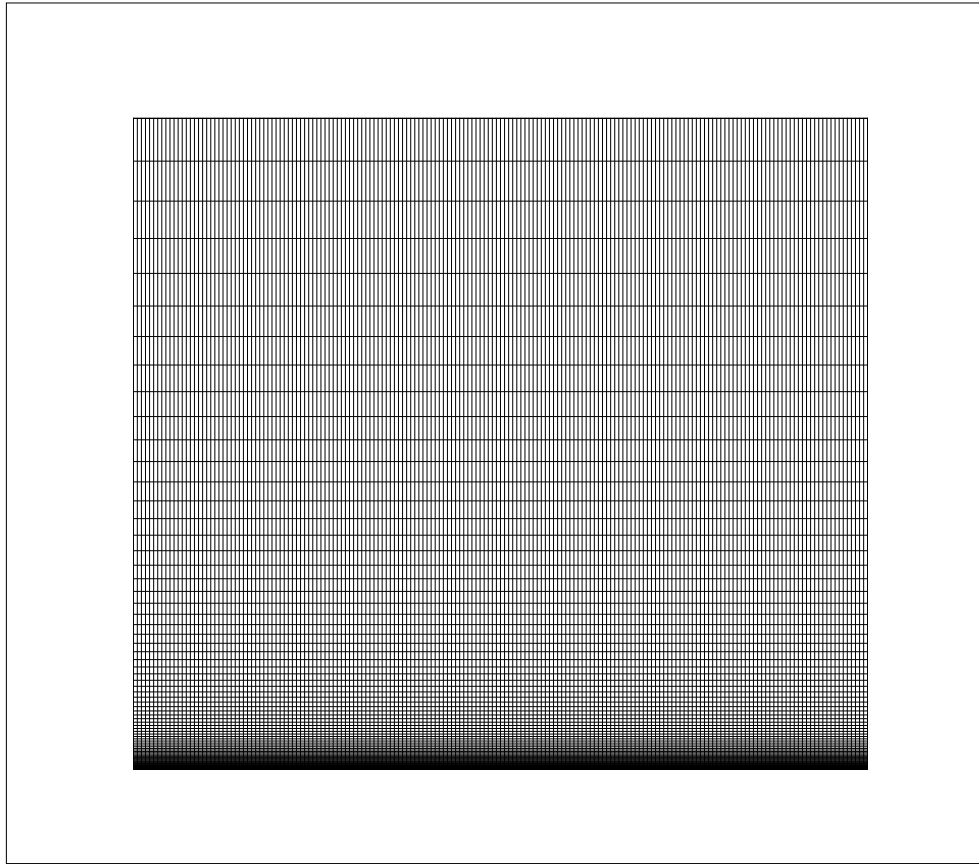
Figure 4.1: The mesh for subsonic flat plate

A model, the CFL number can be set to 100 for the LDE scheme. But for the Roe scheme, it can be only set to about 10. That means the Roe scheme needs more time steps to converge a result than the LDE scheme and hence, need more computational time. Fig. 4.3 shows the solution residuals of the LDE scheme and the Roe scheme for S-A and B-L turbulence model. The LDE scheme only use about $\frac{1}{5}$ of the iterations required by the Roe scheme.
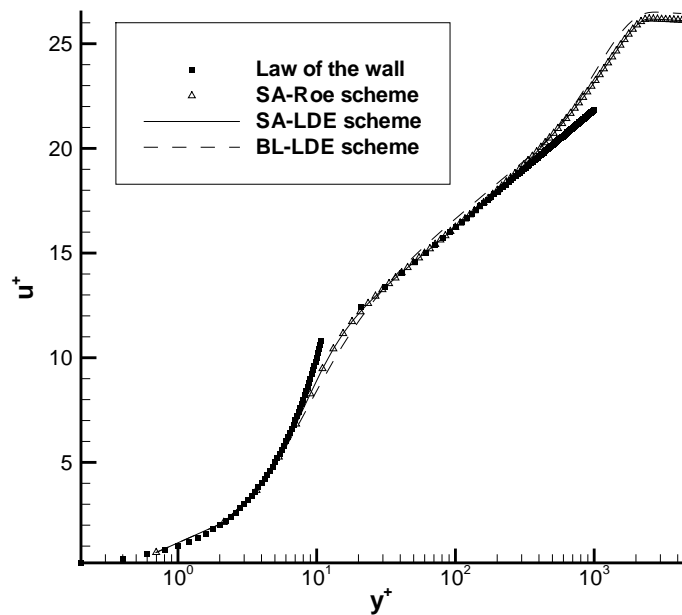
Figure 4.2: Comparison of velocity profiles
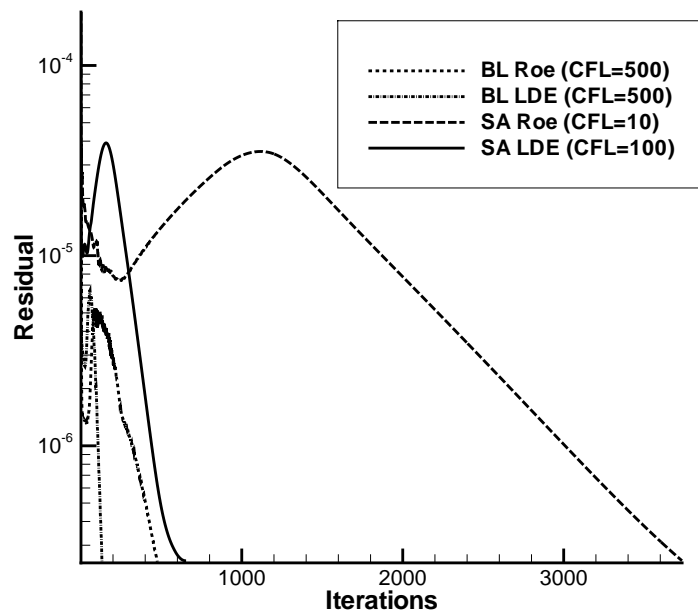
Figure 4.3: The L2 solution residual history of flat plate

4.2   RAE2822 Transonic Airfoil

The RAE2822 transonic airfoil is used to compare the performance of the LDE and Roe scheme with S-A model for computing 2D turbulent transonic flows. The mesh is a two-block O-grid with dimensions of $2 \times (129 \times 56)$ as shown in Fig. 4.4. The Reynolds number is 6.5×10^6 based on the chord length. The Mach number is 0.729. The angle of attack is $2.31°$.
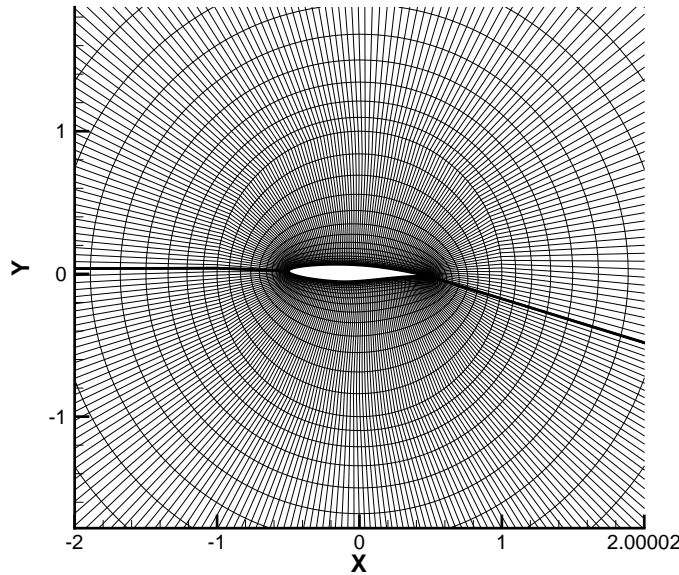

Figure 4.4: 2-Block grids for RAE2822

Fig. 4.5 shows the convergence histories of the LDE scheme and the Roe scheme. The maximum CFL number that the Roe scheme can use is 6.0, whereas the LDE scheme can use 10. The LDE scheme achieves significantly faster convergence rate and lower residual level. Fig. 4.6 presents the comparison of pressure coefficients between the experimental data and computation results. The results of the LDE scheme and Roe scheme are virtually identical and the predicted shock locations agree well with the experiment.
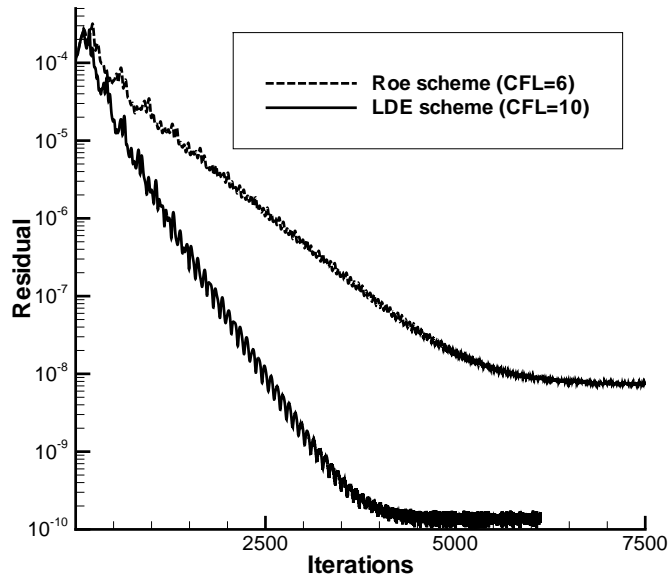
Figure 4.5: The L2 solution residual history of RAE2822
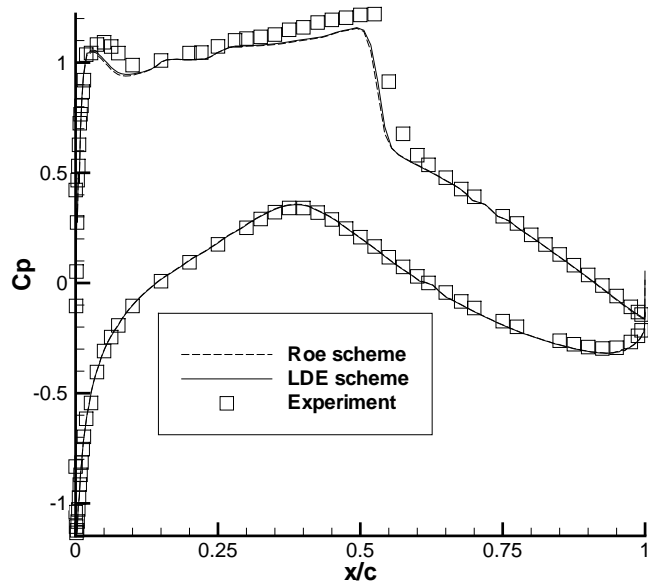
Figure 4.6: The surface pressure coefficient distribution of RAE2822

4.3   Transonic Inlet-Diffuser

The transonic inlet-diffuser is used to examine the performance of the LDE scheme for shock wave/turbulent boundary layer interaction. The mesh is a single-block, 2D H-grid

with dimension of 193×97(Fig. 4.7). The Reynolds number is 4.38×10^5 based on the throat height. The inlet Mach number is 0.5. The exit back pressure equals to 0.72 times of the inlet total pressure.
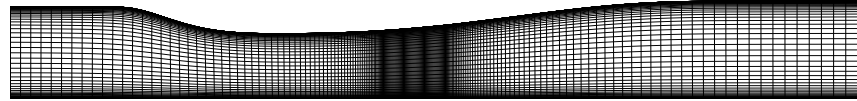

Figure 4.7: The mesh for 2D Inlet diffuser

Fig. 4.8 presents the comparison of the experimental data and the computational results. It shows that, with the S-A model, the LDE scheme and Roe scheme have nearly identical results. The S-A model predicts the results significantly better than the B-L model.
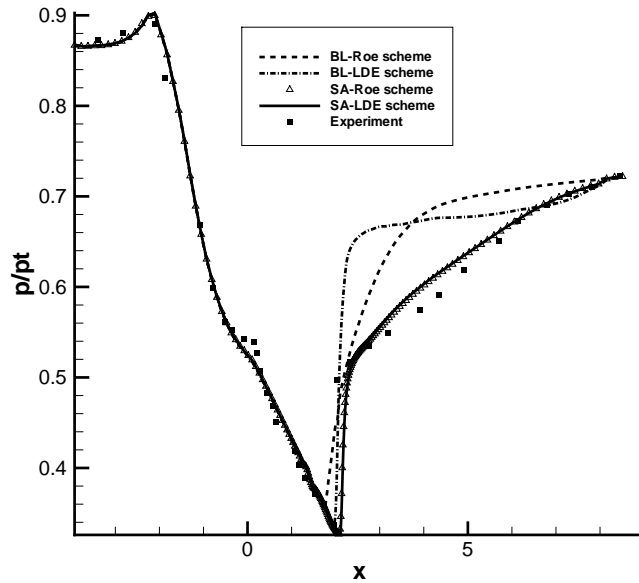

Figure 4.8: Upper wall pressure distribution of the inlet diffuser

Fig. 4.9 is the pressure contours of the LDE scheme. A curved λ-shock is clearly captured due to the shock wave/turbulent boundary layer interaction.

Fig. 4.10 is the computed stream lines. It indicates that the upper wall boundary layer is separated due to the shock/boundary layer interaction. This case shows that the turbulence

Figure 4.9: The contours of the pressure for inlet diffuser

model is a critical factor for the prediction accuracy of the shock wave/turbulent boundary layer interaction.
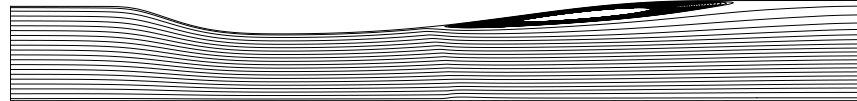

Figure 4.10: The stream lines of inlet diffuser

4.4 Transonic ONERA M6 Wing

The transonic ONERA M6 wing is calculated to examine the performance of the LDE scheme for three dimensional cases. The mesh is composed of 16 block grids which are obtained by partitioning a single block O-H-grid with the dimensions of $145 \times 61 \times 41$ (Fig. 4.11). The Mach number is 0.8395. The Reynolds number is 1.97×10^7 based on the averaged chord. The angle of attack is $3.06°$.

Fig. 4.12 and Fig. 4.13 present the comparison of the pressure distributions between the experiment and computation at the different sections. The location of $z/b = 0.2$ is near the root and $z/b = 0.99$ is near the tip of the wing. The computation results agree well with the experimental data except at the section of z/b=0.8, where the double-shock pattern is not well resolved as most of other CFD simulations.

Fig. 4.14 and Fig. 4.15 plot the contours of pressure on the surfaces of M6 wing using the LDE and Roe schemes respectively. The pressure contours of the pressure and suction surface are put on the left and right respectively to have a clear view of the 3D wing surfaces. Both schemes clearly capture the flow pattern that two shock waves merge near the wing tip on the suction surface and highlight a typical lambda-shape. One shock wave is
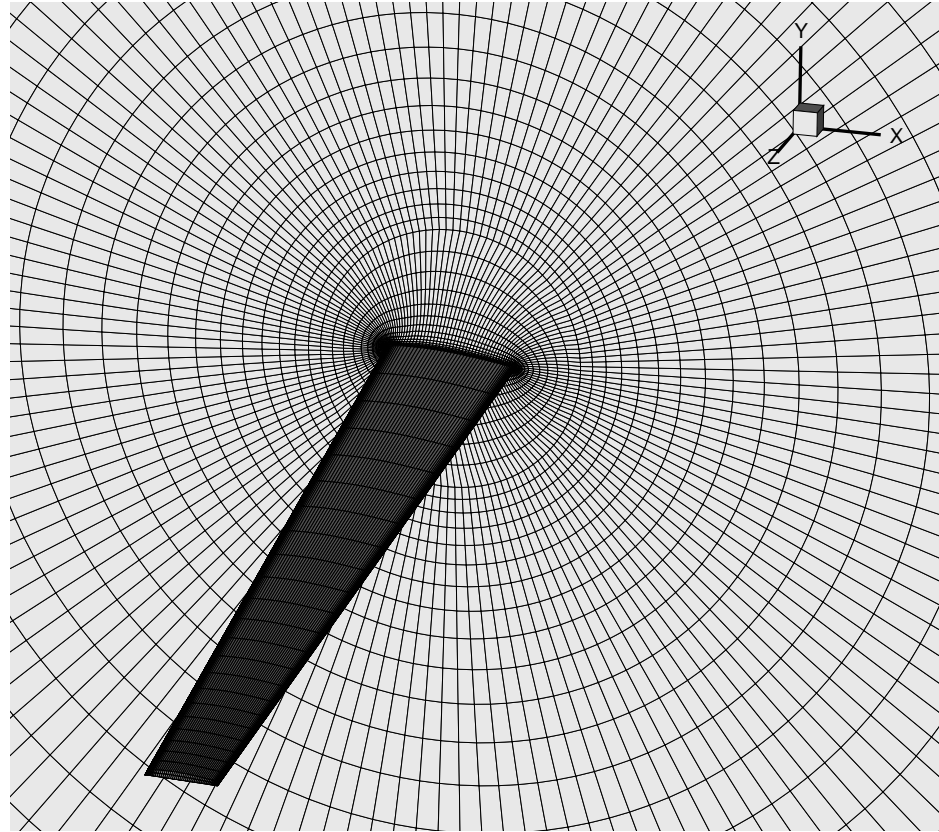
Figure 4.11: M6 wing mesh

near the leading edge, and the other impinges the root just after the half of the cord, while it touches almost at the leading edge at the tip. The two figures indicate that the LDE and Roe schemes predict nearly the same results.

Similar to the 2D cases, the maximum CFL number of the LDE scheme is larger than that of the Roe scheme. Fig. 4.16 shows the convergence histories of the LDE scheme with $CFL = 5$ and the Roe scheme with $CFL = 2$. The LDE scheme achieves significantly faster convergence rate and lower residual level.
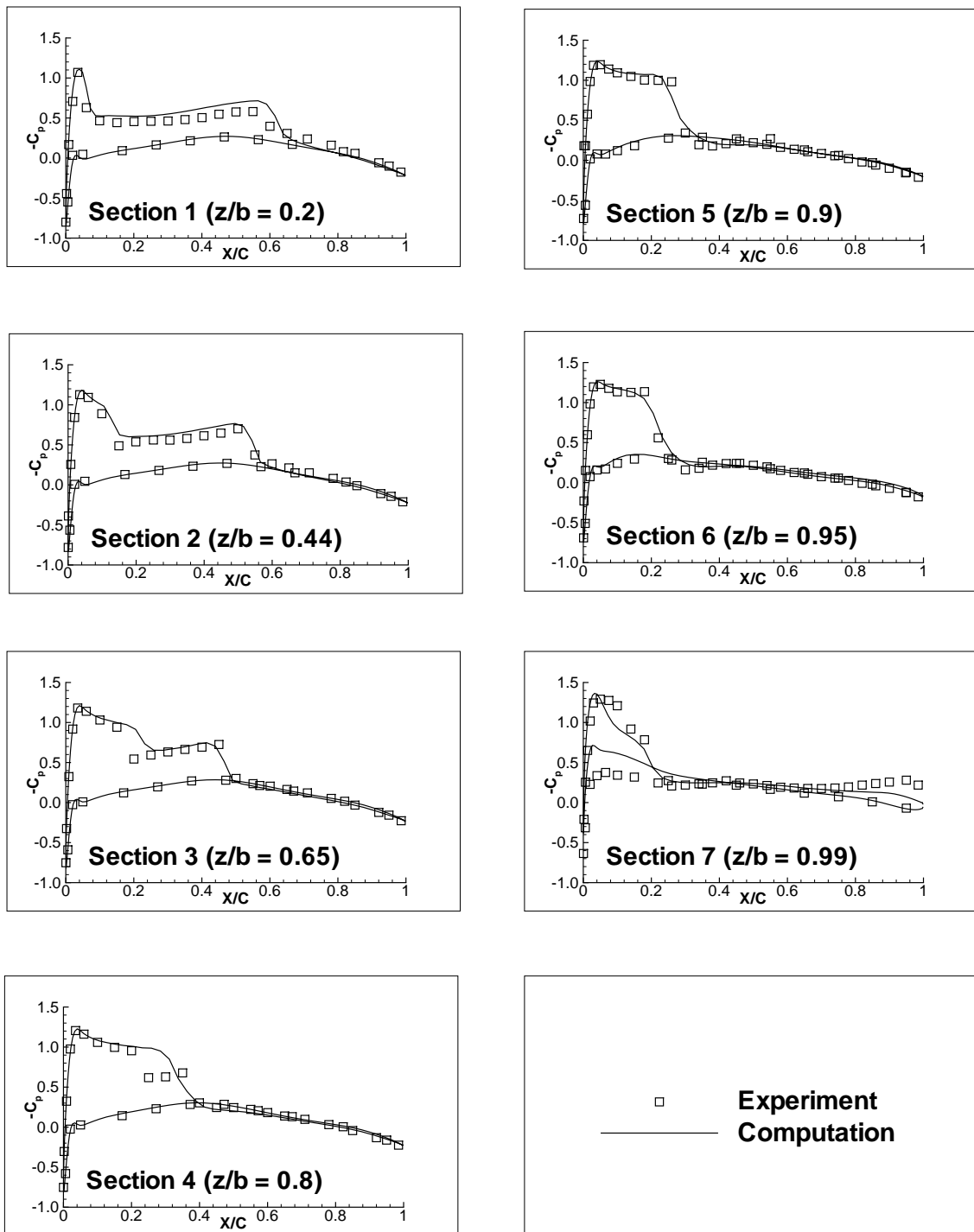
Figure 4.12: The surface pressure coefficient distribution of M6 wing using LDE scheme
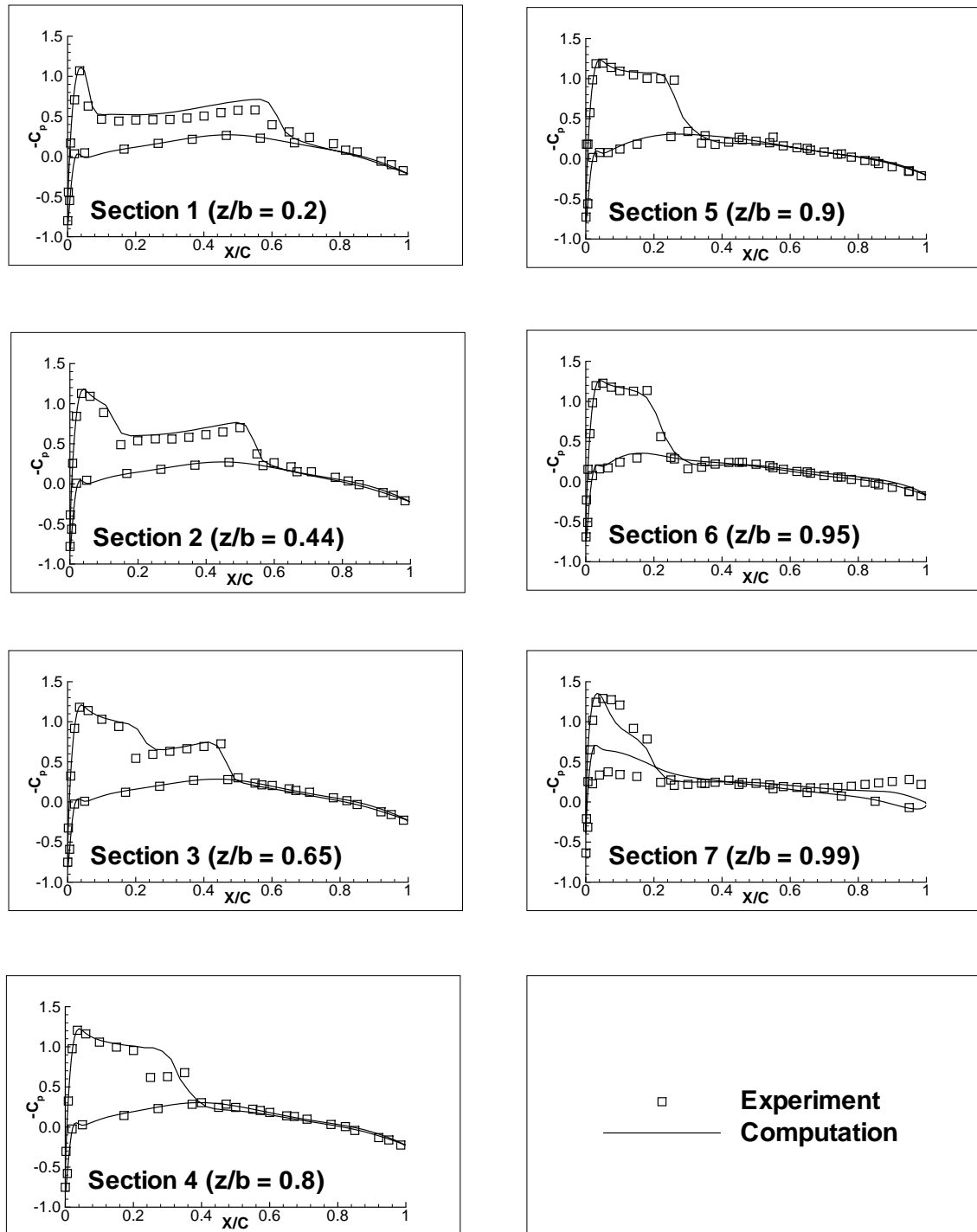
Figure 4.13: The surface pressure coefficient distribution of M6 wing using Roe scheme
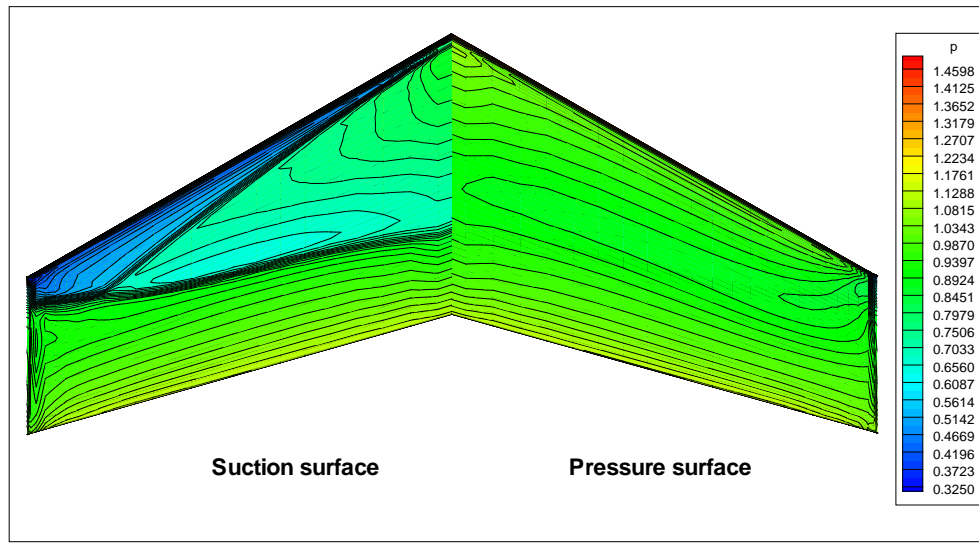
Figure 4.14: The contours of surface pressure for M6 wing using LDE scheme
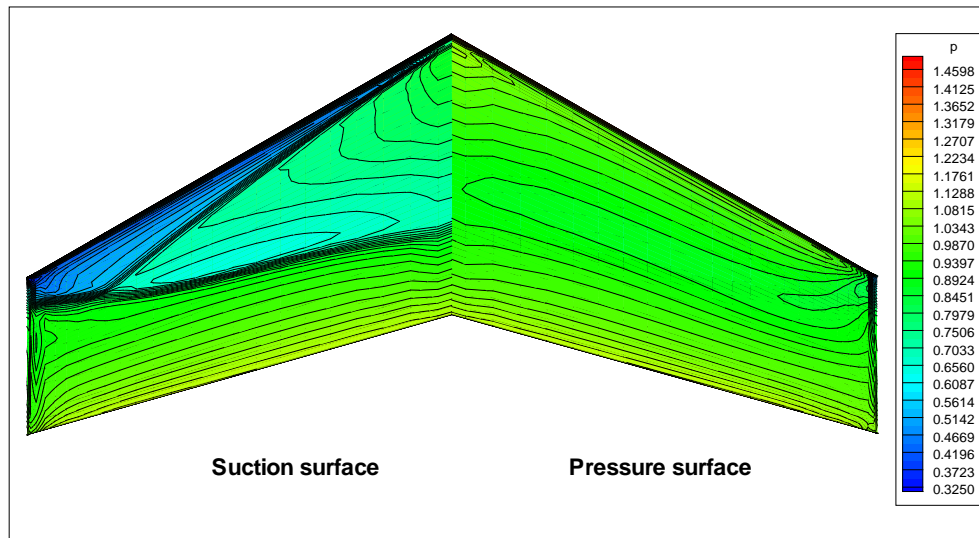
Figure 4.15: The contours of surface pressure for M6 wing using Roe scheme
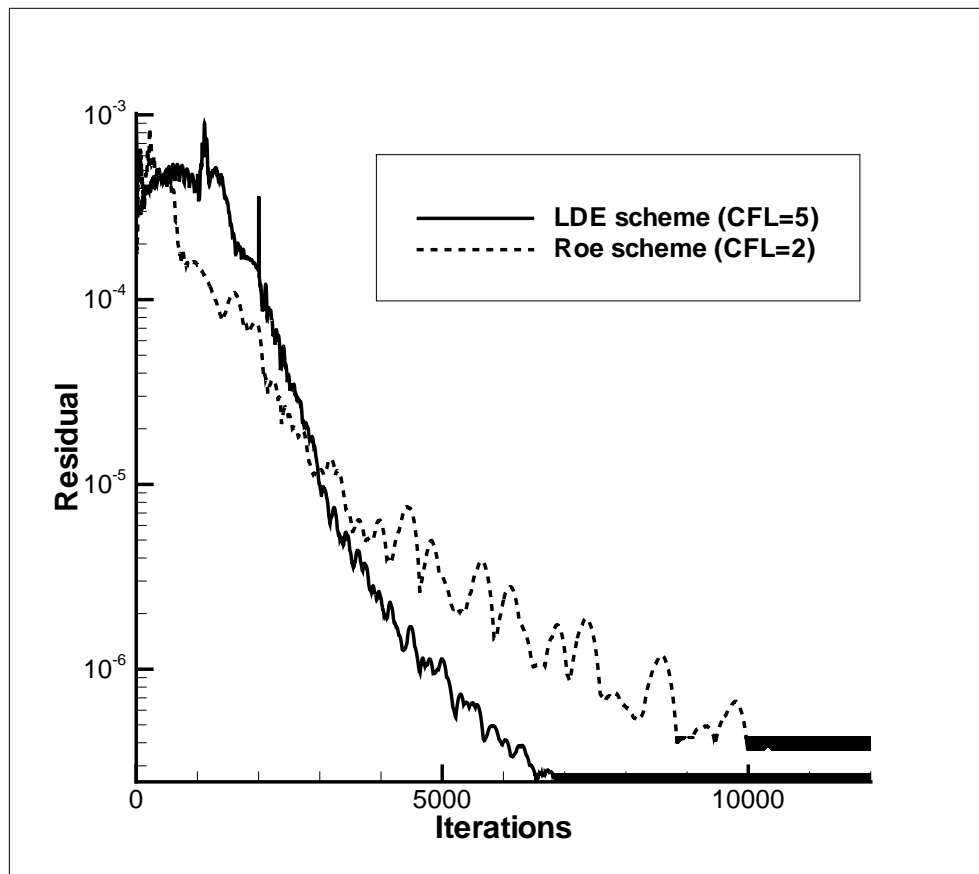
Figure 4.16: The maximum solution residual history of M6 wing

4.5 3D Transonic Channel Flow

The 3D transonic channel flow is used to examine the performance of the LDE scheme and the Roe scheme for 3D shock wave/turbulent boundary layer interaction problems with the S-A model. A single H-grid with the dimensions of $90 \times 60 \times 60$ is used in the computation(Fig. 4.17). The Reynolds number is 10^6 based on the entrance height. For boundary conditions, the total pressure, total temperature and flow angle are fixed at the inlet and the static pressure at the outlet is adjusted to match the position of the shock wave obtained by the experiment.
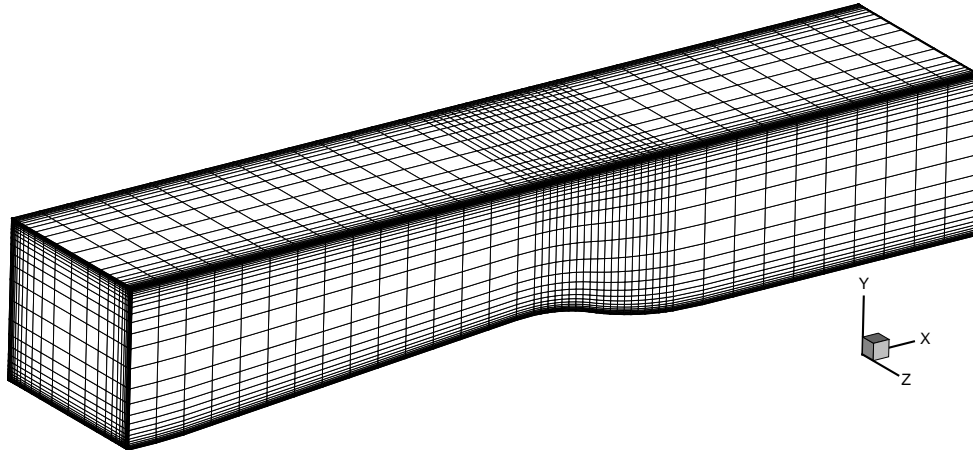
Figure 4.17: Transonic duct 3D mesh

Fig. 4.18 to Fig. 4.20 present the comparison of the Mach number contours between experiment and computation at three spanwise sections. The computed shock wave structures of the LDE scheme and the Roe scheme agree well with each other and are similar to that of the experiment. At the two locations close to the side wall at $z = 60mm$ and $z = 90mm$, both the computations over predict the size of separation zone. At the mid section $z = 70mm$, the predicted separation size and pattern agree well with the experiment.
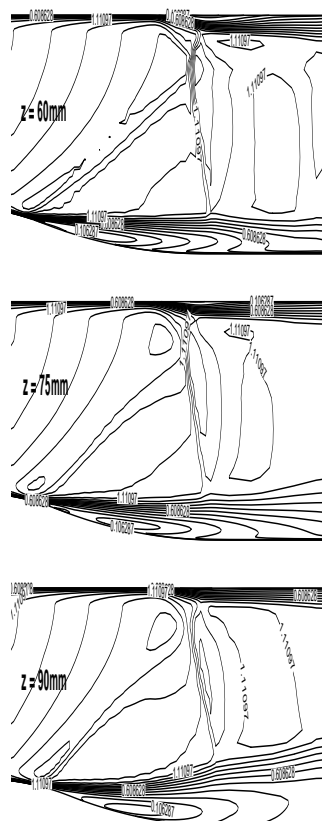
Figure 4.18: LDE scheme　　　Figure 4.19: Roe scheme　　　Figure 4.20: Experiment
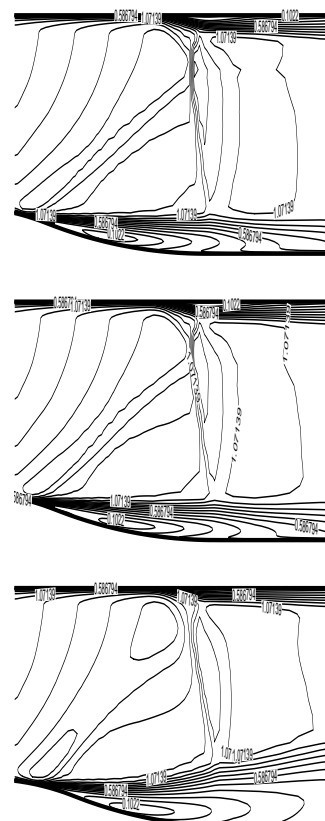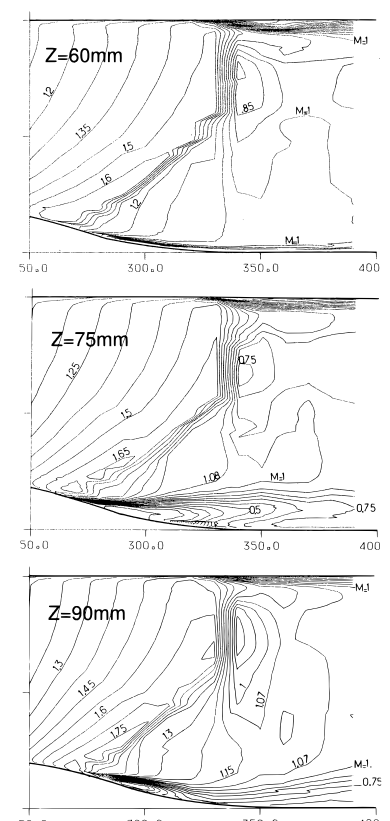
Chapter 5

Parallel Computation

In this chapter, the sub-domain boundary mapping procedure used for parallel computation is described in details. The 3D Navier-Stokes solver using an implicit time marching scheme with line Gauss-Seidel relaxation is parallelized with the SPMD parallel strategy. This procedure is used for both the 2nd order and high order schemes. Several 2D and 3D cases are computed to test the parallel computing efficiency and robustness of the parallel code.

5.1   The Mapping Procedure

5.1.1   Inner Boundary and Relationship Between Adjacent Blocks

The indices i, j, k are used to express the mesh index of an arbitrary sub-domain block. For any structured grid block with the mesh dimensions of $i_{max} = n1, j_{max} = n2, k_{max} = n3$, we can uniquely define an arbitrary block, face and edge using the two diagonal points at the opposite corner of each entity. For example, the block, face and edge shown in Fig. 5.1 can be defined as the following

$$block: \qquad start = 1,1,1, end = n1,n2,n3$$

$$face\,(i = n1): \qquad start = n1,1,1, end = n1,n2,n3$$

$$edge\,(i = n1, j = 1): \quad start = n1,1,1, end = n1,1,n3$$
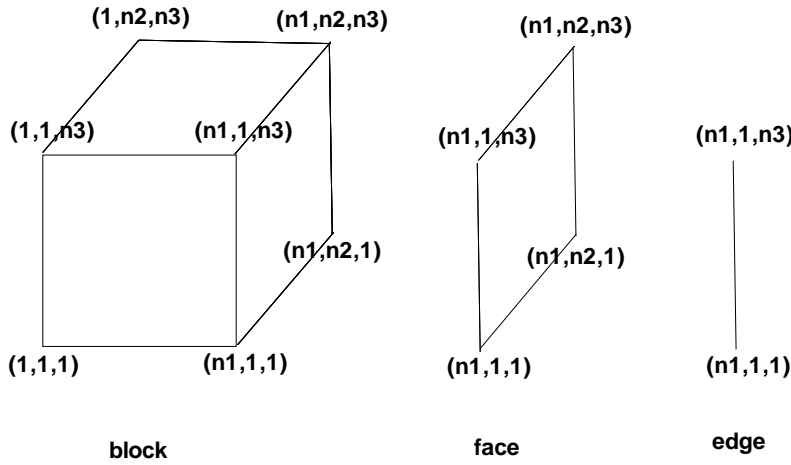
Figure 5.1: Definition of a block, face and edge

Where, *start* and *end* are one-dimensional arrays with 3 elements. For simplicity, assume that the blocks are numbered from 1 to n and there are only two halo layers of overlapping grid points for the inner boundaries (Fig. 5.2). Thus two layers of data need to be communicated at each inner boundary between the adjacent blocks. The number of halo layers can be arbitrary depending on the accuracy order of the scheme to be used. In our code, we have used up to four halo layers for 7th order WENO scheme [141].

For an arbitrary block p, to uniquely define its inner boundaries and their relationship with the adjacent blocks, the following information is needed:
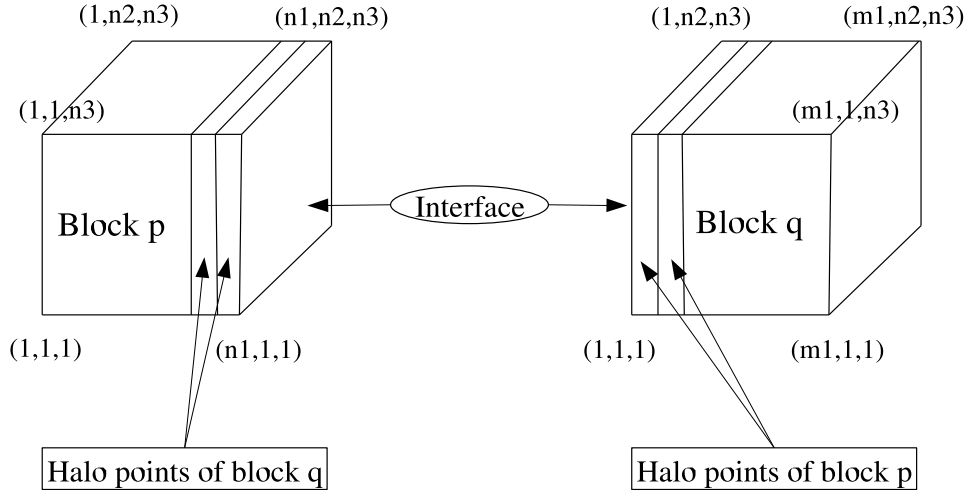
Figure 5.2: Inner boundary of two adjacent blocks

1) The block number of the adjacent block q.

2) The inner boundary definition, *i.e.* the two diagonal points of the boundary between block p and q.

3) The relationship of the MISs between block p and q, which is needed for packing/unpacking the data for exchange.

A term, "*Order*", is introduced to express the MIS of a block. The numbers $1, 2, 3$ represent the mesh axis directions of i, j, k respectively for a block. The mesh axis index sequence of the current block p will be always $(1, 2, 3)$. The *Order* of the adjacent block q is always defined based on the mesh axis directions of the current block p. There are 6 possibilities for the *Order* of block q as shown in Fig. 5.3. An *Order* is independent of axis directions. For example, in Fig. 5.3, *Order* 1 of the block q shows two opposite I-axis direction. Hence, for each order there are in total six combinations of index axis directions. In this manner, mesh axis direction does not need to follow the right hand rule. The *Order* is numbered from 1 to 6 as given in table 5.1 and Fig. 5.3. An inner boundary and its relationship with the adjacent block can be uniquely defined by the current block number p, the adjacent block number q, the inner boundary diagonal points of block p and block q, and the *Order* of block q.
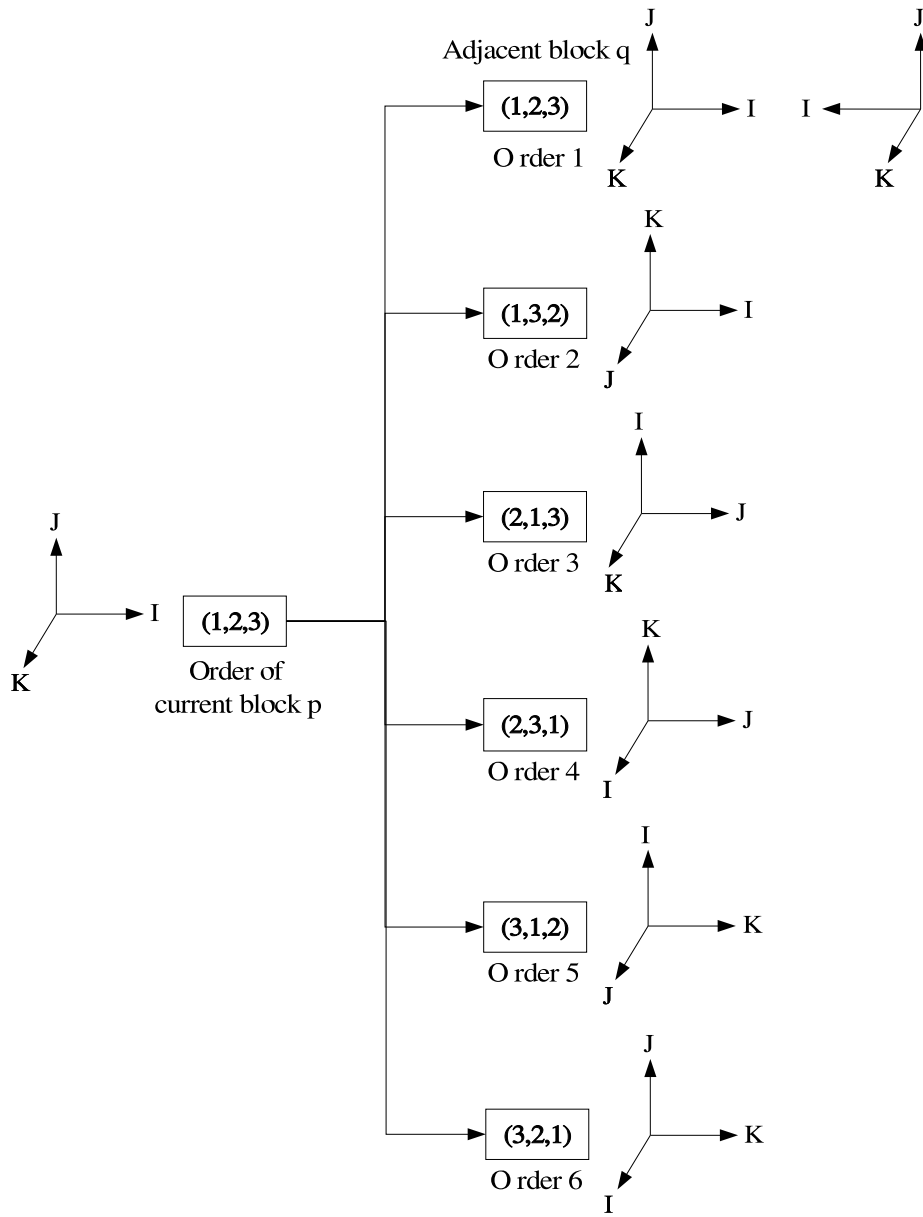
Figure 5.3: MIS relationship of adjacent blocks

The *Order* of block *p* corresponding to the MIS of block *q* can be uniquely defined based on the *Order* of *q* corresponding to block *p*. The relationship is given in table 5.2 based on the relationship indicated in Fig. 5.3. Table 5.2 indicates that most of the orders are the same except *Orders* 4 and 5.

With the *Order* information of any two adjacent blocks, an inner boundary only needs

Table 5.1: The *Order* of the block *q*

Order Number of Block *q*	1	2	3	4	5	6
The *Order* of Block *q*	(1,2,3)	(1,3,2)	(2,1,3)	(2,3,1)	(3,1,2)	(3,2,1)

Table 5.2: The relative relationship of *Orders* for two blocks

Order Number of Block *q*	1	2	3	4	5	6
The *Order* of *q* based on MIS of *p*	(1,2,3)	(1,3,2)	(2,1,3)	(2,3,1)	(3,1,2)	(3,2,1)
The *Order* of *p* based on MIS of *q*	(1,2,3)	(1,3,2)	(2,1,3)	(3,1,2)	(2,3,1)	(3,2,1)
Order Number of Block *p*	1	2	3	5	4	6

to be defined for one block, as the other will take its *Order* according to table 5.2. Thus, the probability of making mistakes in defining the inner boundary conditions is minimized.

As an example, the inner boundary (see Fig. 5.2) between block *p* and block *q* can be defined as the following:

$block = p, start = n1, 1, 1, end = n1, n2, n3,$

$iblock = q, istart = 1, 1, 1, iend = 1, n2, n3, order = 1, 2, 3$

Where, the *block* and *iblock* represent the current block number and adjacent block number respectively. The *start*, *end* and *istart*, *iend* are the diagonal points defining the inner boundary. The *start*, *end* and *istart*, *iend* are given according to the local MIS of the sub-domain, which is independent of other sub-domains. The *order* in the above example represents the *Order* of block *q* corresponding to block *p*.

5.1.2   Pack and Unpack Data Procedures

For CFD parallel computation with multi-block grids the inner boundary data of the flow field are exchanged after each iteration according to the *Order* relationship of the inner boundary defined in the last section. To be efficient, a one dimension array is used for data communication. For each block, two operations need to be done for data exchange:

1) pack the inner boundary data into an one-dimensional array and send them to the

adjacent block to be used for the halo cells.

2) unpack the one-dimensional array received from the adjacent block and assign it to the halo cells of the inner boundary.

The pack/unpack procedure for a 2D problem is simpler than the 3D one as the 2D boundaries are edges and the 3D boundaries are faces. Hence, we will describe the pack/unpack procedures for 2D and 3D problems separately.

5.1.2.1   2-D Problems

The pack/unpack procedures are implemented using the following rules:

1) Inner boundary data are packed into an one-dimensional array in the inward direction of the interface, *i.e.* from the outermost edge to the innermost edge.

2) The one-dimensional array received from the adjacent block is unpacked in the reversed (outward) direction.

For example, assuming the number of the halo layer is l and letting $n3 = 1$, the pack/unpack procedure of the 2D problem shown in Fig. 5.2 for block p is given as the following:

Pack:

$$i1 = 0$$

$$do\ i = start(1), start(1) - l + 1, -1$$

$$do\ j = start(2), end(2)$$

$$i1 = i1 + 1$$

$$bcb(i1) = x(i, j)$$

$$end\ do$$

$$end\ do$$

Unpack:

$$i1 = 0$$

$$do\ i = start(1) + 1, start(1) + l$$

$$do\ j = start(2), end(2)$$

$$i1 = i1 + 1$$

$$x(i, j) = bcb(i1)$$

end do

end do

where, $l = 2$ is used for the example shown in Fig. 5.2, $start(1) = n1, start(2) = 1, end(2) = n2$, bcb is the one-dimensional array used for data communication, and x is the data array of the flow field.

5.1.2.2   3-D Problems

For 3D problems the data will be packed from the outermost plane to innermost plane in the current block. The data is unpacked in the reversed direction. However, since the inner boundary is a surface for a 3-D problem, the *Orders* of the adjacent blocks are needed to determine the sequence that the data is to be packed and unpacked in the remaining two directions on an inner boundary surface.

To define the data packing sequence, it is necessary to introduce another term, "*Orientation*", to specify the orientation and location of the inner boundary interfaces of a block. The *Orientation* is defined based on each inner boundary interface as given in table 5.3. Therefore, any inner boundary of a block has an *Orientation* numbered from 1 to 6.

Table 5.3: The relationship between the *Orientation* and faces

Face	i=1	i=n1	j=1	j=n2	k=1	k=n3
Orientation	1	2	3	4	5	6

Unpacking in 3D

First, we need to decide a rule for unpacking for the current block to simplify the pack/unpack procedure. The rule we adopt is that, when the *Orientation* is determined, the

data unpacking sequence for the remaining two axis directions is always from the larger axis number to the smaller one. In this way, the unpack procedure will be independent of the *Order* of the adjacent blocks when the *Orientation* is determined. For example, if the *Orientation* of an inner boundary of the current block p is 2, the unpacking is done by the following DO loops:

Unpack:

$i1 = 0$

$do\ i = start(1) + 1, start(1) + l$

$do\ j = start(2), end(2)$

$do\ k = start(3), end(3)$

$i1 = i1 + 1$

$x(i, j, k) = bcb(i1)$

end do

end do

end do

If the *Orientation* of an inner boundary of the current block p is 4, the unpacking is done by the following DO loops:

Unpack:

$i1 = 0$

$do\ j = start(2) + 1, start(2) + l$

$do\ i = start(1), end(1)$

$do\ k = start(3), end(3)$

$i1 = i1 + 1$

$x(i, j, k) = bcb(i1)$

end do

end do

end do

If the *Orientation* of an inner boundary of the current block p is 6, the unpacking is done by the following DO loops:

Unpack:

$$i1 = 0$$

$$do\ k = start(3) + 1, start(3) + l$$

$$do\ i = start(1), end(1)$$

$$do\ j = start(2), end(2)$$

$$i1 = i1 + 1$$

$$x(i, j, k) = bcb(i1)$$

$$end\ do$$

$$end\ do$$

$$end\ do$$

For the odd *Orientation* numbers, the DO loops of the unpack procedure are similar.

Packing in 3D

To match the unpack procedure, the data packing sequence in the current block must match the MIS of the adjacent block which is defined by the *Order* of the adjacent block.

Assuming that the *Orientation* of the inner boundary of the current block p is 2, the remaining two directions of the data packing for the current block p are then $(2,3)$. Based on Table 5.1 and Fig. 5.3, for *Order* numbers 1, 3 and 5, the corresponding two directions of the adjacent block q are $(2,3)$, $(1,3)$ and $(1,2)$ respectively. To match the data unpacking sequence in the adjacent block q, the packing sequence in the current block then must be from the larger axis number to the smaller one. Specifically, the data packing DO loops are the following:

Pack:

$$i1 = 0$$

$$do\ i = start(1), start(1) - l + 1$$

$$do\ j = start(2), end(2)$$

$$do\ k = start(3), end(3)$$

$$i1 = i1 + 1$$

$$bcb(i1) = x(i, j, k)$$

end do

end do

end do

Where, i, j and k correspond to 1, 2 and 3 respectively. For *Order* numbers 2, 4 and 6, the corresponding two directions of the adjacent block q are $(3,2)$, $(3,1)$ and $(2,1)$ respectively. To match the data unpacking sequence in the adjacent block q, the packing sequence in the current block must be from the smaller axis number to the larger one, which will have the following DO loops:

Pack:

$$i1 = 0$$

$$do\ i = start(1), start(1) - l + 1$$

$$do\ k = start(3), end(3)$$

$$do\ j = start(2), end(2)$$

$$i1 = i1 + 1$$

$$bcb(i1) = x(i, j, k)$$

end do

end do

end do

The above two types of DO loops cover all the scenarios under *Orientation* 2. For other *Orientation* numbers, the DO loops are similar.

5.1.3   Send/Receive Procedure

As shown in Fig. 5.4, the send/receive procedure for CFD parallel computation is for all blocks to send data to all adjacent blocks first, and then all blocks receive data from all adjacent blocks [142]. This procedure can avoid the communication deadlock, but a communication blockage may occur because of limits to computer buffer space which is used to temporarily save the exchanged data. To avoid communication blockage, a secure send/receive procedure is implemented in the following way.

The basic idea of the secure send/receive procedure is to do the send/receive operations in a pair simultaneously. That is, when a block sends data, the receiving block will receive the data at the same time (Fig. 5.5). The procedure is implemented based on the following rules for a block:

1) Send data to the adjacent blocks with greater block numbers and receive data from the adjacent blocks with smaller block numbers.

2) Send data to the adjacent blocks with smaller block numbers and receive data from the adjacent blocks with greater block numbers.
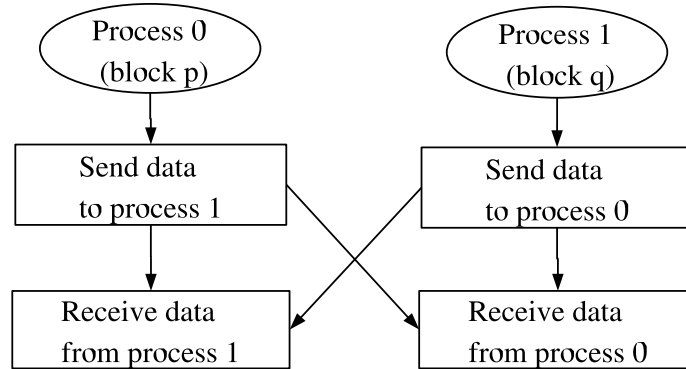
Figure 5.4: The send/receive procedure that
may create buffer space blockage

This procedure ensures the one-to-one correspondence between send and receive operations requiring minimal buffer space to avoid communication blockage. Specifically, the procedure is implemented by two DO loops.
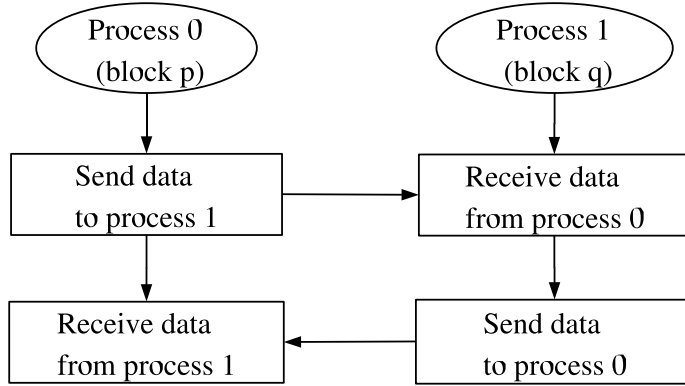
Figure 5.5: The secure communication procedure that minimize buffer space usage

Loop 1 (For all interfaces):

1) Obtain the block number of the adjacent block.

2) If the block number of the adjacent block is greater than the block number of the current block, send data; otherwise, receive data.

Loop 2 (For all interfaces):

1) Obtain the block number of the adjacent block again.

2) If the block number of the adjacent block is smaller than the block number of the current block, send data; otherwise, receive data.

Fig. 5.6 shows the flow chart of the exchanging procedure.

This method is proved to be very effective in removing the communication blockage problem and has a high efficiency of data communication in our numerical experiments.

5.2   Implementation

5.2.1   Flow Charts

The in-house Navier-Stokes code [34–36] is converted to have parallel computing capability using the suggested general sub-domain boundary mapping procedure. Based on multi-block grids, the Single Program Multiple Data (SPMD) parallel strategy is employed in the
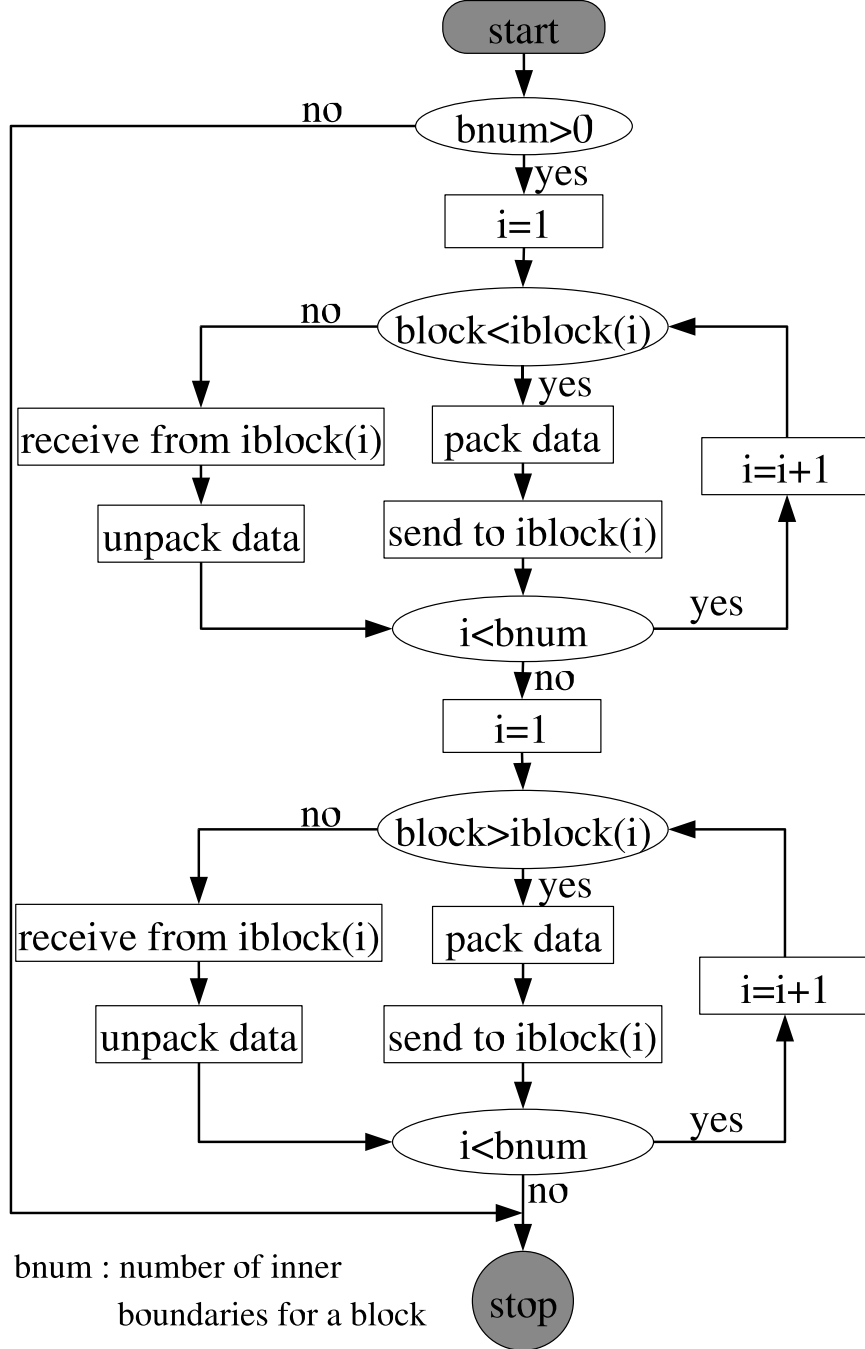
Figure 5.6: Flow-chart of exchanging procedure for parallel computation

parallelization. In this strategy, the CFD solver is designed as a block solver which solves flow governing equations in each block. The interface is taken as a boundary, called inner boundary. After a time step, the data of the halo cells of inner boundaries are exchanged across the interface by the mapping procedure described in section 5.1. The SPMD flow

chart for the parallel computation is given as the following
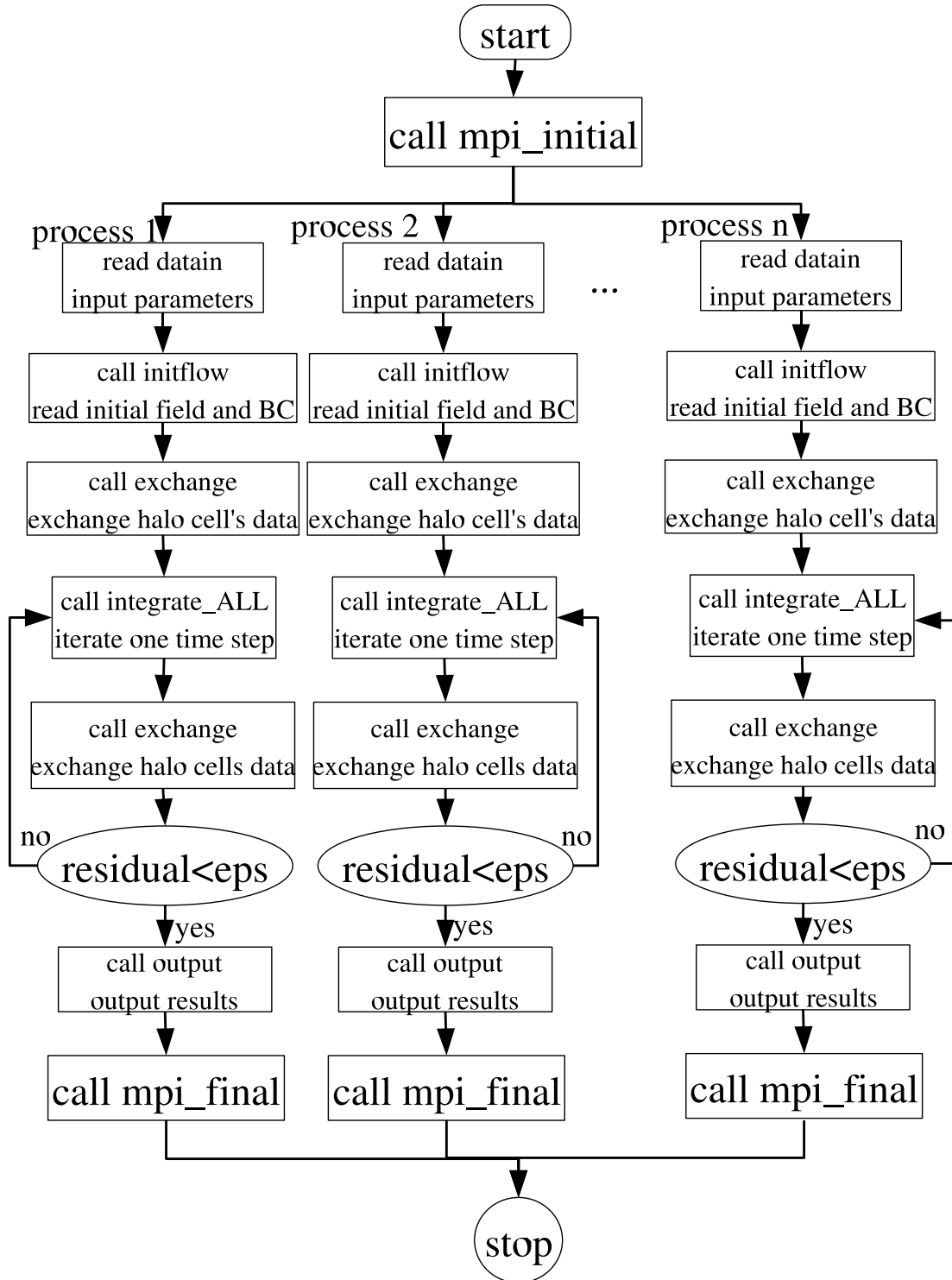
Figure 5.7: The flow chart for parallel computation in SPMD strategy

5.2.2 Implicit Gauss-Seidel Iteration

Gauss-Seidel line iteration needs a special treatment when a single block is splitted into multi-block to do parallel computation. For example, following lines along direction i with the index from small to large, Eq. (3.36) can be written in a matrix form (ignore the dash lines here):

$$
\begin{bmatrix}
\bar{B}_1 & B_1^+ & & & | & & & \\
B_2^- & \bar{B}_2 & B_2^+ & & | & & 0 & \\
& & \ddots & & | & & & \\
& & B_m^- & \bar{B}_m & | & B_m^+ & & \\
-- & -- & -- & -- & + & -- & -- & -- \\
& & & B_{m+1}^- & | & \bar{B}_{m+1} & B_{m+1}^+ & \\
& 0 & & & | & & \ddots & \\
& & & & | & & B_n^- & \bar{B}_n
\end{bmatrix}
\begin{bmatrix}
\Delta Q_1 \\
\Delta Q_2 \\
\vdots \\
\Delta Q_m \\
-- \\
\Delta Q_{m+1} \\
\vdots \\
\Delta Q_n
\end{bmatrix}
=
\begin{bmatrix}
\mathbf{RHS}_1^{'} \\
\mathbf{RHS}_2^{'} \\
\vdots \\
\mathbf{RHS}_m^{'} \\
-- \\
\mathbf{RHS}_{m+1}^{'} \\
\vdots \\
\mathbf{RHS}_n^{'}
\end{bmatrix}
$$

$$(5.1)$$

When using multi-block parallel computation, for example two blocks, Eq. (5.1) will be partitioned into two sub-matrices as indicated by the dash lines in Eq. (5.1). The variables $\Delta Q_1 \rightarrow \Delta Q_m$ and $\Delta Q_{m+1} \rightarrow \Delta Q_n$ are solved on two separate processors by conducting the matrix inversion iteration on each sub-matrix. A simple treatment is to discard the corner matrices B_m^+ on the first sub-matrix and B_{m+1}^- on the second sub-matrix. They are the coefficients computed based on the variables from the adjacent sub-domain. In the present work, these two coefficients are treated as zero in the implicit solver for the sub-domain computations. The two sub-domain matrix systems obtained are:

$$
\begin{bmatrix}
\bar{B}_1 & B_1^+ & & \\
B_2^- & \bar{B}_2 & B_2^+ & \\
& & \ddots & \\
& & B_m^- & \bar{B}_m
\end{bmatrix}
\begin{bmatrix}
\Delta Q_1 \\
\Delta Q_2 \\
\vdots \\
\Delta Q_m
\end{bmatrix}
=
\begin{bmatrix}
\mathbf{RHS}_1^{'} \\
\mathbf{RHS}_2^{'} \\
\vdots \\
\mathbf{RHS}_m^{'}
\end{bmatrix}
\qquad (5.2)
$$

$$
\begin{bmatrix}
\bar{B}_{m+1} & B^+_{m+1} & & & \\
B^-_{m+2} & \bar{B}_{m+2} & B^+_{m+2} & & \\
& & \ddots & & \\
& & & B^-_n & \bar{B}_n
\end{bmatrix}
\begin{bmatrix}
\Delta Q_{m+1} \\
\Delta Q_{m+2} \\
\vdots \\
\Delta Q_n
\end{bmatrix}
=
\begin{bmatrix}
\mathbf{RHS}'_{m+1} \\
\mathbf{RHS}'_{m+2} \\
\vdots \\
\mathbf{RHS}'_n
\end{bmatrix}
\tag{5.3}
$$

The advantages of discarding the matrices B^+_m and B^-_{m+1} is that it avoids exchanging the matrices across the sub-domain boundaries and hence reduces communication time. The disadvantage is that it does not preserve the exact matrices as in the single processor computation and may affect the convergence efficiency. However, the computation experiments indicate that the slowing down of convergence due to this non-exact treatment is small, particularly when the mesh size is large. It should be pointed out that discarding the matrices B^-_{m+1} and B^+_m will not affect the accuracy of the solution when it is converged. This is because the variables at the sub-domain boundaries are exchanged exactly matching the result of the single domain calculation to calculate the RHS of Eqs. (3.34), which determines the accuracy of the solutions.

5.3   Results and Discussion

To validate the accuracy of the parallel computation procedure and examine the scalability, a 2D and 3D transonic flows are calculated. The 3rd order MUSCL scheme for inviscid fluxes and 2nd order central differencing scheme for the viscous terms are used [136]. The governing equations are solved based on finite volume method.

5.3.1   RAE2822 Transonic Airfoil

The RAE2822 transonic airfoil is calculated to examine the accuracy of the CFD solver and parallel computation efficiency for 2D problems. The multi-block grids (Fig. 4.4) are obtained by partitioning a single block O-grid with dimensions of 257×56. The Reynolds number is 6.5×10^6 based on the chord length. The Mach number is 0.729. The angle of

attack is 2.31°. Fig. 5.8 shows the convergence history with different number of processors (blocks) from 1 through 8. The convergence rate with multiple processors is slightly affected by the approximate implicit treatment at the sub-domain boundaries. Fig. 5.9 presents the comparison of pressure coefficients between the experiment and computation with 1 and 8 processors. The computed results are identical and agree very well with the experiment. Excellent speed up and efficiency for parallel computation are obtained as shown in table 5.4 and Fig. 5.10, which indicate that a super-linear scalability is achieved up to 8 processors with the sub-domain grid size of 33×56.
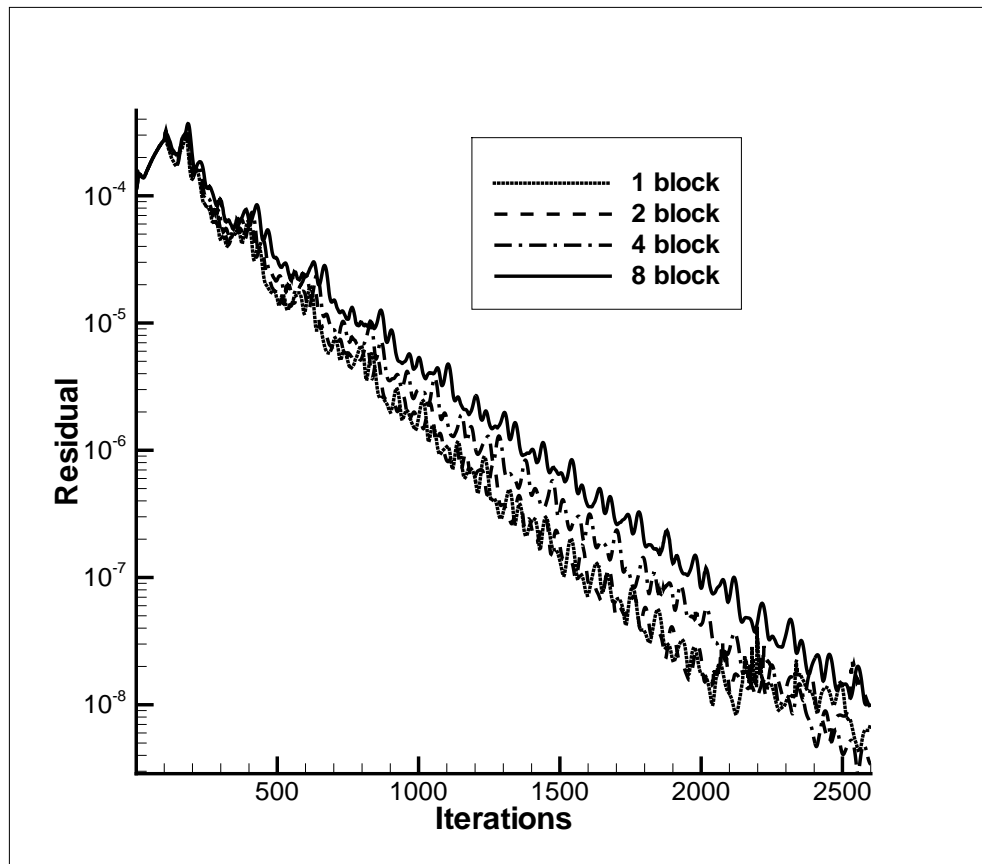

Figure 5.8: Comparison of the L2 residual convergence histories of RAE2822 airfoil
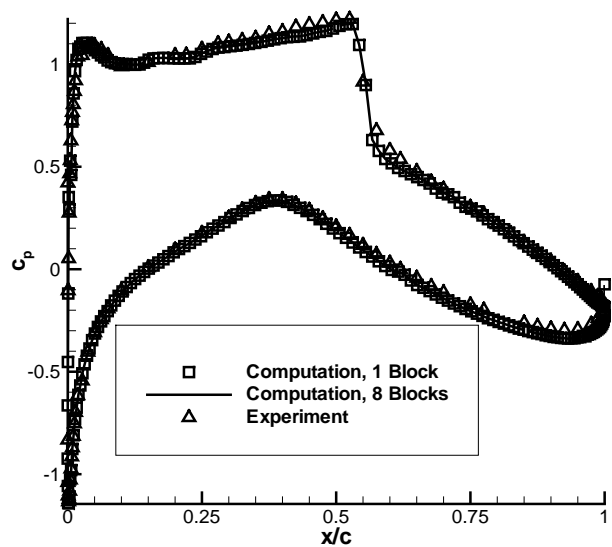
Figure 5.9: The surface distribution of pressure coefficient of the RAE2822 airfoil
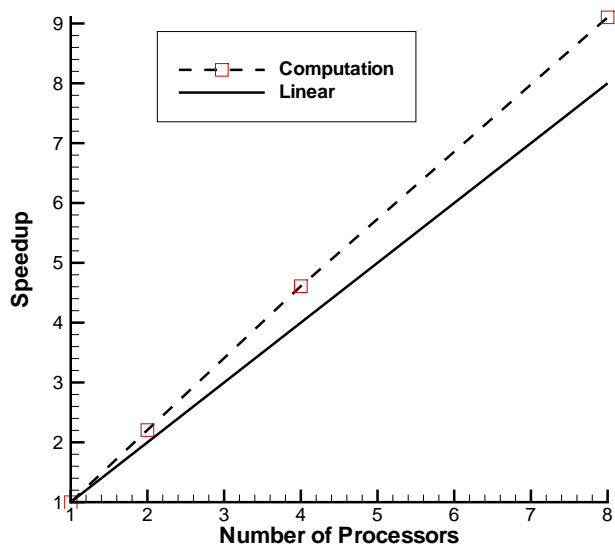
Figure 5.10: Speedup of parallel computation for RAE2822 airfoil

Table 5.4: The parallel computing performance for 2D RAE2822 airfoil

Number of nodes	1	2	4	8
time (sec/step)	0.355	0.161	0.077	0.039
speed up		2.205	4.610	9.103
Efficiency (%)		110.3	115.3	113.8
Grid size (per block)	257×56	129×56	65×56	33×56

5.3.2 Transonic ONERA M6 Wing

This case is to examine the CFD solver accuracy and parallel computation efficiency for 3D problems. The multi-block grids are obtained by partitioning a single block O-H-grid with the dimensions of $145 \times 61 \times 41$(Fig. 4.11). The Mach number is 0.8395. The Reynolds number is 1.97×10^7 based on the averaged chord. The angle of attack is $0°$.

Fig. 5.11 presents the comparison of surface pressure distributions between the experiment and computation using 2-block mesh at different span-wise sections. The location of $z/b = 0.2$ is near the root and $z/b = 0.99$ is near the tip of the wing. The computation results agree well with the experimental data. Comparing Fig. 5.11 and Fig. 4.12 which uses 16-block mesh, the computed results are almost identical.

Fig. 5.12 shows the convergence history using 2 and 16 processors (blocks). The convergence rate using 16 processors is also slightly affected by the approximate implicit treatment at the sub-domain boundaries.

Again, excellent speed up and efficiency for the parallel computation are obtained as shown in table 5.5 and Fig. 5.13.
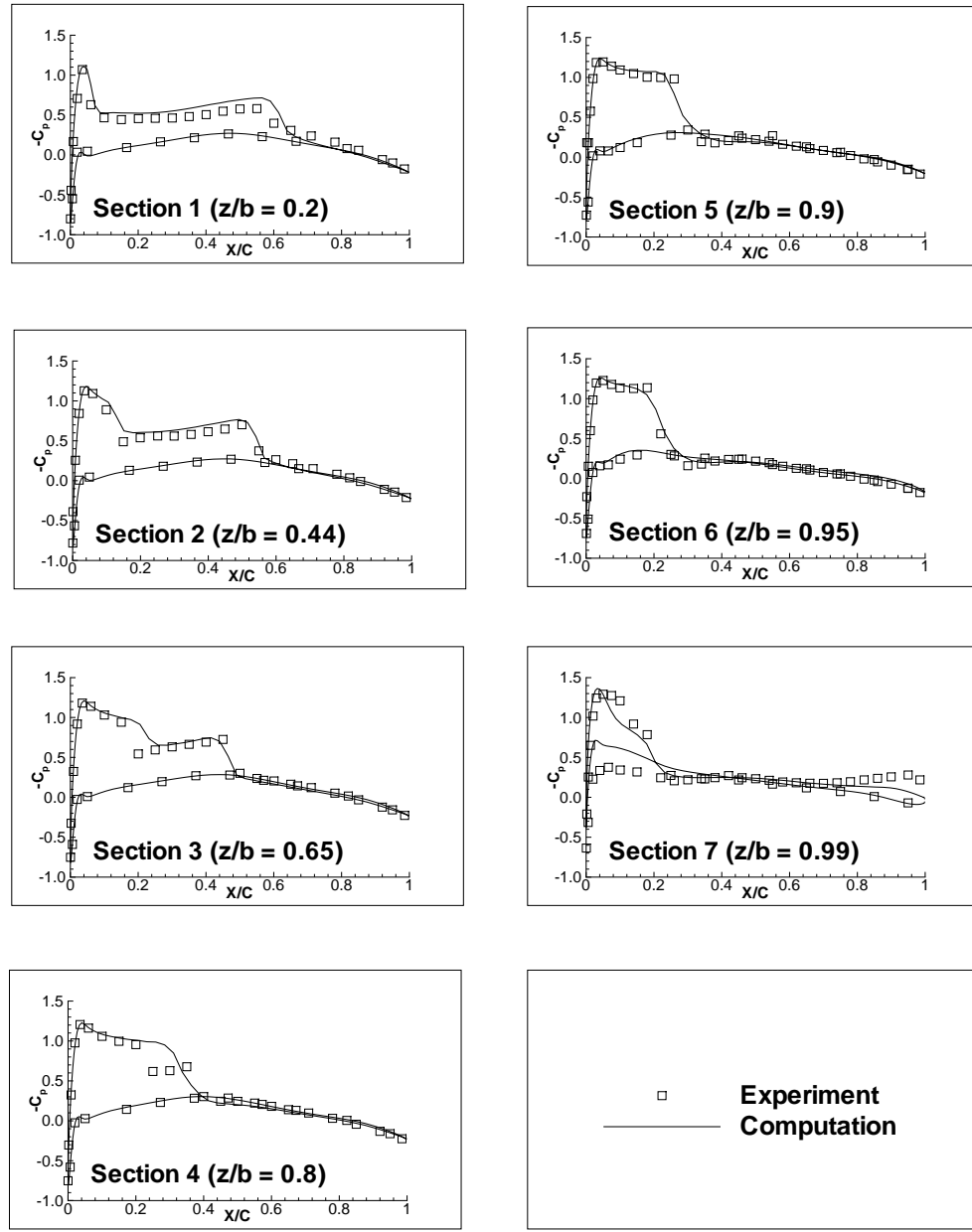
Figure 5.11: Surface pressure distribution of M6 wing at different span-wise locations

Table 5.5: The parallel computing performance for 3D M6 wing

| Number of nodes	1	2	4	8	16
time (sec/step)	10.747	4.912	2.484	1.298	0.697
speed up		2.188	4.326	8.280	15.419
Efficiency (%)		109.4	108.2	103.5	96.37
Grid size (per block)	$145 \times 61 \times 41$	$73 \times 61 \times 41$	$37 \times 61 \times 41$	$19 \times 61 \times 41$	$10 \times 61 \times 41$
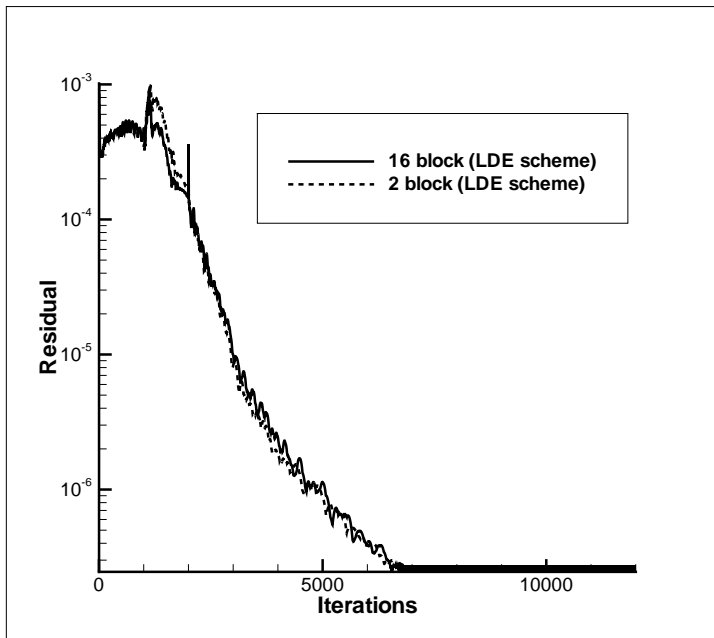
Figure 5.12: Comparison of the maximum residual convergence histories of M6 wing
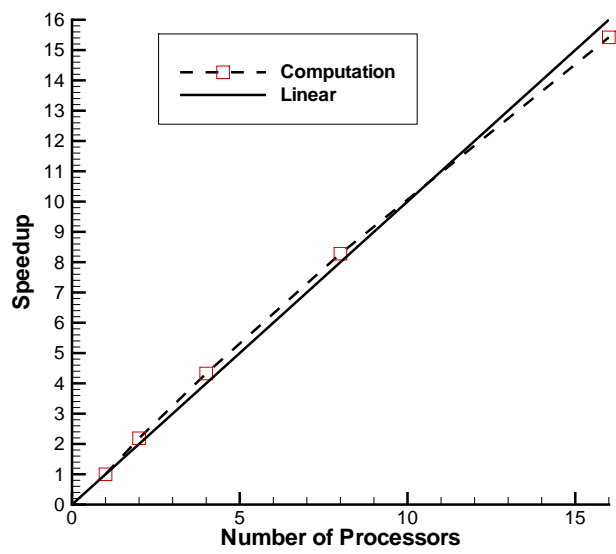
Figure 5.13: Speedup of the parallel computation for M6 wing

Chapter 6

Detached-Eddy Simulation

As a validation of the DES methodology, a circular cylinder flow is calculated. The 5th order WENO finite differencing scheme and the 4th order central differencing scheme described in Chapter3 with the LDE Riemann solver and implicit time marching are used.

6.1   DES of a Circular Cylinder Flow

In this study, the flow around a cylinder at a Reynolds number of 3900 is calculated using DES. The Mach number is 0.2. The spanwise length is πD, where D is the cylinder diameter. The dimensions of the baseline grid are $(121 \times 81 \times 33)$ (see Fig. 6.1 and Fig. 6.2). The computation is conducted on an MPI based computer cluster composed of 200 Intel Xeon 5150 processors with the floating calculation speed of 2.66Ghz.

A non-dimensional time step of 0.01 was used for the cases. The non-dimensional time is defined as $\bar{t} = \frac{t}{D/U_\infty}$. The computation begins with a uniform flow field. All the results are time-averaged from $\bar{t} = 100$ to 300.

Fig. 6.3 shows the mean pressure coefficients on the cylinder surface. For $Re = 3900$, only the coefficient of back pressure (C_p at $\theta = 180°$) is available . The computed mean pressure coefficient agrees very well with the experiment at $0 \leq \theta \leq 60°$. The present result using baseline grid is better than the LES result of Kasliwal et al. [143] in this region. In
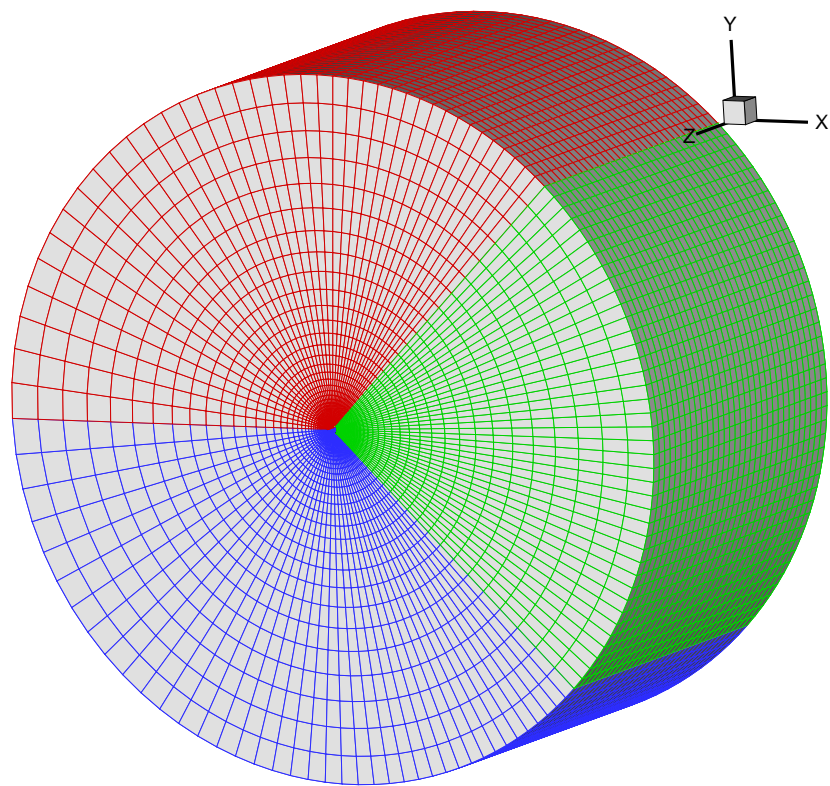
Figure 6.1: The computational grid of cylinder
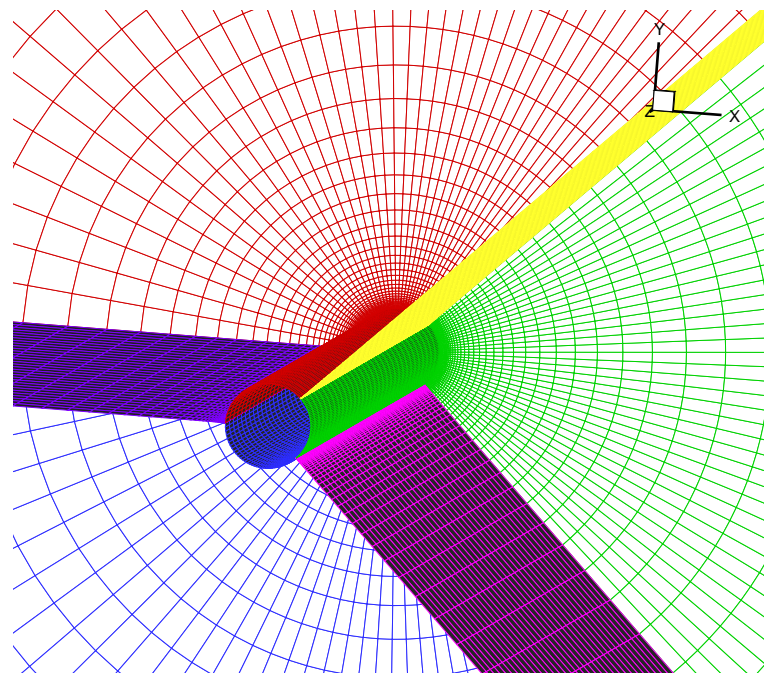
Figure 6.2: Close-up view of the computational grid

the region of $\theta = 60° \sim 180°$, the computed pressure lies among the experimental results.
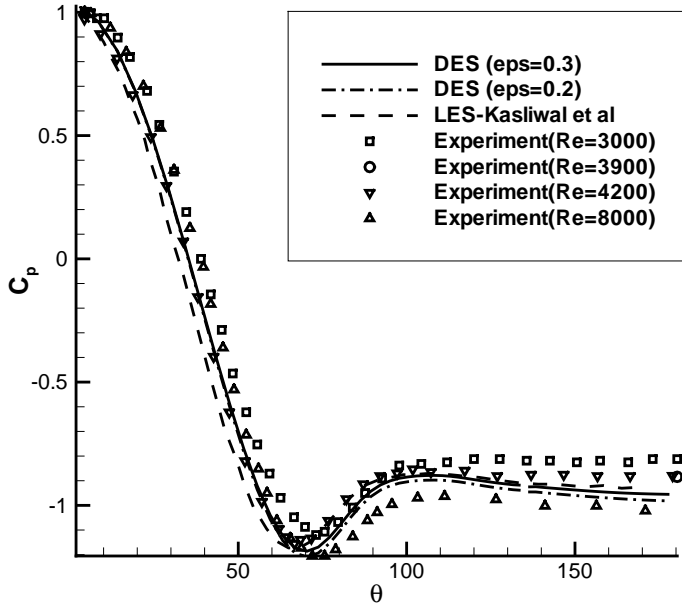

Figure 6.3: Mean pressure coefficient variation on the surface of the cylinder

Fig. 6.4 is the averaged mean streamwise velocity on the centerline in the wake of the cylinder. The present result agrees better with the experiment [144] than those of LES [143, 145] conducted by Kravchenko-Moin and Kasliwal et al.

Fig. 6.5 through Fig. 6.7 show the Reynolds stress components located at $x/D = 1.54$ plane. The computed streamwise Reynolds stress $(\overline{u'u'})$ is quite symmetric about the center line, whereas the experiment [146] has asymmetric profile. The computed $(\overline{u'u'})$ agrees well with the experiment except it does not reach the asymmetric high peak.

The computed shear Reynolds stress component $(\overline{u'v'})$ in Fig. 6.6 under-predicts the amplitude of the peaks measured in the experiment. Fig. 6.7 also shows that the peak of the lateral Reynolds stress $(\overline{v'v'})$ is under predicted. However, all the present results are significantly better than the LES results of Rizzetta et al. [147] which use 6-order compact scheme with mesh dimensions of $199 \times 197 \times 53$ as shown from Fig. 6.5$\sim$ 6.7.
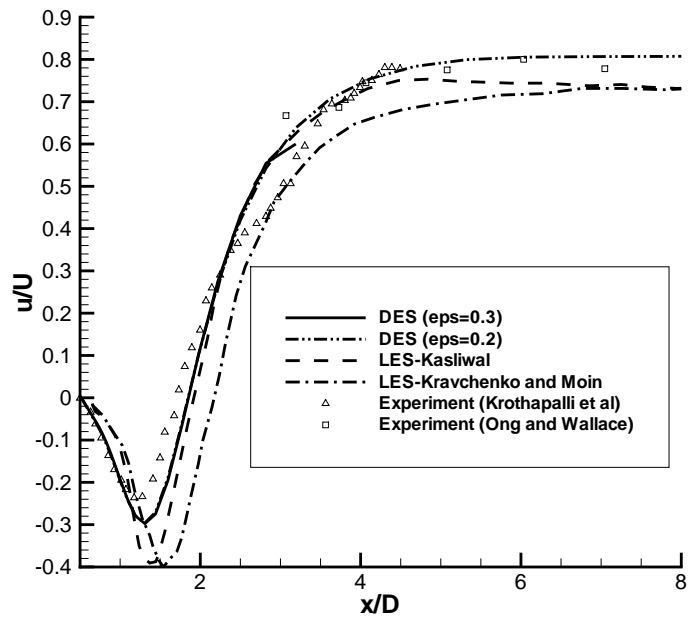
Figure 6.4: Streamwise velocity in the wake at y/D=0
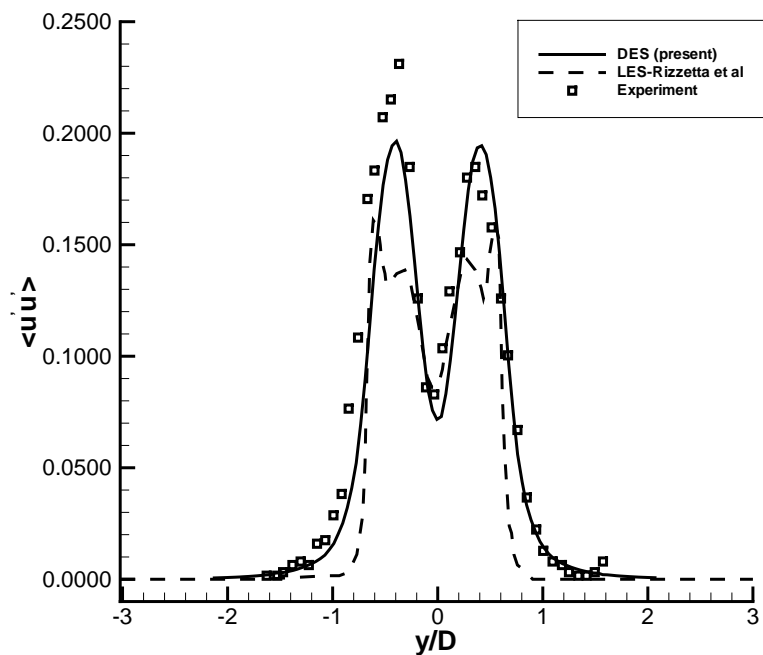
Figure 6.5: Streamwise Reynolds stress at x/D=1.54
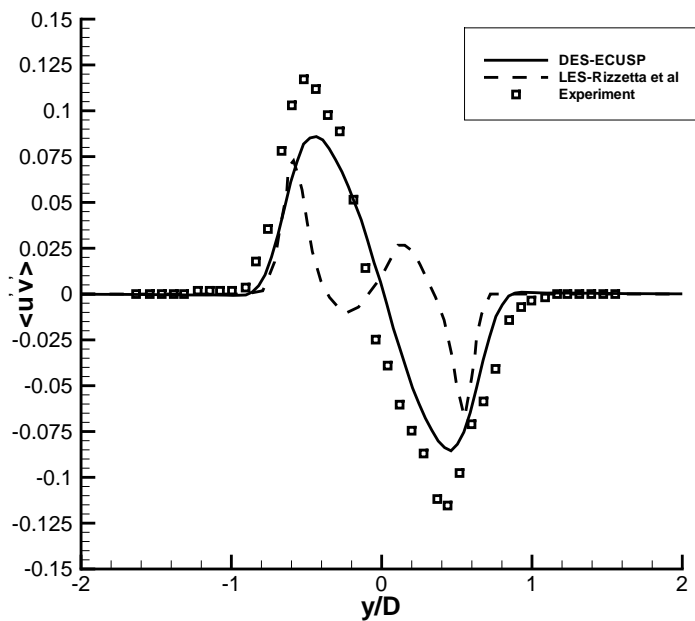
Figure 6.6: Shear Reynolds stress at x/D=1.54
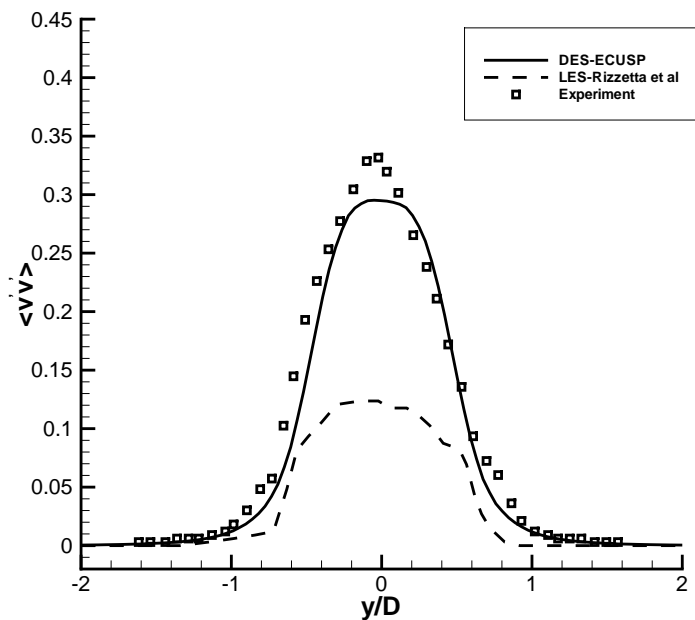
Figure 6.7: Lateral Reynolds stress at x/D=1.54

Fig. 6.8 and Fig. 6.9 plot the averaged mean streamwise velocity and mean crossflow velocity at three streamwise locations, $x/D = 1.06$, $x/D = 1.54$ and $x/D = 2.02$. The present results agree well with the computed results of Kravchenko-Moin [145] and Kasliwal et al. [143].
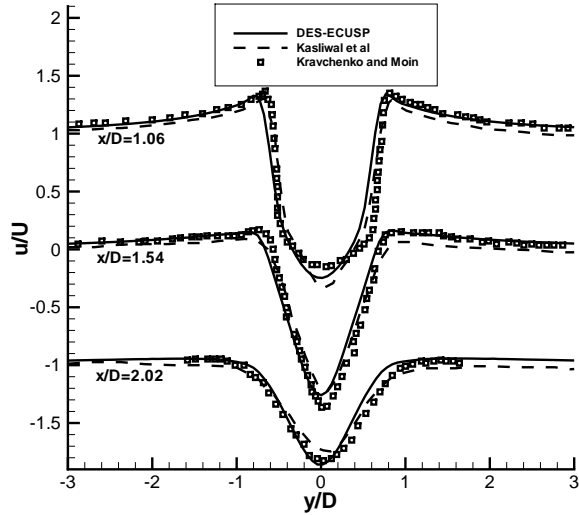

Figure 6.8: Mean streamwise velocity profiles in the wake
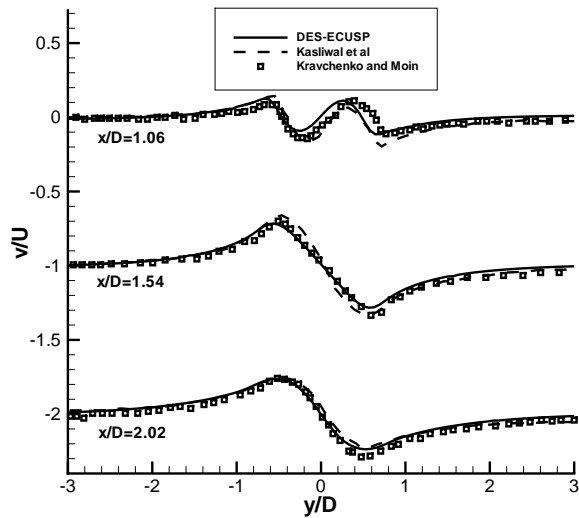
Figure 6.9: Mean crossflow velocity profiles in the wake

To investigate the solution sensitivity to spanwise length, the cylinder with spanwise length doubled to $2\pi D$ is calculated. The grid density is the same as the baseline grid. Fig. 6.10 through Fig. 6.14 indicate that the spanwise length has only a small effect on the computed results. The computed surface pressure is nearly identical to the baseline results. For the $2\pi D$ spanwise length, the computation gives slightly lower minimum mean streamwise velocity in the wake region. There is also little difference for the Reynolds stress component predicted with $2\pi D$ spanwise length.

The mesh refinement is also performed in this study. The dimensions of the baseline grid are increased by 1.5 times to $(181 \times 121 \times 49)$. The grid is divided into 12 blocks for parallel computation. The mesh refinement has a significant effect on the computed results. The clear difference between the refined and baseline mesh is that the refined mesh has larger vortex shedding area. Fig. 6.15 and Fig. 6.16 show the contours of the averaged mean vorticity magnitude of the baseline grid and refined grid respectively. Both display the symmetry of the mean flow field after a long time average. The refined grid predicts a larger recirculation zone behind the cylinder.

Fig. 6.10 shows that the mean pressure distribution is raised up in the region $\theta = 60^\circ \sim 180^\circ$ and matches closer with the experiment of Reynolds number 3000. The streamwise velocity distribution is shifted away from the measurement value as shown in Fig. 6.11. The computed shear Reynolds stress components are sharply reduced and are closer to the LES results of Rizzetta et al.

Fig. 6.17 shows the contours of the instantaneous vorticity magnitude at $\bar{t} = 300$. The refined mesh catches more small scale vortex structures. Fig. 6.18 shows a 3D instantaneous vorticity magnitude of the $2\pi D$ cylinder at $\bar{t} = 300$. It indicates that DES resolves some small vortex structures.

In summary, for the baseline grid of $121 \times 81 \times 33$ with πD spanwise length, the computed surface pressure and velocity in the wake region agree well with the experiment. The computed Reynolds stress are also in good agreement with the experiment except that the peak values are some what under predicted. To minimize the numerical dissipation, the ε

value of 0.3 in the WENO scheme is used.

The study indicates that the spanwise length of πD is sufficient. Doubling the spanwise length yields little difference of the results. The computation of mesh refinement indicates that DES is significantly affected by grid size. The clear difference is that the vortex shedding region is increased when the mesh is refined. The increased recirculation zone hence changes the mean values of the flow field.
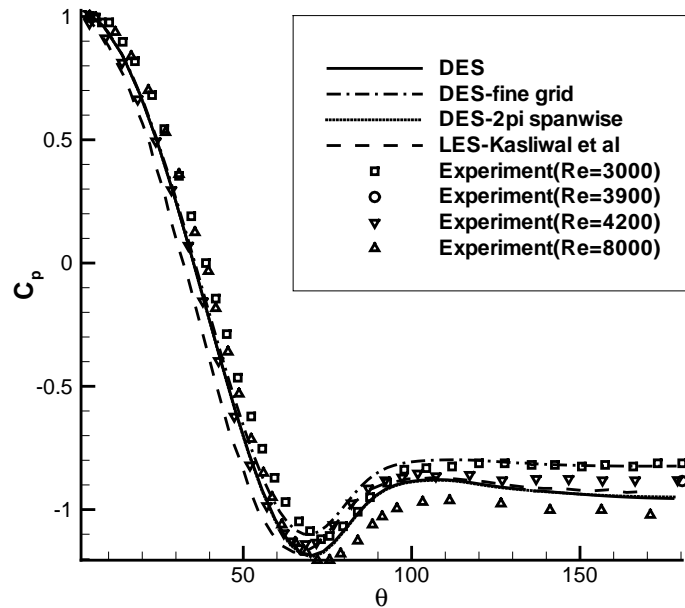
Figure 6.10: Mean pressure coefficient variation on the surface of the cylinder
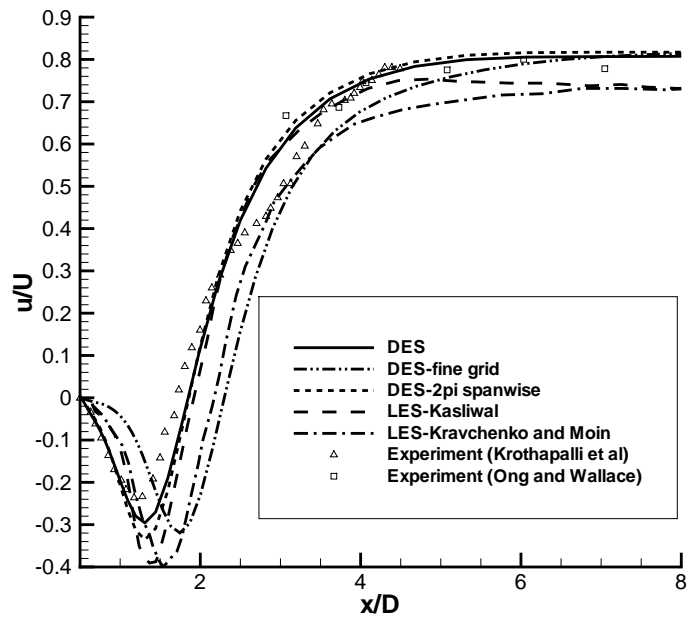
Figure 6.11: Streamwise velocity in the wake at y/D=0
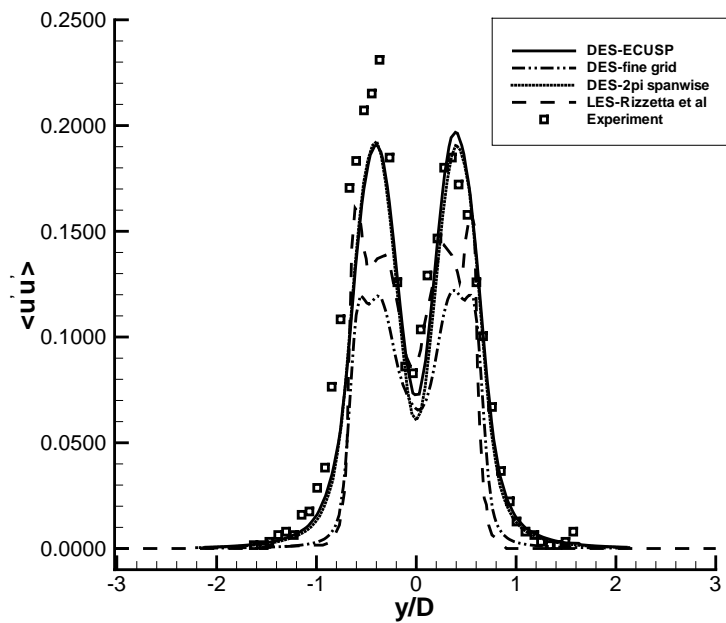
Figure 6.12: Streamwise Reynolds stress at x/D=1.54
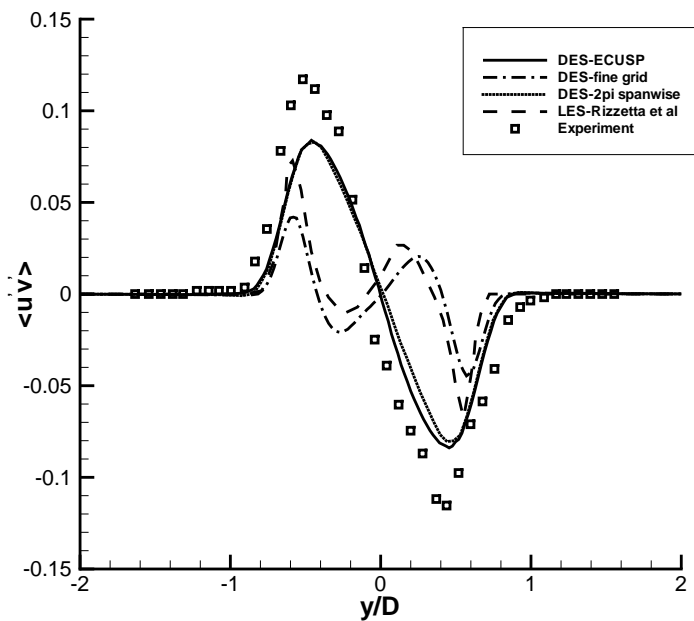
Figure 6.13: Shear Reynolds stress at x/D=1.54
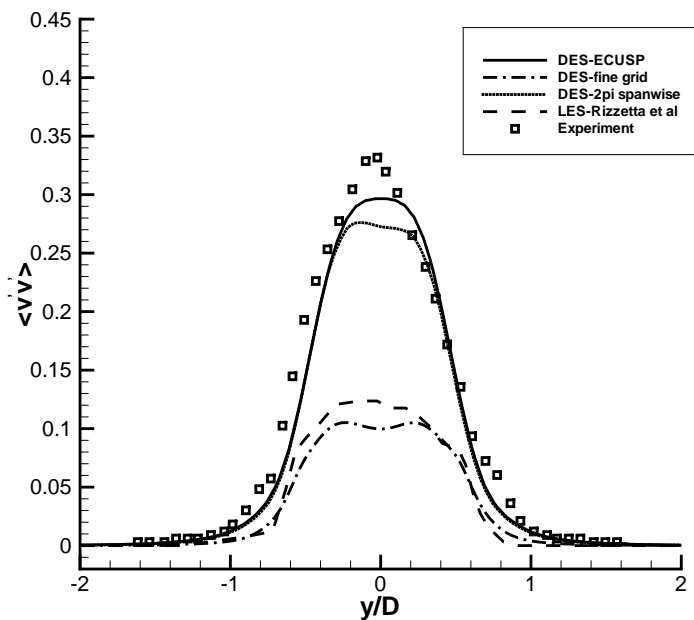
Figure 6.14: Lateral Reynolds stress at x/D=1.54
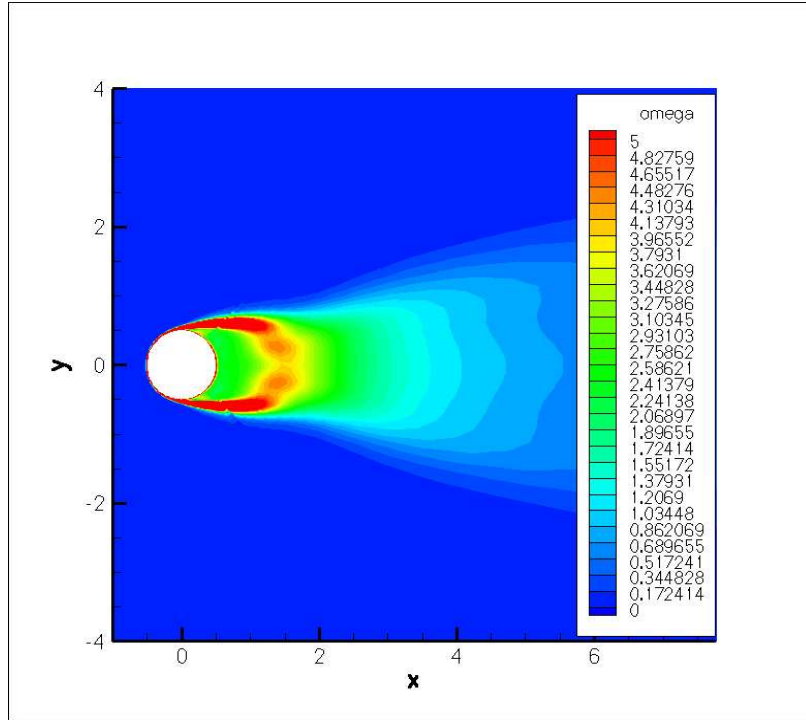
Figure 6.15: Contours of mean vorticity calculated on the baseline grid
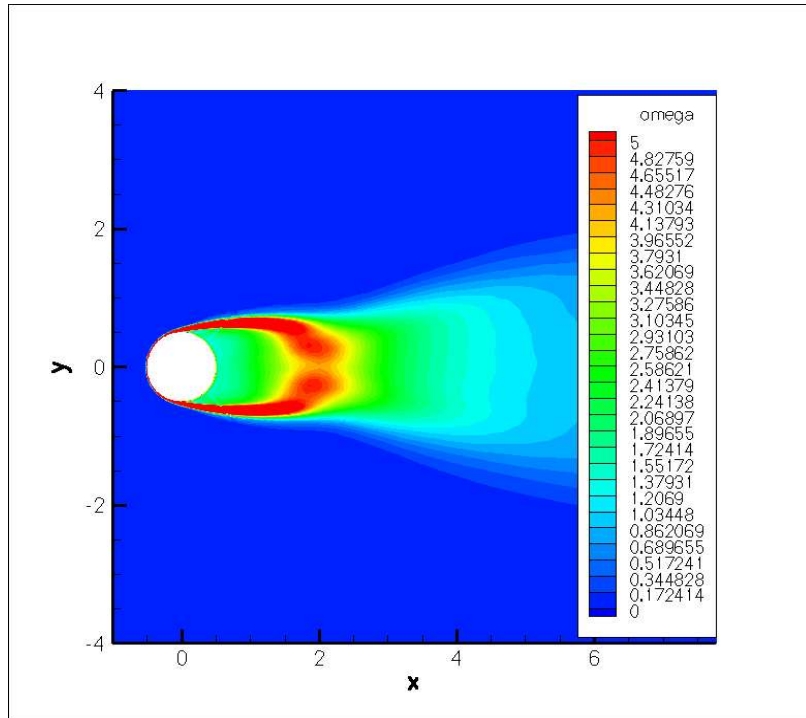
Figure 6.16: Contours of mean vorticity calculated on the refined grid
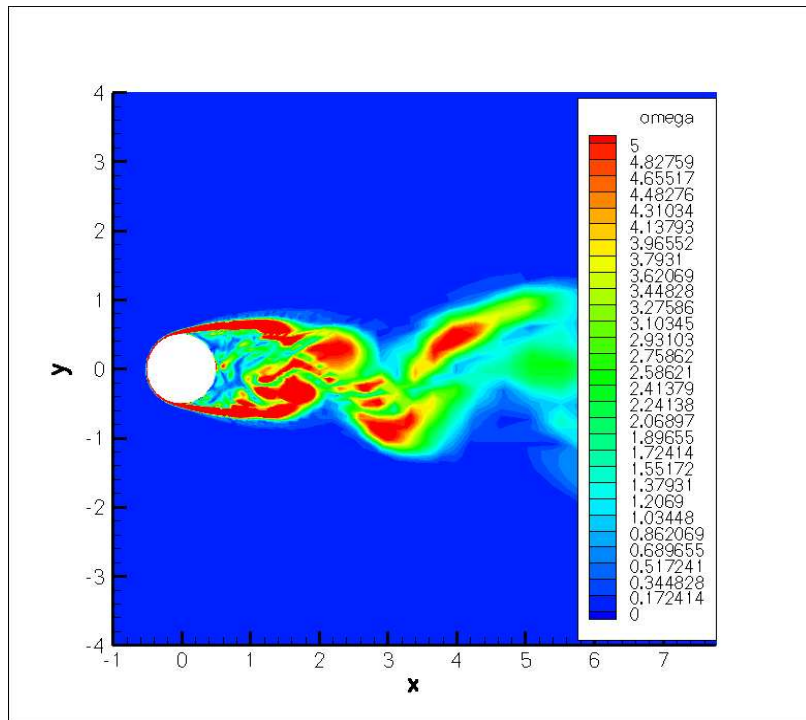
Figure 6.17: Contours of instantaneous vorticity at t=300T
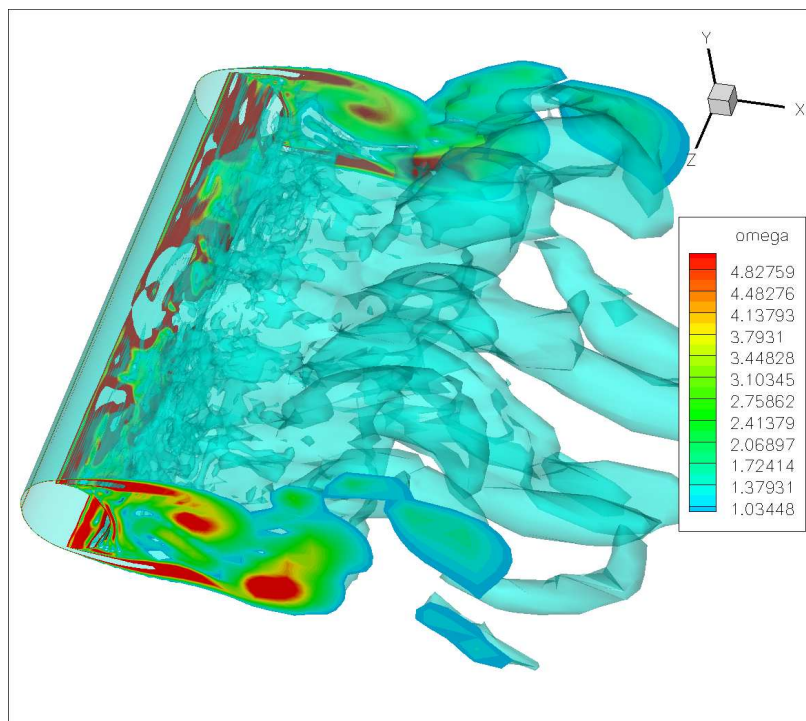
Figure 6.18: Overview of the contours of instantaneous vorticity at t=300T

Chapter 7

Validations of FSI Model

To validate the high order fully coupled FSI methodology developed in this research, the vortex induced vibration of a cylinder and a forced pitching airfoil are simulated.

7.1   Vortex-Induced Oscillating Cylinder

In this section, the vortex-induced oscillations of an elastically mounted circular cylinder is computed using the LDE and 5th order WENO scheme. The 4th-order fully conservative central differencing is employed for the viscous terms. The unsteady laminar Navier-Stokes equations and the linear structural equation are fully coupled implicitly via successive interaction with pseudo time stepping. The vortex-induced oscillation of 3D cylinder is simulated for the first time in this research.

7.1.1   2D Simulation

The stationary cylinder is simulated first to provide a initial flow field for the simulation of vortex-induced oscillating cylinder.

7.1.1.1 Stationary Cylinder

The mesh used for the computation of stationary cylinder and vortex-induced oscillating cylinder is shown in Fig. 7.1. The dimensions of the grid are 121×81. The free-stream Mach number is 0.2. The Reynolds number based on the diameter of the cylinder is 500. The laminar Navier-Stokes equations are solved because of the low Reynolds number.
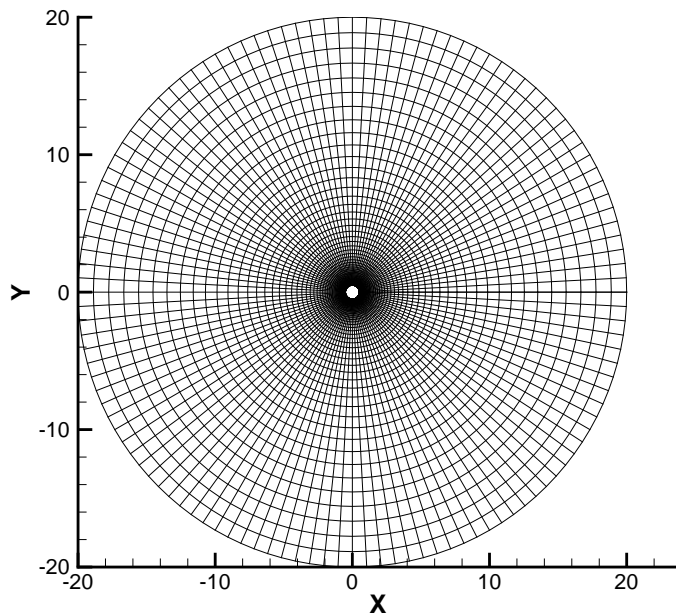
Figure 7.1: The computational grid of cylinder

The time history of the computed drag and lift coefficients is shown in Fig. 7.2. As shown in the figure, the lift oscillates at a frequency in terms of the Strouhal number St_{C_l}, which is in a good agreement with the experiments of Roshko and Goldstein [148, 149] as shown in table 7.1. The drag coefficient oscillates with twice that frequency, St_{C_d}. The computed results using this baseline mesh are in good agreement with the results using refinement mesh in Ref. [33] as indicated in table 7.1. The reason is that the fifth-order WENO and newly developed LDE schemes have better accuracy. Table 7.1 shows the comparison.

Fig. 7.3 and Fig. 7.4 show the vorticity contours around the stationary cylinder with the

Table 7.1: Comparison of computed results with the experiments

Mesh dimension	St_{C_d}	St_{C_l}	$C_l max$	$C_d ave$
120×80	0.4496	0.2248	1.1822	1.4658
120×80 [33]	0.4395	0.2197	1.181	1.453
200×120 [33]	0.4516	0.2246	1.227	1.484
384×96 [28]	0.4674	0.2331	1.149	1.315
(Roshko 1954 [148])		0.2075		
(Goldstein 1938 [149])		0.2066		
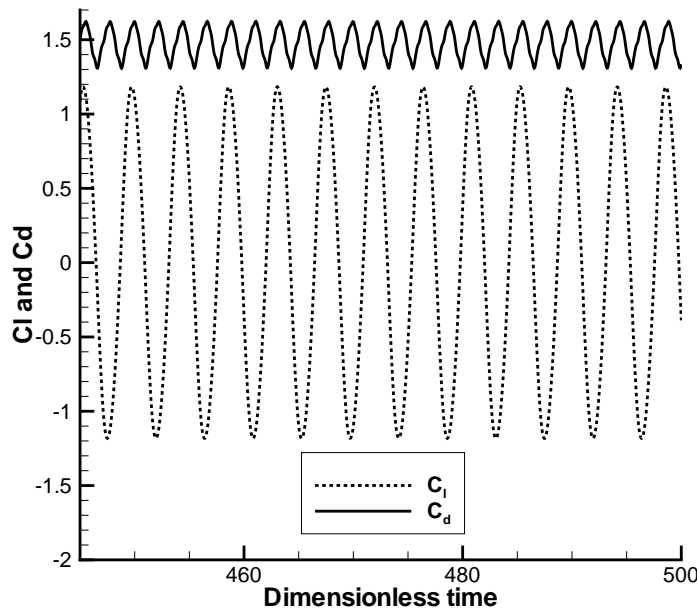
Figure 7.2: Time history of the lift and drag of the stationary cylinder

largest and smallest lift coefficients respectively. The vortex shedding is clearly simulated in these figures.

7.1.1.2   Vortex Induced Oscillating Cylinder

The motion of the elastically mounted cylinder is controlled by the governing equation described in section 2.3.1. The flow conditions for this oscillating cylinder are the same as those used for the stationary cylinder. The reduced velocity is determined by *St* number:
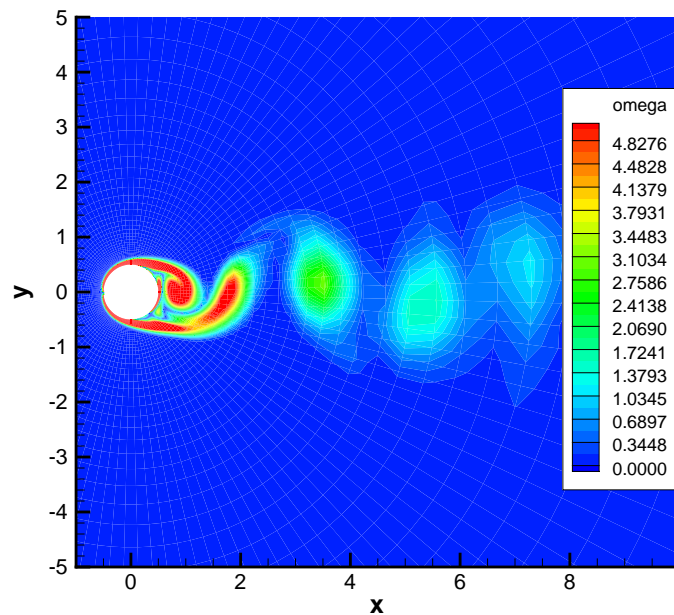
Figure 7.3: Vorticity contours of the stationary cylinder with the largest lift coefficient
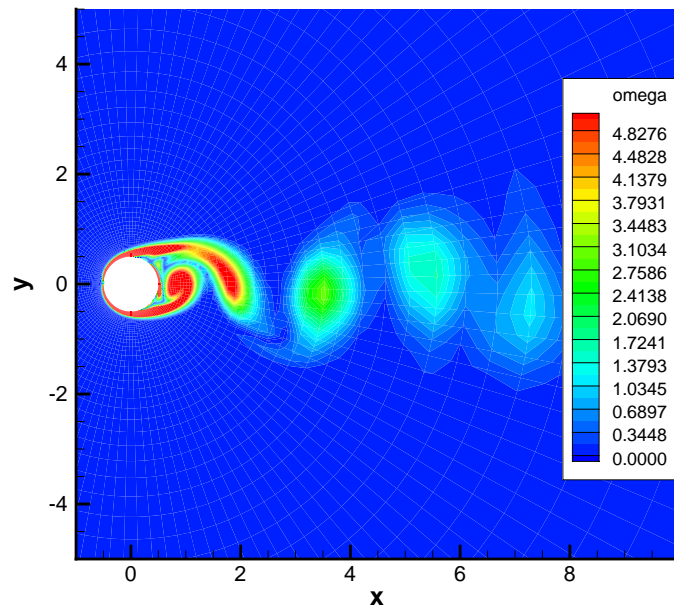
Figure 7.4: Vorticity contours of the stationary cylinder with the smallest lift coefficient

$\bar{u} = \frac{1}{\pi St}$. In the present computation, the St number is set to be 0.2, corresponding to $\bar{u} =$ 1.5915. The mass ratio, μ_s is 12.7324. The damping ratio, ζ is 0.1583. The dimensionless physical time step of 0.05 is used.

The time history of the computed lift and drag coefficients shown in Fig. 7.5 indicates that the averaged drag coefficient is larger than that of the stationary cylinder. It means the motion of a cylinder enlarges the drag coefficient. The amplitude of the drag coefficients is also enlarged due to the motion. On the contrary, the amplitude of the lift coefficients is decreased because of the motion.

The trajectory of the central point of the cylinder is shown in Fig. 7.6. The trajectory is similar to the results computed by [150] and [28].

Fig. 7.7 and Fig. 7.8 show the vorticity contours around the oscillating cylinder with the positive and negative peak lift coefficients respectively. It can be seen that the vortexes keep their coherent shedding pattern similar to the one simulated around the stationary cylinder because the displacement is small. With the increase of the displacement, the vortex shedding pattern will become more and more irregular [33].
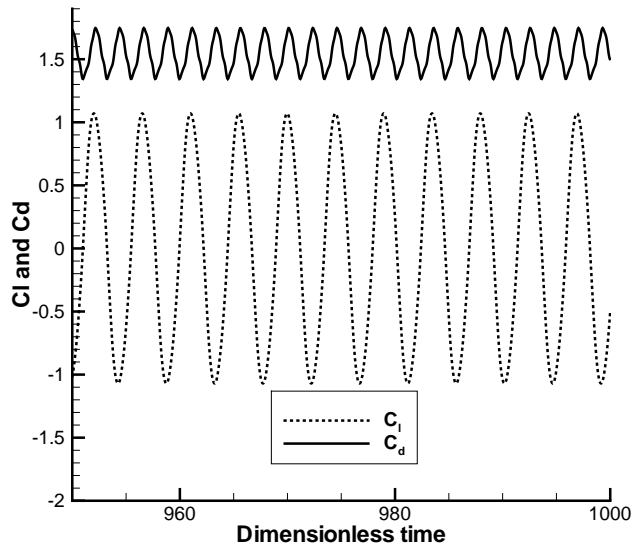
Figure 7.5: Time history of the lift and drag of the oscillating cylinder
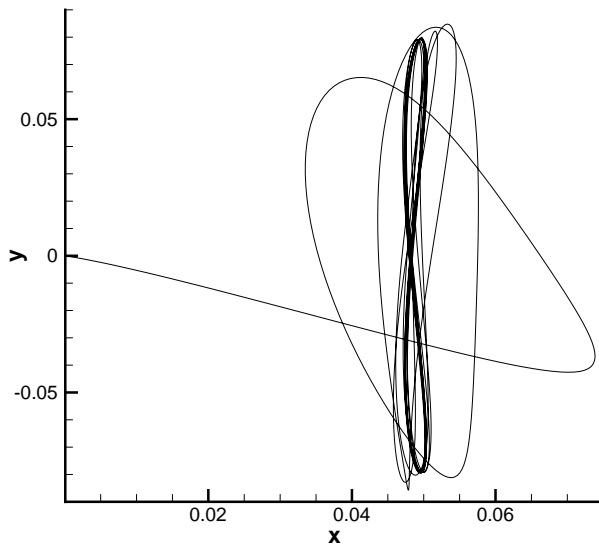
Figure 7.6: Time history of the displacement of the oscillating cylinder
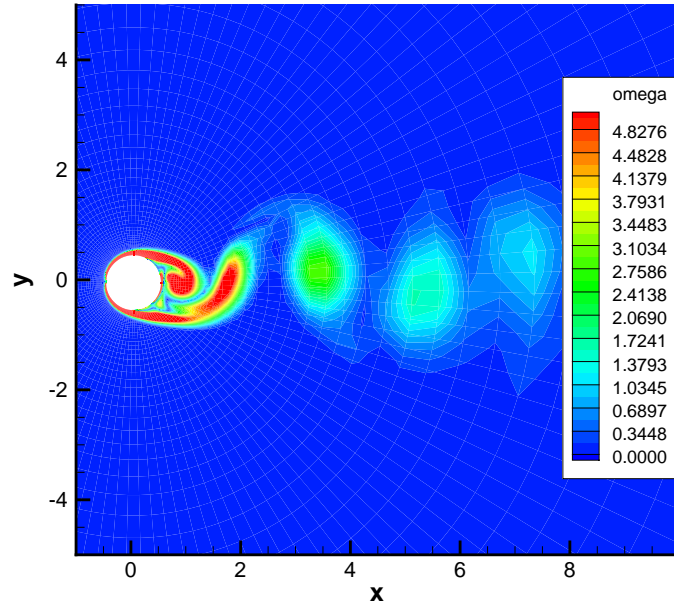
Figure 7.7: Vorticity contours of the oscillating cylinder with the largest lift coefficient

7.1.2   3D Simulation

The 3D cylinder and mesh is obtained by simply extending 2D cylinder and mesh to one diameter long in spanwise direction (see Fig. 7.9). The dimensions of the grid are
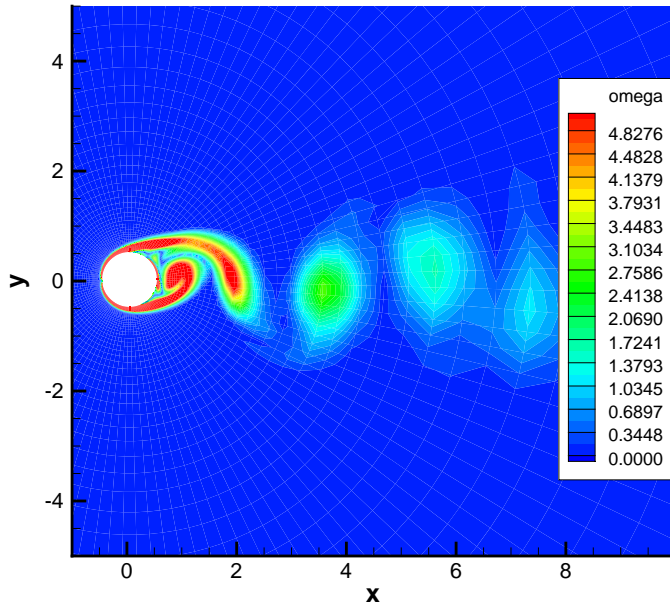
Figure 7.8: Vorticity contours of the oscillating cylinder with the smallest lift coefficient

$121 \times 81 \times 11$. The same 2D structural equations given in section 2.3.1 is employed in 3D computation. The unsteady lift and moment coefficients are integrated from the 3d unsteady flow fields. To compare with the 2D results, the same flow and structure parameters are use in the 3D computation.

7.1.2.1 Stationary Cylinder

Fig.7.10 plots the time history of the computed lift and drag coefficients. The comparison of results for 2D and 3D computation is shown in table 7.2. They indicate that the computed Strouhal number of 3D is slightly better than those of 2D when compared with the experiments [148, 149]. Both lift and averaged drag coefficients are slightly decreased compared with the 2D results.

The vorticity contours around the stationary cylinder with the positive and negative peak lift coefficients are shown in Fig. 7.11 and Fig. 7.12 respectively. The coherent vortex shedding pattern is the same as the 2D case.
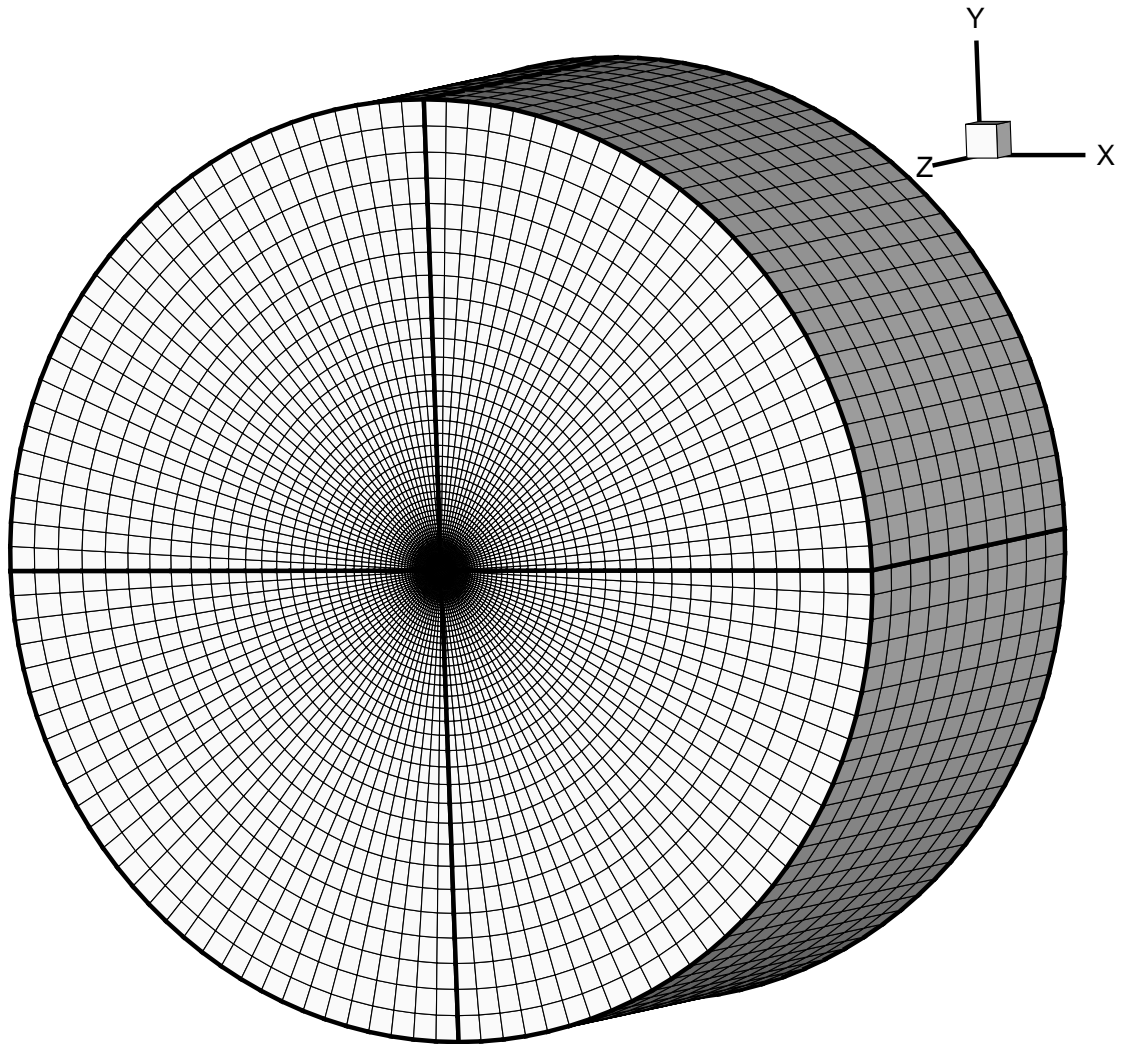
Figure 7.9: The computational grid of 3D cylinder

7.1.2.2 Oscillating Cylinder

As shown in Fig. 7.13, the amplitude of lift coefficients caused by the oscillating cylinder is dramatically decreased compared with stationary cylinder results. Different from the 2D case, the cylinder motion in 3D has a smaller effect on the drag coefficients. Fig. 7.14 plots the time history of cylinder displacement and the amplitude is smaller than that of the 2D case.

Fig. 7.15 and Fig. 7.16 show the vorticity contours of the oscillating cylinder with the

Table 7.2: Comparison of results for 2D and 3D computation

	St_{C_d}	St_{C_l}	$C_l max$	$C_d ave$
2D computation	0.4496	0.2248	1.1822	1.4658
3D computation	0.4422	0.2211	1.0585	1.4294
(Roshko 1954 [148])		0.2075		
(Goldstein 1938 [149])		0.2066		
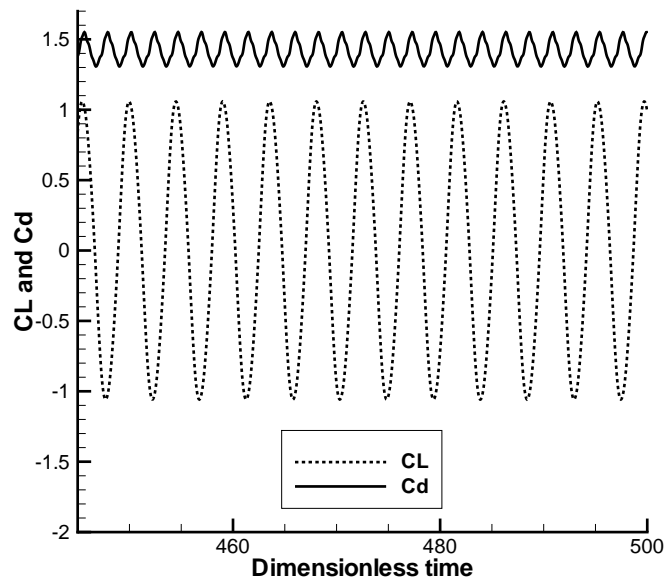
Figure 7.10: Time history of the lift and drag of the stationary cylinder

high and low peak lift coefficients respectively. Same as the 2D case, the vortexes keep their coherent shedding pattern similar to the one obtained for the stationary cylinder.
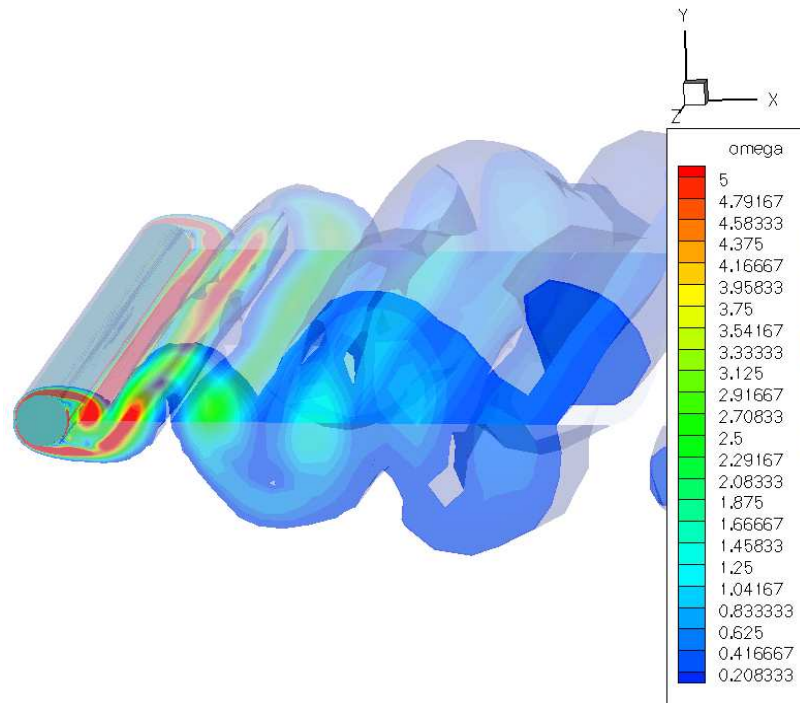
Figure 7.11: Vorticity contours of the stationary cylinder with the largest lift coefficient
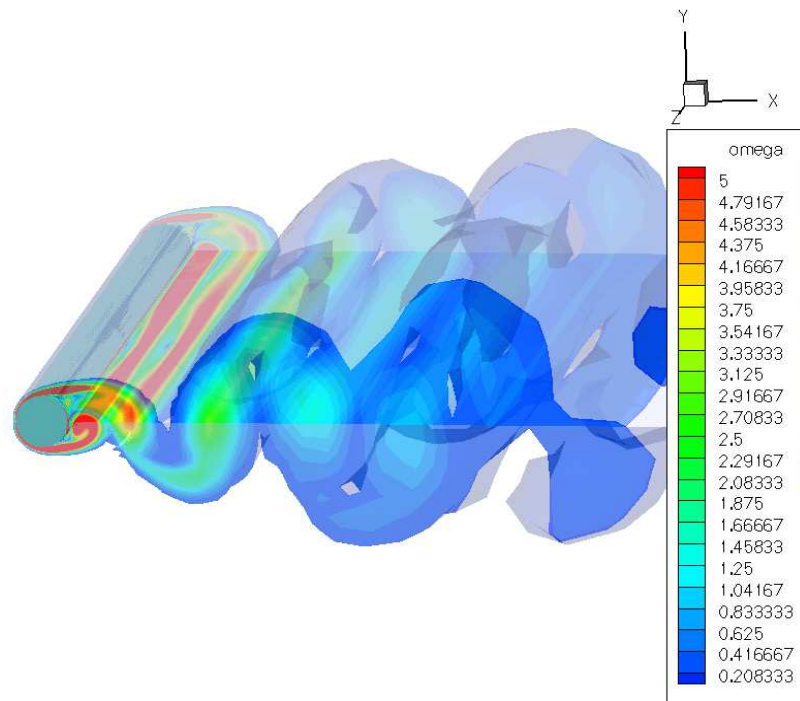
Figure 7.12: Vorticity contours of the stationary cylinder with the smallest lift coefficient
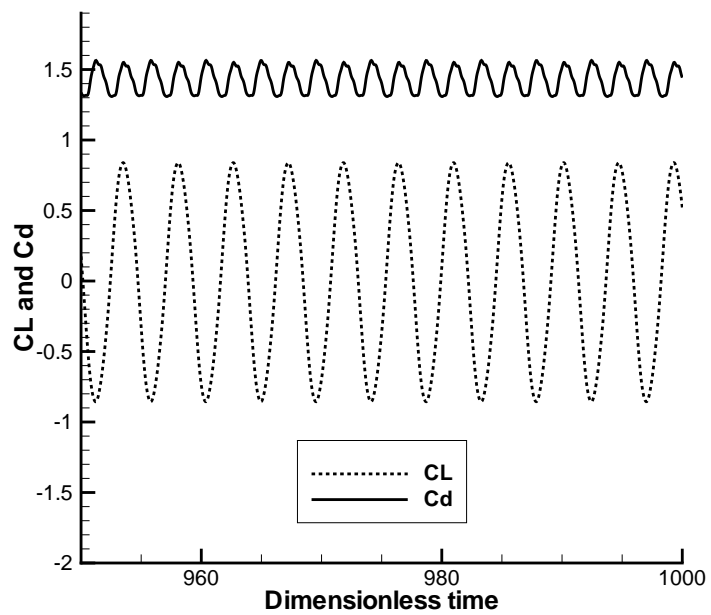
Figure 7.13: Time history of the lift and drag of the oscillating cylinder
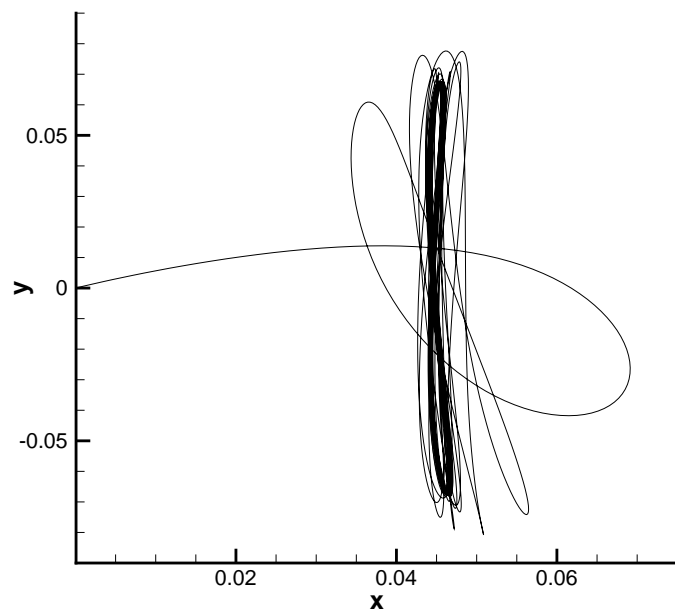
Figure 7.14: Time history of the displacement of the oscillating cylinder
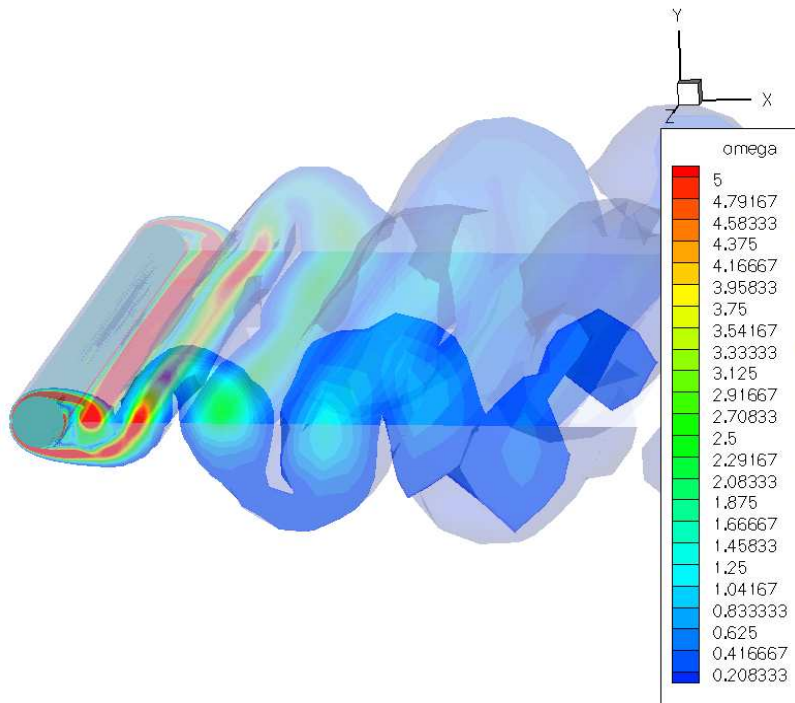
Figure 7.15: Vorticity contours of the oscillating cylinder with the largest lift coefficient
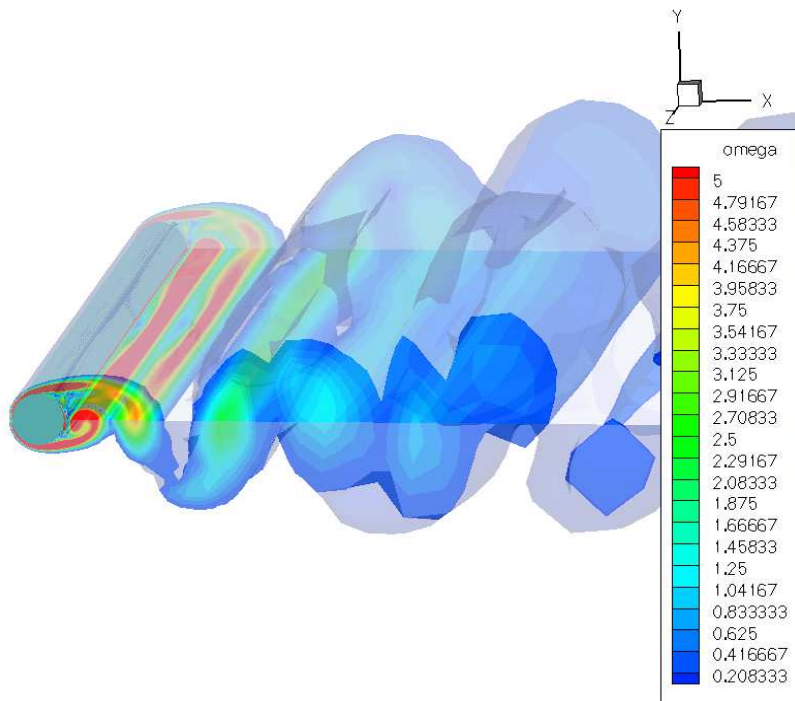
Figure 7.16: Vorticity contours of the oscillating cylinder with the smallest lift coefficient

7.2   Forced Pitching Vibration of NACA 64A010 Airfoil

As a validation case of DES for fluid-structural interaction, a forced pitching airfoil, NACA64A010 is calculated. The NACA64A010 airfoil is selected as the validation case because the experimental data are available. The forced pitching airfoil is simulated first using 2D RANS.

7.2.1   2D Simulation Using RANS

For this transonic airfoil, an O-type grid is generated with the dimensions of 281×66 (see Fig. 7.17).
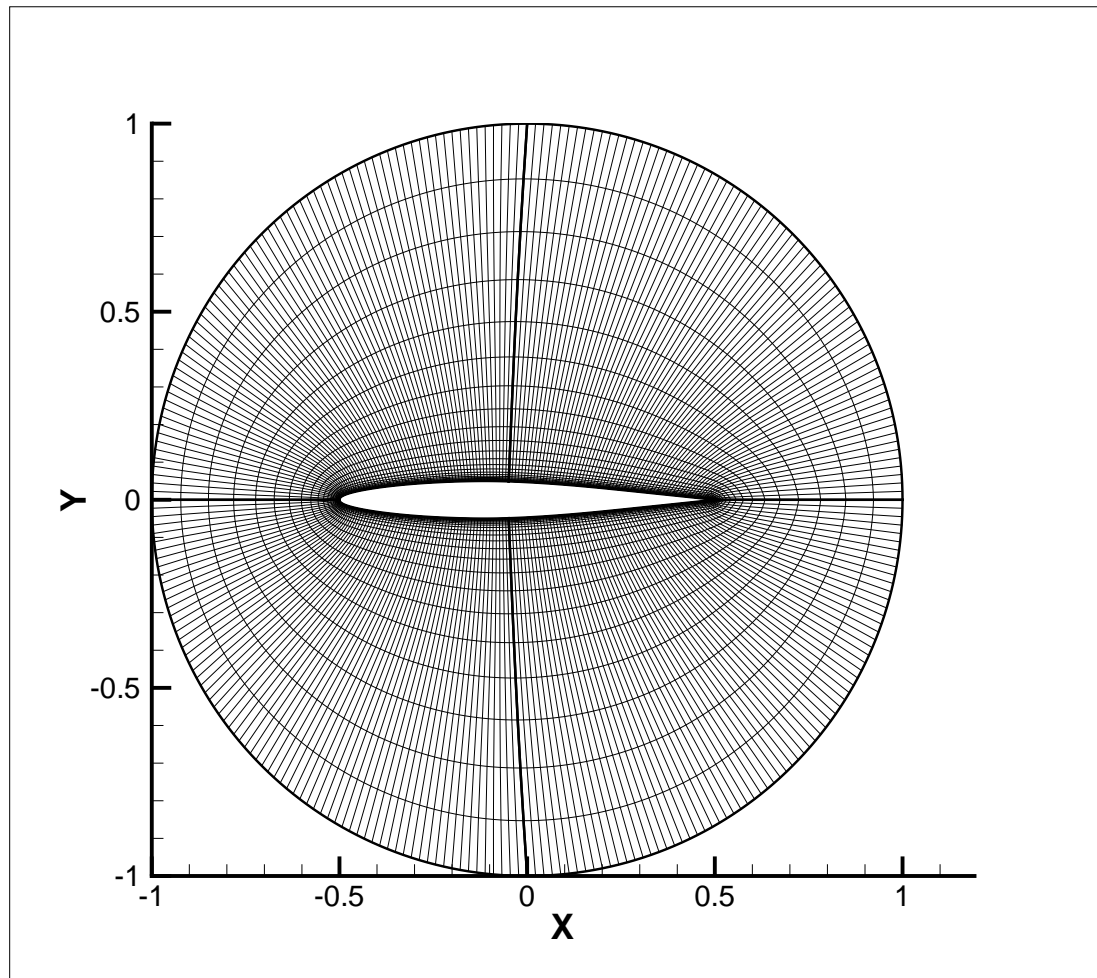
Figure 7.17: The computational grid of NACA64A010 airfoil

The airfoil is forced in pitch about its quarter chord sinusoidally. The airfoil oscillation

is defined by a function of the time dependent variation of its AoA,

$$\alpha(t) = \alpha_0 + \alpha_A \sin(\omega t) \tag{7.1}$$

where $\alpha(t)$ is the time dependent AoA. α_0 is the mean of the oscillating angle. α_A is the amplitude of the oscillating angle. ω is the angular frequency, which is directly related to the reduced frequency

$$k_c = \frac{\omega C}{2U_\infty} \tag{7.2}$$

where C is the chord of the airfoil, and U_∞ is the free-stream velocity.

To be consistent with the experiment, the following primary parameters are employed in the unsteady calculation: $\alpha_0 = 0$, $\alpha_A = 1.01°$, Reynolds number (based on chord), $Re = 1.256 \times 10^7$, free-stream Mach number, $M_\infty = 0.8$, reduced frequency, $k_c = 0.202$. The computation begins with a uniform flow field of free stream at $0°$ AoA. The dimensionless time step is $\Delta t = 0.05$.

Fig. 7.18 shows the lift coefficients varying with the AoA after the flow field reaches its temporally periodic solution. The computed lift coefficients agree well with the experiment [151]. Fig. 7.19 shows the moment coefficients varying with the AoA. The agreement of the moment coefficient is not as good as that of the lift coefficient. However, the agreement in the current results is better than the recent result computed by McMullen et al. in 2002 [152]. The discrepancy between the computation and the experiment in the moment coefficient may be caused by the inadequacy of the shock/turbulence boundary layer interaction, which may not predict the surface friction accurately.
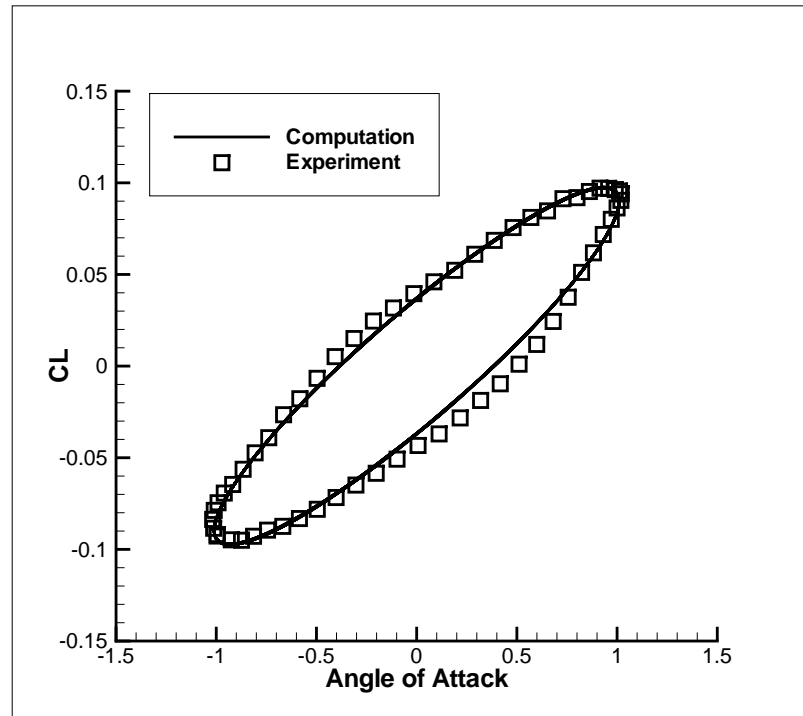
Figure 7.18: Comparison of computed lift coefficient with experimental data for the forced pitching airfoil
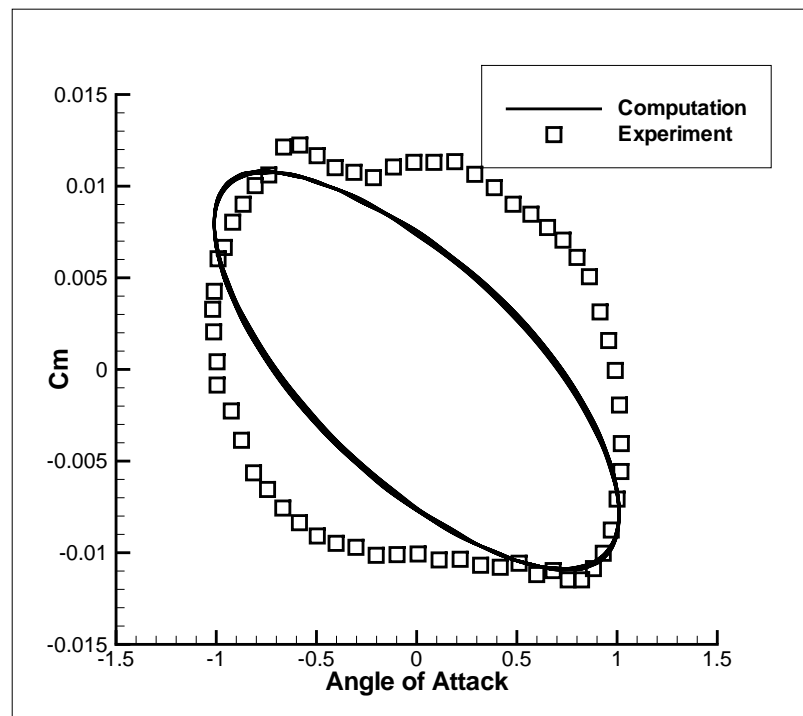
Figure 7.19: Comparison of computed moment coefficient with experimental data for the forced pitching airfoil

Chapter 8

DES of Fluid-Structural Interaction

This chapter simulates NLR7301 airfoil limit cycle oscillation (LCO) caused by fluid-structural interaction (FSI) using DES method. As a validation case, the forced pitching NACA64A010 airfoil is simulated firstly. Then the 2D NLR7301 airfoil limit cycle oscillation (LCO) is simulated using RANS method. Finally, the 3D NLR7301 airfoil LCO is simulated using DES method. The low diffusion E-CUSP (LDE) scheme with 5th order weighted essentially non-oscillatory scheme (WENO) is employed to calculate the inviscid fluxes. The fully conservative 4th order central differencing is used for the viscous terms. The fully coupled fluid-structural interaction model is employed in all the cases.

8.1   Validation for Forced Pitching Airfoil

A DES validation is conducted to simulate the fluid-structural interaction of the forced pitching NACA64A010 airfoil. Since DES must be 3D for LES of turbulence, the airfoil is extended in spanwise direction. An O-H-type is generated with the dimensions of $281 \times 66 \times 49$ (see Fig. 8.1). The spanwise length extended is 4 times of the chord length of the airfoil. The forced pitching equation and parameters are the same as those used in the 2D computation described in section 7.2.1.

Fig. 8.2 shows the lift coefficients varying with the AoA after the 3D flow field reaches
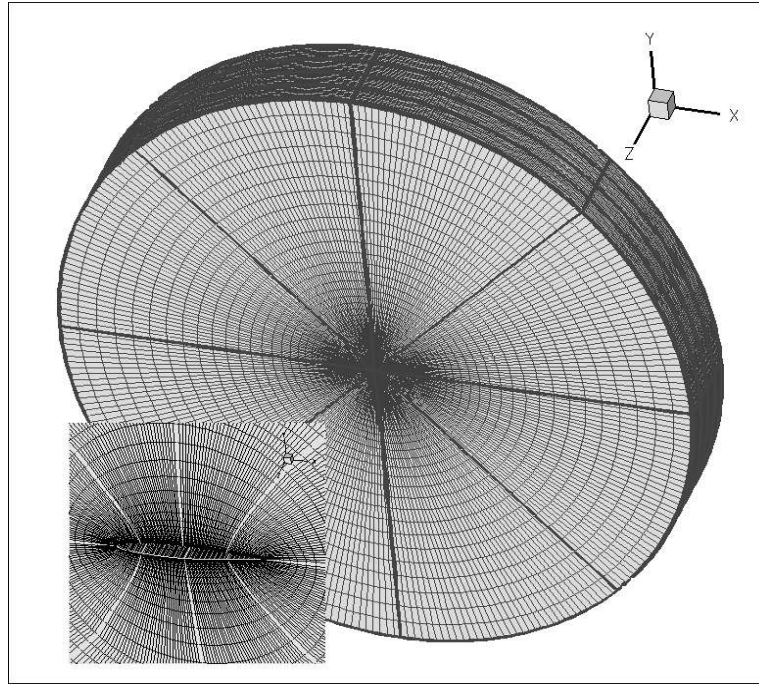
Figure 8.1: The computational grid of NACA64A010 airfoil

its temporally periodic solution. The computed lift coefficients using DES agree very well with the experiment.

Fig. 8.3 shows the moment coefficients varying with the AoA. The computed moment coefficients using DES have a deviation compared with the experiment. The discrepancy between the computation and the experiment in the moment coefficient may be caused by the inadequacy of the shock/turbulence boundary layer interaction, which may not predict the surface friction accurately

Since there are no separations in the flow field, the lift and moment using DES can be considered as the spanwise-averaged values. Thus, the lift and moment using DES are almost the same as those using RANS in section 7.2.1.

8.2 Limit Cycle Oscillations of NLR7301 Airfoil Using RANS

In this section, the fluid-structural interaction of the elastically mounted NLR7301 airfoil is simulated by using RANS with S-A one equation model. The RANS simulation is to
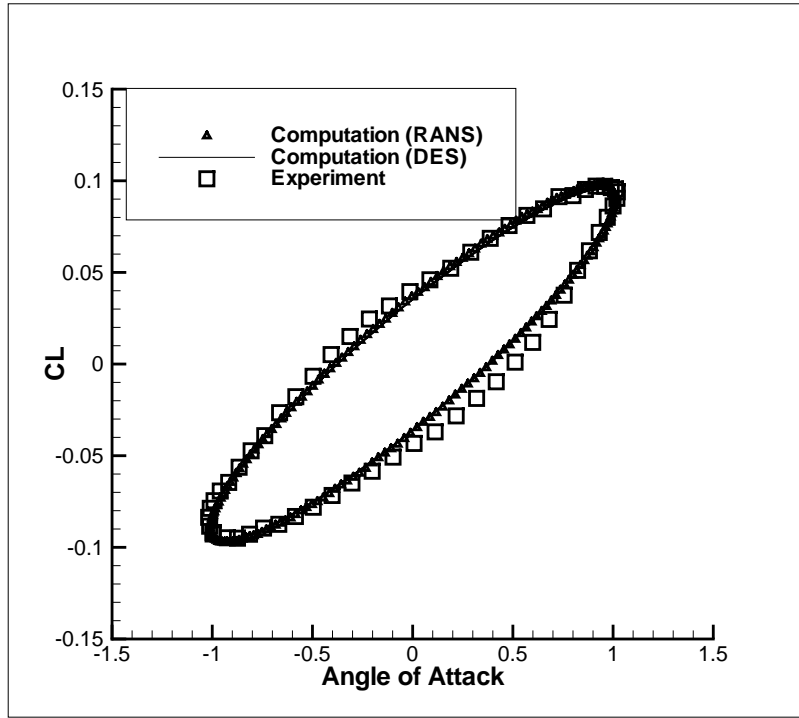
Figure 8.2: Comparison of computed lift coefficient with experimental data for the forced pitching airfoil

search the initial condition to match the experimental LCO. The initial condition is then used for DES to save CPU time.

The case simulated is the test case No.77 [40, 41, 153] of NLR7301 airfoil. The chord length of the airfoil is $0.3m$ and the mean angle of attack is $1.28°$. The experimental conditions are at a free-stream Mach number of 0.768 and a Reynolds number of 1.727×10^6 based on the chord length. The experiment was conducted at a total pressure of $p_t = 0.45$ bar and a dynamic pressure of $p_{dyn} = 0.126$ bar.

The elastically mounted NLR7301 airfoil has two degree of freedom, plunge and pitch. The structural motion equation are given in section 2.3.2.

The non-dimensional structural parameters used for the computation of fluid-structural interaction are summarized in table 8.1

For numerical simulation, there are several initial conditions affecting LCO: free stream Mach number, initial AoA and α_0. The present research investigates the effects of these initial conditions and finds the optimum values of them that generate the LCO matching
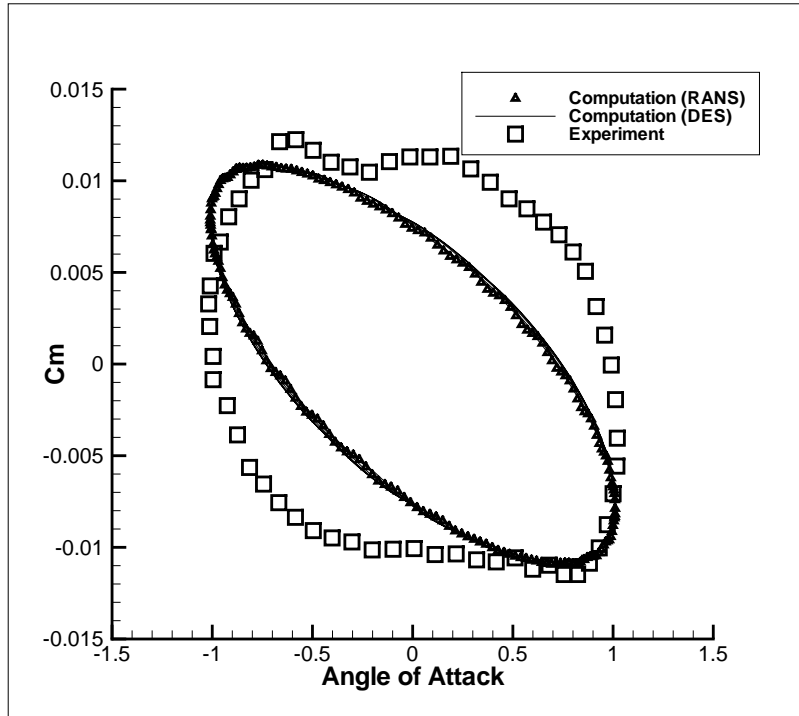
Figure 8.3: Comparison of computed moment coefficient with experimental data for the forced pitching airfoil

Table 8.1: The non-dimensional structural parameters used for computation

Mach number	x_α	r_α	δ_α	δ_h	μ	ω_α	ω_h
0.768	0.0484	0.197	0.0041	0.0073	942	0.31988	0.24306
0.753	0.0484	0.197	0.0041	0.0073	942	0.32625	0.24790

best with the experiment. Two different procedures are used to simulate the LCO.

Procedure 1

The first procedure follows the criterion used by Weber et al. [39] and Tang et al. [2], in which, both free stream Mach number and initial AoA are adjusted to match the computed steady state surface pressure distribution with experiment as much as possible. The obtained Mach number and AoA are then used in the LCO simulation by adjusting the α_0 until the computed time-averaged AoA is close to the obtained AoA of the steady state computation.

Procedure 2

The second procedure is developed in the present research, in which the free stream Mach number is fixed and the α_0 as well as initial AoA both are iterated to match the experimental LCO amplitudes. The resulted time-averaged lift and moment are also taken into account to compare with the experiment.

All simulations are conducted on an MPI based computer cluster with parallel computation. The parallel computation is performed by the high efficiency parallel computing algorithm described in Chapter 5 [134].

8.2.1 Steady State Flow Computation

The baseline grid is a single block O-type grid with grid dimensions of 193×97 and is equally partitioned into 16 sub-blocks with 8 blocks in the circumferential direction and two blocks in radial direction as shown in Fig. 8.4. The dimensions of each sub-domain is 25×49.
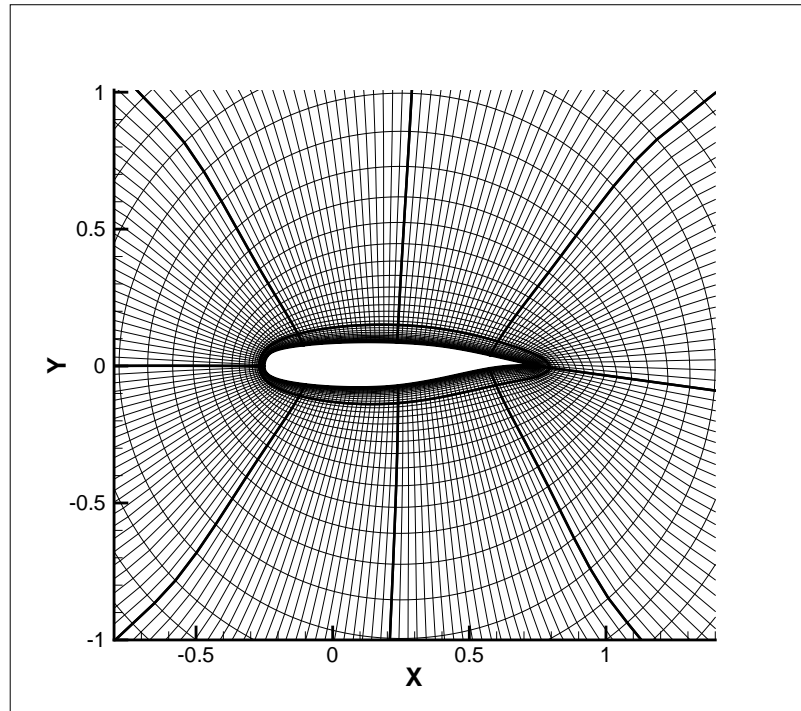
Figure 8.4: The computational grid of NLR7301 airfoil

The steady state computations are conducted first to search for the flow conditions that match the computed pressure distribution best with the experiment. Both the widely used Mach number of 0.753 for CFD [2, 39] and the experimental Mach number of 0.768 are simulated. It is found that the steady state surface pressure agrees best with experiment at $AoA = -0.45°$ for Mach 0.753 and at $AoA = -0.2°$ for Mach 0.768. However, both cases have some discrepancy with the experiment. Fig. 8.5 shows the surface pressure distribution for the two cases. For the case of Mach number 0.753, the shock location at suction surface agrees better with the experiment, whereas for the Mach 0.768, the shock location at pressure surface agrees better. Overall, the computed case with the experimental Mach number of 0.768 is closer to the experiment upstream and downstream of the shocks.

The mesh refinement is performed for the steady state case at Mach 0.768 to confirm that the baseline mesh is sufficient to be used for unsteady LCO simulation. The baseline mesh is refined in both directions with the mesh size increased by 4 times to 385×193. As shown in Fig. 8.5, the computed surface pressure distributions between the baseline and refined mesh have little difference, except that the refined mesh has sharper shock profile due to the denser mesh.

8.2.2 2D LCO Simulation

The first series of LCO search use the procedure 1 at $Mach = 0.753$ and $AoA = -0.45°$, which are the conditions used by the research groups of Weber et al. and Tang et al. [2, 39]. The LCO computation is conducted by adjusting α_0, the off-wind value of α to make the time-averaged AoA agree with $AoA = -0.45°$. The LCO computation is conducted using two different initial flow fields to investigate the effects of initial flow and perturbation. One initial field is the solution of the steady state computation. The other initial field is the uniform free stream flow. Both LCO computations start at $AoA = 0°$. The dimensionless physical time step of 0.01 is used which is defined as $t_c = t/(c/u_\infty)$. t is the physical time. Fig. 8.6 and 8.7 show the computed LCO amplitudes at Mach number of 0.753 and α_0 of 0.25°. Both initial fields predict the final LCOs with about the same amplitudes
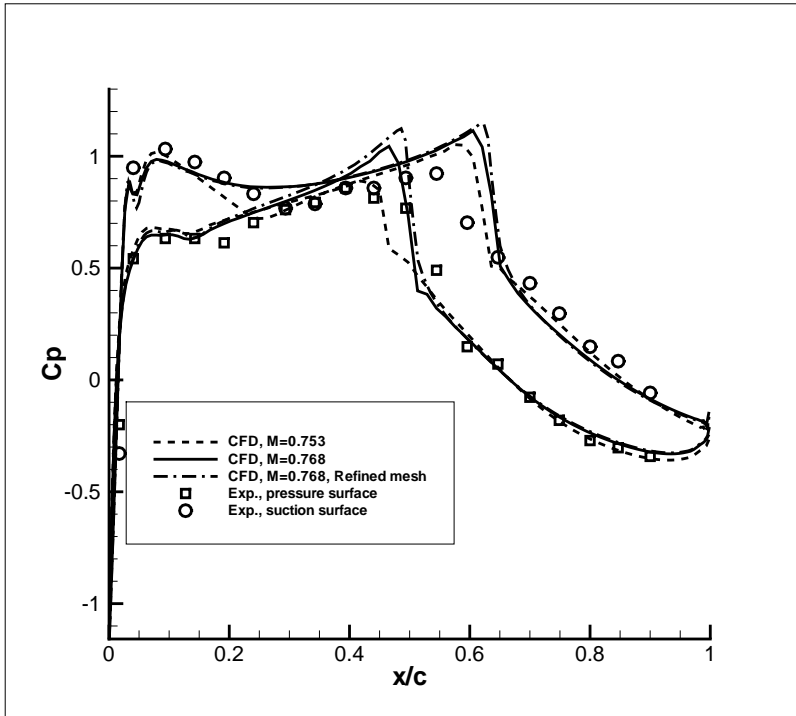
Figure 8.5: Pressure coefficient distribution on the surface of NLR7301 airfoil

even though the transition period is different. Fig. 8.8 and 8.9 plot the lift and moment coefficients respectively. The convergence history within a typical physical time step is shown in Fig. 8.10.

The second series of LCO search use the procedure 2 at the Mach 0.753. The LCO is conducted by iterating α_0 and initial AoA to match the measured LCO amplitudes as close as possible.

Table 8.2 lists all the trail iteration cases at Mach 0.753. Case A shows the computed results using procedure 1. Case B to Case F show the computed results with the initial field setup as uniform free stream at the different AoA and α_0 using procedure 2.

It can be seen from Table 8.2 that the Case A matches the lift and moment coefficients best with the experiment among all the cases. However, the predicted LCO amplitudes are an order of magnitude higher than the experiment, just like all other cases.

Table 8.2 indicates that both AoA and α_0 have influence on the amplitudes of LCO. However, the computation is not able to match the amplitudes by adjusting AoA and α_0
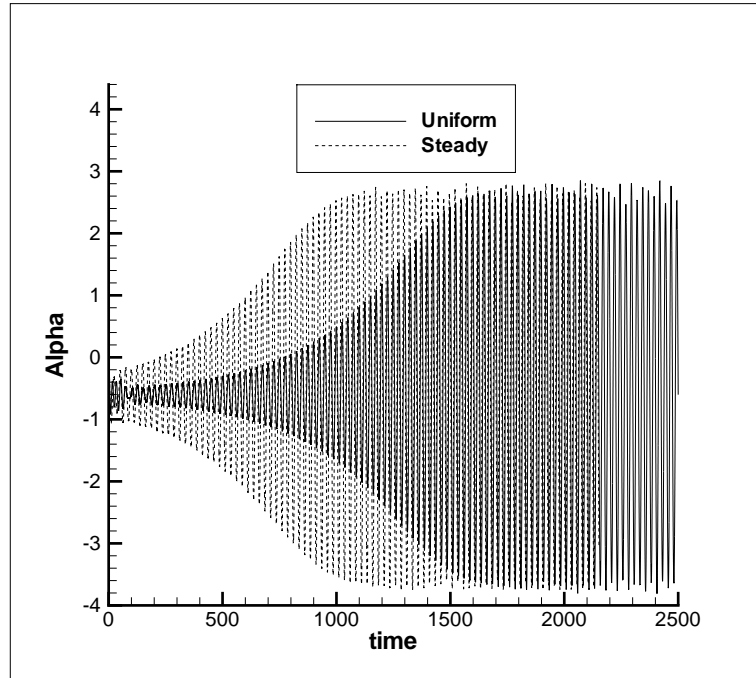
Figure 8.6: Pitch motion predicted by RANS ($M = 0.753, AoA = -0.45°$)
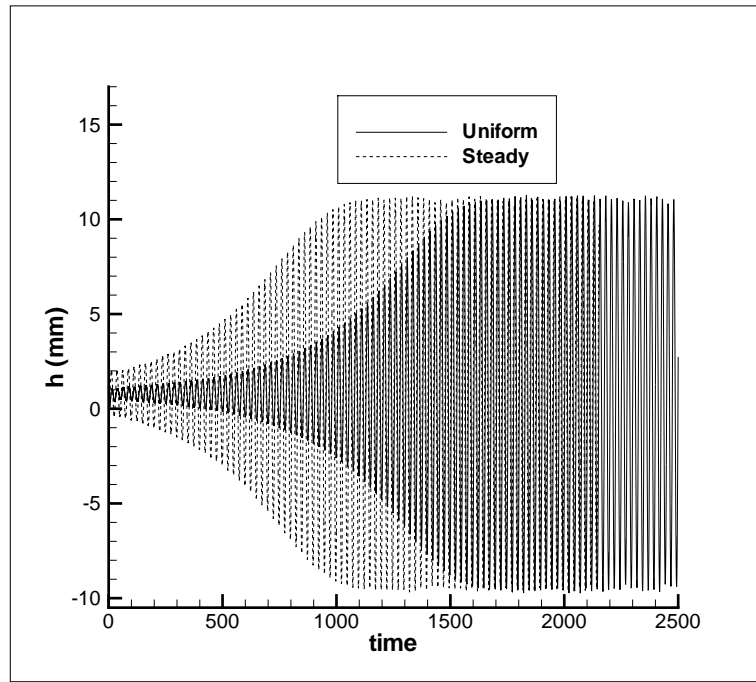
Figure 8.7: Plunge motion predicted by RANS ($M = 0.753, AoA = -0.45°$)

due to the Mach number that is different from the experiment.

Fig. 8.11 shows the contours of Mach number labeled from (a)-(j) with the interval of
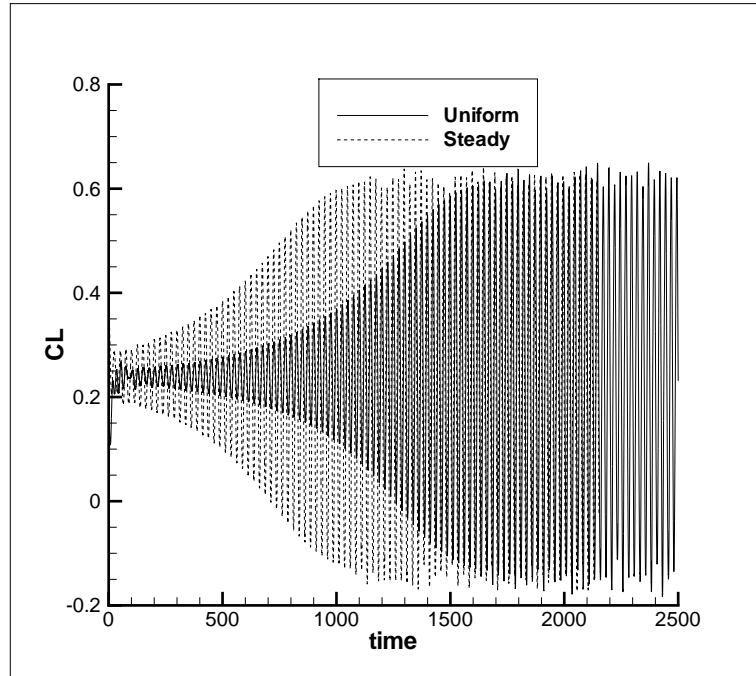
Figure 8.8: Lift coefficient predicted by RANS ($M = 0.753, AoA = -0.45°$)
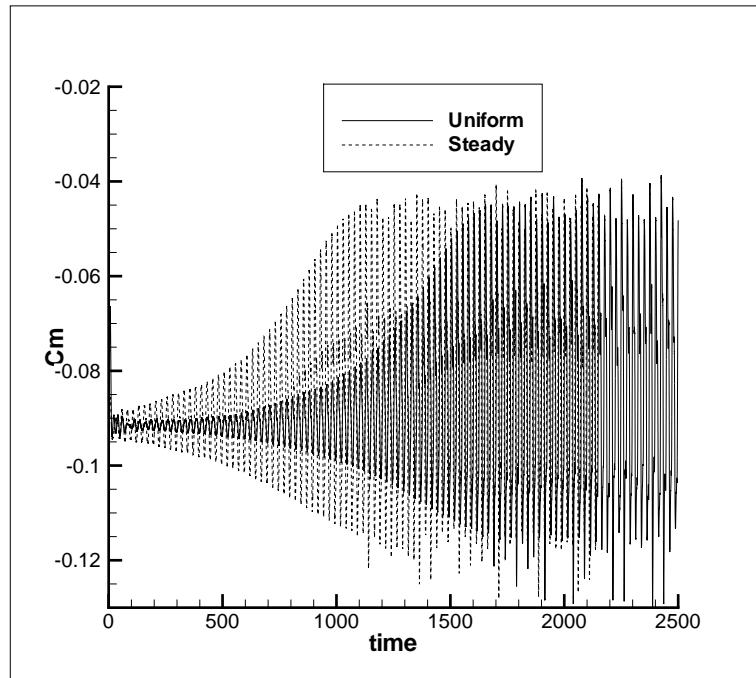
Figure 8.9: Moment coefficient predicted by RANS ($M = 0.753, AoA = -0.45°$)

1/10 of a cycle for Case E, which has the smallest amplitudes in all the cases at the Mach number 0.753. Fig. 8.12 and Fig. 8.13 plot the corresponding positions of (a) to (j) in
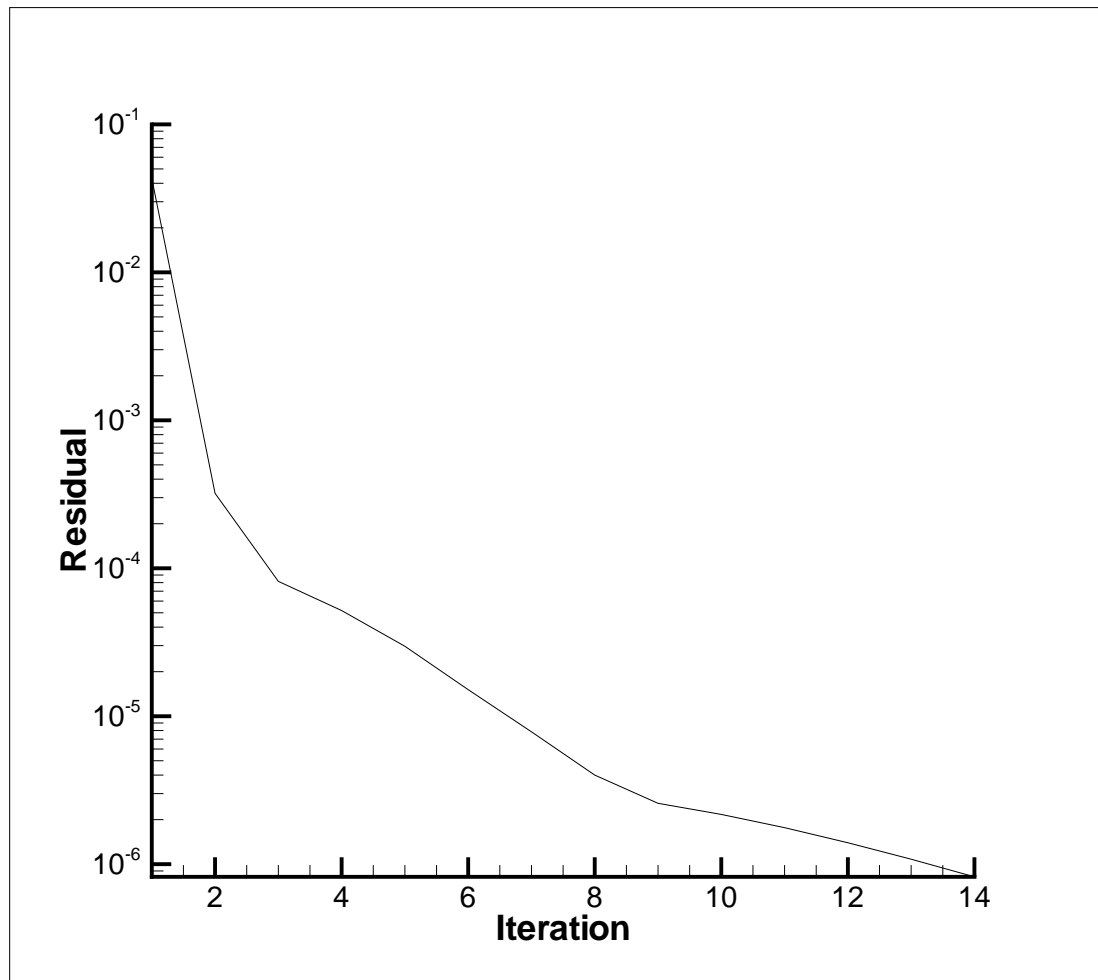
Figure 8.10: Convergence history within a typical physical time step for $M = 0.768$

Table 8.2: Comparison of the test cases at $M = 0.753$

NLR7301 LCO	Initial AoA	α_0°	Lift Coef.	Moment Coef.	$h(mm)$	α°
Case A	0.0	0.25	0.2318	-0.0800	10.134	3.1942
Case B	0.0	0.60	0.2944	-0.0744	9.6768	2.9796
Case C	0.0	0.75	0.3180	-0.0756	8.6943	2.6921
Case D	0.0	0.85	0.3365	-0.0770	7.8386	2.4352
Case E	0.0	0.95	0.3548	-0.0790	6.9359	2.1566
Case F	0.05	0.85	0.3455	-0.0784	7.3517	2.2863
Experiment			0.272	-0.082	0.75	0.20

a cycle for pitching and plunging movement respectively. The phase difference between pitching and plunging movement is $168°$. The experimental data is $176°$. Under this large amplitude LCO, the shock location and strength vary significantly. At position (a), the AoA is maximum. There is only one strong shock on suction surface. With the AoA decreased from (b) to (e), the suction surface shock is weakened. At position (e), the AoA is the minimum. The double shock pattern is formed on suction surface and the boundary layer on suction surface is the thinest. This is because the shock strength is the weakest with double shock. While the suction surface shock is weakened, a shock appears on pressure surface. After position (e), the AoA is increased. The shock on suction surface is strengthened with a single shock. The boundary layer on suction surface becomes thick again due to the strong shock/turbulent boundary layer interaction. From position (h) to (j), while the suction surface shock becomes stronger, the pressure surface shock disappears. As shown in Fig. 8.14, when the AoA is maximum, there is a small boundary layer separation on the trailing edge.

The third series of LCO search still use the procedure 2, but at the experimental Mach number of 0.768. The dimensionless physical time step is the same as that used at Mach 0.753.

Table 8.3 lists the iteration cases at Mach 0.768. The computed averaged lift, moment coefficients, frequencies and amplitudes of Case E all agree excellently with the experiment. Fig. 8.15, 8.16, 8.17 and 8.18 show the computed LCO amplitudes of pitch, plunge,
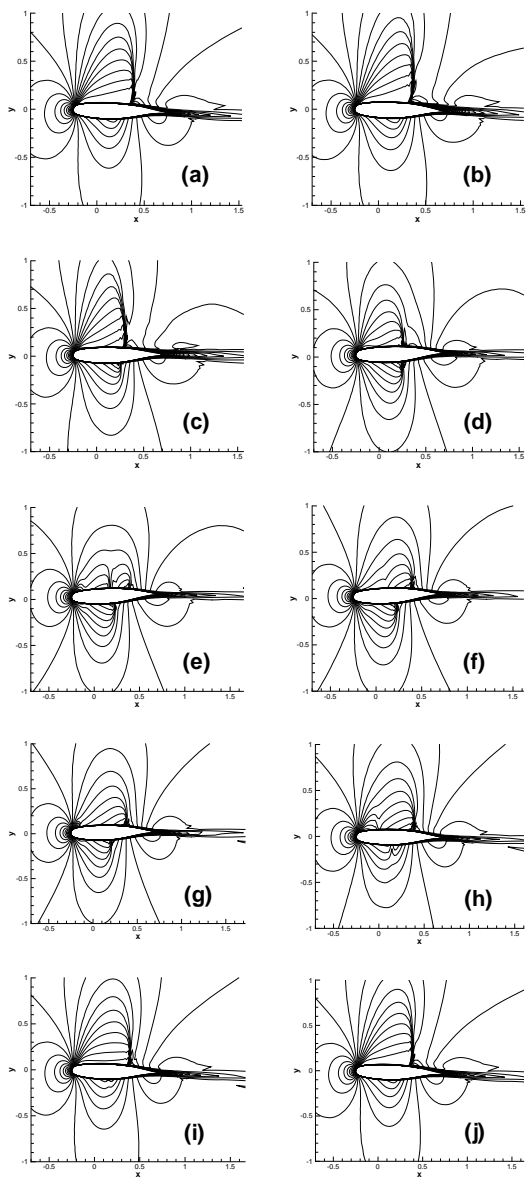
Figure 8.11: Contours of Mach number for $M = 0.753, AoA = 0°, \alpha_0 = 0.95°$
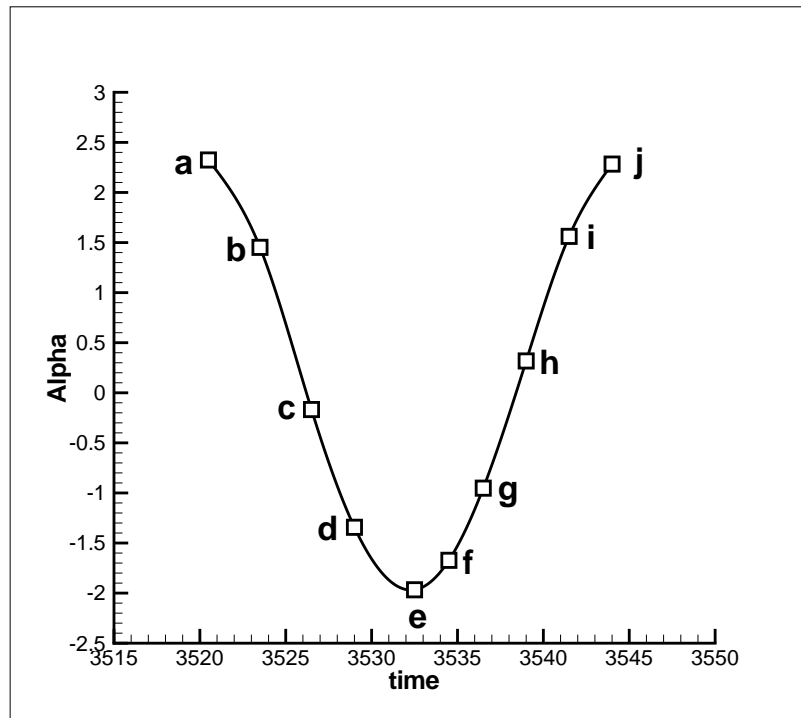
Figure 8.12: Positions of pitching movement in Fig. 8.11
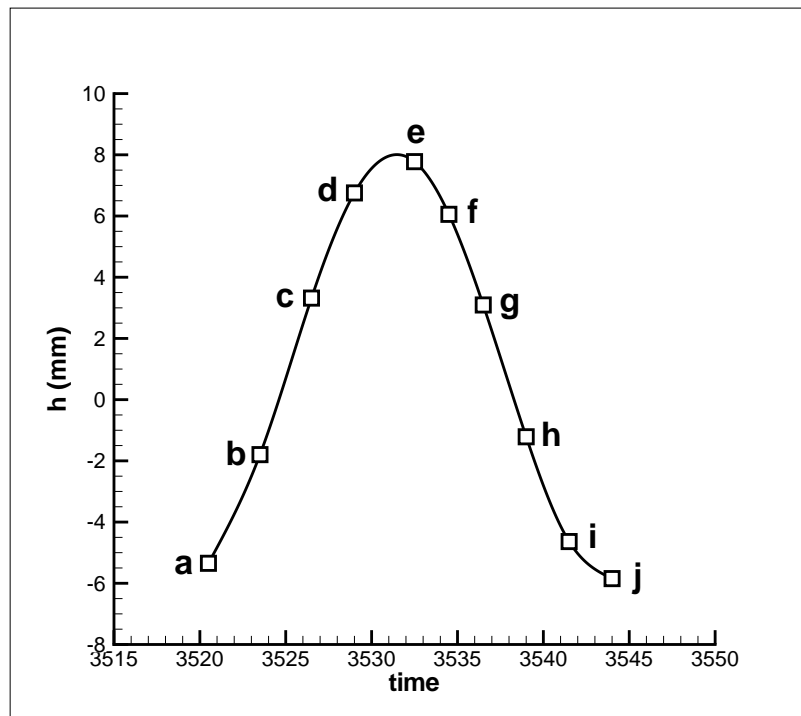
Figure 8.13: Positions of plunging movement in Fig. 8.11
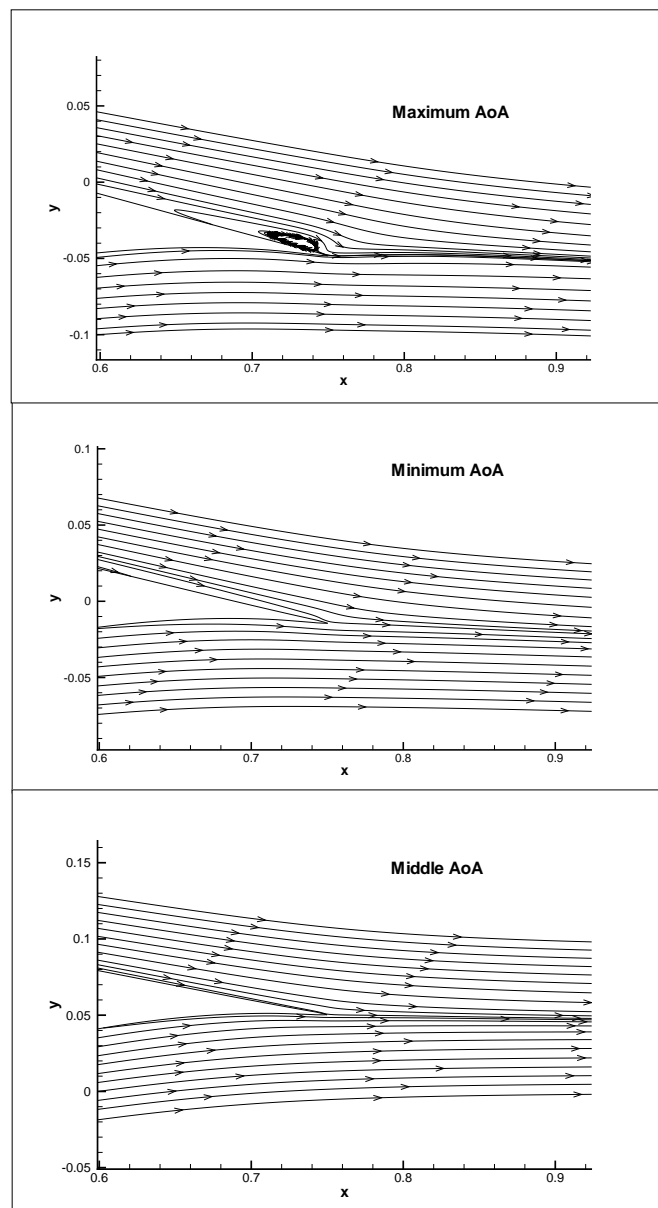
Figure 8.14: Stream line for Case E

lift and moment coefficient at Mach number of 0.768 for Case E. Compared with results predicted at *Mach* = 0.753 as shown in Fig. 8.6, 8.7, 8.8 and 8.9, it can be seen that the predicted amplitudes at *Mach* = 0.768 are more than one order of magnitude smaller. This means that the Mach number has a significant effect on the amplitudes of plunge and pitching oscillation. The reason may be that the different Mach number causes different shock strength, different shock/boundary layer interaction patterns and hence different unsteady non-linear forcing and moment.
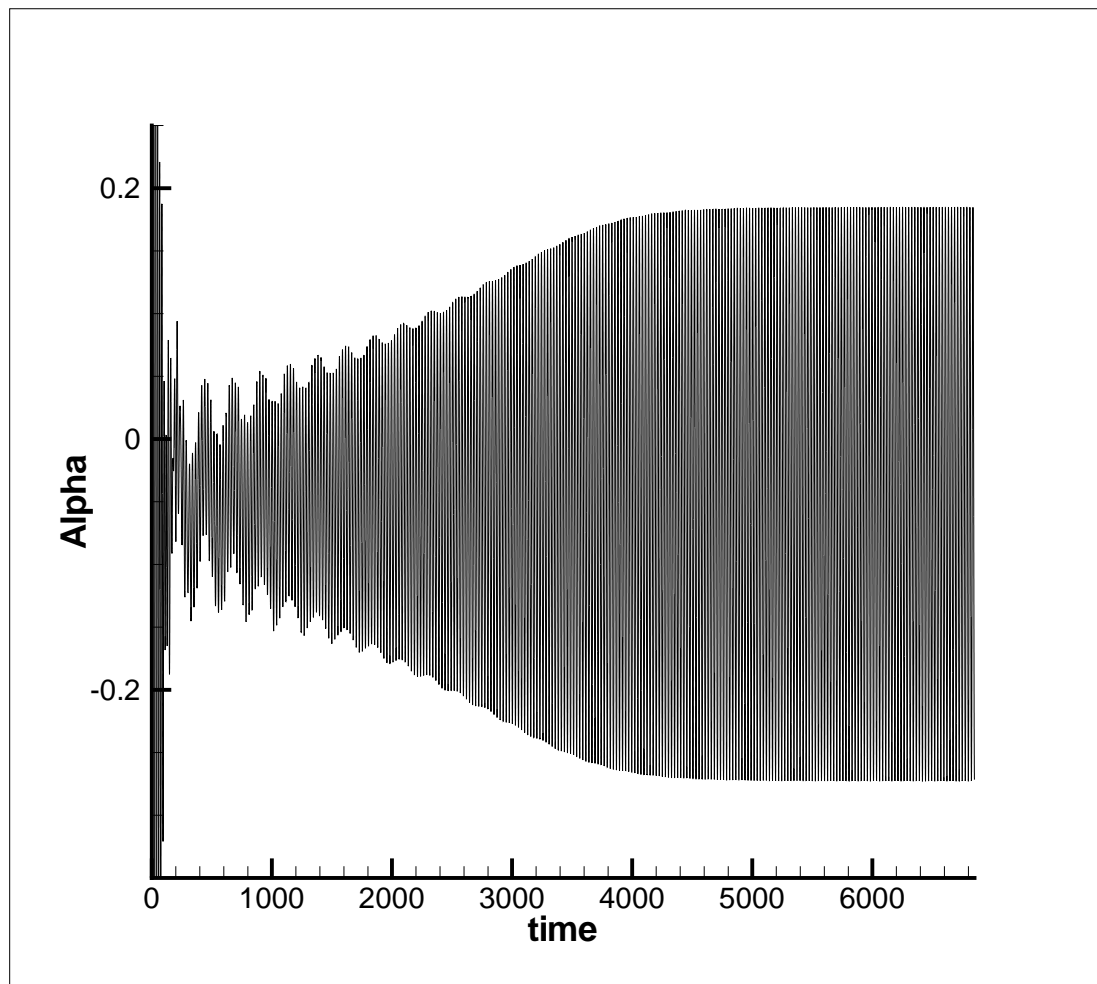
Figure 8.15: Pitch motion predicted by RANS ($M = 0.768$)

Totally 685,000 physical time steps are performed in the computation of case E with $t_c = 6850$. The stabilized LCO period in the simulation is up to $2250t_c$ and 88 cycles. The convergence history within a typical physical time step is shown in Fig. 8.19. It indicates
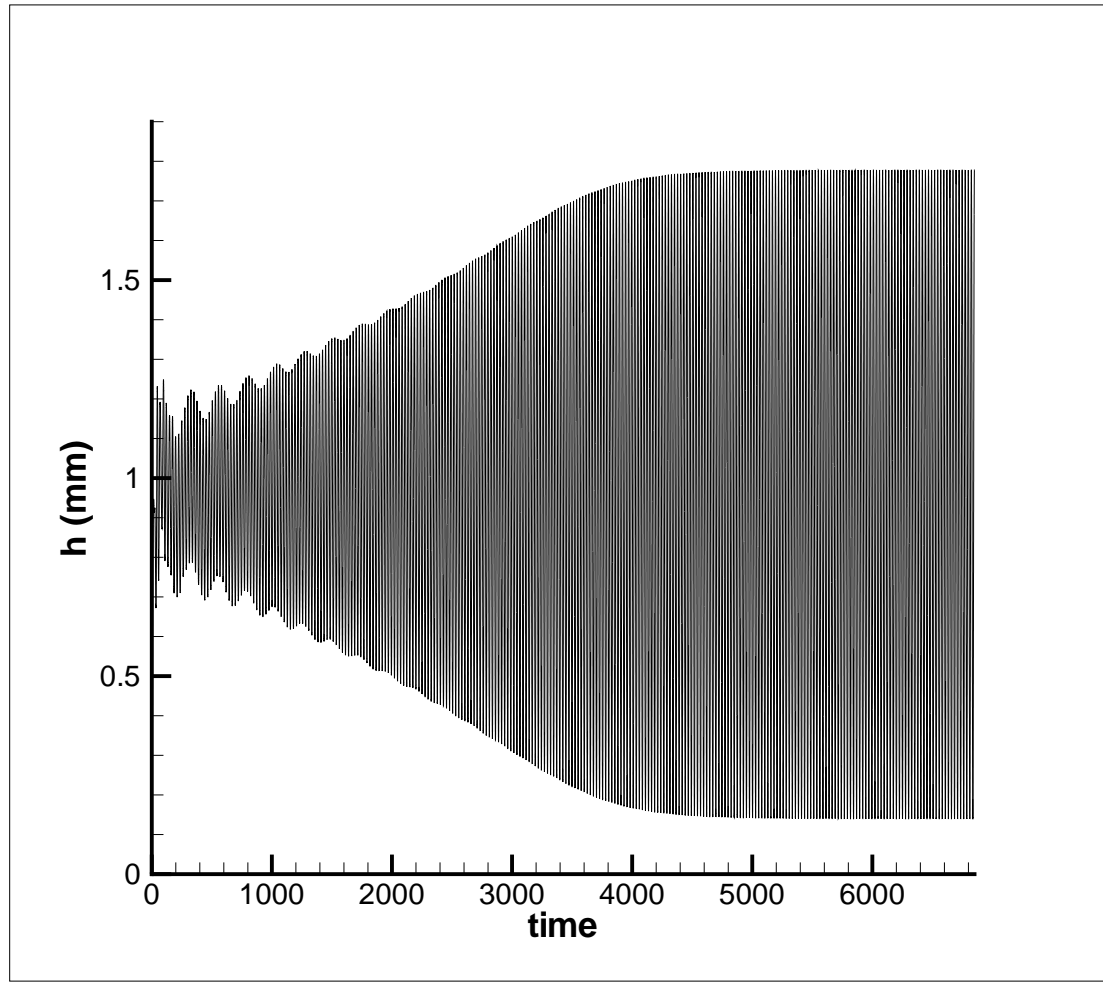
Figure 8.16: Plunge motion predicted by RANS ($M = 0.768$)

that only about 7 pseudo time steps are needed to reach the convergence criteria of 10^{-6} in this computation. Fig. 8.20 shows the contours of Mach number at one cycle for case E. Fig. 8.21 and Fig. 8.22 plot the corresponding positions of (a) to (j) in a cycle for pitching and plunge movement respectively. The computed phase difference between pitching and plunge movement is $172°$, which agrees very well with the experimental phase difference of $176°$. Different from the LCO computation at Mach 0.753, there is no separation in the simulated flow field at Mach 0.768 as shown in Fig. 8.23. The reason is that the very small amplitudes of the LCO captured at Mach 0.768 does not cause large AoA variation.

Table 8.4 summarizes the computed LCO amplitudes and frequencies at different conditions compared with the experimental results [40]. At *Mach* $= 0.753$, the present com-
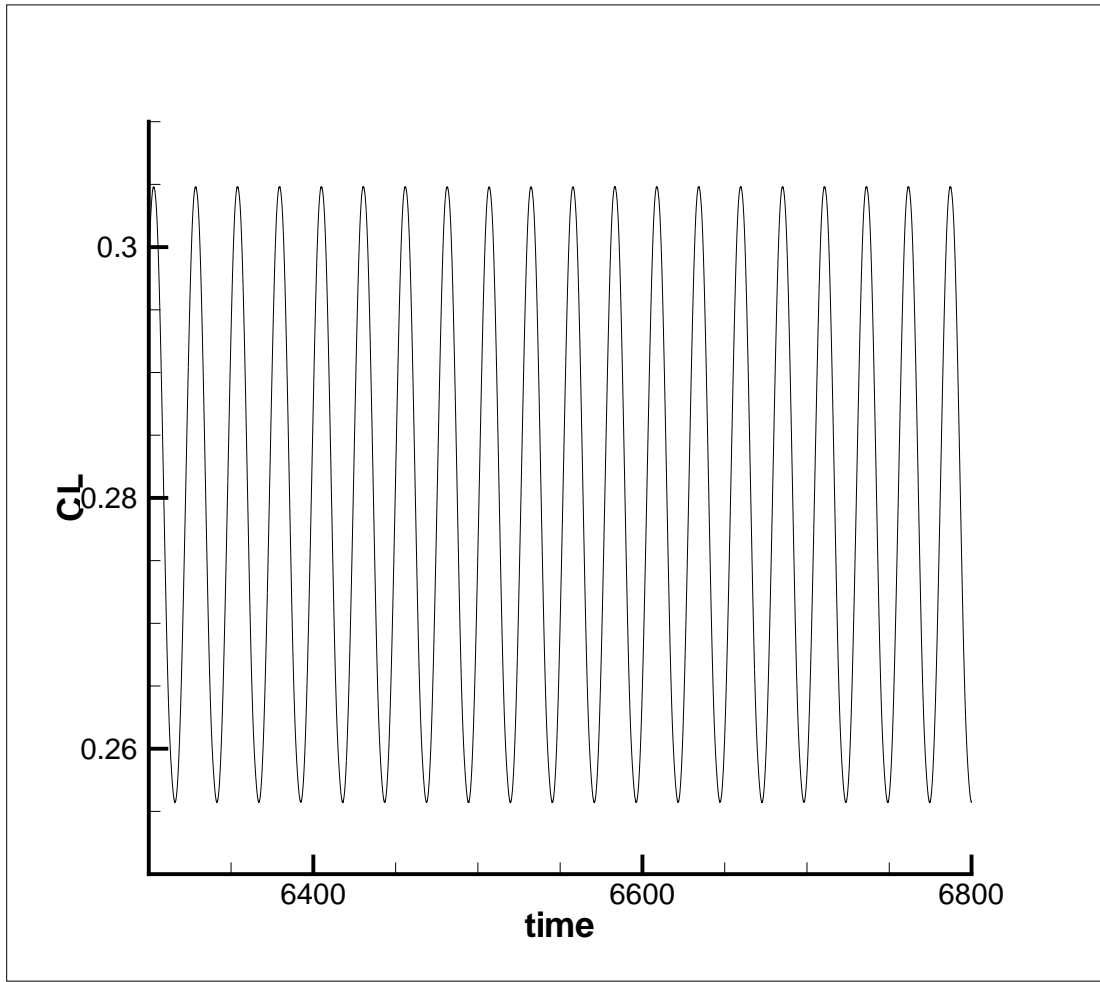
Figure 8.17: Lift coefficient predicted by RANS ($M = 0.768$)

puted results are comparable to those of Weber et al. and Tang et al. However, at Mach 0.768 of the experimental condition, both the predicted plunge and pitching amplitudes agree excellently with the experiment, whereas the previous results predicted by other researchers [2, 39] at $Mach = 0.753$ are more than one order of magnitude higher. This is the first time that a numerical simulation of NLR7301 airfoil LCO matches the experiment.

In general, the prediction accuracy of Case E at Mach 0.768 is on the same order of the experiment measurement uncertainty. The only primary difference from the experiment for Case E is that the α_0 used in the simulation is $0.75°$ whereas the experimental value is $1.28°$. The α_0 only affects the initial moment imposed on the elastic system and remains as a constant in the whole LCO process. Such difference may be attributed to the
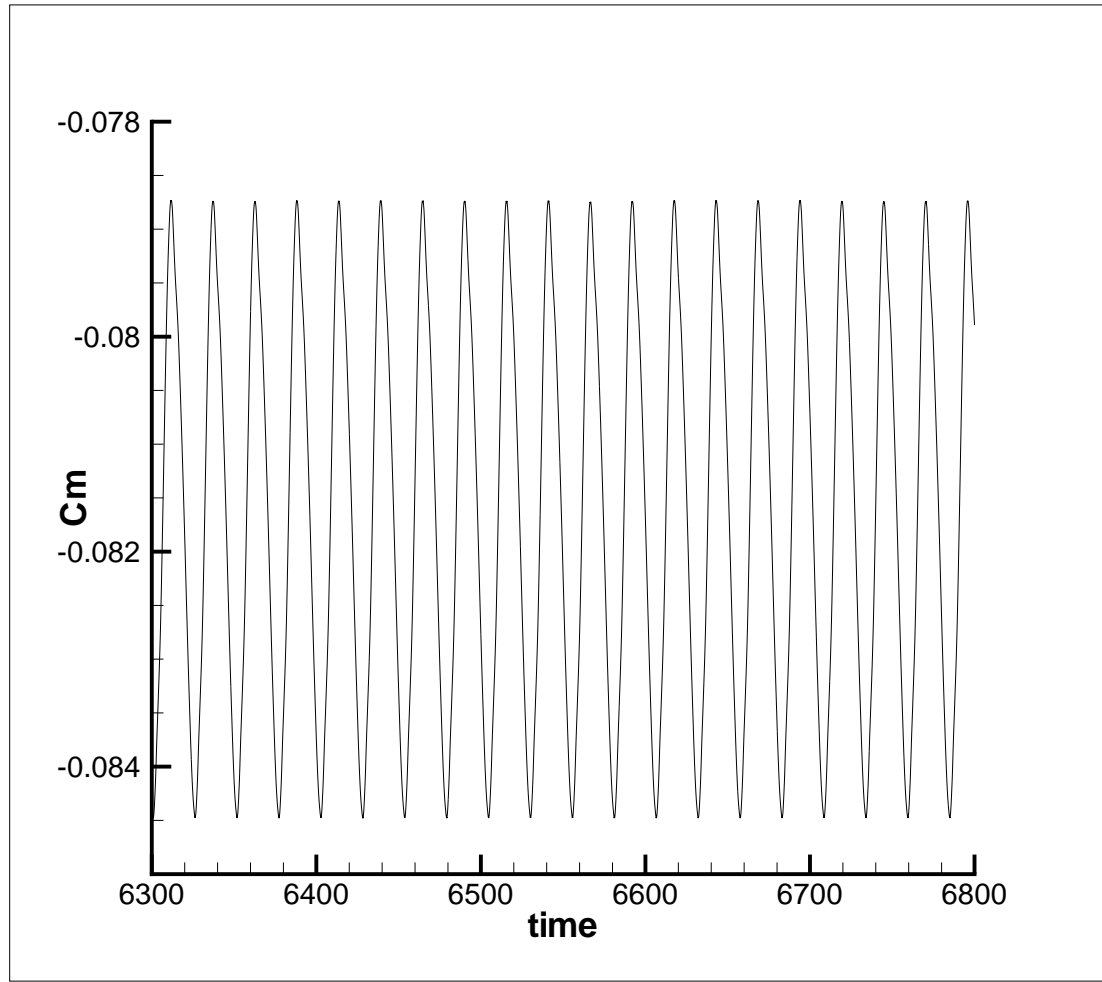
Figure 8.18: Moment coefficient predicted by RANS ($M = 0.768$)

uncertainty of the experiment and numerical simulation, and the sensitive nature of LCO to initial perturbations, which are difficult if not impossible to be made the same between the experiment and numerical simulation.

Note that the final LCO plunge amplitude is about 2.7/1000 of the chord length and the pitching amplitude is $0.2287°$. These are some very small values. The accurate resolution of such small scale vibration motion without being damped out in the long time calculation may be attributed to the high order low diffusion numerical schemes and the fully coupled FSI model employed in this research.

It needs to point out an important phenomenon that the LCO amplitudes are dependent on the initial flow fields. The results in Table 8.3 are computed using the initial field set
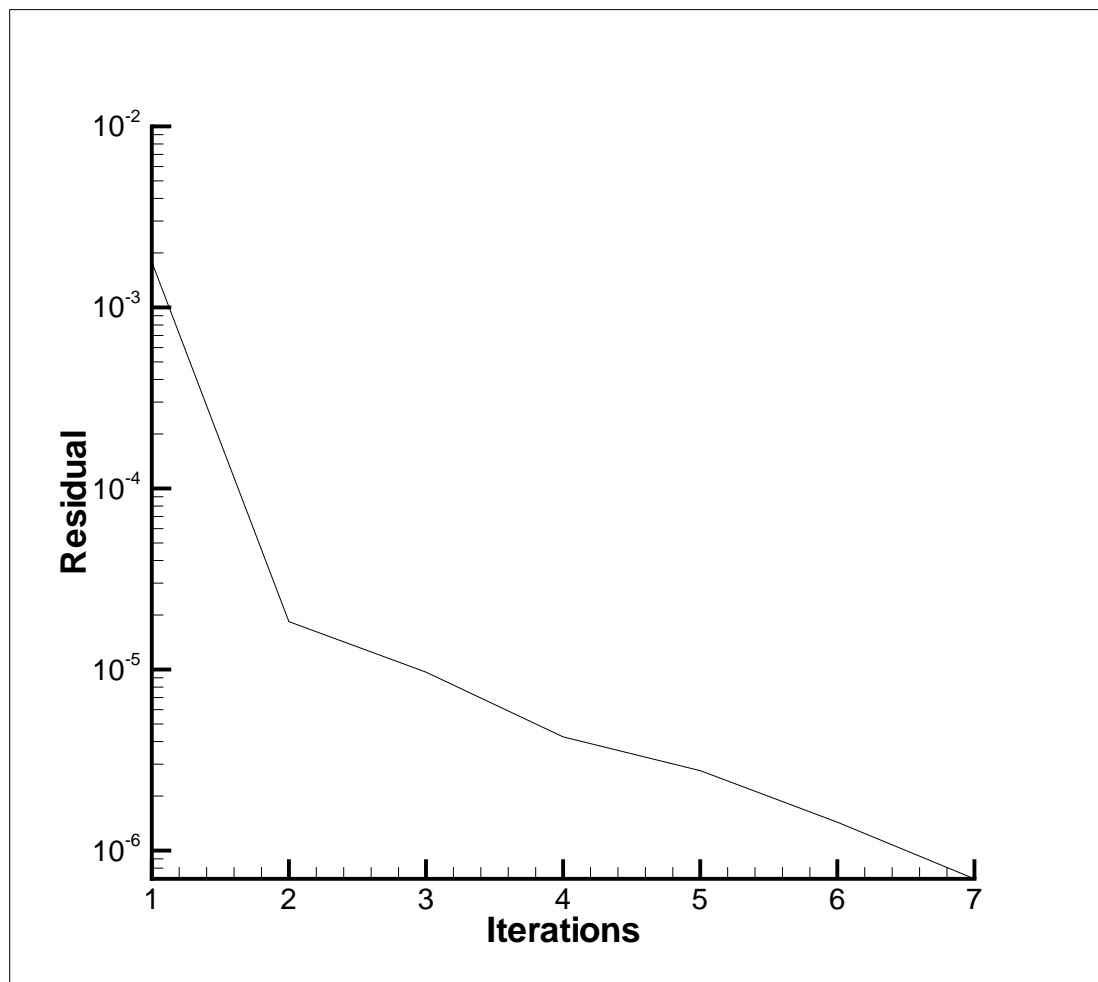
Figure 8.19: Convergence history within a typical physical time step for $M = 0.768$
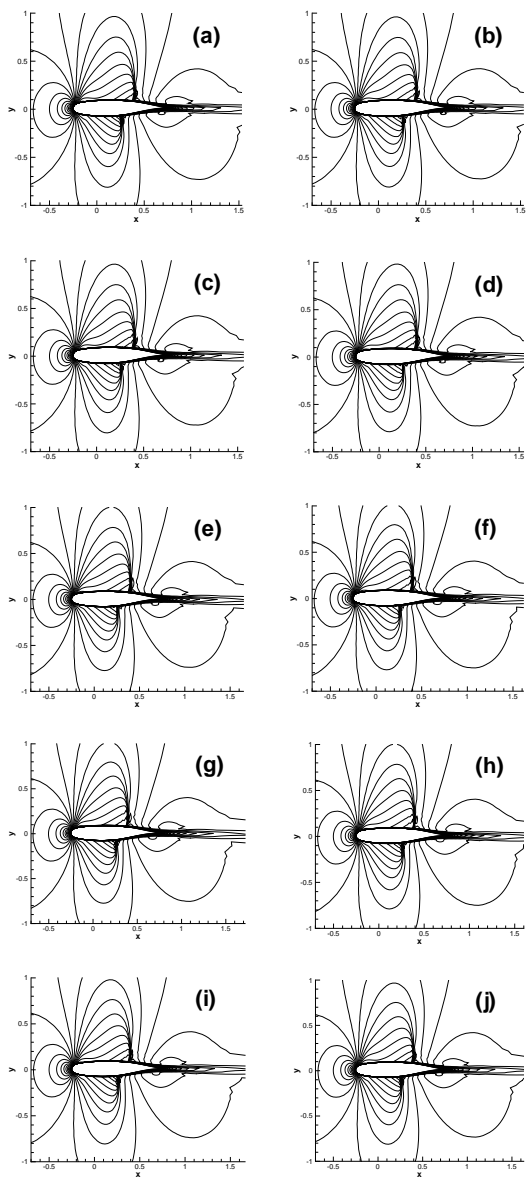
Figure 8.20: Contours of Mach number for *Mach* = 0.768
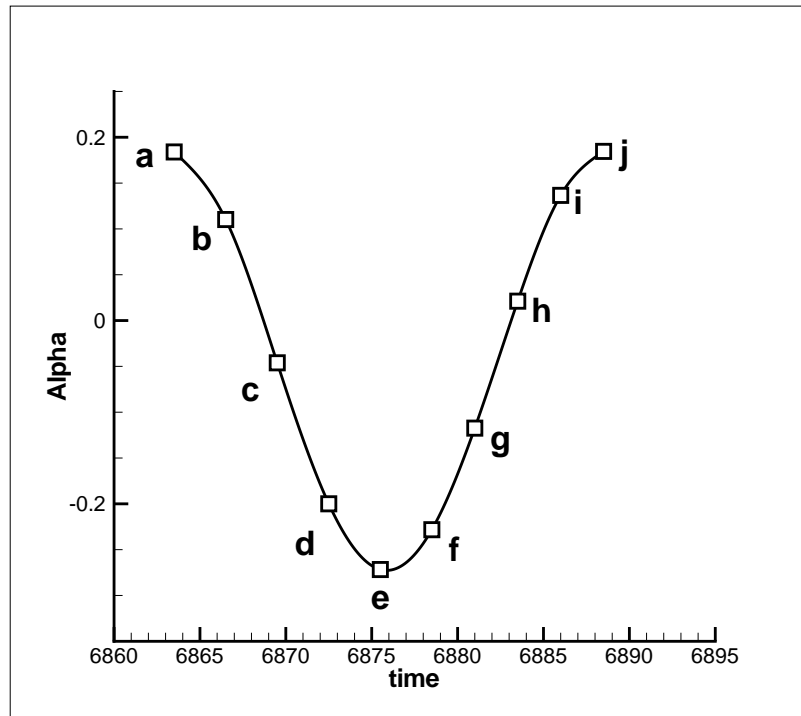
Figure 8.21: Positions of pitching movement in Fig. 8.20
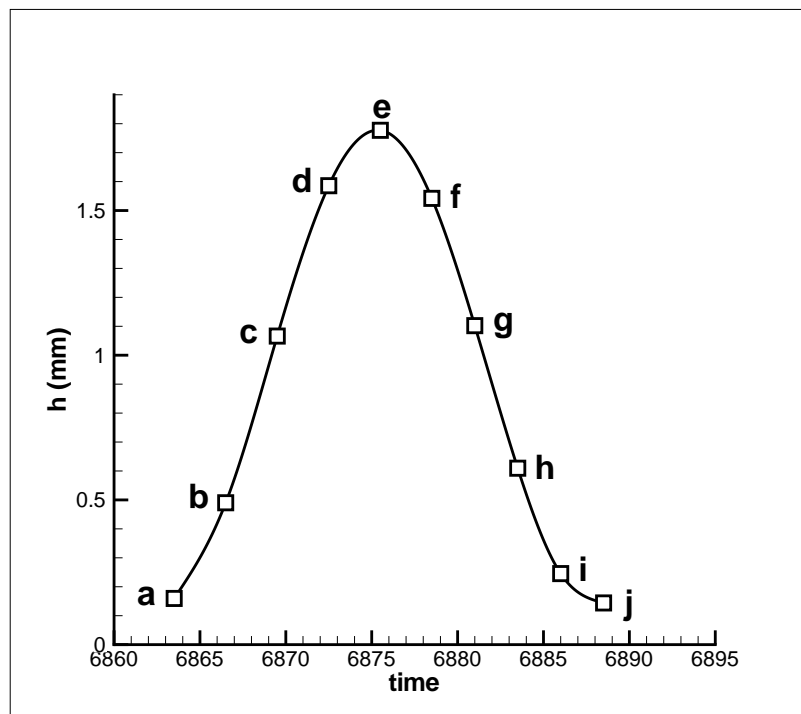
Figure 8.22: Positions of plunging movement in Fig. 8.20
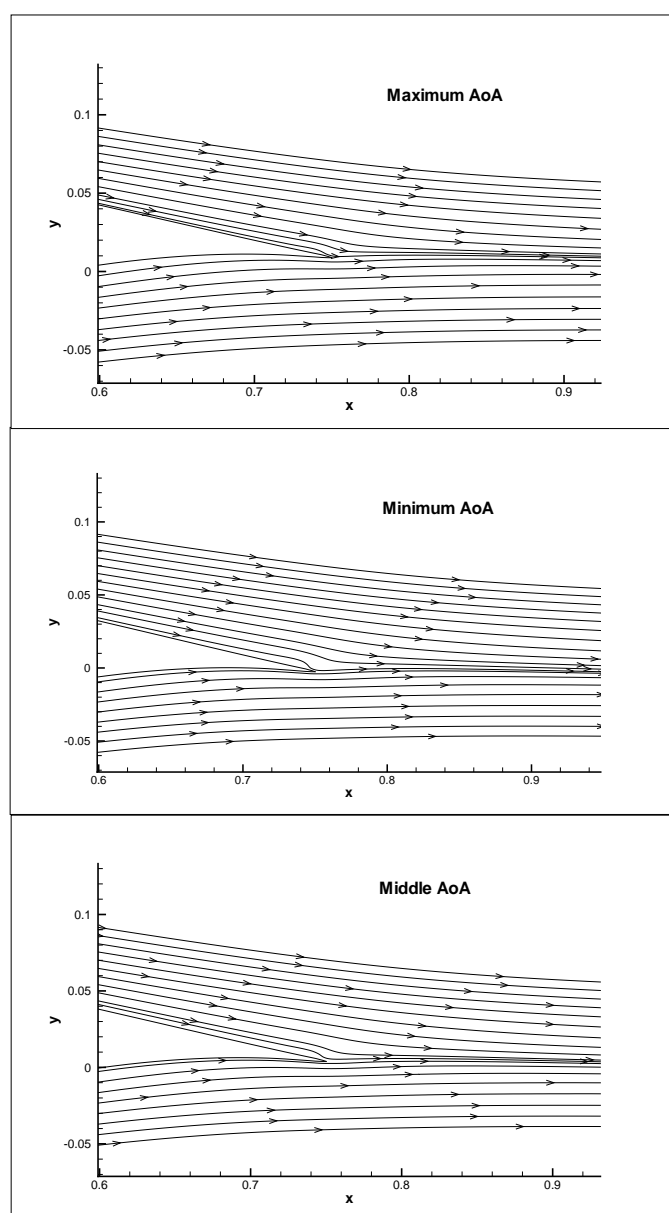
Figure 8.23: Stream line for Case E

Table 8.3: Comparison of the test cases at $M = 0.768$

NLR7301 LCO	Ini. AoA	α_0°	C_l	C_m	$h(mm)$	α°	$f(Hz)$
Case A	0.0	0.68	0.2610	-0.0796	1.6509	0.4632	33.35
Case B	0.0	0.70	0.2758	-0.0807	4.2453	1.2349	33.36
Case C	0.0	0.75	0.2729	-0.0805	1.2617	0.3524	33.38
Case D	-0.033	0.75	0.2673	-0.0799	1.4351	0.4015	33.39
Case E	0.05	0.75	0.2803	-0.0816	0.8192	0.2287	33.36
Experiment		1.28	0.272	-0.082	0.75	0.20	32.74

Table 8.4: LCO comparison of computation and experiment

NLR7301 LCO	Mach	$h(mm)$	err (mm)	α°	err	$f(Hz)$	err (Hz)
Present	0.768	0.8192	0.069	0.2287°	0.0287°	33.36	0.62
Present	0.753	10.134	9.384	3.1942°	2.9942°	33.49	0.75
Weber (2001) [39]	0.753	10.5	9.75	4.09°	3.89°	33.42	0.68
Tang (2003) [2]	0.753	8.99	8.24	3.17°	2.97°	34.3	1.56
Experiment [40]	0.768	0.75		0.20°		32.74	

equal to the uniform free-stream everywhere. If a converged steady state solution is used as the initial field, the LCO amplitudes may be very different with significantly greater magnitude. The different α_0 and initial AoA also setup the initial lift and moment to certain values. In other words, different initial perturbation may generate very different LCO solutions. This appears to be the bifurcation phenomenon due to the non-linear aerodynamic loading of lift and moment, which are caused by the pattern of shock wave/turbulent boundary layer interaction. If we can understand the systematic relationship between the LCO amplitude and initial perturbation, it may be possible to control the LCO and mitigate or prevent it. Even though the LCO amplitudes are very different as shown in Table 8.3 and 8.4, the computed frequency varies little and agrees well with the experimental value.

8.3   Limit Cycle Oscillations of NLR7301 Airfoil Using DES

Based on the experience of the 2D LCO simulation using RANS, the 3D DES of LCO for the same experimental conditions is conducted. The same structural equations (2.44)-(2.46) are used with fully coupled fluid-structural interaction procedure. The unsteady lift and moment coefficients are integrated from the 3d unsteady flow fields. The computation grid is composed of 24 blocks partitioned from a single block O-H-grid with the dimension of $193 \times 97 \times 33$ (see Fig. 8.24). This simulation is very CPU intensive and will be impossible without parallel computation. The span wise length is 3.33 times of the airfoil chord, which is the same as that used in the experiment. The dimensionless physical time interval is 0.01. The Procedure 2 is adopted in the 3D LCO simulation. Based on the experience of 2D LCO simulation, the computation is conducted with the experimental Mach number 0.768 only. Three cases are performed with different initial AoA and α_0.

Case A: $AoA = 0.05°$, $\alpha_0 = 0.75°$

In this case, $AoA = 0.05°$, $\alpha_0 = 0.75°$ are used in the computation which are the same as the 2D Case E at $Mach = 0.768$. The predicted amplitudes of plunge and pitch modes are shown in Fig. 8.25 and Fig. 8.26. Different from the corresponding 2D case, the amplitudes of the 3D case are 4 times higher than the experiment. Fig. 8.27 and Fig. 8.28 plot the variation of lift and moment coefficients with the time after the LCO is formed. As indicted in table 8.5, the predicted time-averaged lift coefficient is greater than those of the corresponding 2D case. The predicted time-averaged moment coefficient is lower than those of the 2D case.

Table 8.5: Comparison of LCO using RANS and DES

NLR7301 LCO	Ini. AoA	$\alpha_0°$	h (mm)	$\alpha°$	C_l	C_m	$f(Hz)$
DES	0.05	0.75	2.8424	0.8066	0.2934	-0.0831	33.41
RANS	0.05	0.75	0.8192	0.2287	0.2803	-0.0816	33.36
Experiment		1.28	0.75	0.20	0.272	-0.082	32.74
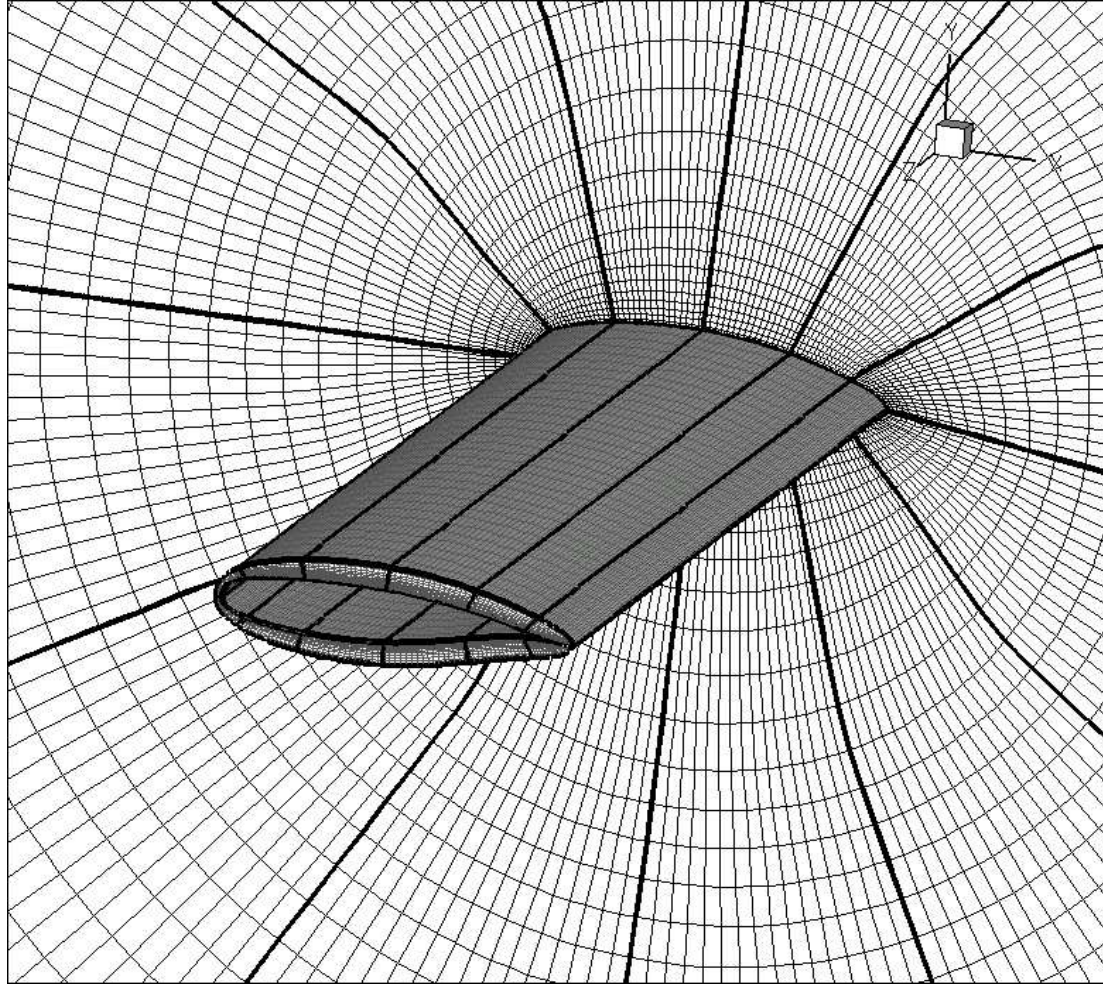
Figure 8.24: The 3D computational grid of NLR7301 airfoil

Case B: $AoA = 0°$, $\alpha_0 = 0.75°$

In this case, the initial AoA is decreased to zero to observe the variation of the LCO. The predicted amplitudes of plunge and pitch modes are shown in Fig. 8.29 and Fig. 8.30. Fig. 8.31 and Fig. 8.32 plot the variation of lift and moment coefficients with the time after the LCO is formed. As shown in table 8.6, the amplitudes of the LCO are greater than those of case A. Compared with case A, the predicted time-averaged lift coefficient is decreased, but the predicted time-averaged moment coefficient is increased. The absolute value of the moment coefficient is decreased.
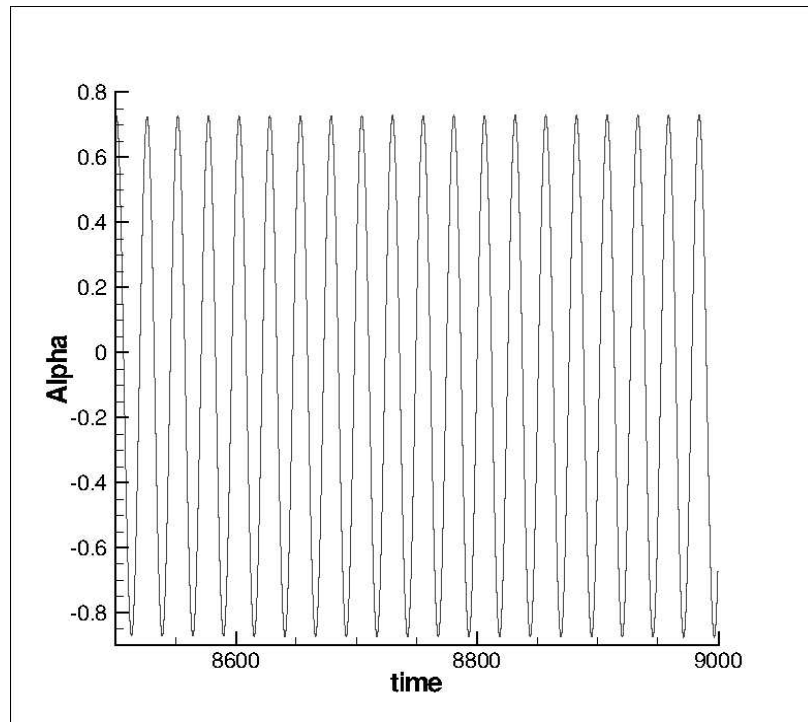
Figure 8.25: Pitch motion predicted by DES ($AoA = 0.05°, \alpha_0 = 0.75°$)
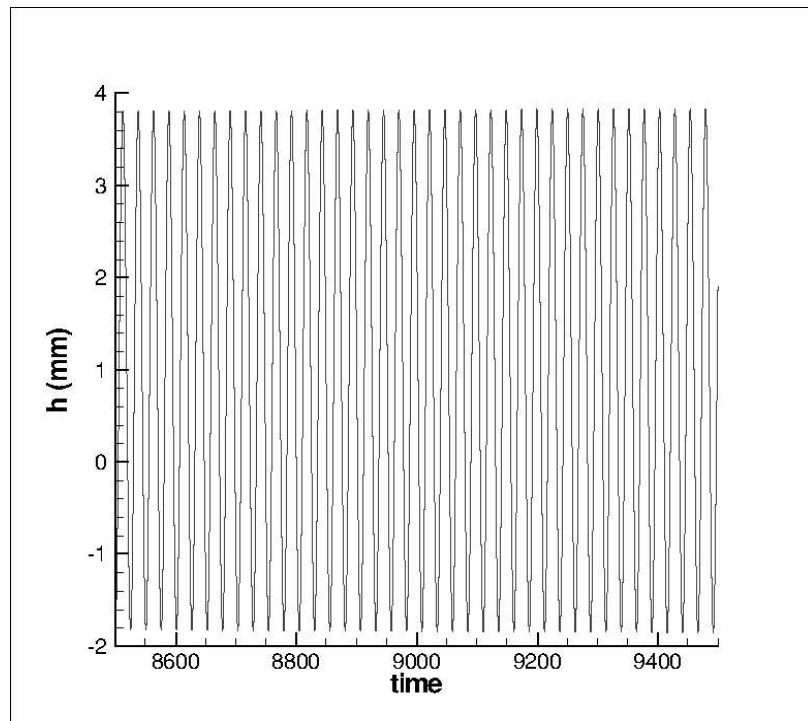
Figure 8.26: Plunge motion predicted by DES ($AoA = 0.05°, \alpha_0 = 0.75°$)
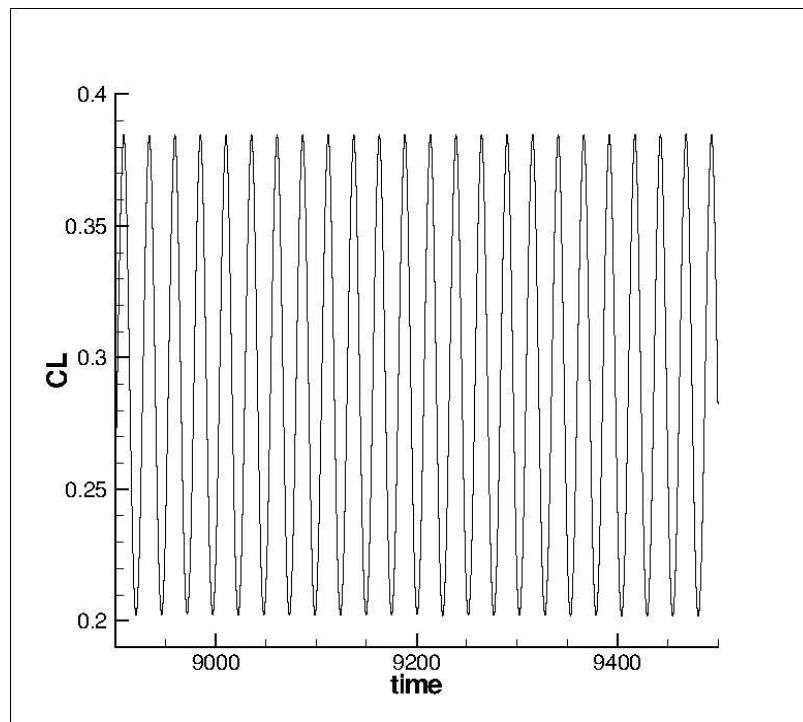
Figure 8.27: Lift coefficient predicted by DES ($AoA = 0.05°, \alpha_0 = 0.75°$)
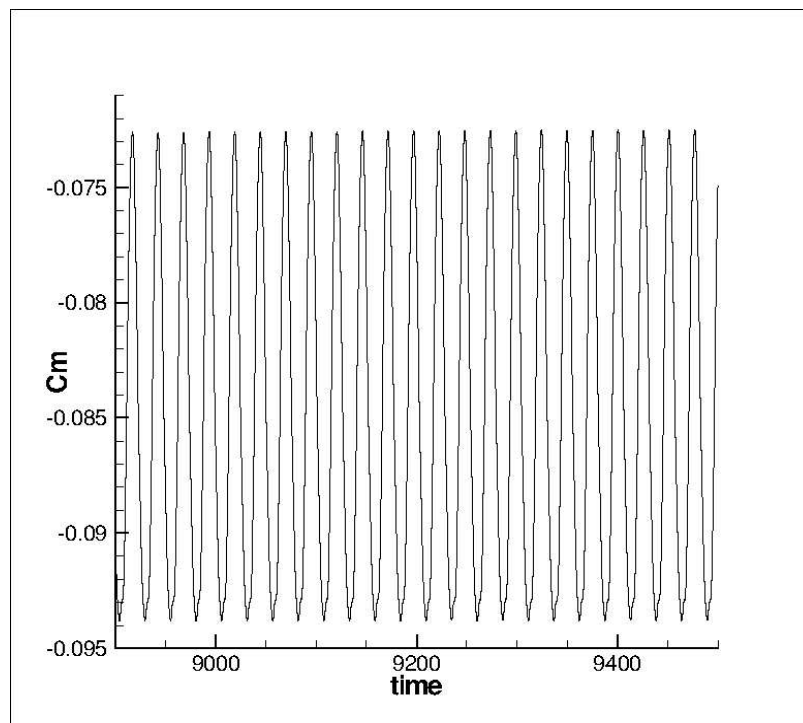
Figure 8.28: Moment coefficient predicted by DES ($AoA = 0.05°, \alpha_0 = 0.75°$)
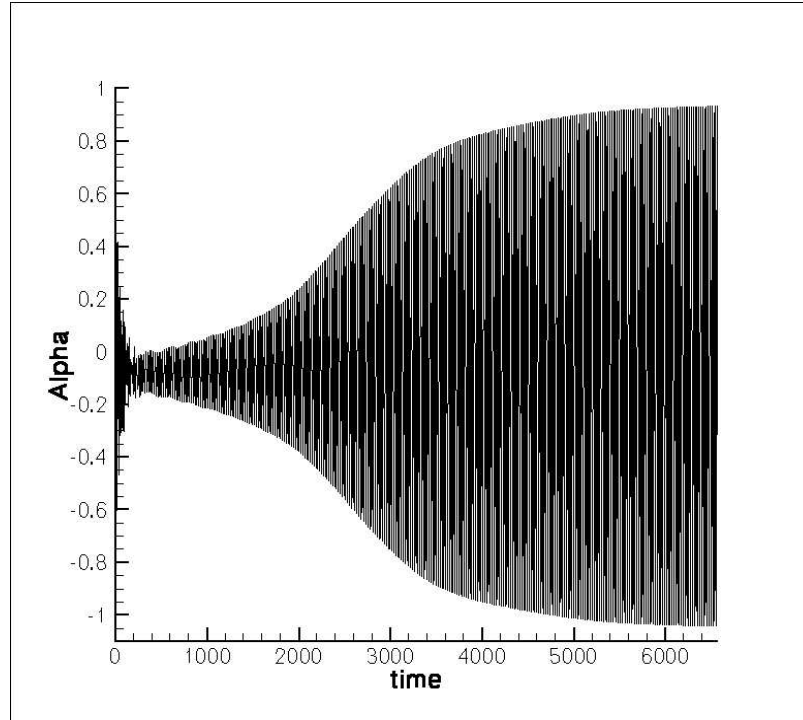
Figure 8.29: Pitch motion predicted by DES ($AoA = 0.0°, \alpha_0 = 0.75°$)
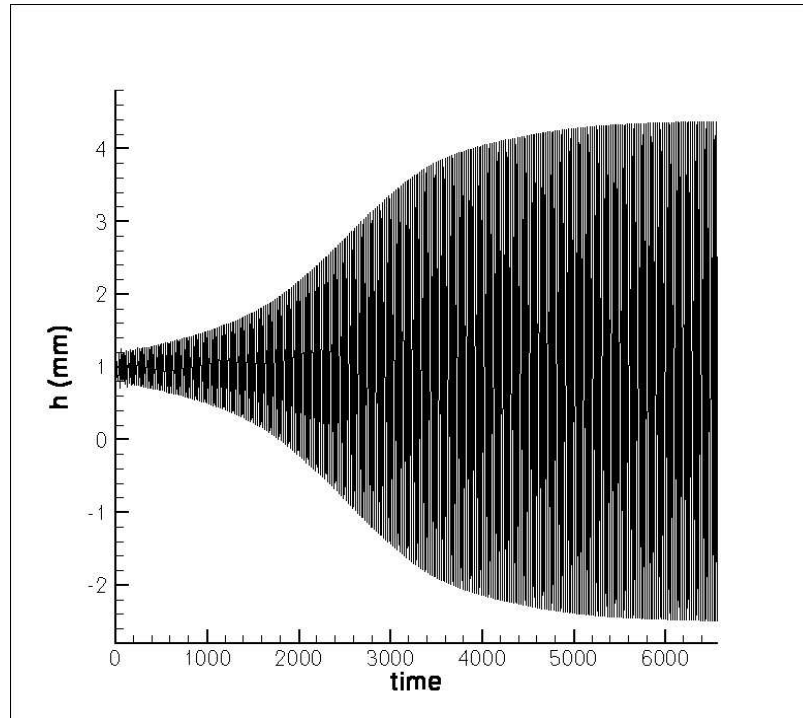
Figure 8.30: Plunge motion predicted by DES ($AoA = 0.0°, \alpha_0 = 0.75°$)
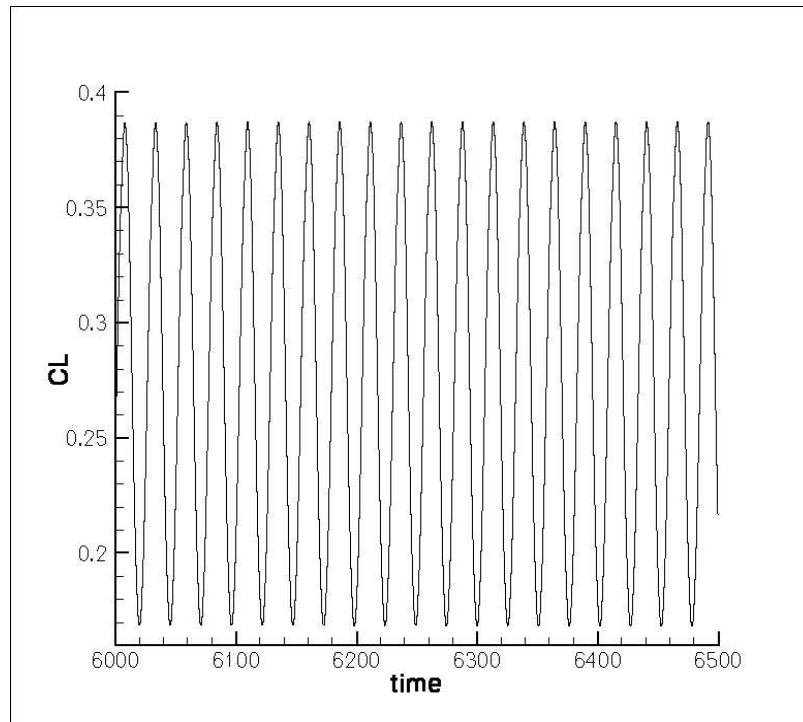
Figure 8.31: Lift coefficient predicted by DES ($AoA = 0.0°, \alpha_0 = 0.75°$)
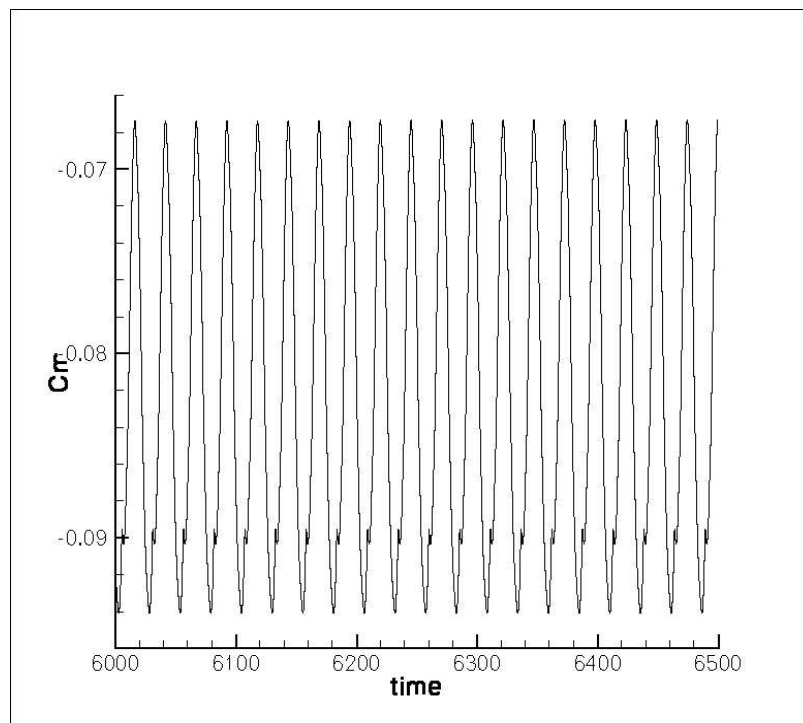
Figure 8.32: Moment coefficient predicted by DES ($AoA = 0.0°, \alpha_0 = 0.75°$)

Case C: $AoA = 0°$, $\alpha_0 = 0.85°$

In this case, the α_0 is increased to $0.85°$, which is closer to the experimental data $1.28°$. The initial AoA is kept the same as the case B. The predicted amplitudes of plunge and pitch modes are shown in Fig. 8.33 and Fig. 8.34. Fig. 8.35 and Fig. 8.36 plot the variation of lift and moment coefficients with the time after the LCO is formed. As shown in table 8.6, the amplitudes of the LCO are significantly decreased compared with case A and case B. They are much closer to the experiment than case A and case B. The predicted time-averaged lift coefficient is larger than case A. The predicted time-averaged moment coefficient is lower than case A.
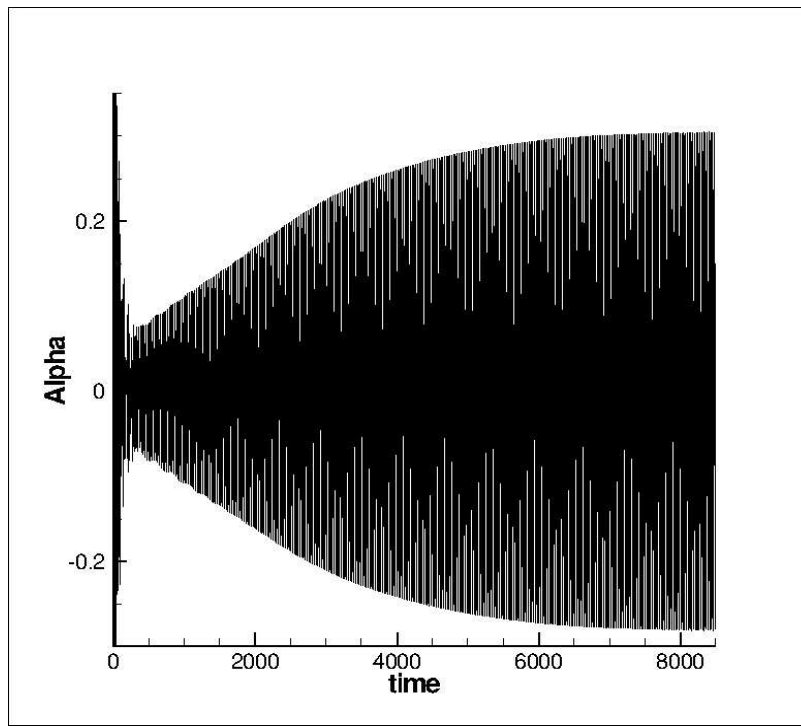
Figure 8.33: Pitch motion predicted by DES ($AoA = 0.0°$, $\alpha_0 = 0.85°$)

The instantaneous vorticity magnitudes at three spanwise locations, which are located at the left most, right most and middle sections respectively, are shown in Fig. 8.37 when the time dependent AoA reaches its maximum. The vorticity contours show a strong shock on suction surface and a weak shock on pressure surface which are similar to those demonstrated in Fig. 8.20. Some small vortex structures due to the shock wave/boundary layer
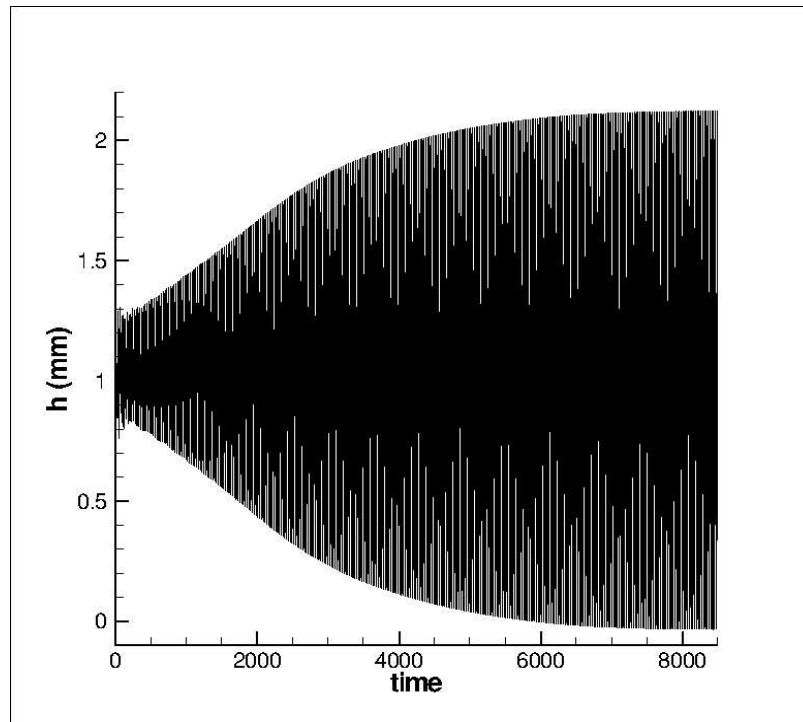
Figure 8.34: Plunge motion predicted by DES ($AoA = 0.0°, \alpha_0 = 0.85°$)
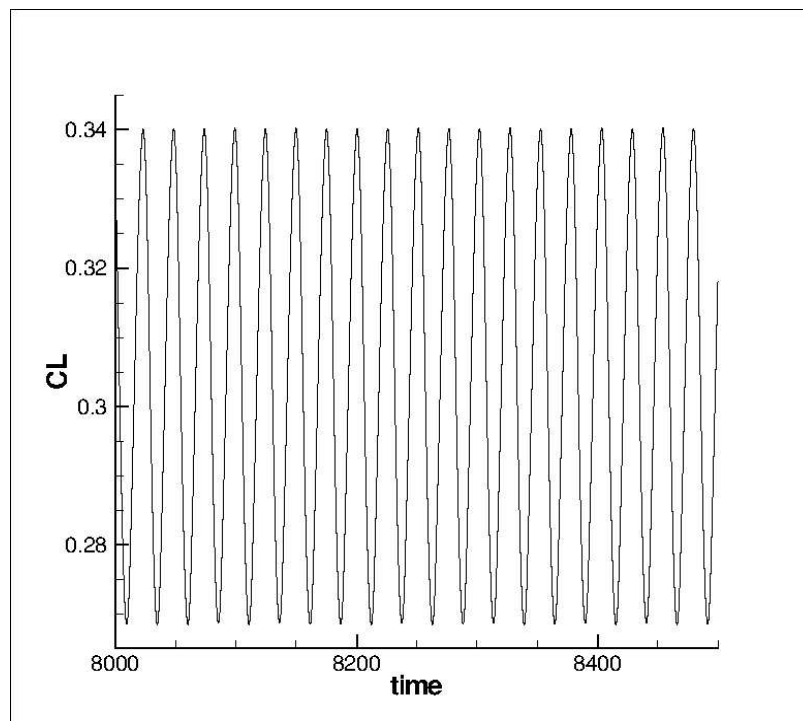
Figure 8.35: Lift coefficient predicted by DES ($AoA = 0.0°, \alpha_0 = 0.85°$)
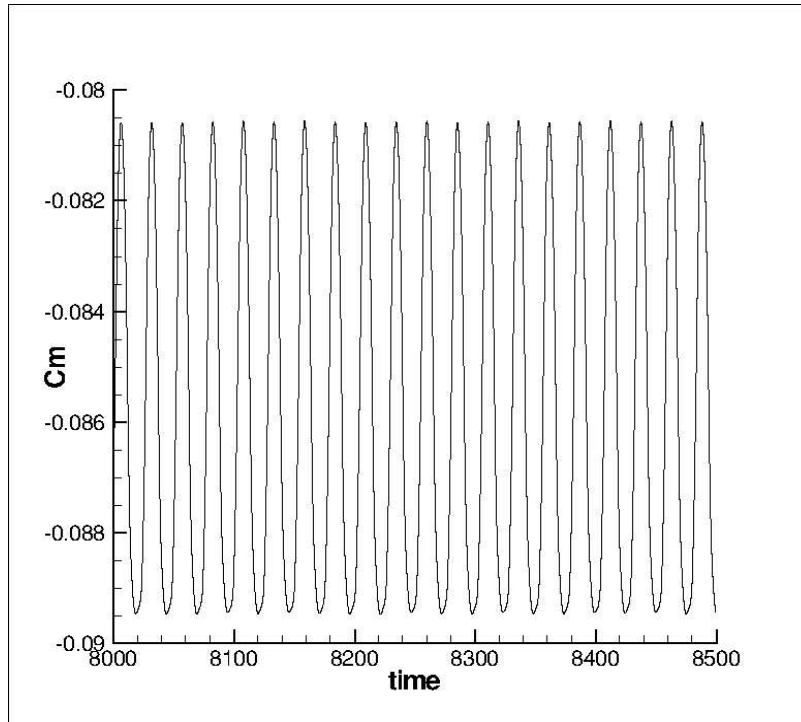
Figure 8.36: Moment coefficient predicted by DES ($AoA = 0.0°, \alpha_0 = 0.85°$)

interaction are resolved by the DES.

Case D: $AoA = -0.015°$, $\alpha_0 = 0.88°$

In this case, the initial AoA is decreased to $-0.015°$. The α_0 is increased to $0.88°$. The predicted amplitudes of plunge and pitch modes are shown in Fig. 8.38 and Fig. 8.39. Fig. 8.40 and Fig. 8.41 plot the variation of lift and moment coefficients with the time after the LCO is formed. As shown in table 8.6, the amplitudes of the LCO agree excellently with the experiment. The α_0 used in the simulation is closer to the experiment than the best 2D case. The predicted time-averaged lift and moment coefficients have slight differences from the experiment. Same as the 2D cases, the computed frequency varies little and agrees well with the experimental value. In summary, the computed results of this 3D LCO case match the experiment very well, better than the 2D case.
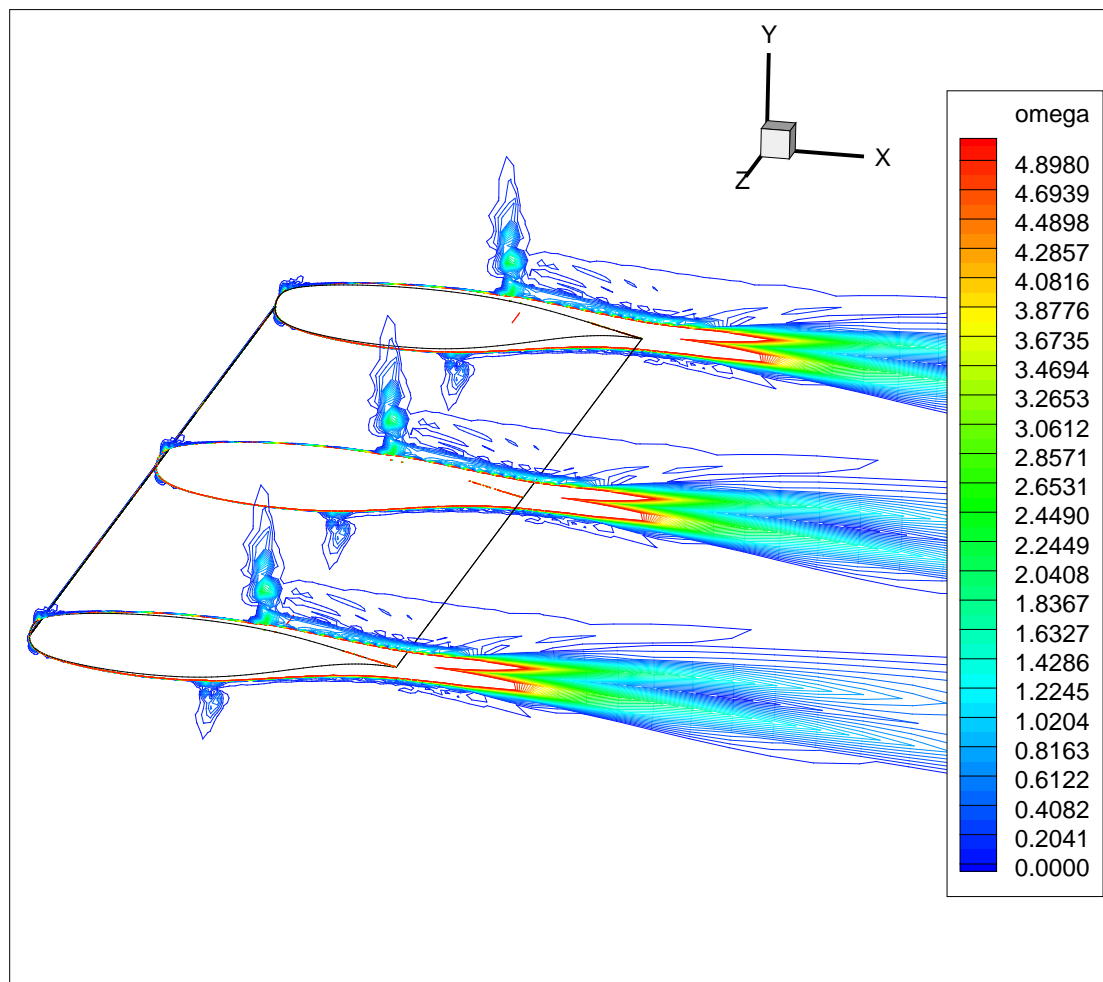
Figure 8.37: Instantaneous vorticity magnitude predicted by DES ($AoA = 0.0°, \alpha_0 = 0.85°$)
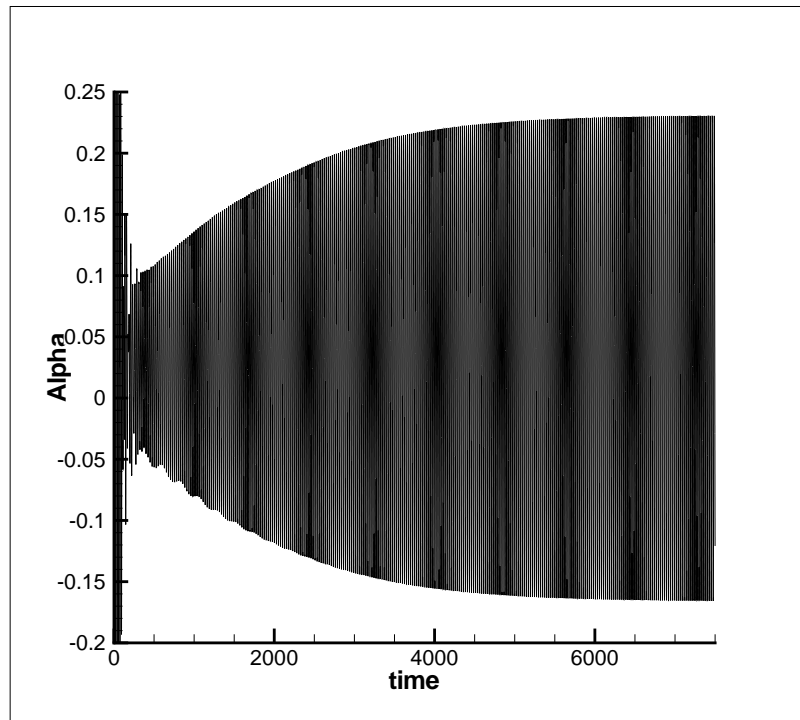
Figure 8.38: Pitch motion predicted by DES ($AoA = -0.015°, \alpha_0 = 0.88°$)
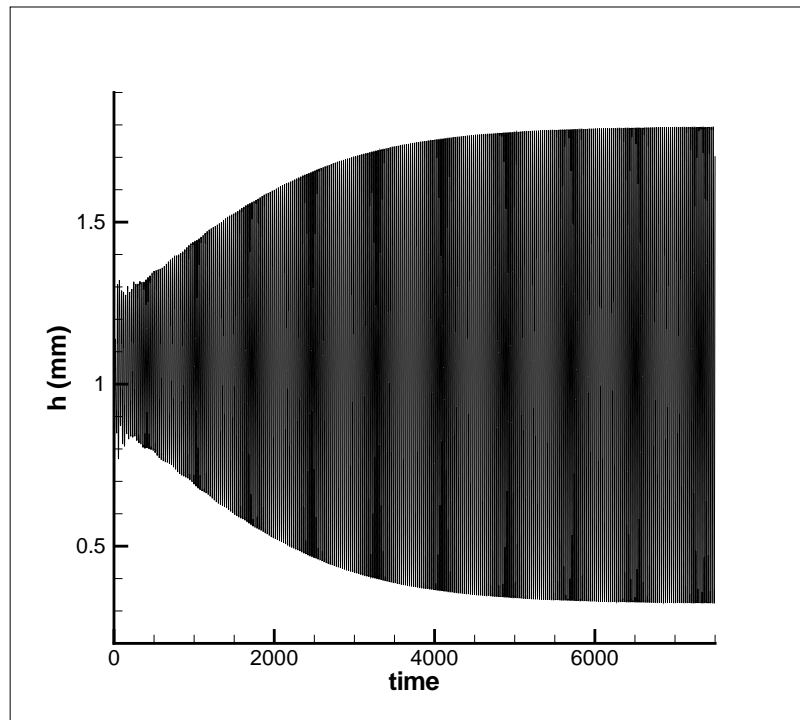

Figure 8.39: Plunge motion predicted by DES ($AoA = -0.015°, \alpha_0 = 0.88°$)
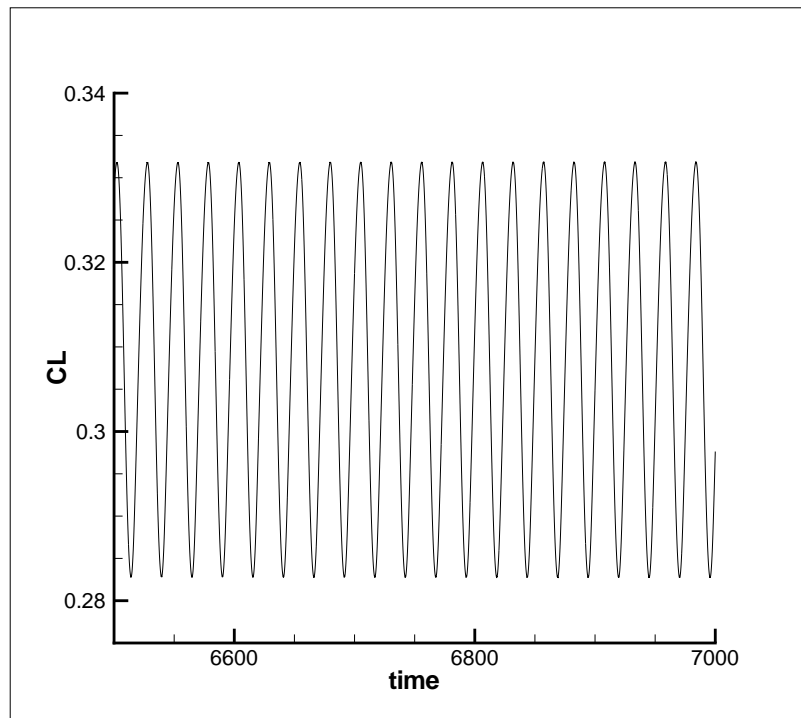
Figure 8.40: Lift coefficient predicted by DES ($AoA = -0.015°, \alpha_0 = 0.88°$)
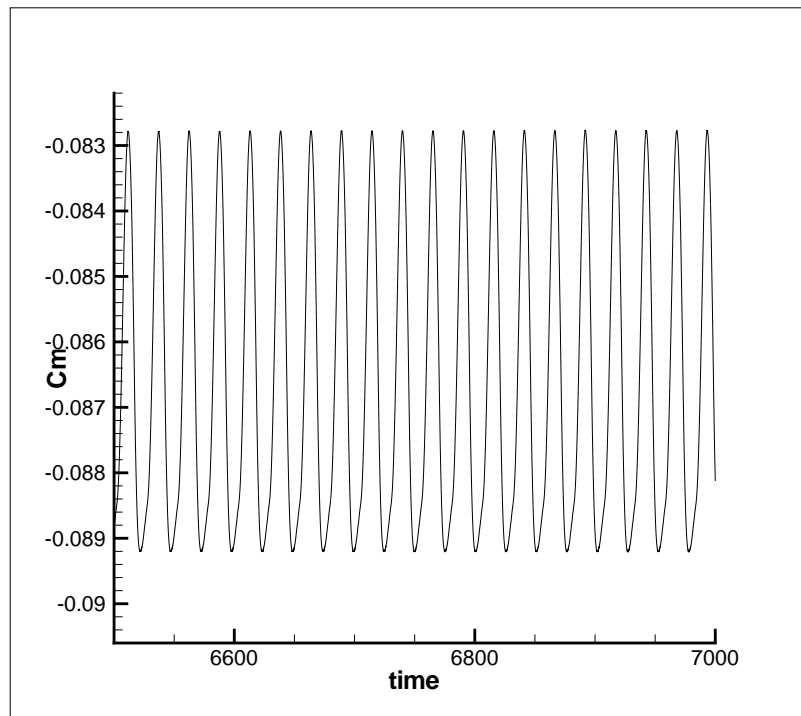
Figure 8.41: Moment coefficient predicted by DES ($AoA = -0.015°, \alpha_0 = 0.88°$)

Table 8.6: Comparison of LCO for different initial AoA and α_0 at $M = 0.768$ using DES

NLR7301 LCO	Ini. AoA	α_0°	h (mm)	α°	C_l	C_m	$f(Hz)$
Case A	0.05	0.75	2.8424	0.8066	0.2934	-0.0831	33.41
Case B	0.0	0.75	3.4313	0.9871	0.2780	-0.0788	33.39
Case C	0.0	0.85	1.0776	0.2920	0.3044	-0.0850	33.51
Case D	-0.015	0.88	0.7344	0.1980	0.3073	-0.0860	33.53
Experiment		1.28	0.75	0.20	0.272	-0.082	32.74

Chapter 9

Conclusions

This research developed an efficient and accurate methodology to resolve flow non-linearity of fluid-structural interaction. A numerical strategy to apply the detached-eddy simulation with a fully coupled fluid-structural interaction model is established for the first time. The following novel numerical algorithms are created: a general sub-domain boundary mapping procedure for parallel computation to reduce wall clock simulation time, an efficient and low diffusion E-CUSP (LDE) scheme used as a Riemann solver to resolve discontinuities with minimal numerical dissipation, and an implicit high order accuracy WENO scheme to capture shock waves.

The Detached-Eddy Simulation is based on the model proposed by Spalart in 1997. Near solid walls within wall boundary layers, the Reynolds averaged Navier-Stokes (RANS) equations are solved. Outside of the wall boundary layers, the 3D filtered compressible Navier-Stokes equations are solved based on large eddy simulation(LES). The Spalart-Allmaras one equation turbulence model is solved to provide the Reynolds stresses in the RANS region and provide the subgrid scale stresses in the LES region. The validation of the DES strategy is performed by simulating the flow field of a cylinder. The computed results agree well with the experiment except that the peak values of Reynolds stress are some what under predicted. The computation of mesh refinement indicates that DES is significantly affected by grid size due to the modeled stress depletion (MSD) effect. The

implementation of DDES as the next step is expected to remove this problem.

The numerical experiments show that the developed LDE scheme is able to capture crisp shock profiles and exact contact surfaces with the improved 5th order finite differencing WENO scheme. The fully conservative 4th order finite central differencing schemes used for the viscous terms are verified to be efficient and accurate. The LDE scheme is more efficient than the Roe scheme when coupled with the S-A one equation model. The extra equation of the S-A turbulence model changes the Jacobian of the Roe scheme, weakens the diagonal dominance, reduces the maximum CFL number permitted by the Roe scheme, and hence decreases the convergence rate. Both the LDE and the Roe scheme predict good results when compared with the experiment in the validation cases. The computed results of the LDE scheme agree very well with those of Roe scheme. The numerical experiments also show that the strategy of using conservative finite differencing discretization to an existing finite volume code is achieved without changing the structure of the code. Hence, the code runs with high efficiency when using high order WENO scheme. For the time accurate unsteady simulation, the Jameson's dual time step method with the unfactored Gauss-Seidel relaxation iteration shows very good performance in this research.

A general sub-domain boundary mapping procedure is developed for arbitrary topology multi-block structured grids with grid points matched on sub-domain boundaries. The interface of two adjacent blocks is uniquely defined according to each local mesh index system (MIS) which is specified independently. A pack/unpack procedure based on the definition of the interface is developed to exchange the data in a 1D array to minimize data communication. A secure send/receive procedure is employed to remove the possibility of blocked communication and achieve optimum parallel computation efficiency. Two terms, "*Order*" and "*Orientation*", are introduced as the logics defining the relationship of adjacent blocks. The domain partitioning treatment of the implicit matrices is to simply discard the corner matrices so that the implicit Gauss-Seidel iteration can be implemented within each subdomain. The numerical experiments indicate that the effect of this implicit treatment on the convergence rate is small. The message passing interface (MPI) protocol is

used for the data communication. The code is portable to any platform as long as the MPI is available. The numerical experiments including 2D and 3D RANS and DES simulations show that the general mapping procedure developed in this research is robust and have high scalability

The DES solver with fully coupled fluid-structural interaction methodology is validated with vortex induced vibration of a cylinder and a transonic forced pitching airfoil. For the cylinder, the laminar Navier-Stokes equations are solved due to the low Reynolds number. The 3D effects are observed in both stationary and oscillating cylinder simulation because of the flow separations behind the cylinder. For the transonic forced pitching airfoil DES computation, there is no flow separation in the flow field. The DES results agree well with the RANS results. These two cases indicate that the DES has more effects on the flow fields with separation.

The code is then used to simulate the limited cycle oscillation of NLR7301 airfoil in 2D RANS mode with the S-A one equation model and 3D DES mode. At experimental Mach number of 0.768, the computed LCO amplitudes and frequency are in excellent agreement with experiment by adjusting AoA and α_0. The time averaged lift and moment coefficients also match the experiment very well using RANS model. The free-stream Mach number has the major effect on the amplitudes of LCO due to different shock/boundary layer interaction patterns. The initial flow field or initial perturbation has a strong influence on the amplitudes of LCO. The prediction accuracy is on the same order of the experiment measurement uncertainty. The only primary difference from the experiment is that the α_0 used in the simulation is $0.75°$ for RANS model and $0.88°$ for DES model, whereas the experimental value is $1.28°$. The α_0 only affects the initial moment imposed on the elastic system and remains as a constant in the whole LCO process. Such difference may be attributed to the uncertainty of the experiment and numerical simulation, and the sensitive nature of LCO to initial perturbations, which are difficult if not impossible to be made the same between the experiment and numerical simulation.

This research appears to be the first time that a numerical simulation of NLR7301 airfoil

LCO matches the experiment. It may be attributed to the high order low diffusion numerical schemes, the fully coupled FSI model, and the turbulence model used in this research.

The simulations of LCO also confirm some of the experimental observations and answers some important questions. First, The LCOs with the small relative amplitude is captured with unbounded flows in the numerical simulation. This means they should not be the artifacts of the wind-tunnel experiment and most likely are the factual phenomenon. Second, the co-existence of multiple LCOs at constant flow conditions is confirmed in our simulation. The reason that other numerical simulations only capture the LCOs with large amplitudes may be due to their high numerical dissipation that either smears out the small amplitude LCO or is only able to resolve the large amplitudes LCOs. Third, the numerical simulation of this research confirms that the wall boundary layer transition from laminar to turbulent does not have a large effect on LCOs at high Reynolds number because our simulation assumes that the boundary layer is fully turbulent from the airfoil leading edge. Fourth, the simulation confirms that the wind tunnel wall interference with or without perforated test section does not have much effect on LCOs because the present simulation uses the unbounded flow condition with no wind tunnel wall effect at all. Fifth, the numerically captured LCO at Mach 0.768 is not accompanied with any flow separation due to the very small amplitude. This may modify the hypothesis that the LCOs are caused by the nonlinearity of flow separation induced by shock/boundary layer interaction. In other words, the nonlinearity of shock/boundary layer interaction with no flow separation is sufficient to trigger a LCO. This may also make reduced numerical models feasible to capture LCOs with reasonable accuracy.

In conclusion, the numerical strategy of the high order DES with fully coupled FSI model and parallel computing developed in this research is demonstrated to have high accuracy, robustness, and efficiency.

Chapter 10

Future Work

Although a good progress has been achieved in the present research, the following are the areas that need to be further improved.

Multi-grid Method

Computation efficiency is always an important issue in the numerical simulation. High order CFD schemes are generally more CPU time consuming because of the large amount of mesh points used and the complicated numerical algorithms. The multi-grid method has been shown to be a effective convergence acceleration method. It is expected that the multi-grid method with the implicit Gauss-Seidel relaxation may further improve the computation convergence and reduce the CPU time.

Detached-Eddy Simulation

Detached-eddy simulation is a relatively new method. Numerical experiments show that it is affected by the grid due to the MSD. To overcome the MSD problem and make the DES limiter independent of grid spacing, Spalart suggested a modification to the original DES97 model in 2006 [63], referred to as Delayed DES(DDES). The DDES model has

demonstrated excellent agreement with experiment and a significant improvement over the DES97 for the tested cases. The implementation of DDES is expected to remove the MSD problem.

Wall Boundary Condition

At the current work, it is observed that sometimes the high order wall boundary condition (BC) are not as robust as the 2nd order wall BC. Further work is needed to make the high order wall BC more robust.

Control of Limit Cycle Oscillation

By using different initial flow condition, various factors affecting LCO have been investigated. A group of parameters have been found sensitive to the LCO of NLR7301 airfoil. This make it possible to control the formation of LCO by adjusting the initial flow field, which could be a new interesting research area.

Appendix A

Nonlinear equations of airfoil vibration motion

A solid flexibly supported airfoil is shown in Fig. A.1, A.2 and A.3. In Fig. A.1, the position of the elastic axis (EO), the center of gravity (T) and the airfoil chord (c) are sketched. The airfoil can be vertically displaced and rotated about EO. Fig. A.2 shows the elastic support of the airfoil on translational and rotational springs.
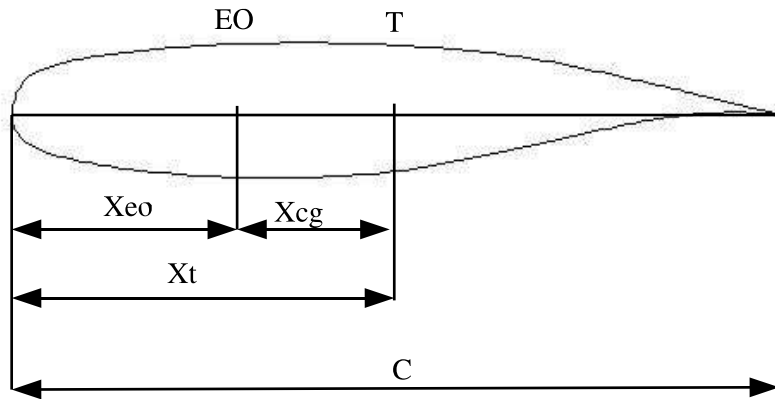
Figure A.1: The position of the elastic axis (EO), the centre of gravity (T) and the chord (c)

The pressure and viscous forces acting on the vibrating airfoil are determined by the components of the stress tensor and result in the lift force $L(t)$ and the torsional moment $M(t)$. The airfoil in neutral and deformed positions is shown in Fig. A.3. Based on the

neutral position, the horizontal and vertical displacements of any point on the airfoil chord
can be expressed as

$$u = x(1 - cos\alpha), w = h + xsin\alpha \tag{A.1}$$

respectively. Here x denotes the local coordinates measured along the airfoil chord c from
the elastic axis. The kinetic energy E_K of the airfoil has the form

$$
\begin{aligned}
E_K &= \int_c \frac{1}{2}\left[\left(\frac{\partial w}{\partial t}\right)^2 + \left(\frac{\partial u}{\partial t}\right)^2\right]\rho_S(x)\,dx \\
&= \frac{1}{2}\int_c\left[(\dot{h} + x\dot{\alpha}cos\alpha)^2 + (x\dot{\alpha}sin\alpha)^2\right]\rho_S(x)\,dx
\end{aligned}
\tag{A.2}
$$

where ρ_S denotes the density of the airfoil per unit length. With further rearrangement of
Eq. (A.2) we obtain

$$
\begin{aligned}
E_K &= \frac{1}{2}\dot{h}^2\int_c\rho_S(x)\,dx + \dot{h}\dot{\alpha}cos\alpha\int_c x\rho_S(x)\,dx + \\
&\quad \frac{1}{2}\dot{\alpha}^2cos^2\alpha\int_c x^2\rho_S(x)\,dx + \frac{1}{2}\dot{\alpha}^2sin^2\alpha\int_c x^2\rho_S(x)\,dx \\
&= \frac{1}{2}\dot{h}^2 m + \dot{h}\dot{\alpha}cos\alpha S_\alpha + \frac{1}{2}\dot{\alpha}^2 I_\alpha
\end{aligned}
\tag{A.3}
$$

where

$m = \int_c\rho_S(x)\,dx$ is the mass of the airfoil,

$S_\alpha = \int_c x\rho_S(x)\,dx$ is the static moment around the elastic axis EO,

$I_\alpha = \int_c x^2\rho_S(x)\,dx$ is the inertia moment around the elastic axis EO,

The potential energy V of the airfoil is

$$V = \frac{1}{2}k_h h^2 + \frac{1}{2}k_\alpha \alpha^2 \tag{A.4}$$

where k_h and k_α are the bending stiffness and torsional stiffness respectively.

Kinetic and potential energy have to satisfy the Lagrange equations

$$\frac{d}{dt}\frac{\partial E_K}{\partial \dot{q}_j} - \frac{\partial E_K}{\partial q_j} + \frac{\partial V}{\partial q_j} = Q_j \tag{A.5}$$

where q_j (j=1,2) are generalized coordinates, i.e. h and α in this case, and Q_j are general-

ized forces, i.e. the aerodynamic force $L(t)$ and the moment $M(t)$.
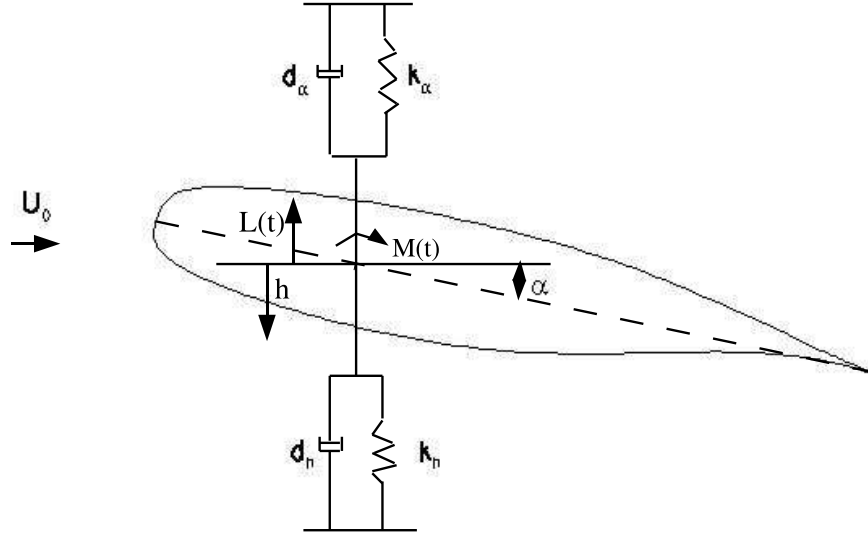
Figure A.2: The elastic support of the airfoil on translational and rotational springs

Thus, for j=1,2 we have

$$\frac{d}{dt}\left[\dot{h}m + \dot{\alpha}cos\alpha S_\alpha\right] + k_h h = -L(t)$$
$$\frac{d}{dt}\left[\dot{h}cos\alpha S_\alpha + \dot{\alpha}I_\alpha\right] + \dot{h}\dot{\alpha}sin\alpha S_\alpha + k_h = M(t) \tag{A.6}$$

Differentiation with respect to time in Eq. (A.6) yields the nonlinear equations of motion of the airfoil

$$m\ddot{h} + S_\alpha\ddot{\alpha}cos\alpha - S_\alpha\dot{\alpha}^2 sin\alpha + k_h h = -L(t)$$
$$S_\alpha\ddot{h}cos\alpha + I_\alpha\ddot{\alpha} + k_\alpha\alpha = M(t) \tag{A.7}$$

For small values of the angle α and of its derivative $\dot{\alpha}$ (i.e. $sin\alpha \approx \alpha, cos\alpha \approx 1, \dot{\alpha}\alpha \approx 0$), Eq. (A.7) yield the well known linearized system

$$m\ddot{h} + S_\alpha\ddot{\alpha} + k_h h = -L(t)$$
$$S_\alpha\ddot{h} + I_\alpha\ddot{\alpha} + k_\alpha\alpha = M(t) \tag{A.8}$$

Including viscous damping terms leads to the governing equations
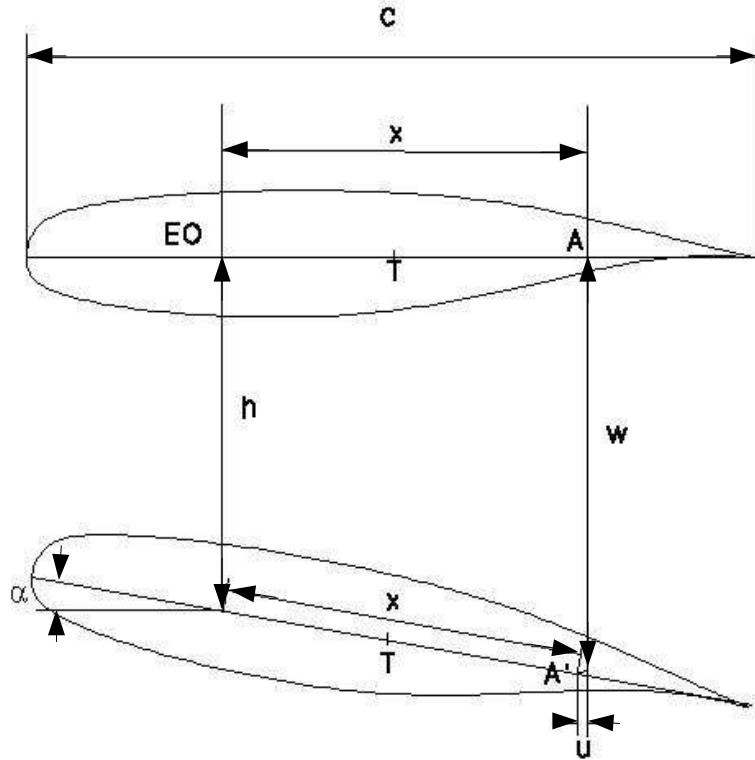
Figure A.3: The airfoil in neutral and deformed position

$$m\ddot{h} + S_\alpha \ddot{\alpha} + d_h \dot{h} + k_h h = -L(t)$$
$$S_\alpha \ddot{h} + I_\alpha \ddot{\alpha} + d_\alpha \dot{\alpha} + k_\alpha \alpha = M(t)$$

(A.9)

Appendix B

Derivation of Spalart-Allmaras Equation (Eq.(2.23))

For the left hand side of Eq.(2.22),

$$
\begin{aligned}
\rho \frac{D\tilde{v}}{Dt} &= \rho \left(\frac{\partial \tilde{v}}{\partial t} + \vec{V} \cdot \nabla \tilde{v} \right) \\
&= \rho \frac{\partial \tilde{v}}{\partial t} + \rho \vec{V} \cdot \nabla \tilde{v} \\
&= \frac{\partial \rho \tilde{v}}{\partial t} - \tilde{v} \frac{\partial \rho}{\partial t} + \nabla \cdot \left(\rho \tilde{v} \vec{V} \right) - \tilde{v} \nabla \cdot \left(\rho \vec{V} \right) \\
&= \frac{\partial \rho \tilde{v}}{\partial t} + \nabla \cdot \left(\rho \tilde{v} \vec{V} \right) - \tilde{v} \left[\frac{\partial \rho}{\partial t} + \nabla \cdot \left(\rho \vec{V} \right) \right] \\
&= \frac{\partial \rho \tilde{v}}{\partial t} + \nabla \cdot \left(\rho \tilde{v} \vec{V} \right)
\end{aligned}
\tag{B.1}
$$

For the right hand side of Eq.(2.22),

$$
\begin{aligned}
&\frac{\rho}{\sigma} \left[\nabla \cdot \left((v + \tilde{v}) \nabla \tilde{v} \right) + c_{b2} (\nabla \tilde{v})^2 \right] \\
&= \frac{\rho}{\sigma} \nabla \cdot \left((v + \tilde{v}) \nabla \tilde{v} \right) + \frac{\rho}{\sigma} c_{b2} (\nabla \tilde{v})^2 \\
&= \nabla \cdot \left[\frac{\rho}{\sigma} (v + \tilde{v}) \nabla \tilde{v} \right] - \frac{1}{\sigma} (v + \tilde{v}) \nabla \tilde{v} \cdot \nabla \rho + \frac{\rho}{\sigma} c_{b2} (\nabla \tilde{v})^2
\end{aligned}
\tag{B.2}
$$

Let S_v be the source term:

$$
\begin{aligned}
S_v = \ & \rho c_{b1} \tilde{S} \tilde{v} (1 - f_{t2}) - \rho \left(c_{w1} f_w - \frac{c_{b1}}{\kappa^2} f_{t2} \right) \left(\frac{\tilde{v}}{d} \right)^2 - \\
& \frac{1}{\sigma} (v + \tilde{v}) \nabla \tilde{v} \cdot \nabla \rho + \frac{\rho}{\sigma} c_{b2} (\nabla \tilde{v})^2 + \rho f_{t1} (\Delta q)^2
\end{aligned}
\tag{B.3}
$$

The conservative form of Eq.(2.22) can be written as

$$\frac{\partial \rho \tilde{v}}{\partial t} + \nabla \cdot \left(\rho \tilde{v} \vec{V} \right) = \nabla \cdot \left[\frac{\rho}{\sigma} (v + \tilde{v}) \nabla \tilde{v} \right] + S_v \tag{B.4}$$

The dimensionless flow variables in the governing equations are defined as the following,

$$\bar{x} = \frac{x}{L}, \quad \bar{y} = \frac{y}{L}, \quad \bar{z} = \frac{z}{L},$$
$$\bar{u} = \frac{u}{U_\infty}, \quad \bar{v} = \frac{v}{U_\infty}, \quad \bar{w} = \frac{w}{U_\infty},$$
$$\bar{\rho} = \frac{\rho}{\rho_\infty}, \quad \bar{\tilde{v}} = \frac{\tilde{v}}{\mu_\infty/\rho_\infty}, \quad \bar{t} = \frac{t}{L/U_\infty}$$

where the bar denotes dimensionless variable, the free stream conditions are denoted by ∞, L is the reference length used in the Reynolds number Re_L,

$$\mathrm{Re}_L = \frac{\rho_\infty U_\infty L}{\mu_\infty} \tag{B.5}$$

For the left hand side of Eq.(B.4),

$$\begin{aligned}
\frac{\partial \rho \tilde{v}}{\partial t} + \nabla \cdot \left(\rho \tilde{v} \vec{V} \right) &= \frac{\partial \rho \tilde{v}}{\partial t} + \frac{\partial \rho u \tilde{v}}{\partial x} + \frac{\partial \rho v \tilde{v}}{\partial y} + \frac{\partial \rho w \tilde{v}}{\partial z} \\
&= \frac{\mu_\infty u_\infty}{L} \left[\frac{\partial \bar{\rho} \bar{\tilde{v}}}{\partial \bar{t}} + \frac{\partial \bar{\rho} \bar{u} \bar{\tilde{v}}}{\partial \bar{x}} + \frac{\partial \bar{\rho} \bar{v} \bar{\tilde{v}}}{\partial \bar{y}} + \frac{\partial \bar{\rho} \bar{w} \bar{\tilde{v}}}{\partial \bar{z}} \right] \\
&= \frac{\mu_\infty u_\infty}{L} \left[\frac{\partial \bar{\rho} \bar{\tilde{v}}}{\partial \bar{t}} + \bar{\nabla} \cdot \left(\bar{\rho} \bar{\tilde{v}} \vec{\bar{V}} \right) \right]
\end{aligned} \tag{B.6}$$

where,

$$\bar{\nabla} = \vec{i} \frac{\partial}{\partial \bar{x}} + \vec{j} \frac{\partial}{\partial \bar{y}} + \vec{k} \frac{\partial}{\partial \bar{z}}$$

For the right hand side of Eq.(B.4),

$$\nabla \cdot \left[\frac{\rho}{\sigma} (v + \tilde{v}) \nabla \tilde{v} \right] = \frac{\mu_\infty^2}{L^2 \rho_\infty} \bar{\nabla} \cdot \left[\frac{\bar{\rho}}{\sigma} (\bar{v} + \bar{\tilde{v}}) \bar{\nabla} \bar{\tilde{v}} \right] \tag{B.7}$$

The first term of S_v:

$$\rho c_{b1}\tilde{S}\tilde{v}\left(1-f_{t2}\right)=\bar{\rho}c_{b1}\left(1-f_{t2}\right)\left(\frac{\mu_{\infty}U_{\infty}}{L}\bar{S}+\frac{\mu_{\infty}^{2}}{L^{2}\rho_{\infty}}\frac{\bar{\tilde{v}}}{\kappa^{2}\bar{d}^{2}}f_{v2}\right)\bar{\tilde{v}} \tag{B.8}$$

The second term of S_{v}:

$$\rho\left(c_{w1}f_{w}-\frac{c_{b1}}{\kappa^{2}}f_{t2}\right)\left(\frac{\tilde{v}}{d}\right)^{2}=\frac{\mu_{\infty}^{2}}{L^{2}\rho_{\infty}}\bar{\rho}\left(c_{w1}f_{w}-\frac{c_{b1}}{\kappa^{2}}f_{t2}\right)\left(\frac{\bar{\tilde{v}}}{\bar{d}}\right)^{2} \tag{B.9}$$

The third term of S_{v}:

$$\frac{1}{\sigma}(v+\tilde{v})\nabla\tilde{v}\cdot\nabla\rho=\frac{\mu_{\infty}^{2}}{L^{2}\rho_{\infty}}\frac{1}{\sigma}\left(\bar{v}+\bar{\tilde{v}}\right)\bar{\nabla}\bar{\tilde{v}}\cdot\bar{\nabla}\bar{\rho} \tag{B.10}$$

The fourth term of S_{v}:

$$\frac{\rho}{\sigma}c_{b2}(\nabla\tilde{v})^{2}=\frac{\mu_{\infty}^{2}}{L^{2}\rho_{\infty}}\frac{\bar{\rho}}{\sigma}c_{b2}\left(\bar{\nabla}\bar{\tilde{v}}\right)^{2} \tag{B.11}$$

The fifth term of S_{v}:

$$\rho f_{t1}\left(\Delta q\right)^{2}=\rho_{\infty}U_{\infty}^{2}\bar{\rho}f_{t1}\left(\Delta\bar{q}\right)^{2} \tag{B.12}$$

The Eq.(B.4) then can be written as the following,

$$
\begin{aligned}
\frac{\partial\bar{\rho}\bar{\tilde{v}}}{\partial\bar{t}}+\bar{\nabla}\cdot\left(\bar{\rho}\bar{\tilde{v}}\bar{\vec{V}}\right) &=\frac{1}{Re}\bar{\nabla}\cdot\left[\frac{\bar{\rho}}{\sigma}(\bar{v}+\bar{\tilde{v}})\bar{\nabla}\bar{\tilde{v}}\right]+\bar{\rho}c_{b1}\left(1-f_{t2}\right)\left(\bar{S}+\frac{1}{Re}\frac{\bar{\tilde{v}}}{\kappa^{2}\bar{d}^{2}}f_{v2}\right)\bar{\tilde{v}}-\\
&\quad\frac{1}{Re}\bar{\rho}\left(c_{w1}f_{w}-\frac{c_{b1}}{\kappa^{2}}f_{t2}\right)\left(\frac{\bar{\tilde{v}}}{\bar{d}}\right)^{2}-\frac{1}{Re}\frac{1}{\sigma}\left(\bar{v}+\bar{\tilde{v}}\right)\bar{\nabla}\bar{\tilde{v}}\cdot\bar{\nabla}\bar{\rho}+\\
&\quad\frac{1}{Re}\frac{\bar{\rho}}{\sigma}c_{b2}\left(\bar{\nabla}\bar{\tilde{v}}\right)^{2}+Re\bar{\rho}f_{t1}\left(\Delta\bar{q}\right)^{2}
\end{aligned}
\tag{B.13}
$$

For convenience, we drop the bar used in Eq.(B.13). Following the deriving process of Hu's PhD thesis [136], Eq.(B.13) can be transformed from Cartesian coordinate system to the generalized coordinate system as the following

$$
\begin{aligned}
\frac{\partial\frac{1}{J}\rho\tilde{v}}{\partial t}+\frac{\partial\rho\tilde{v}U}{\partial\xi}+\frac{\partial\rho\tilde{v}V}{\partial\eta}+\frac{\partial\rho\tilde{v}W}{\partial\zeta} &=\\
\frac{1}{Re}\left(\frac{\partial\frac{\rho}{\sigma}(v+\tilde{v})(\mathbf{l}\bullet\nabla\tilde{v})}{\partial\xi}+\frac{\partial\frac{\rho}{\sigma}(v+\tilde{v})(\mathbf{m}\bullet\nabla\tilde{v})}{\partial\eta}+\frac{\partial\frac{\rho}{\sigma}(v+\tilde{v})(\mathbf{n}\bullet\nabla\tilde{v})}{\partial\zeta}+\frac{1}{J}S_{v}\right)
\end{aligned}
\tag{B.14}
$$

It is the Eq.(2.23).

Appendix C

Publications

Journal Papers

1. Wang, B.-Y. and Zha, G.-C., "A General Sub-Domain Boundary Mapping Procedure For Structured Grid CFD Parallel Computation", *AIAA Journal of Aerospace Computing, Information, and Communication, Vol.5, No.11, pp425-447*, Nov.2008.

2. Wang, B.-Y., Haddoukessouni, B., Levy, J. and Zha, G.-C., "Numerical Investigations of Injection Slot Size Effect on the Performance of Co-Flow Jet Airfoil", *AIAA Journal of Aircraft, Vol.45, No.6, pp2084-2091*, Nov.-Dec.2008.

3. Shen, Y.-Q. and Zha, G.-C. and Wang, B.-Y., "Improvement of Stability and Accuracy for Weighted Essentially Nonoscillatory Scheme", *AIAA Journal, Vol.47, No.2, pp331-344*, Feb.2009.

4. Chen, X.-Y. and Zha, G.-C. and Yang, M.-T. "Numerical Simulation of 3-D Wing Flutter with Fully Coupled Fluid-Structural Interaction ", *Journal of Computers & Fluids, Vol. 36, No. 5,* June 2007, pp856-867

5. Chen, X. and Zha, G.-C., "Implicit Application of Non-Reflective Boundary Conditions for Navier-Stokes Equations in Generalized Coordinates ", *International Journal for Numerical Methods in Fluids*, Vol. 50, No. 7, pp767-793, 2006

167

6. Chen, X. and Zha, G.-C.,"Fully Coupled Fluid-Structural Interactions Using an Efficient High Solution Upwind Scheme", *Journal of Fluid and Structure*, Vol. 20, No. 8, Nov. 2005, pp1105-1125,

Conference Papers

1. Y. Shen and G.-C. Zha, "High Order Finite Differencing Schemes and Their Accuracy for CFD ", AIAA Paper 2009-1137, 47th AIAA Aerospace Sciences Meeting, 5 - 8 Jan. 2009, Orlando, FL

2. Y. Shen and G.-C. Zha, "Comparison of High Order Schemes for Large Eddy Simulation of Circular Cylinder Flow", AIAA Paper 2009-0945, 47th AIAA Aerospace Sciences Meeting, 5 - 8 Jan. 2009, Orlando, FL

3. Yiqing Shen, Ge-Cheng Zha, and Xiangying Chen "High Order Conservative Differencing for Viscous Terms and the Application to Vortex-Induced Vibration Flows", AIAA Paper 2008-4059, AIAA 38th Fluid Dynamics Conference and Exhibit, 23 - 26 Jun 2008, Seattle, Washington

4. Yiqing Shen and Ge-Cheng Zha "Improvement of the WENO Scheme Smoothness Estimator", AIAA Paper 2008-3993, AIAA 38th Fluid Dynamics Conference and Exhibit, 23 - 26 Jun 2008, Seattle, Washington

5. Yiqing Shen and Ge-Cheng Zha, "A Robust Seventh-order WENO Scheme and Its Applications", AIAA Paper 2008-0757, 46th AIAA Aerospace Sciences Meeting and Exhibit, Jan. 7-10, 2008, Reno, NV

6. Yiqing Shen, Baoyuan Wang and G. Zha, "Comparison Study of Implicit Gauss-Seidel Line Iteration Method for Transonic Flows",AIAA Paper 2007-4332 18th AIAA Computational Fluid Dynamics Conference, June 25-28, 2007

7. Yiqing Shen, Baoyuan Wang and G. Zha, "Implicit WENO Scheme and High Order Viscous Formulas for Compressible Flows",AIAA Paper 2007-4431 25th AIAA Applied Aerodynamics Conference, June 25-28, 2007

8. Baoyuan Wang and Ge-Cheng Zha, "Detached-Eddy Simulation of Transonic Limit Cycle Oscillations Using High Order Schemes", AIAA Paper 2009-1507, AIAA 47th AIAA Aerospace Sciences Meeting and Exhibit,Jan. 5-8, 2009, Orlando, FL.

9. Baoyuan Wang, Ge-Cheng Zha, and Yiqing Shen "Detached-Eddy Simulations of a Circular Cylinder Using a Low Diffusion E-CUSP and High-Order WENO Scheme", AIAA Paper 2008-3855, AIAA 38th Fluid Dynamics Conference and Exhibit, June 23-26, 2008, Seattle, Washington.

10. Baoyuan Wang and Ge-Cheng Zha, "Comparison of a Low Diffusion E-CUSP and the Roe Scheme for RANS Calculation",AIAA Paper 2008-0596, 46th AIAA Aerospace Sciences Meeting and Exhibit, Jan. 7-10, 2008, Reno, NV.

11. Ge-Cheng Zha, Yiqing Shen and Baoyuan Wang, "Calculation of Transonic Flows Using WENO Method with a Low Diffusion E-CUSP Upwind Scheme", AIAA Paper 2008-0745, 46th AIAA Aerospace Sciences Meeting and Exhibit, Jan. 7-10, 2008, Reno, NV.

12. John Aguirre, Baoyuan Wang and G.-C. Zha, "Conceptual Design and Study of "Engineless" Airplane Using Co-Flow Jet Airfoil",AIAA Paper 2007-4441 25th AIAA Applied Aerodynamics Conference, June 25-28, 2007, Miami, FL.

13. Yiqing Shen, Baoyuan Wang and G. Zha, "Comparison Study of Implicit Gauss-Seidel Line Iteration Method for Transonic Flows",AIAA Paper 2007-4332 18th AIAA Computational Fluid Dynamics Conference, June 25-28, 2007, Miami, FL.

14. Yiqing Shen, Baoyuan Wang and G. Zha, "Implicit WENO Scheme and High Order Viscous Formulas for Compressible Flows",AIAA Paper 2007-4431 25th AIAA Applied Aerodynamics Conference, June 25-28, 2007, Miami, FL.

References

[1] Bendiksen, O. O. and Seber, G., "Fluid-structure interactions with both structural and fluid nonlinearities," *Journal of Sound and vibration*, Vol. 315, 2008.

[2] Tang, L., Bartels, R. E., Chen, P.-C., and Liu, D. D., "Numerical investigation of transonic limit cycle oscillations of a two-dimensional supercritical wing," *Journal of Fluid and Structures*, Vol. 17, 2003.

[3] Bendiksen, O. O., "Role of Shock Dynamics in Transonic Flutter," AIAA Paper 92-2121.

[4] Hall, K. C., Thomas, J., and Dowell, E., "Proper orthogonal decomposition technique for transonic unsteady aerodynamic flows," *AIAA Journal*, Vol. 38, 2000.

[5] Dowell, E. and Hall, K., "Modeling of Fluid-Structure Interaction," *Annual Review of Fluid Mechanics*, Vol. 33, 2001.

[6] Thomas, J., Dowell, E., and Hall, K. C., "Three-dimensional transonic aeroelasticity using proper orthogonal decomposition based reduced-order models," *Journal of Aircraft*, Vol. 40, 2003.

[7] Dowell, E., Thomas, J., and Hall, K., "Transonic limit cycle oscillation analysis using reduced order aerodynamic models," *Journal of Fluid and Structures*, Vol. 19, 2004.

[8] Lucia, D., Beran, P., and Silva, J., "Reduced-order models: new approaches for computational physics," *Progress in Aerospace Sciences*, Vol. 40, 2004.

[9] Beran, P. and Silva, J., "Reduced-order modeling: new approaches for computational physics," AIAA Paper 2001-0853.

[10] Silva, W. A. and Raveh, D. E., "Development of unsteady aerodynamic state-space models from CFD-based pulse responses," AIAA Paper 2001-1213.

[11] Silva, W. A. and Bartels, R. E., "Development of reduced-order models for aeroelastic analysis and flutter prediction using the CFL3Dv6.0 code," *Journal of Fluid and Structures*, Vol. 19, 2004.

[12] Sarkar, S. and Venkatraman, K., "Model order reduction of unsteady flow past oscillating airfoil cascades," *Journal of Fluid and Structures*, Vol. 19, 2004.

[13] Beran, P., Lucia, D., and Pettit, C. L., "Reduced-order modelling of limit-cycle oscillation for aeroelastic systems," *Journal of Fluid and Structures*, Vol. 19, 2004.

[14] Tang, D. M. and Dowell, "Effects of geometric structural non-linearity on flutter and limit cycle oscillations of high-aspect-ratio wings," *Journal of Fluid and Structures*, Vol. 19, 2004.

[15] Tran, D.-M., Liauzun, C., and Labaste, C., "Methods of fluid-structure coupling in frequency and time domain using linearized aerodynamics for turbomachinery," *Journal of Fluid and Structures*, Vol. 17, 2004.

[16] Moffatt, S. and He, L., "On decoupled and fully-coupled methods for blade forced response prediction," *Journal of Fluid and Structures*, Vol. 20, 2004.

[17] Melville, R. B. and Morton, S. A., "Fully Implicit Aeroelasticity on Oveerset Grid Systems ," AIAA Paper-98-0521, 1998.

[18] Bendiksen, O. and Kousen, K., "Transonic Flutter Analysis Using the Euler Equations," AIAA Paper 87-0911, 1987.

[19] Guruswamy, G., "Unsteady Aerodynamic and Aeroelastic Calculations for Wings Using Euler Equations," *AIAA Journal*, Vol. 28, March 1990, pp. 461–469.

[20] Lee-Rausch, E. and Batina, J., "Wing Flutter Computations Using an AerodynamicsModel Based on the Navier-Stokes Equations," *Journal of Aircraft*, Vol. 33, 00, pp. 1139–1147.

[21] Smith, M., "Flight Loads Prediction Methods for Aircraft: Vol I. Euler/Navier-Stokes Aeroelastic Method (ENS3DAE) Technical Development Summary: Version 4.0," WRDC-TR-89-3104, 1989.

[22] Vermeersch, S., Raj, P., Weed, R., and Sankar, L., "Towards Cost-Effective Aeroelastic Analysis on Advanced Parallel Computing Systems ," AIAA Paper 97-0646, 1997.

[23] Darracq, S., Champagneux, S., and Corjon, A., "Computation of Unsteady Turbulent Airfoil Flows with an Aeroelastic AUSM+ Implicit Solver," AIAA Paper-98-2411, 1998.

[24] Prananta, B. B., L., H. M. H., and J., Z. R., "Two-Dimensional Transonic Aeroelastic Analysis Using Thin-Layer Navier-Stokes Method," *Journal of Fluid and Structures*, Vol. 12, 1998, pp. 655–676.

[25] Bohbot, J. and Darracq, D., "Time Domain Analysis of Two D.O.F. Airfoil Flutter Using an Euler/Turbulent Navier-Stokes Implicit Solver," International Forum on Aeroelasticity and Structural Dynamics, Madrid, Spain, June 5-7, 2001.

[26] Blom, F. J. and Leyland, P., "Analysis of Fluid-Structure Interaction by Means of Dynamic Unstructured Meshes," AD-Vol. 53-3, 4th International Symposium on Fluid-Structure Interaction, Aeroelasticity, Flow-Induced Vibrations and Noise, Volume I, ASME, 1997.

[27] Alonso, J. J. and Jameson, A., "Fully-Implicit Time-Marching Aeroelastic Solutions," AIAA Paper 94-0056, 1994.

[28] Alonso, J., Martinelli, L., and Jameson, A., "Multigrid Unsteady Navier-Stokes Calculations with Aeroelastic Applications," AIAA Paper 95-0048, 1995.

[29] Morton, S. A., Melville, R. B., and Visbal, M. R., "Accuracy and Coupling Issues of Aeroelastic Navier-Stokes Solutions on Deforming Meshes," AIAA Paper-97-1085, 1997.

[30] Melville, R. B. and Morton, S. A. and Rizzetta, D. P., "Implementation of a Fully-Implicit, Aeroelastic Navier-Stokes Solver," AIAA Paper-97-2039, 1997.

[31] Liu, F., Cai, J., Zhu, Y., Wong, A., and Tsai, H., "Calculation of Wing Flutter by a Coupled CFD-CSD Method," *Journal of Aircraft*, Vol. 38, 2001.

[32] Chen, X.-Y., Zha, G.-C., and Hu, Z.-J., "Numerical Simulation of Flow Induced Vibration Based on Fully Coupled-Structural Interactions," AIAA Paper 2004-2240, AIAA 34th AIAA Fluid Dynamics Conference,, Jaun 28 - July 1, 2004.

[33] Chen, X.-Y. and Zha, G.-C., "Fully Coupled Fluid-Structural Interactions Using an Efficient High Resolution Upwind Scheme," *Journal of Fluids and Structures*, Vol. 20, 2005, pp. 1105–1125.

[34] Chen, X.-Y., Zha, G.-C., and Yang, M.-T., "Numerical Simulation of 3-D Wing Flutter with Fully Coupled Fluid-Structural Interaction," *Journal of Computers & Fluids*, Vol. 36, No. 5, 2007, pp. 856–867.

[35] Hu, Z.-J. and Zha, G.-C., "Calculations of 3D Compressible Using an Efficient Low Diffusion Upwind Scheme," *International Journal for Numerical Methods in Fluids*, Vol. 47, 2004, pp. 253–269.

[36] Zha, G.-C. and Hu, Z.-J., "Calculation of Transonic Internal Flows Using an Efficient High Resolution Upwind Scheme," *AIAA Journal*, Vol. 42, No. 2, 2004, pp. 205–214.

[37] Zha, G.-C., "Low Diffusion Efficient Upwind Scheme ," *AIAA Journal*, Vol. 43, 2005.

[38] Morton, S. and Beran, P. S., "Hopf-bifurcation analysis of airfoil flutter at transonic speeds," *Journal of Aircraft*, Vol. 36, 1999.

[39] Weber, S., Jones, K. D., and Ekaterinaris, J. A.and Platzer, M. F., "Transonic flutter computations for the NLR 7301 supercritical airfoil," *Aerospace Science and Technology*, Vol. 5, 2001.

[40] Schewe, G., Hai, H., and Dietz, G., "Nonlinear effects in transonic flutter with emphasis on manifestations of limit cycle oscillation," *Journal of Fluid and Structures*, Vol. 18, 2003.

[41] Dietz, G., Schewe, G., and Hai, H., "Experiments on Heave/Pitch Limit-Cycle Oscillations of a Supercritical Airfoil Close to the Transonic Dip," *Journal of Fluid and Structures*, Vol. 19, 2004.

[42] Gordnier, R. E., "Computation of Limit-Cycle Oscillations of a Delta Wing," *Journal of Aircraft*, Vol. 40, 2003.

[43] Castro, B., Ekaterinaris, J. A., and Platzer, M. F., "Analysis of the effect of propous wall interference on transonic airfoil flutter," AIAA Paper 2001-2725.

[44] Smagorinsky, J., "General Circulation Experiments with the Primitive Equations, I. The Basic Experiment," *Monthly Weather Review*, Vol. 91, 1963, pp. 99–164.

[45] Lilly, D., "The Presentation of Small-Scale Turbulent in Numerical Simulation Experiments," *IBM Scientific Computing Symp. on Environmental Sciences*, 1967, pp. 195.

[46] Germano, M., Piomeli, U., Moin, P., and Cabot, W., "A Dynamic Subgrid-scale Eddy Viscosity Model," *Physics of Fluids A*, Vol. 3, July 1991, pp. 1760–1765.

[47] Piomeli, U., Cabot, W., Moin, P., and Lee, S., "Subgrid Scale Backscatter in Turbulent and Transitional Flows," *Physics of Fluids A*, Vol. 3, July 1991, pp. 1766–1771.

[48] Deardorff, J., "A Numerical Study of Three Dimensional Turbulent Channel Flow at Large Reynolds Numbers," *Journal of Fluid Mechanics*, Vol. 41, 1970, pp. 453–480.

[49] Kawamura, T. and Kuwahara, K., "Computation of High Reynolds Number Flow Around a Circular Cylinder with Surface Roughness," AIAA Paper-84-0340, 1984.

[50] Grinstein, F., "Dynamics of Coherent Structures and Transition to Turbulence in Free Square Jet," AIAA Paper-96-0781, 1978.

[51] Spalart, P., Jou, W.-H., Strelets, M., and Allmaras, S., "Comments on the Feasibility of LES for Wings, and on a Hybrid RANS/LES Approach," Advances in DNS/LES, 1st AFOSR Int. Conf. on DNS/LES, Greyden Press, Columbus, H., Aug. 4-8, 1997.

[52] Spalart, P. R., "Young-Person's Guide to Detached-Eddy Simulation Grids," NASA/CR-2001-211032, 2001.

[53] Spalart, P. R., "Topics in Detached-Eddy Simulation," .

[54] Tarvin, A., Shur, M., Strelets, M., and Spalart, P., "Detached-Eddy Simulations Past a Circular Cylinder," *Flow Turbulence and Combustion*, Vol. 63, 1999.

[55] Forsythe, J. R., Hoffmann, K. A., and Cummings, R. M. Squires, K. D., "Detached-Eddy Simulations with Compressibility Corrections Applied to Supersonic Axisymmetric Base Flow," *Journal of Fluids Engineering*, Vol. 124, 2002.

[56] Viswanathan, A., Klismith, K., Forsythe, J., and Squires, K. D., "Detached-Eddy Simulation around a Forebody at High Angle of Attack," AIAA-2003-0263, 2003.

[57] Squires, K. D., "Detached-Eddy Simulation: Current Status and Perspectives," .

[58] Squires, K. D., Forsythe, J. R., and Spalart, P. R., "Detached-Eddy Simulation of the Seperated Flow Around a Forebody Cross-Section," .

[59] Hansen, R. P. and Forsythe, J. R., "Large and Detached Eddy Simulation of a Circular Cylinder Using Unstructured Grids," AIAA Paper 2003-0775, Jan. 2003.

[60] Subbareddy, P. and Candler, G. V., "Numerical Investigations of Supersonic Base Flows Using DES," AIAA Paper 2005-0886, Jan. 2005.

[61] Wang, B.-Y. and Zha, G.-C., " Detached Eddy Simulations of a Circular Cylinder Using a Low Diffusion E-CUSP and High-Order WENO Scheme," AIAA Paper 2008-3855, AIAA 38th Fluid Dynamics Conference, Seattle, Washington, June 23-26, 2008.

[62] Wang, B.-Y. and Zha, G.-C., "Dettached Eddy Simulation of Transonic Airfoil Limited Cycle Oscillation with High Order WENO Scheme," AIAA Paper 2009-1507, the 47th AIAA Aerospace Sciences Meeting and Exhibit, Orlando, Florida, 5 - 8 Jan 2009.

[63] Spalart, P., Deck, S., Shur, M., and Squires, K., "A new Version of Detached-Eddy Simulation, Resistant to Ambiguous Grid Densities," *Theoritical and Computational Fluid Dynamics*, Vol. 20, 2006, pp. 181–195.

[64] Rumsey, C., "Successes and Challenges for FLow Control Simulations," AIAA Paper 2008-4311,AIAA 4th Flow COntrol Conference, Seattle, Washington, 23-26 June 2008.

[65] Menter, F. and Kuntz, M., "Adaptation of Eddy-Viscosity Turbulence Models to Unsteady Separated Flow Behind Vehilces, *The Aerodynamics of Heavy Vehicles: Trucks, Buses and Trains, Edited by McCallen, R. Browand, F. and Ross, J. ;" Springer, Berlin Heidelberg New York, 2004*, 2-6 Dec. 2002.

[66] Liu,X. D. and Osher, S. and Chan, T. , "Weighted essentially non-oscillatory schemes," *J.Comput.Phys.*, Vol. 126, 1994, pp. 200–212.

[67] Jiang, G. S. and Shu, C. W. , "Efficient implementation of weighted ENO schemes," *J.Comput.Phys.*, Vol. 126, 1996, pp. 202–228.

[68] Titarev, V. A. and Toro, E. F. , "Finite-volume WENO schemes for three-dimensional conservation laws," *J.Comput.Phys.*, Vol. 201, 2004, pp. 238–260.

[69] Zhou, T. and Li, Y. and Shu, C. W. , "Numerical comparison of WENO finite volume and Runge-Kutta discontinuous Galerkin methods," *J.Sci.Comput.*, Vol. 16, 2001, pp. 145–171.

[70] Latini, M. and Schilling, O. and Don, W. S. , "Effects of WENO flux reconstruction order and spatial resolution on reshocked two-dimensional Richtmyer-Meshkov instability," J. Comput. Phys., 2006, doi:10.1016/j.jcp.2006.06.051, 2006.

[71] Nelida Crnjaric-Zic, Senka Vukovic, Luka Sopta, "Balanced finite volume WENO and central WENO schemes for the shallow water and the open-channel flow equations," *J.Comput.Phys.*, Vol. 200, 2004, pp. 512–548.

[72] Beaza, A. and Mulet, P. , "Adaptive mesh refinement techniques for high-order shock capturing schemes for multi-dimensional hydrodynamic simulations," *International Journal for Numerical Methods in Fluids*, Vol. 52, 2006, pp. 455–471.

[73] Sjogreen, B. and Yee, H. C. , " Low dissipative high-order numerical simulations of supersonic reactive flows," *International Journal for Numerical Methods in Fluids*, Vol. 43, 2003, pp. 1221–1238.

[74] Shu, C.-W., "Essentially Non-Oscillatory and Weighted Essentially Schemesfor Hyperbolic Conservation Laws," NASA/CR-97-206253, 1997.

[75] Van Leer, B., "Towards the Ultimate Conservative Difference Scheme, III," *Journal of Computational Physics*, Vol. 23, 1977, pp. 263–75.

[76] Chen, Y. N. and Yang, S. C. and Yang, J. Y. , "Implicit weighted essentially non-oscillatory schemes for the incompressible Navier-Stokes equations ," *International Journal for Numerical Methods in Fluids*, Vol. 31, 1999, pp. 747–765.

[77] Yang, J. and Perng, Y. and Yen, R. , "Implicit weighted essentially nonoscillatory schemes for the compressible Navier-Stokes equations," *AIAA J.*, Vol. 39, 2001, pp. 2082–2090.

[78] Cadiou, A. and Tenaud, C. , "Implicit WENO shock capturing scheme for unsteady flows. Application to one-dimensional Euler equations," *International Journal for Numerical Methods in Fluids*, Vol. 45, 2004, pp. 197–229.

[79] Yuan, L. , "Comparison of implicit multigrid schemes for three-dimensional incompressible flows," *J. Compu. Phys.*, Vol. 177, 2002, pp. 134–155.

[80] Shen, Y.-Q. and Zha, G.-C., "A Comparison Study of Gauss-Seidel Iteration Methods for Internal and External Flows ," AIAA Paper 2007-4332, 2007.

[81] Zhang, S. H. and Shu, C. W. , "A new smoothness indicator for the WENO schemes and its effect on the convergence to steady state solutions," *Journal of Scientific Computing*, Vol. 31, 2007, pp. 273–305.

[82] Henrick, A. K. and Aslam, T. D. and Powers, J. M. , "Mapped weighted essentially non-oscillatory schemes:Achiving optimal order near critical points," *J.Comput.Phys.*, Vol. 208, 2005, pp. 206–227.

[83] Pantano, C. and Deiterding, R. and Hill, D. J. and Pullin, D. I. , "A low numerical dissipation patch-based adaptive mesh refinement method for large-eddy simulation of compressible flows," *J.Comput.Phys.*, Vol. 221, 2007, pp. 63–87.

[84] Taylor, E.M. and Martin, M.P., "Stencil Adaptation Properties of a WENO Scheme in Direct Numerical Simulations of Compressible Turbulence," *Journal of Scientific Computing*, Vol. 30, 2007, pp. 533–554.

[85] Piraux, J. and Lombard, B. , "A New Interface Method for Hyperbolic Problems with Discontinuous Coefficients: One-Dimensional Acoustic Example," *J.Comput.Phys.*, Vol. 168, 2001, pp. 227–248.

[86] Jameson, A., "Time Dependent Calculations Using Multigrid with Applications to Unsteady Flows Past Airfoils and Wings," AIAA Paper 91-1596, 1991.

[87] Shen, Y.-Q., Zha, G.-C., and Wang, B.-Y., "Improvement of Stability and Accuracy for Weighted Essentially Nonoscillatory Scheme," *AIAA Journal*, Vol. 47, No.2, 2009, pp. 331–344.

[88] Shen, Y.-Q., Zha, G.-C., and Chen, X., "High Order Conservative Differencing for Viscous Terms and the Application to Vortex-Induced Vibration Flows," AIAA Paper 2008-4059, 38th AIAA Fluid Dynamics Conference and Exhibit, Seattle, Washington, 23 - 26 June, 2008.

[89] Jameson, A., Schmidt, W., and Turkel, E., "Numerical Simulation of the Euler Equations by Finite Volume Methods Using Runge-Kutta Time Steping Schemes," AIAA Paper 81-1259, 1981.

[90] Zha, G., *Numerical Solutions of Three-Dimensional Transonic Flows Based on Upwind Schemes*, Ph.D. thesis, University of Montreal, December 1993.

[91] Roe, P., "Approximate Riemann Solvers, Parameter Vectors, and Difference Schemes," *Journal of Computational Physics*, Vol. 43, 1981, pp. 357–372.

[92] Van Leer, B., Thomas, J., Roe, P. L., and Newsome, R., "A Comparison of Numerical Flux Formulas for the Euler and Navier-Stokes Equations," AIAA paper 87-1104, 1987.

[93] Liou, M.-S. and Steffen, C. J., "A New Flux Splitting Scheme," *Journal of Computational Physics*, Vol. 107, 1993, pp. 1–23.

[94] Wada, Y. and Liou, M.-S., "An Accurate and Robust Splitting Scheme for Shock and Contact Discontinuities," AIAA Paper 94-0083, 1994.

[95] Liou, M.-S., "Progress Towards an Improved CFD Methods: AUSM$^+$," AIAA Paper 95-1701-CP, June, 1995.

[96] Liou, M.-S., "A Sequel to AUSM: AUSM$^+$," *Journal of Computational Physics*, Vol. 129, 1996, pp. 364–382.

[97] Liou, M.-S., "Ten Years in the Making-AUSM-Family," AIAA 2001-2521, 2001.

[98] Hänel, D., Schwane, R., and Seider, G., "On the Accuracy of Upwind Schemes for the Solution of the Navier-Stokes Eqautions," AIAA paper 87-1105 CP, 1987.

[99] Edwards, J. R., "A Low-Diffusion Flux-Splitting Scheme for Navier-Stokes Calculations," AIAA Paper 95-1703-CP, June, 1995.

[100] Edwards, J. R., "A Low-Diffusion Flux-Splitting Scheme for Navier-Stokes Calculations," *Computer & Fluids*, Vol. 6, 1997, pp. 635–659.

[101] Jameson, A., "Analysis and Design of Numerical Schemes for Gas Dynamics I: Artificial Diffusion, Upwind Biasing, Limiters and Their Effect on Accuracy and Multigrid Convergence in Transonic and Hypersonic Flow," AIAA Paper 93-3359, July, 1993.

[102] Jameson, A., "Analysis and Design of Numerical Schemes for Gas Dynamics I: Artificial Diffusion, Upwind Biasing, Limiters and Their Effect on Accuracy and Multigrid Convergence in Transonic and Hypersonic Flow," *Journal of Computational Fluid Dynamics*, Vol. 4, 1995, pp. 171–218.

[103] Jameson, A., "Analysis and Design of Numerical Schemes for Gas Dynamics II: Artificial Diffusion and Discrete Shock Structure," *Journal of Computational Fluid Dynamics*, Vol. 5, 1995, pp. 1–38.

[104] Zha, G.-C. and Bilgen, E., "Numerical Solutions of Euler Equations by Using a New Flux Vector Splitting Scheme ," *International Journal for Numerical Methods in Fluids*, Vol. 17, 1993, pp. 115–144.

[105] Zha, G.-C., "Numerical Tests of Upwind Scheme Performance for Entropy Condition ," *AIAA Journal*, Vol. 37, 1999, pp. 1005–1007.

[106] Zha, G.-C., "Comparative Study of Upwind Scheme Performance for Entropy Condition and Discontinuities," AIAA Paper 99-CP-3348, June 28- July 1, 1999.

[107] Zha, G.-C., Shen, Y., and Wang, B., "Calculation of Transonic Flows Using WENO Method with a Low Diffusion E-CUSP Upwind Scheme," AIAA Paper 2008-0745, 46th AIAA Aerospace Sciences Meeting, Reno, NV, Jan. 2008.

[108] Wang, B.-Y. and Zha, G.-C., "Comparison of a Low Diffusion E-CUSP and the Roe Scheme for RANS Calculation," AIAA Paper 2008-0596, 46th AIAA Aerospace Sciences Meeting and Exhibit, Jan. 7-10, 2008.

[109] Zha, G.-C., "A Low Diffusion E-CUSP Upwind Scheme for Transonic Flows," AIAA Paper 2004-2707, to appear in AIAA Journal, 34th AIAA Fluid Dynamics Conference, June 28 - July 1 2004.

[110] Beam, R. and Warming, R., "An Implicit Factored Scheme for the Compressible Navier-Stokes Equations ," *AIAA Journal*, Vol. 16, No. 4, 1978, pp. 393–402.

[111] Taylor III, A. C. and Ng, W. F. and Walters, R. W. , "An improved upwind finite volume relaxation method for high speed viscous flows," *J.Compu.Phys.*, Vol. 99, 1992, pp. 159–168.

[112] Rogers, S. E. and Kwak, D. , "An upwind difference scheme for time accurate incompressible Navier-Stokes equations," *AIAA J.*, Vol. 28, 1990, pp. 253–262.

[113] Rogers, S. E. and Menter, F. R. and Mansour, N. N. and Durbin, P. A. , "A comparison of turbulence models in computing multi-element airfoil flows," AIAA 94-0291, Jan. 1994.

[114] Zha, G.-C. and Bilgen, E., "Numerical Study of Three-Dimensional Transonic Flows Using Unfactored Upwind-Relaxation Sweeping Algorithm," *Journal of Computational Physics*, Vol. 125, 1996, pp. 425–433.

[115] Jameson, A. and Yoon, S. , "Lower-upper implicit schemes with multiple grids for the Euler equations," *AIAA J.*, Vol. 7, 1987, pp. 929–935.

[116] Yoon, S. and Jameson, A. , "Lower-upper symmetric-Gauss-Seidel method for the Euler and Navier-Stokes equations," *AIAA J.*, Vol. 26, 1988, pp. 1025–1026.

[117] Klopfer, G. H. and Yoon, S., "Multizonal Navier-Stokes Code with LU-SGS Scheme," AIAA 93-2965, July 1993.

[118] Kandula, M. and Buning, P. G. , "Implementation of LU-SGS Algorithm and Roe Upwinding Scheme in OVERFLOW Thin-Layer Navier-Stokes Code," AIAA 94-2357, Jun. 1994.

[119] Jameson, A. and Caughey, D. A. , "How many steps are required to solve the Euler equations of steady, compressible flow: in search of a fast solution algorithm," AIAA-2001-2673, Jun. 2001.

[120] Rogers, S. E. , "Comparison of implicit schemes for the incompressible Navier-Stokes equations," *AIAA J.*, Vol. 33, 1995, pp. 2066–2072.

[121] Rogers, S. E. and Kwak, D. and Kiris, C. , "Numerical solution of the incompressible Navier-Stokes equations for steady-state and time-dependent problems," *AIAA J.*, Vol. 29, 1991, pp. 603–610.

[122] Liou, M. S., Arnone, A., and Povinelli, L. A., "Multi-grid Time-accurate Integration of Navier-Stokes Equations," AIAA Paper 93-3361-CP, 7 1993.

[123] McBean, I. W., Liu, F., Hourigan, K., and Thompson, M., "Navier-Stokes Simulation of 2-D Unsteady Aerodynamics of a Turbine Cascade," 14th Australasian Fluid Mechanics Conference, 12 2001.

[124] Ji, S. and Liu, F., "Flutter computation of turbomachinery cascades using a parallel unsteady Navier-Stokes code," *AIAA Journal*, Vol. 37, No. 3, 1999, pp. 320–327.

[125] Cinnella, P., De Palma, P., Pascazio, G., and Napolitano, M., "A Numerical Method for Turbomachinery Aeroelasticity," *Journal of Turbomachinery*, Vol. 126, 2004, pp. 310–316.

[126] Tu, S. and Aliabadi, S. , "A Robust Parallel Implicit Finite Volume Solver for High-Speed Compressible Flows," AIAA Paper 2005-1396, 2005.

[127] Cai, J. and Tsai, H. M. and Liu, F. , "A Parallel Viscous Flow Solver on Multi-Block Overset Grids," *Journal of Computers & Fluids*, Vol. 35, 2006, pp. 1290–1301.

[128] Ohta, T., "An Object-Oriented Programming Paradigm for Parallel Computational Fluid Dynamics on Memory Distributed Parallel Computers ," eds, D.R. Emerson, A. Ecer, J. Periaux, N. Satofuka and P. Fox, Parallel Computational Fluid Dynamics, 1998.

[129] Allwright, S. E., "Multiblock Techniques for Transonic Flow Computation about Complex Aircraft Configuration ," K.W. Morton and M.J. Baines, eds., Numerical Methods for Fluid Dynamics, III, 1988.

[130] Evans, E. W. and Johnson, S. P. and Leggett, P. F. and Cross, M. , "Automatic Generation of Multi-Dimensionally Partitioned Parallel CFD Code in A Parallelisation Tool ," D.R. Emerson, A. Ecer, J. Periaux, N. Satofuka and P. Fox, eds., Parallel Computational Fluid Dynamics, 1998.

[131] Merazzi, S., "MEM-COM An Integrated Memory and Data Management, System Mem-Com User Manual Version 6.0 ," SMR TR-5060, Mar. 1991.

[132] Legland, P. and Vos, J. B. and Van Kemenade, V. and Ytterstrom, A. , "NSMB: A Modular Navier-Stokes Multiblock Code for CFD ," AIAA Paper 1995-0568, 1995.

[133] Ecer, A. and Akay, H. U. and Kemle, W. B. and Wang, H. and Ercoskun, D. , "Parallel Computation of Fluid Dynamics Problems ," *Computer Methods in Applied Mechanics and Engineering*, Vol. 112, 1994, pp. 91–108.

[134] Wang, B.-Y. and Zha, G.-C., "A General Sub-Domain Boundary Mapping Procedure For Structured Grid CFD Parallel Computation," *AIAA Journal of Aerospace Computing, Information, and Communication*, Vol. 5, No.11, 2008, pp. 425–447.

[135] Knight, D., Zhou, G., Okong'o, N., and Shukla, V., "Compressible Large Eddy Simulation Using Unstructured Grids," AIAA Paper 98-0535, 1998.

[136] Hu, Z., "Parallel Computation of Fluid-Structure Interaction Using High Resolution Upwind Schemes," Ph.D. Thesis, University of Miami, May 2005.

[137] Spalart, P. and Allmaras, S., "A One-equation Turbulence Model for Aerodynamic Flows," AIAA-92-0439, 1992.

[138] Shur, M., Spalart, P., Strelets, M., and Travin, A., "Detached-Eddy Simulation of an Airfoil at High Angle of Attack", 4th Int. Symp. Eng. Turb. Modelling and Measurements, Corsica," May 24-26, 1999.

[139] De Rango, S. and Zingg, D. W. , " Aerodynamic computations using a higher-order algorithm ," AIAA 99-0167, 1999.

[140] Zingg, D. W. and De Rango, S. and Nemec, M. and Pulliam, T. H. , "Comparison of Several Spatial Discretizations for the Navier-Stokes Equations," *Journal of Computational Physics*, Vol. 160, 2000, pp. 683–704.

[141] Shen, Y.-Q. and Zha, G.-C., "A Robust Seventh Order WENO Scheme and Its Applications," AIAA Paper 2008-0757, 46th AIAA Aerospace Sciences Meeting, Reno. NV, Jan. 2008.

[142] Daniela di Serafino, "A Parallel Implementation of A Multigrid Multiblock Euler Solver on Distributed Memory Machines," *Parallel Computing*, Vol. 23, 1997, pp. 2095–2113.

[143] Kasliwal, A., Ghia, K., and Ghia, U., " Higher-order accurate solution for flow past a circular cylinder at $Re = 13,4000$," AIAA-2005-1123, 43rd AIAA Aerospace Sciences Meeting and Exhibit, Reno, Nevada,10-13 Jan., 2005.

[144] Krothapalli, A., Shih, C., and Lourenco, L., " The near wake of a circular cylinder at $0.3 < M_\infty < 0.6$: a PIV study ," 32nd Aero Sciences Meeting and Exhibit, AIAA Paper 94-0063, 1994.

[145] Kravchenko, G. and Moin, P., " Numerical studies of flow over a circular cylinder at $Re_D = 3900$," *Phys.Fluids* , Vol. 12, 2000, pp. 403–417.

[146] Lourenco, L.M. and Shih, C., " Characteristics of the plane turbulent near wake of a circular cylinder, A particle image velocity study ," private communication by Beaudan and Moin (data taken from [145]), 1993.

[147] Rizzetta, D.P. and Visbal, M.R. and Blaisdell, G.A., " A time-implicit high-order compact differencing and flitering scheme for Large-eddy simulation ," *Int.J.Numer.Meth.Fluids* , Vol. 42, 2003, pp. 665–693.

[148] Roshko, A., "On the Development of Turbulent Wakes From Vortex Streets," NACA Rep. 1191, 1954.

[149] Goldstein, S., "Modern Developments in Fluid Dynamics," Clarendon Press, Oxford, 1938.

[150] Blackburn, H. and Karniadakis, G., "Two and Three-Dimensional Vortex-Induced Vibration of a Circular Cylinder," ISOPE-93 Conference, Singapore, 1993.

[151] Davis, S. S., "NACA 64 A010 (NACA Ames Model) Oscillatory Pitching," Tech. Rep. AGARD Report No. 702, AGARD, August 1982.

[152] McMullen, M., Jameson, A., and Alonso, J., "Application of a Non-Linear Frequency Domain Solver to the Euler and Navier-Stokes Equations," AIAA Paper-2002-0120, 2002.

[153] Knipfer, A., Schewe, G., and Wendt, V., "Numerische und experimentelle Untersuchungen an einem schwingenden NLR 7301-Profil in transsonischer Stromung," Teil 1: Flatern und erzwungene Schwingungen, DLR Bericht IB 232-98 J 05, 1998.